Development of tungsten alloy plasma-facing materials for the fusion power plant

DISSERTATION
zur Erlangung des Grades eines Doktors der Naturwissenschaften
an der Fakultät für Physik und Astronomie der Ruhr-Universität Bochum
gemeinsam mit dem Grad
eines Doktors des Physikingenieurwesens an der Fakultät für
Ingenieurswissenschaften und Architektur der Universität Gent

Doctoral thesis submitted in order to obtain the academic degree of
Doctor of Natural Science
(Faculty of Physics and Astronomy, Ruhr-Universität Bochum)
jointly with the degree of
Doctor of Engineering Physics
(Faculty of Engineering and Architecture, Ghent University)

Janina Schmitz
from Warendorf

1. Gutachter: Prof. Dr. Ch. A. E. Linsmeier
2. Gutachter: Prof. Dr. A. von Keudell

Tag der Disputation: 09.06.2020

Contents

List of acronyms

ALI Auger, LEED, Ion scattering

AUG ASDEX (axisymmetric divertor experiment) Upgrade

BCA Binary Collision Approximation

BSE Backscattered Electron

CX Charge Exchange

EDX Energy-Dispersive X-ray analysis

ELM Edge-Localised Mode

FIB Focussed Ion Beam

FIB-SEM Focussed Ion Beam - Secondary Electron Microscopy

FWHM Full Width at Half Maximum

IBA Ion Beam Analysis

SE Secondary Electron

iSE ion generated Secondary Electron

LCFS Last Closed Flux Surface

LEIS Low-Energy Ion Scattering

LOCA Loss-Of-Coolant Accident

LSCM Laser Scanning Confocal Microscope

Magnum-PSI MAgnetized plasma Generator and NUMerical modeling for Plasma Surface Interaction

NRA Nuclear Reaction Analysis

OES Optical Emission Spectroscopy

PFC Plasma-Facing Component

PFM Plasma-Facing Material

PSI Plasma-Surface Interaction

PWI Plasma-Wall Interaction

QMS Quadrupole Mass Spectrometry

SEM Scanning Electron Microscopy

SI Secondary Ion

SIMS Secondary Ion Mass Spectrometry

SOL Scrape-Off Layer

TGA Thermogravimetric Analyser

TS Thomson Scattering

XPS X-ray Photoelectron Spectroscopy

Abstract

Tungsten-chromium-yttrium (WCrY) smart alloys are developed to suppress W oxidation in case of a loss-of-coolant accident with additional air ingress in a future fusion power plant. When coming into contact with oxygen a passivating Cr oxide layer forms on top of the WCrY alloy. WCrY with an optimum composition of 67.9 at% W - 31.1 at% Cr - 1.0 at% Y demonstrated superior oxidation resistance compared to pure W and previously investigated W-based self-passivating alloys. The alloys are called smart as they should adapt to the accidental reactor scenario but behave like pure W due to preferential sputtering of the alloying elements during normal plasma operation. One has to ascertain that the advantages of using W as armour material are not deteriorated due to the addition of alloying elements.

The aim of this thesis is to evaluate the suitability of self-passivating WCrY smart alloys as first wall material of future fusion devices such as DEMO, focussing on the material's plasma performance. Dedicated experiments were carried out in the linear plasma devices PSI-2 and Magnum-PSI to investigate especially the alloy's erosion behaviour under different plasma conditions. Two main test regimes for plasma exposures were determined. On the one hand a large fraction of the plasma particles in a fusion reactor will have impact energies which lie below the threshold for W sputtering (*mild* plasma regime). On the other hand there will be particles with impact energies at or above the threshold and therefore causing significant W erosion (*harsh* plasma regime). The sample temperature in all plasma experiments was set to 900 K corresponding to DEMO first wall conditions. For experiments in PSI-2, modelling using the binary collision code SDTrimSP was used to simulate the impact of the ion irradiation onto the alloy composition and to investigate the effect of added thermal diffusion. Additional experiments employing surface-sensitive analysis methods focussed on the temperature dependence of the alloy's composition.

Since prior to this work no investigations on the plasma performance of WCrY had been carried out, it serves as an overview and aims at finding out which processes are performance-relevant. Using ion beam analysis, strong Cr segregation (with a segregation energy of $\Delta H_{Cr} = 0.7\,\mathrm{eV}$) and Y segregation ($\Delta H_Y = 0.3\,\mathrm{eV}$) were found starting from a temperature of 700 K. Further, thermal diffusion counteracts the build-up of Cr concentration gradients induced by preferential sputtering. The sputter yields of a multicomponent material depend on the concentration profiles in the surface layer from which target atoms are sputtered. Since thermal transport processes and erosion compete, concentration profiles are flux- and temperature-dependent. In case diffusive transport is the dominating process, preferentially sputtered species are resupplied constantly to the surface leading to an enhanced erosion of WCrY. This effect was found to be especially strong during plasma exposures for ion energies close to the sputter thresh-

old of W due to lowering of the W sputter threshold in the vicinity of Cr. When the erosion rate is of comparable magnitude to the rate of diffusive transport, small changes in the plasma composition or sample temperature result in either enhanced or equal erosion of WCrY in comparison to W. In general, the rates of the different processes impacting the alloy's surface composition and its erosion behaviour form a complex system of coupled differential equations containing many interdependencies. The erosion rate u depends mainly on the ion flux J, the incident ion energy E_{ion} and the mass of the incident ions m_{ion} and therefore the plasma composition. The diffusive flux D, replenishing the preferentially sputtered elements at the alloy's surface, depends mainly on the sample temperature T and on the depth (x)-dependent elemental concentration profiles $c_i(x)$ as well as on the specific material microstructure, called M, for instance the material's grain size and distribution. Erosion and diffusion are counteracting and at the same time interdependent processes which both impact $c_{ss}(x)$, the composition of the surface layer from which sputtering occurs, which consequently is a function of u and D: $c_{ss} = f(u(J, E_{ion}, m_{ion}), D(T, c, M))$
Experimental results and SDTrimSP modelling suggest that for exposures in the *mild* plasma regime, at a sample temperature of 900 K and ion energies of 120 eV in pure deuterium (D) plasma, WCrY erosion is similar to that of pure W for fluxes of 1×10^{21} ions/(m^{2}s) in PSI-2 and 1×10^{23} ions/(m^{2}s) in Magnum-PSI and fluences up to 2×10^{27} ions/m^2. The erosion rate of WCrY is determined by the W erosion rate, making WCrY behave like pure W. The rates of Cr transport to the surface, due to diffusion and segregation, are negligible.
In the *harsh* plasma regime, experiments were conducted in PSI-2 at fluxes in the order of 1×10^{21} ions/(m^{2}s) and fluences up to 1×10^{26} ions/m^2, a sample temperature of 900 K and different ion energies depending on the plasma composition: two exposures were conducted with ion energies at the sputter threshold for W: one experiment in pure D plasma at an ion energy of 220 eV and another one in mixed D+5 % helium (He)+1 % argon (Ar) plasma at an ion energy of 120 eV. In both experiments, WCrY erosion was found to be enhanced in comparison to that of pure W due to Cr diffusion to the surface leading to enhanced W sputtering in WCrY. Via SDTrimSP modelling the diffusion coefficient of Cr in WCrY was determined to be of the order of 1×10^{-17} m^2 s^{-1}. Consequently, in this experimental conditions the rate of Cr diffusion and the erosion rate are of comparable magnitude, the W erosion rate does not dominate. In contrast, the third experiment conducted in the harsh regime, with a plasma composition of D+1 % Ar and at an incident ion energy of 120 eV which is significantly above the sputter threshold for Ar on W, showed similar erosion for W and WCrY. Again, the WCrY erosion rate is determined mainly by that of pure W.
Oxidation tests proved that the WCrY samples exposed in the different PSI-2 experiments successfully suppress W oxidation. The complex geometry of WCrY samples meant for plasma exposure differs from the simple cubic shape of standard oxidation test WCrY samples. Geometry effects do not play a role after 40 h of oxidation. However, it has to be ascertained that for prolonged plasma exposure and thus Cr loss during several years of reactor operation, enough Cr for effective passivation is left in the alloy.

Zusammenfassung

Wolfram-Chrom-Yttrium (WCrY) intelligente Legierungen werden zur Unterdrückung von W Oxidierung für ein Unfallszenario mit Verlust des Kühlmittels und zusätzlichem Lufteintritt in einem zukünftigen Fusionskraftwerk entwickelt. Tritt die Legierung mit Sauerstoff in Kontakt, bildet sich eine passivierende Cr Oxid Schicht oben auf der Legierung. WCrY mit einer optimalen Zusammensetzung von 67.9 at% W - 31.1 at% Cr - 1.0 at% Y wies eine ausgezeichnete Oxidationsbeständigkeit im Vergleich zu reinem W und vormals untersuchten W-basierten selbst-passivierenden Legierungen auf. Die Legierung wird als intelligent bezeichnet, da sie sich dem Unfallszenario anpassen und sich während des normalen Plasmabetriebs durch präferentielle Zerstäubung der Legierungselemente jedoch wie reines W verhalten soll. Es ist sicherzustellen, dass die Vorteile von W als Schutzmaterial der ersten Wand nicht durch die Legierungselemente degradiert werden.

Das Ziel dieser Arbeit ist die Evaluierung der Eignung der selbst-passivierenden WCrY Legierungen als Material der ersten Wand zukünftiger Fusionskraftwerke wie DEMO, wobei der Fokus auf dem Plasmaverhalten des Materials liegt. Dedizierte Experimente wurden in den linearen Plasmaanlagen PSI-2 und Magnum-PSI durchgeführt, um insbesondere das Erosionsverhalten der Legierung unter verschiedenen Plasmabedingungen zu untersuchen. Zwei Haupttestregime für die Plasmaexponierungen wurden festgelegt. Einerseits wird ein Großteil der Plasmapartikel in einem Fusionsreaktor Energien besitzen die unter dem Schwellwert für W Zerstäubung liegen (*mildes* Plasmaregime). Zudem wird es Partikel mit Aufprallenergien an oder über dem Schwellwert geben, die somit signifikante W Erosion verursachen (*harsches* Plasmaregime). Die Probentemperatur aller Experimente wurde entsprechend der Bedingungen an der ersten Wand von DEMO auf 900 K festgelegt. Für Experimente in PSI-2 wurde Modellierung mittels des binären Kollisionscodes SDTrimSP verwendet, um die Einwirkung der Ionenbestrahlung auf die Legierungszusammensetzung zu simulieren und den Effekt zusätzlicher thermischer Diffusion zu evaluieren. Weitere Experimente mit oberflächen-sensitiven Analysemethoden fokussierten sich auf die Temperaturabhängigkeit der Legierungszusammensetzung.

Da es im Vorfeld dieser Arbeit keine Untersuchungen des Plasmaverhaltens von WCrY gab, dient sie als Übersicht und zielt darauf ab herauszufinden welche Prozesse dieses Verhalten relevant beeinflussen. Mittels Ionenstrahlanalyse wurde starke Cr Segregation (mit einer Segregationsenergie $\Delta H_{Cr} = 0.7\,\text{eV}$) und starke Y Segregation ($\Delta H_Y = 0.3\,\text{eV}$) bei Temperaturen oberhalb 700 K festgestellt. Des Weiteren wirkt thermische Diffusion der Bildung von Cr Konzentrationsgradienten induziert durch präferentielle Zerstäubung entgegen. Die Zerstäubungsraten eines Mehrkomponentenmaterials hängen von den Konzentrationsprofilen in der Oberflächenschicht aus der die Targetatome zerstäubt werden ab. Da thermische Transportprozesse und Erosion konkurrieren, sind

die Konzentrationsprofile fluss- und temperaturabhängig. Ist diffusiver Transport der dominante Prozess, werden die präferentiell zerstäubten Spezies konstant an der Oberfläche nachgeliefert, was in einer erhöhten Erosion von WCrY resultiert. Dieser Effekt stellte sich als besonders stark im Falle von Ionenenergien nahe des Zerstäubungsschwellwertes von W, bedingt durch das Absenken dieses Schwellwertes in der Umgebung von Cr, dar. Ist die Erosionsrate von gleicher Größenordnung wie die Rate des diffusiven Transports, resultieren kleine Änderungen in der Plasmazusammensetzung oder der Probentemperatur entweder in erhöhter oder gleicher Erosion von WCrY im Vergleich zu W. Im Allgemeinen bilden die Raten der verschiedenen Prozesse die Einfluss auf die Oberflächenzusammensetzung der Legierung und dessen Erosionsverhalten haben ein komplexes System gekoppelter Differentialgleichungen mit vielen Interdependenzen. Die Erosionsrate u hängt größtenteils von dem Ionenfluss J, der Ioneneinfallsenergie E_{ion} und der Ionenmasse m_{ion} und somit der Plasmakomposition ab. Der diffusive Fluss D, der für das Nachliefern der präferentiell zerstäubten Elemente an der Legierungsoberfläche sorgt, hängt größtenteils von der Probentemperatur T und der tiefenabhängigen (Tiefe x) Profile der elementaren Konzentrationen $c_i(x)$ sowie von der spezifischen Materialmikrostuktur M, beispielsweise der Korngröße und -verteilung, ab. Erosion und Diffusion sind konkurrierende und gleichzeitig voneinander abhängige Prozesse, die beide Einfluss nehmen auf c_{ss}, der Zusammensetzung der Oberflächenschicht aus der Zerstäubung resultiert, welche also eine Funktion von u und D darstellt: $c_{ss} = f(u(J, E_{ion}, m_{ion}), D(T, c, M))$

Experimentelle Ergebnisse und SDTrimSP Modellierung zeigten, dass für Exponierungen im *milden* Plasmaregime, bei einer Probentemperatur von 900 K und Ionenenergien von 120 eV in reinem Deuterium (D) Plasma, die Erosion von WCrY vergleichbar mit der von reinem W für Flüsse von 1×10^{21} ions/(m^{2}s) in PSI-2 und 1×10^{23} ions/(m^{2}s) in Magnum-PSI und Fluenzen bis zu 2×10^{27} ions/m^2 ist. Die Erosionsrate von WCrY ist bestimmt durch die W Erosionsrate, sodass WCrY sich wie reines W verhält. Die Raten des Cr-Transports zur Oberfläche, durch Diffusion und Segregation, sind vernachlässigbar.

Im *harschen* Plasmaregime wurden Experimente bei Flüssen in der Größenordnung 1×10^{21} ions/(m^{2}s) und Fluenzen bis zu 1×10^{26} ions/m^2, einer Probentemperatur von 900 K und verschiedenen Ionenenergien je nach Plasmazuammensetzung in PSI-2 durchgeführt: bei zwei Experimenten lag die Ionenenergie an der Zerstäubungsschwelle von W: ein Experiment in reinem D Plasma bei einer Ionenenergie von 220 eV und ein weiteres in gemischtem D+5 % Helium (He)+1 % Argon (Ar) Plasma bei einer Ionenenergie von 120 eV. In beiden diesen Experimenten war, aufgrund von Cr Diffusion zur Oberfläche und daraus resultierender erhöhter W Erosion in WCrY, eine erhöhte Erosion von WCrY gegenüber der von reinem W festzustellen. Mithilfe von SDTrimSP Modellierung wurde der Diffusionskoeffizient von Cr in WCrY auf einen Wert in der Größenordnung von $1 \times 10^{-17}\,\mathrm{m}^2\,\mathrm{s}^{-1}$ bestimmt. Folglich sind bei diesen experimentellen Bedingungen die Rate der Cr Diffusion und die Erosionsrate von vergleichbarer Größenordnung, sodass die W Erosionsrate nicht dominiert. Gegensätzlich dazu wurde im dritten Experiment innerhalb des *harschen* Plasmaregimes, mit einer Plasmazusammensetzung von D+1 % Ar und einer Ioneneinfallsenergie von 120 eV, welche signifikant über dem Schwellwert für W Zerstäubung durch Ar liegt, vergleichbare Erosion für W und WCrY festgestellt. Wieder ist die WCrY Erosionsrate von der des reinen W dominiert.

Oxidationstests zeigten, dass WCrY Proben, welche in den verschiedenen PSI-2 Experimenten exponiert wurden, erfolgreich W Oxidierung unterdrücken. Die komplexe Geometrie der für das Plasma bestimmten WCrY Proben unterscheidet sich von der simplen kubischen Geometrie der WCrY Proben die standardmäßig in Oxidationstests verwendet werden. Geometrische Effekte spielen nach einer Oxidationszeit von 40 h keine Rolle mehr. Nichtsdestotrotz muss sichergestellt werden, dass nach langandauernder Plasmaexponierung und dem damit verbundenen Cr Verlust während mehrerer Jahre Reaktorbetrieb genug Cr zur effektiven Passivierung in der Legierung zurückbleibt.

Samenvatting

Wolfraam-chroom-yttrium (WCrY) slimme legeringen worden ontwikkeld om W-oxidatie te onderdrukken bij een ongeval, met verlies van koeling en extra luchtinsluiting, in een toekomstige fusie-energiecentrale. Bij contact met zuurstof vormt zich bovenop de WCrY-legering een passiverende Cr-oxide laag. WCrY met een optimale samenstelling van 67.9 at% W - 31.1 at% Cr - 1.0 at%, toonde een superieure oxidatieweerstand in vergelijking met zuiver W en eerder onderzochte W-gebaseerde zelf-passiverende legeringen. De legeringen worden slim genoemd omdat ze zich kunnen aanpassen aan het incidenteel reactorscenario, maar zich gedragen als zuiver W, als gevolg van preferentiële sputtering van de legeringselementen, bij normale plasma werking. Er moet nagegaan worden dat de voordelen van het gebruik van W als wapening materiaal niet aangetast worden door het toevoegen van legeringselementen.

Het doel van dit proefschrift is om de geschiktheid van zelf-passiverende WCrY slimme legeringen te evalueren als eerste wandmateriaal van toekomstige fusie-installaties zoals DEMO, waarbij de nadruk ligt op de plasma werking van het materiaal. Specifieke experimenten werden uitgevoerd in de lineaire plasma apparaten PSI-2 en Magnum-PSI. Voornamelijk om het erosiegedrag van de legering onder verschillende plasmacondities te onderzoeken. Twee belangrijke testregimes voor plasma-blootstellingen werden bepaald. Enerzijds zal een groot deel van de plasmadeeltjes in een fusiereactor een impactenergie hebben onder de drempelwaarde voor W sputteren (mild plasma regime). Anderzijds zullen er deeltjes zijn met een impact energie gelijk aan of boven de drempelwaarde en daardoor aanzienlijke W-erosie veroorzaken (hard plasmaregime). De sample temperatuur in alle plasma-experimenten werd ingesteld op 900 K, wat overeenkomt met omstandigheden in DEMO's eerst wand. Voor experimenten in PSI-2, werd modellering met behulp van de binaire botsingscode SDTrimSP gebruikt om het effect van de ionenstraling op de samenstelling van de legering te simuleren en het effect van toegevoegde thermische diffusie te onderzoeken. Aanvullende experimenten met behulp van oppervlakte-gevoelige analysemethoden richtte zich op de temperatuur afhankelijkheid van de samenstelling van de legering.

Aangezien voorafgaand aan dit werk geen onderzoek naar de plasmaprestaties van WCrY gedaan is, dient dit werk als een overzicht en is het bedoeld om te achterhalen welke processen relevant zijn voor de plasmaprestaties van WCrY. Met behulp van ionenbundelanalyse werd vanaf een temperatuur van 700 K sterke Cr-segregatie (met een segregatie-energie van$\Delta H_{Cr} = 0.7\,\mathrm{eV}$) en Y-segregatie ($\Delta H_Y = 0.3\,\mathrm{eV}$) gevonden. Verder gaat thermische diffusie de opbouw van Cr-concentratiegradiënten tegen die worden geïnduceerd door preferentiële sputtering. De sputter ratio's van een multi-componenten materiaal zijn afhankelijk van de concentratieprofielen in de oppervlaktelaag van waaruit doelatomen worden gesputterd. Aangezien thermische transportprocessen en erosie met

elkaar concurreren, zijn concentratieprofielen flux- en temperatuurafhankelijk. In het geval dat diffusie transport het dominante proces is, worden preferentieel gesputterde atomen voortdurend naar het oppervlak aangevoerd, wat leidt tot een verhoogde erosie van WCrY. Dit effect bleek voornamelijk sterk te zijn bij plasma-blootstelling met ionenergieën in de buurt van de sputterdrempel van W als gevolg van het verlagen van de W-sputterdrempel bij W in de buurt van Cr. Wanneer de erosiesnelheid vergelijkbaar is met de snelheid van diffusie transport, resulteren kleine veranderingen in de plasmasamenstelling of sampletemperatuur in een versterkte of gelijke erosie van WCrY in vergelijking met W.

In het algemeen vormen de snelheid van de verschillende processen die van invloed zijn op de oppervlaktesamenstelling van de legering en het erosiegedrag van de legering een complex systeem van gekoppelde differentiaalvergelijkingen met veel onderlinge afhankelijkheden. De erosiesnelheid u hangt voornamelijk af van de ionenflux J, de inkomende ionenenergie E_{ion} en de massa van de invallende ionen m_{ion} en derhalve de plasmasamenstelling. De diffusie flux D, die de bij voorkeur gesputterde elementen aan het oppervlak van de legering aanvult, hangt voornamelijk af van de sampletemperatuur T en van de diepte (x)-afhankelijke elementaire concentratie profielen $c_i(x)$ alsook van de specifieke materiaalmicrostructuur, M genaamd, bijvoorbeeld de korrelgrootte en verdeling van het materiaal. Erosie en diffusie zijn processen die elkaar tegenwerken en tegelijkertijd onderling afhankelijk zijn van elkaar. Beide processen zijn van invloed op de oppervlaktelaag c_{ss}, van waaruit sputteren optreedt, wat bijgevolg een functie is van u en D: $c_{ss} = f(u(J, E_{ion}, m_{ion}), D(T, c, M))$

Experimentele resultaten en SDTrimSP-modellering suggereren dat voor blootstelling in het milde plasmaregime bij een sampletemperatuur van 900 K met een ion-energie van 120 eV in zuiver Deuterium (D) plasma, WCrY-erosie vergelijkbaar is met de erosie van zuiver W voor fluxen van $1 \times 10^{21}\,\text{ions}/(\text{m}^2\text{s})$ in PSI-2 en $1 \times 10^{23}\,\text{ions}/(\text{m}^2\text{s})$ in Magnum-PSI en fluenties tot $2 \times 10^{27}\,\text{ions}/\text{m}^2$. De erosiesnelheid van WCrY wordt bepaald door de W-erosiesnelheid, waardoor WCrY zich gedraagt als zuiver W. De snelheid van Cr-transport naar het oppervlak, als gevolg van diffusie en segregatie, is verwaarloosbaar.

In het harde plasma regime, werden experimenten uitgevoerd in PSI-2 bij fluxen in de grootteorde van $1 \times 10^{21}\,\text{ions}/(\text{m}^2\text{s})$ en fluenties tot $1 \times 10^{26}\,\text{ions}/\text{m}^2$, een sampletemperatuur van 900 K en verschillende ion-energieën afhankelijk van de plasmasamenstelling: twee experimenten werden gedaan met de ion-energie bij de sputterdrempel voor W: één experiment in zuiver D plasma bij een ion-energie van 220 eV en een ander in gemengd D+5 % helium (He)+1 % argon (Ar) bij een ion-energie van 120 eV. In beide experimenten bleek de erosie van WCrY sterker dan die van zuiver W door Cr diffusie naar het oppervlak, wat leidt tot een versterkt sputteren van W in WCrY. Via SDTrimSP modellering werd vastgesteld dat de diffusiecoëfficiënt van Cr in WCrY in de grootteorde van $1 \times 10^{-17}\,\text{m}^2\,\text{s}^{-1}$ ligt. Bijgevolg, zijn de snelheid van Cr diffusie en de erosie snelheid van gelijkaardig grootte onder de voorwaarden van dit experiment, de erosie snelheid van W domineert niet. Het derde experiment daarentegen, uitgevoerd in het harde regime, met een plasmasamenstelling van D+1 % Ar en bij een incidentele ion-energie van 120 eV, wat aanzienlijk hoger is dan de sputterdrempel voor Ar op W, vertoonde een soortgelijke erosie voor W en WCrY. Ook hier wordt de WCrY-erosiesnelheid hoofdzakelijk bepaald door dat van pure W. Oxidatietests hebben aangetoond dat de WCrY-samples die in de verschillende PSI-2-experimenten zijn blootgesteld, met succes W-oxidatie onderdrukken. De complexe geometrie van WCrY samples bedoeld voor plasma blootstelling verschilt van de eenvoudige kubusvorm van standaard WCrY samples gebruikt voor oxidatietests. Geometrie-effecten spelen na 40 h oxidatie geen rol meer. Er moet echter wel nog onderzocht worden of bij langdurige plasma-blootstelling en dus Cr-verlies gedurende meerdere jaren aan reactor werking, genoeg Cr voor een efficiënte passivering overblijft in de legering.

1. Introduction

1.1. Motivation

The world population is steadily increasing. 7.6 billion people inhabited the world in 2017. According to UN predictions, this number will increase to nearly 10 billion in 2050. While Europe's population is expected to remain constant at 0.7 billion or even to slightly decrease, Africa's population is expected to almost double from 1.3 billion to 2.5 billion [1]. At the same time the world's energy demand constantly increases. While the primary energy consumption per capita of developed countries such as Germany has been stable since 2000, there was a sharp rise in newly industrialised countries such as China and India: for Germany it was at 6.7 MWh/capita in 2000 and at 7.0 MWh/capita in 2016, while it rose from 1.0 MWh/capita to 4.3 MWh/capita in China and from 0.4 MWh/capita to 0.9 MWh/capita in India, respectively. Especially for African countries just starting to industrially develop the energy consumption per capita is on the rise [2]. Those are the countries where the population growth rates are among the highest.

In contrast to the growing population and energy consumption, the world's natural resources decline. Since the start of the industrial revolution in the 18th century, coal has been intensively mined. Later petroleum and natural gas gained equal importance as fossil fuels and have been extensively exploited since. Not only are fossil fuels finite, burning them also leads to the emission of greenhouse gases. More than 80 % of Germany's greenhouse gas emissions originate from combustion of fossil fuels. The great majority of the emissions consist of carbon dioxide (CO_2) [3]. The greenhouse effect describes the warming of a planet's surface due to radiation emitted from the planet's atmosphere. Other ways of energy production are nuclear fission or the usage of renewable energies. These are virtually omitting the emission of greenhouse-gasses, yet there are also drawbacks. Nuclear fission remains under discussion since the high-level radioactive waste remains dangerous to humans for millennia. Renewable energy technologies are on the rise, especially wind and solar power plants have spread in Germany and other countries during the last decades. However, renewable energy production technologies are subject to fluctuating natural conditions. Efficient storage solutions are still under development. For this reasons a clean energy supply relying solely on renewables is not possible at the moment. The world is in need of a solution to its growing energy problem.

1.2. Nuclear Fusion

A possible solution are power plants relying on a nuclear fusion reaction. Unlike conventional nuclear power plants, which are based on nuclear fission reactions, the fusion reaction does not produce long-lasting radioactive waste. Just like conventional nuclear power plants, energy generation eventually is based on Einstein's famous mass-energy equivalence, $E = mc^2$. This equation states that every mass has an equivalent amount of energy and vice versa. Since the binding energy per nucleon differs between elements as shown in Figure 1.1, energy can be generated for example by fissioning heavier elements into lighter ones. In a fusion reaction light nuclei are fused together to form a heavier nucleus. The Sun for instance, uses a proton-proton reaction as energy source. On Earth, a reaction involving the heavy hydrogen isotopes deuterium (D) and tritium (T) is favoured for energy production. D and T are fused to form a neutron (n) plus a helium (He) nucleus (α-particle). The reaction and the respective energies are written in Equation (1.1).

$$\mathrm{D} + \mathrm{T} \longrightarrow {}^4\mathrm{He}\,(3.5\ \mathrm{MeV}) + n\,(14.1\ \mathrm{MeV}) \tag{1.1}$$

D is easily available for example in sea water with a natural abundance of 0.0115 % on Earth. T has a half-life time of about 12 years and hence does not naturally occur on Earth, which is why it must be "bred" from the naturally occurring lithium (Li) by neutron bombardment via the two reactions shown below (1.2) [5].

$$\mathrm{n} + {}^6\mathrm{Li} \longrightarrow {}^4\mathrm{He} + \mathrm{T} + 4.8\ \mathrm{MeV}, \mathrm{n} + {}^7\mathrm{Li} \longrightarrow {}^4\mathrm{He} + \mathrm{T} + \mathrm{n}^* - 2.5\ \mathrm{MeV} \tag{1.2}$$

To make the positively charged D and T nuclei fuse, the Coulomb barrier has to be overcome. Thanks to quantum tunnelling, particles with energies slightly below this

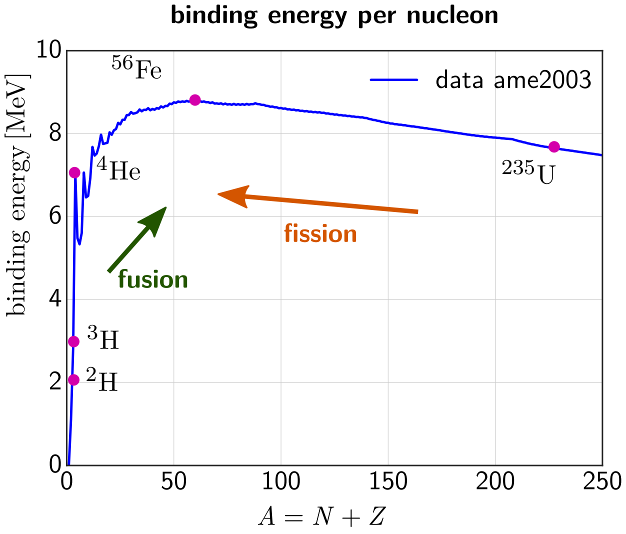

Figure 1.1.: Binding energy per nucleon with data taken from [4]

barrier can already pass it. Still D and T ions need to possess high kinetic energies to come close enough together. This energy is transferred to them via heat. If a gas is heated to temperatures of more than 100 000 K, the electrons become separated from the atomic nuclei. The ionised gas is called a plasma. Although it is a mixture of charged particles, ions and electrons, it appears neutral for distances greater than the Debye length λ_{Debye}. One fifth of the energy from fusing D and T is transferred to the He nuclei created during the reaction. These transfer their energy to the plasma. When adequate confinement conditions are provided, this α-particle heating solely maintains the plasma temperature against energy losses. At this point, which is called ignition, the plasma burns self-sustainingly [6], i.e. no more external heating is applied. The ignition condition is given in Equation (1.3).

$$n_e \tau_E > \frac{12}{<\sigma\nu>} \frac{T}{\epsilon_\alpha}, \tag{1.3}$$

with the temperature T, the reaction rate $<\sigma\nu>$, the energy carried by the α-particle ϵ_α, the plasma density n_e and the energy confinement time τ_E. The product of density and confinement time, $n_e\tau_E$, is referred to as Lawson criterion. In the early days of fusion research Lawson identified this product as a critical parameter for a thermonuclear reactor. Now the fusion triple product, defined as $n_e T \tau_E$ and derived from the ignition condition (Equation (1.3)), is most frequently used as the figure of merit characterising a fusion plasma since it brings out clearly the requirements on density, temperature and confinement time [6].

The remaining four fifths of the reaction energy not transferred to the He nucleus is carried by the neutron. Neutrons are not bound to magnetic field lines and impinge on the walls of the vacuum vessel, which encloses the plasma. The neutrons penetrate deep into the wall and deposit their energy. Just as for conventional power plants, the deposited energy is then converted into electric energy by heating water and driving steam turbines. At temperatures of more than 1×10^8 K the D-T fusion reaction rate reaches its maximum of about $1 \times 10^{-21}\,\mathrm{m}^2\,\mathrm{s}^{-1}$. Thus this temperature is targeted to have as many D-T reactions in a fusion plasma as possible. This temperature exceeds by far the melting point of any existing material. Further, direct contact of the plasma with the surrounding wall material needs to be avoided to prevent cooling of the plasma. Therefore, the extremely hot plasma has to be confined in a special kind of vessel. Since the plasma is an ensemble of charged particles, it can be formed or guided using magnetic field lines. For both of the currently prevailing reactor geometries, tokamak and stellerator, magnetic fields are used to shape the plasma. In that way the hot ionised particles are prevented from contacting the first wall. The tokamak is a doughnut-shaped device consisting of toroidal field coils. For a stable plasma equilibrium a poloidal magnetic field is necessary, which is mainly produced by the current in the plasma itself. The current is induced using the transformer principle and driven in toroidal direction. While the plasma serves as the second winding, the primary winding is a central solenoid. This can be wound around an iron core placed inside the centre of the torus [6]. The current in the primary winding is ramped for plasma operation, thus a tokamak is operated in pulsed mode. ITER, an international nuclear fusion research reactor which

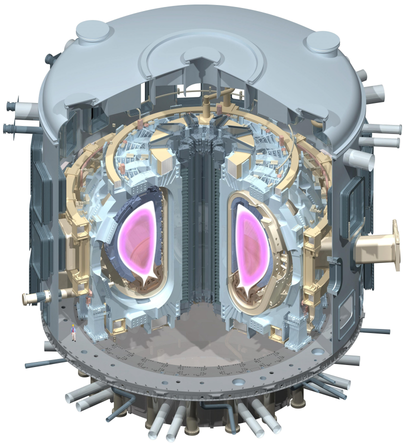

Figure 1.2.: ITER tokamak surrounded by its vacuum vessel and its stainless steel cryostat taken from [8]

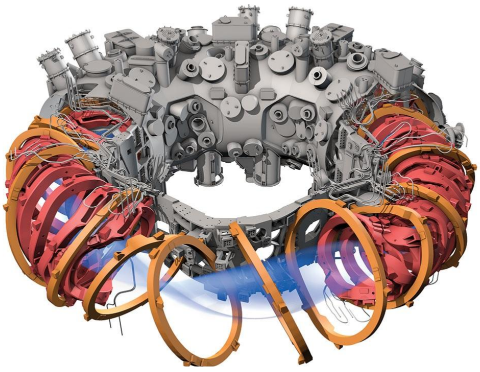

Figure 1.3.: W7-X magnetic field configuration and the vacuum vessel built around it taken from [7]

is currently being built in Cadarache, France, is based on the tokamak principle. A sketch of ITER is shown in Figure 1.2. For DEMO, the reactor following the successful testing of ITER, the exact design is still unclear. The EU assessment of DEMO development has been based on the tokamak principle so far. DEMO shall demonstrate electricity generation from fusion for the first time. The highly symmetric tokamak configuration seems relatively simple when compared to that of a stellerator. This, in contrast, is a device made up of complexly shaped magnetic field coils affording additional freedoms in magnetic field shaping and optimisation [7]. A stellerator can be operated in steady state mode as it does not rely on the transformer principle. The fusion experiment Wendelstein 7-X in Greifswald, Germany, is a stellerator, it is displayed in Figure 1.3. Research is generally lacking some years of experience for this type of fusion reactor since only recently advanced computational resources allowed creating the optimised magnetic field configuration. Although the questions concerning appropriate plasma-facing materials for future fusion reactors are to a great extent congruent for stellerators and tokamaks, there is more detailed knowledge on expected heat and particle loads for the latter devices.

1.3. Plasma-facing materials

An ideal magnetic confinement is impossible to achieve and moreover, the energy and the fusion reaction products need to be exhausted from the walls for energy conversion. Additionally, neutrons from the fusion reaction are not bound to the magnetic field lines and hit the wall at energies of up to 14 MeV. Thus there is always some particle and energy transport to the surrounding walls giving rise to Plasma-Wall Interaction (PWI). The choice of the Plasma-Facing Materials (PFMs) handling particle and energy exhaust is therefore important for building a fusion reactor. Interaction of plasma particles with the wall leads to the erosion of PFM. In turn, the eroded material can get ionised and travel into the plasma leading to its dilution and cooling. Generally, PWI has a great influence on many operation aspects of a fusion reactor: the plasma performance, the material lifetime and therefore the efficiency of a fusion reactor, the fuel (tritium) retention and therefore safety and licensing aspects. Important processes of PWI are erosion, deposition and fuel retention.

Tungsten (W) is currently the preferred wall material for next step fusion devices such as DEMO. It possesses many advantages to be used as PFM. Tungsten has a melting point of around 3700 K, which is the highest melting point of all metals [9]. Due to its high atomic mass of 184 u, W shows low erosion yields during hydrogen isotope ion irradiation. Hydrogen retention is low in W. This ensures that the amount of fuel stored in the wall and thus lost for the fusion reaction is minimised. Moreover, low tritium retention is required for safety reasons. Further advantages are a high thermal conductivity of about 170 W/(mK) at room temperature and a low coefficient of thermal expansion. However, there are also some drawbacks in using W. These have to be improved for the development of W-based wall components. Tungsten is inherently brittle, which may lead to material failure. Tungsten-fibre reinforced tungsten (W_f/W) is an advanced tungsten-based material developed to solve the issue of the brittleness of W by introducing fibres into the W matrix [10]. A further drawback of pure W consists in fast oxidation when coming into contact with oxygen (O). Oxygen leakage into the reactor can occur in case of accidents. W-based self-passivating smart alloys target the problem of W oxidation. These alloys are called smart because they should be able to on the one hand suppress W oxidation during accidental reactor scenarios, and on the other hand behave like pure W during normal plasma operation. The ternary system composed of tungsten, chromium and yttrium (WCrY) demonstrated superior oxidation resistance compared to previously investigated W-based self-passivating alloys. The issue of W oxidation and the development of W-based self-passivating alloys is in more detail described in Chapter 3. While the addition of alloying elements such as Cr can consequently improve the material's resistance to accidental scenarios, one has to ascertain that the advantages of using W as a PFM are not deteriorated by alloying. First plasma tests had been carried out for the tungsten-chromium-titanium (WCrTi) system [11]. However, at the start of this thesis, no work investigating the WCrY system's response to plasma exposure had been undertaken.

Aim of this thesis

The present work focusses on evaluating the plasma performance of W-based self-passivating WCrY smart alloys. Dedicated experiments are carried out to investigate especially the alloy's erosion behaviour besides other parameters like deuterium retention or surface phenomena. The experiments are performed mainly in the linear plasma devices PSI-2, at Forschungszentrum Jülich, Germany, and Magnum-PSI, at DIFFER in Eindhoven, the Netherlands. The objective of installing a WCrY and a W reference sample in the tokamak ASDEX Upgrade for long-term exposure, is to investigate the material's behaviour at the plasma edge of a tokamak. Here results are still pending. During tokamak operation different processes happen simultaneously and possibly lead to synergistic effects which cannot be investigated separately. In addition, ion beam analysis experiments are carried out. These experiments aim at a more in-depth investigation of isolated ion irradiation induced processes. Here the temperature dependence of surface phenomena, partly induced by ion irradiation, is of special interest. Further, SDTrimSP modelling addressing the collisional effects is used to help understanding the alloy's evolution during ion bombardment. Since self-passivating alloys should be able to successfully suppress W oxidation still after plasma exposure, the oxidation behaviour of plasma-exposed samples is tested and compared to reference samples.

Thesis structure

First, an introduction into plasma edge physics and plasma-wall interactions is given. The plasma edge regimes of future fusion devices are examined to define relevant experimental parameters for the plasma exposures of the WCrY alloys. Depending on operational scenarios and particle species, two main test regimes are determined. On the one hand a large fraction of the plasma particles, such as the hydrogen fuel ions, will have impact energies which lie below the threshold for causing W erosion. On the other hand there will be particles with impact energies at or above the threshold and therefore causing significant W erosion. Examples for particles of this regime are neutral particles generated by charge exchange, ions produced from heavier species such as impurities in the plasma or the He produced by the fusion reaction. Next, plasma-wall interaction processes relevant for the present work are described at the end of Chapter 2.

Following this, the concept of self-passivating smart alloys is introduced in Chapter 3. A short introduction on the processes of oxidation and passivation is given, before describing the sample production and preparation procedure of samples used in this work.

The next chapter, Chapter 4, contains descriptions of the experimental facilities: the linear plasma devices and ASDEX Upgrade. Subsequently, the chapter on analysis methods, Chapter 5, is devoted to describing the experimental analysis techniques as well as SDTrimSP modelling.

Chapters 6 and 7 start with giving details on the experiments conducted with WCrY and reference W samples in the linear plasma devices at incident ion energies below, and at or above the W sputter threshold, respectively. Then the experimental results regarding the material's erosion, plasma-induced changes in elemental composition and surface morphology are presented. Additionally, SDTrimSP modelling results are presented for experiments conducted in PSI-2.

Since temperature-dependent processes such as diffusion were found to have a significant impact on WCrY erosion during plasma exposure, the temperature dependence of the alloy's surface composition is investigated. In Chapter 8 these investigations using two different analysis techniques are presented.

Experimental details and results of the oxidation of plasma-exposed and reference WCrY samples are reported in Chapter 9.

Chapter 10 is a general discussion of the results presented in this work. Eventually, the thesis is concluded with a summary and outlook in Chapter 11.

2. Plasma edge physics and plasma-wall interactions

2.1. Magnetic confinement and the plasma edge

2.1.1. Magnetic confinement in a tokamak

In order to develop and qualify new materials, one first has to look at the material's working environment and the challenges coupled to it. W-based self-passivating alloys are developed for the first wall of a DEMO tokamak or stellerator. A typical cross section of a tokamak where the locations of the first wall and the divertor are indicated is shown in Figure 2.1: the plasma particles are confined by magnetic field lines in a D-like shape. The centre of the confined plasma is called plasma core. In order to obtain a considerable cross section for the D+T fusion reaction, the core plasma reaches temperatures of up to 100 keV (1 keV corresponds to ca. 11 600 K). In contrast to this, the walls of the fusion chamber need to be significantly colder to prevent material degradation. Thus fusion power and particles coming from the core plasma need to be exhausted before reaching the wall. Further, energy and particle exhaust is necessary for generating electricity and preventing dilution of the plasma. Dilution of the plasma is prevented through removal of the He ash and avoiding impurity generation caused by wall erosion.

By using an appropriate magnetic field configuration, which is shaped by the aid of toroidally symmetric coils in the case of a tokamak [6], the particles and heat can be guided to be exhausted in a particular region: the divertor. In this way the interaction zone of plasma and material is moved far away from the core. The toroidal direction denotes the direction along the ϕ-axis of the cylindrically shaped tokamak (see Figures 1.2 and 2.1), taking the hole in the middle of the doughnut as its centre. The poloidal direction corresponds to the θ-direction. The tokamak magnetic field has a toroidal component, B_ϕ, which is created by external magnetic coils, and a poloidal component B_θ, which is created by the toroidal plasma current. B_ϕ and B_θ result in a helical magnetic field, with each line lying on one of a nested set of toroidal flux surfaces [12]. Figure 2.1 is a poloidal cross section of a tokamak, the magnetic contours in a poloidal cut through the nested toroidal flux surfaces are displayed. Magnetic field lines which do not interact with a solid surface are termed close, while those passing through a solid surface are termed open [12]. The Last Closed Flux Surface (LCFS) separates the so-called Scrape-Off Layer (SOL), which extends to the vessel walls, from the confined plasma. It is the outermost flux surface not intersecting a solid surface, all surfaces radially further out are open. In the divertor configuration, the field line intersecting at the x-point is called separatrix. The points where the separatrix intersects the material

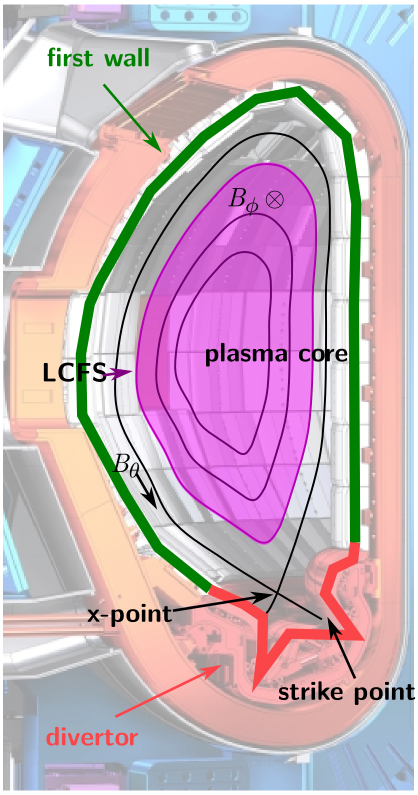

Figure 2.1.: Cross section of a tokamak. The first wall is indicated in green, the divertor at the bottom of the cross section in red. B_θ and B_ϕ are the poloidal and toroidal components of the magnetic field used for plasma confinement. The LCFS is the last flux surface not intersecting the wall, while the separatrix intersects the wall at the strike points. At the x-point, where the field lines intersect, the poloidal magnetic field B_θ is null.

are called strike points. Here heat loads are highest and PWI is most intense, i.e. most PWI processes take place in this region. As the ionised plasma particles are strongly magnetised, parallel transport along magnetic-field lines is very potent [13]. Still, some charged particles escape the confinement and additionally neutral particles are present. These are not bound to the magnetic field lines, which leads to some interaction also with the first wall. Loads on the first wall are considerably lower compared to the divertor and different PWI processes are dominant in this region.

A tokamak can be either operated in diverted configuration as described above, or in limited configuration. The limiter concept is described in detail in [6]. Generally, a limiter is a solid surface defining the edge of the plasma. It is hence the part of the wall closest to the plasma and protects the wall from the plasma during instabilities. There exists a variety of limiter concepts, most commonly used are poloidal or toroidal limiters. As a limiter localises Plasma-Surface Interaction (PSI), the limited configuration can result in gross melting of the surface at increased power levels in the tokamak. This in turn enhances impurity generation close to the confined plasma and is a problem especially in case of long pulse lengths. Therefore, the divertor concept has become the preferred

confinement configuration.
The energy confinement time τ_E is defined as the ratio of the plasma stored energy to the power flowing out across its edge. For its relation to the fusion product Q: $Q \propto \tau_E n_e T$, with the plasma density n_e and the temperature T, τ_E is a key parameter characterising the plasma performance. The fusion product Q parametrises the efficiency of a burning plasma, it is described as the ratio of the power produced by a burning plasma to the power externally applied [14]. An effective nuclear fusion power plant must fulfil $Q \geq 1$. ITER shall have a Q greater than 10, i.e. it should generate 10 times more fusion power than net heating power externally supplied to it. According to [6] there are two basic modes of confinement for tokamak operation with additional plasma heating. These two modes are called L (for low) and H (for high) confinement modes. L mode operation is the starting mode of operation when auxiliary heating (see [6] for more details) is applied to a plasma. In L mode τ_E is relatively low. By sufficiently increasing the power above the so-called L-H threshold, a higher confinement mode, the H-mode, is achieved. In H-mode an edge transport barrier or pedestal is formed. The energy transport is reduced in the pedestal region, which results in steep gradients of plasma density and temperature [14]. In [14] Edge-Localised Modes (ELMs) are described as periodic relaxations of these gradients leading to a loss of particles and energy from the confined plasma. During an ELM, high density power loads are deposited in a short time on the Plasma-Facing Components (PFCs). Another plasma instability leading to severe wall loads is a disruption. During a disruption a large scale magneto-hydrodynamical instability terminates the plasma by throwing it against the wall [15].

2.1.2. Plasma edge physics and processes

Generally, inside a plasma, quasi-neutrality (see Equation (2.1)) holds for length scales greater than the Debye length λ_D (Equation (2.2)). The Debye length is a measure of the distance across which the electrostatic effect of a net charge persists. At the vessel walls surrounding the plasma a thin region of net charge, where quasi-neutrality does not hold anymore, develops once a plasma is generated. This thin region extending over a few λ_D is called plasma or Debye sheath [12]. As, due to their smaller mass, electrons reach the wall first when a plasma is generated, it charges up negatively [16]. The electron flux is reduced as a result of the negative wall potential. In contrast to this, ions are attracted and a positive potential develops in the sheath bordering with the wall. Consequently, the sheath is a region of net charge, where the ion density n_i is increased with respect to the electron density n_e: $n_i > n_e$. A plasma is normally characterised by its electron density, which is why plasma density and electron density are used synonymously.

$$n_e = \sum_i n_i Z_i, \text{ sum over all ions,} \tag{2.1}$$

with the atomic number of the ion Z_i.

$$\lambda_D = \sqrt{\frac{\epsilon_0 k_B T_e}{n_e q_e^2}}, \tag{2.2}$$

with ϵ_0: dielectric permittivity, T_e: electron temperature, k_B: Boltzmann constant, n_e: electron density and q_e: electron charge.

A potential drop V_{sf} arises spontaneously in the sheath between the plasma and the wall for a floating surface. Relative to the plasma, V_{sf} is given by Equation (2.3) below:

$$V_{sf} = \frac{-3k_B T_e}{q_e} \tag{2.3}$$

Charged particles hitting the surface recombine and return as neutrals, a solid surface hence acts as an effective sink for plasma. When the net flux to the wall is zero, a steady state condition called recycling, is established. Hereby charged pairs from the plasma are lost to the surface at the same rate as recombined neutrals re-enter the plasma.

A variety of atomic and molecular reactions occur when the incoming hydrogen isotopes for fuelling meet the energetic ions and electrons from the plasma. Further, impurities from sputtering of PFM enter the plasma and undergo reactions. In [15] the different processes are described in detail. Important atomic reactions concerning the recycling from the wall are excitation, ionisation and charge exchange. These reactions are given in Table 2.1. Ionisation and excitation lead to emission of radiation and thus cooling of the edge plasma. As a consequence, incident ion energies and the rates of physical sputtering are lowered. Radiative cooling is more effective with species of a higher atomic number Z than hydrogen. For this reason certain gas species are introduced on purpose into the plasma edge for cooling. This is called impurity seeding. Charge Exchange (CX) processes in contrast, can lead to effective sputtering of PFM. The neutrals created in the CX reaction are not bound to the magnetic field. An energetic ion turning into an energetic neutral can hence unhinderedly deposit its energy into the PFM.

2.1.3. Plasma edge regimes of future fusion devices

Exact plasma parameters and thus conditions for DEMO have not been fixed yet. For the development and testing of tailored material concepts, it is important to investigate possible conditions. As W-based self-passivating alloys are currently developed for the first wall, special attention is paid to this region.

Impinging plasma and impurity particles in ITER are in the order of 1×10^{21} ions/(m^2s) for the first wall and 1×10^{24} ions/(m^2s) for the divertor [17]. Strong W erosion in the divertor is expected even for pure D plasmas from DIVIMP simulations [18] for ITER limiter geometry. At the first wall erosion caused by ion fluxes is dominant, while the contribution of CX fluxes and ELMs to W erosion is negligible [19].

DEMO requirements will differ from those for ITER [20]. In [21] it is stated that a

Excitation	$\mathrm{H} + \mathrm{e} \longrightarrow \mathrm{H}^* + \mathrm{e}$
Ionisation	$\mathrm{H} + \mathrm{e} \longrightarrow \mathrm{H}^+ + \mathrm{e}$
Charge exchange	$\mathrm{H}^+ + \mathrm{H} \longrightarrow \mathrm{H} + \mathrm{H}^+$

Table 2.1.: Important atomic reactions concerning the recycling of hydrogen isotopes from the wall. H^* describes an H atom in an excited state, i.e. H^+

pulsed baseline DEMO reactor concept is prioritised with the possibility to be upgraded to a long-pulse or steady state machine. The European DEMO design described in [22] assumes a peak heat flux of maximum $1\,\mathrm{MW\,m^{-2}}$ for the first wall. The first wall surface temperature during regular operation is restricted by the temperature limit of the considered structural material. The reduced activation ferritic martensitic steel EUROFER-97 [20] with a temperature limit of around $820\,\mathrm{K}$ [20] is one option considered for the European DEMO. The thermal conductivity of W is about $1 \times 10^2\,\mathrm{W/(mK)}$ and tends to decrease under fusion-relevant radiation conditions [23]. [24] found a value of about $5 \times 10^1\,\mathrm{W/(mK)}$ at temperatures between $770\,\mathrm{K}$ and $970\,\mathrm{K}$ for bulk WCrY samples with compositions similar to the one of the samples used for this work, which means a decrease in the thermal conductivity by a factor of two in comparison to pure W. Considering a $3\,\mathrm{mm}$ thick W or WCrY armour layer, first wall temperatures should not largely exceed $900\,\mathrm{K}$.

Besides heat loads, particle loads of different origin strike the wall leading to its erosion: plasma ions may be accelerated to energies exceeding the sputter thresholds, additional erosion is caused by CX neutrals. The erosion due to energetic neutrals is assumed to be of the same order of magnitude as for ions [25], in some DEMO wall areas their contribution even dominates [26]. Neutrals, not being subject to electromagnetic forces on their path, possess energies up to several hundred eV when impinging on the wall. Moreover, eroded neutrals from the wall are ionised in the plasma and can get accelerated in the Debye sheath near the surface to energies exceeding the wall material's sputter thresholds [26]. In this reference it is stated that fuel ions do not contribute to wall erosion due to low enough plasma temperatures near the wall without ELMs. This assumption is supported by studies presented in [27]: here the gap size, the distance between separatrix and wall, is identified as the most promising control parameter for wall protection. An increased gap size leads to colder plasma close to the wall. Thus ions hitting the wall will be less energetic. Further, [27] states that the perpendicular flux dominates the damage of the main chamber first wall. Temperatures in the DEMO SOL are expected to be below $100\,\mathrm{eV}$ [20]. In [28] ion energies of more than $100\,\mathrm{eV}$ and an average ion flux in the range of $1 \times 10^{20}\,\mathrm{ions/(m^2s)}$ to $1 \times 10^{20}\,\mathrm{ions/(m^2s)}$ are ascribed to steady state DEMO operation. The sputter threshold for D on W is around $220\,\mathrm{eV}$ [29]. No W sputtering is expected in pure D for ion energies of around $100\,\mathrm{eV}$.

Impurity ions generated by wall sputtering, He ash from the fusion reaction and seeding impurities can effectively sputter the armour material due to higher atomic number Z as compared to that of hydrogen fuel ions. According to [22] argon (Ar), krypton (Kr) and xenon (Xe) are foreseen as seeding species for the EU DEMO. [30] and [18] speak of seeding levels in future fusion reactors of up to the order of $1\,\%$. In [18] for instance, $1\,\%$ of Ar is used to investigate the evolution of the W impurity density at the first wall. Particularly the erosion of W generates impurities with a high atomic number Z at the plasma edge. Its high radiative cooling rate especially at electron temperatures typical for the plasma core puts strict constrains on the maximum allowable W core concentration, around 1×10^{-5}, and therefore on the sputtering rate [18]. This again stresses the importance to control sputtering of W first wall armour in future fusion devices such as DEMO.

Generally particle and heat loads will possess an energy distribution in a fusion device. Particles at the high-energy tail of the distribution may lie above the sputter threshold, while the average particle energy stays below it. The design question whether high heat flux limiters will be installed still remains open for DEMO [20]. In limited configuration, e.g. during ramp-up or ramp-down of the plasma, the plasma gets closer to the wall and ion energies are elevated due to higher SOL temperatures as compared to the diverted configuration. As particle and heat loads strike the PFM simultaneously, it is important to consider not only the individual processes but also synergistic effects of both, i.e. by investigating effects induced by irradiation of heated samples.
With the aim of evaluating the plasma response of WCrY alloys to both mild and harsh fusion environments, two experimental ion irradiation regimes were chosen. The first regime treats impact energies of the main plasma ion species below the W sputter threshold. The second regime treats impact energies at or above the threshold and therefore causing significant W erosion. In all reported experiments the sample temperature is set to about 900 K.

2.2. Plasma-wall interaction processes

Particles coming from the confined plasma or being created in various processes at the plasma edge can interact with the PFM in diverse ways. Important interaction processes for qualifying newly developed PFM are erosion, deposition and retention. An extensive description of these and further processes can be found for example in [17] or [31]. In the following section the processes most relevant for this work are briefly described.

2.2.1. Erosion

When bombarding a solid's surface with energetic particles, surface atoms are removed or eroded. This process of removing particles is termed sputtering. Besides leading to sputtering, bombarding particles can be backscattered from the solid's atoms or be implanted, i.e. come to rest in the solid. By doing so they transfer their energy to the electrons and lattice atoms of the solid. A surface target atom is removed as a result of the ion bombardment if a certain threshold energy is overcome. Thresholds for sputtering of the plasma ion species relevant to this work, D, T, Ar, He and residual O, on the materials the smart alloys are mainly made of, W and Cr, are given in Table 2.2.
A useful means of measuring the strength of a material's erosion is the erosion yield Y. It is the ratio of the average flux of eroded particles Γ_{ero} and flux of incoming projectiles Γ_{in} and thus defined as follows:

$$Y = \frac{\Gamma_{ero}}{\Gamma_{in}}, \Gamma_{ero} = \frac{n_{ero}}{At} \left[\mathrm{ions/(m^2s)}\right], \Gamma_{in} = \frac{n_{in}}{At} \left[\mathrm{ions/(m^2s)}\right], \tag{2.4}$$

with n_{ero}: number of eroded particles, n_{in}: number of incoming particles, A: area and t: time. Since a meaningful number of projectiles is considered rather than single projectiles, the yield represents the probability for a material to be eroded. For a specific material this number depends on the kind of interaction between projectile and target and the material properties such as for example the atomic number Z. Different types of erosion mechanisms are explained in the following paragraphs.

Physical sputtering

Physical sputtering simply describes the process of energy transfer from a projectile to a surface atom of the solid. Commonly, physical sputtering is described using the Binary Collision Approximation (BCA). Within this model a single collision between the incoming projectile and the target atom is treated in the classical scattering approach. The projectile ion incident on a target material is approximated to experience a sequence of single collisions with the material's target atoms, this is depicted in Figure 2.2. The projectile can be any energetic particle being directed onto the target, it can be an energetic ion or a neutral particle. Material constants such as the surface binding energy E_{sb} determine the consequences of the collision. E_{sb} is the energy that a target surface atom needs to overcome to get sputtered. Commonly, for BCA models the heat of sublimation is used as an approximation for E_{sb}, as the actual E_{sb} values are unknown [33]. Alloying generally leads to a decrease in surface binding energy. However, the specific E_{sb} values for the WCrY alloy are not known.

Depending on the energy of the incoming particle, there are different sputtering regimes.

Single collision regime: Within this regime the interaction of the projectile with the target is very localised. This is because for light ions possessing low energies usually just one collision occurs inside the material before hitting a surface atom which then gets ejected. Generally, a particle from the surface cannot be eroded when being directly hit by the incoming particle, as the direction of the momentum of the incoming particle points inside the material.

Linear cascade regime: Ions possessing energies greater than several 10 eV generate recoil atoms, i.e. atoms which have been hit by the incident projectile that receive sufficient energy to generate recoil cascades. Hence also neighbouring target atoms take part in the collision. However, the density of recoil atoms in the linear regime is low so that there are only very few collisions between moving atoms.

Thermal spike regime: For high impact energies in the keV to MeV range and high projectile masses, the density of recoil atoms increases so that there are many collisions between them. Inside such a (thermal) spike region most of the atoms are moving. Whereas the single collision and linear cascade regime can be described within the BCA model, in the spike regime many-body processes become important. Within the BCA model only binary collisions between atoms are successively considered in an isolated way. Further, for bombarding energies in the MeV range additional processes have to be

	D	T	Ar	He	O
W	230	154	27	121	44
Cr	35	25	22	22	15

Table 2.2.: Thresholds [eV] for pure elements W, Cr sputtered by D, T, Ar, He and O from [31]. The threshold of O on Cr is taken from [32]

taken into account. Electronic sputtering is an example of such an additional process. It describes the transfer of a major part of the projectile's energy to the electrons along the ion track, which causes additional sputtering.
Generally, physical sputtering occurs for all combinations of projectile and target species. The sputtering yield Y (see Equation (2.4)) depends on this combination as well as on the projectile energy and its angle of incidence. There are several analytical and empirical formulae for Y. Important ones are the Eckstein formula or Sigmund's sputtering theory [34]. The fit for the energy dependence of the sputtering yield at normal incidence introduced by Eckstein and Preuss in 2003 [35] is given in Equation (2.5).

$$Y(E_0) = q s_n^{KrC}(\epsilon) \frac{\left(\frac{E_0}{E_{th}} - 1\right)^{\mu}}{\lambda + \left(\frac{E_0}{E_{th}} - 1\right)^{\mu}}, \tag{2.5}$$

with the threshold energy E_{th}, λ, μ and q being the fit parameters. Further, E_0 is the incident energy of the projectile, ϵ the reduced energy (Equation (2.6)) and s_n^{KrC} the Kr-C interaction potential used to describe the nuclear stopping (see [35] for details).

$$\epsilon = E_0 \frac{M_2}{M_1 + M_2} \frac{a_L}{Z_1 Z_2 e^2}, \tag{2.6}$$

with the atomic numbers Z_1 and Z_2 and M_1 and M_2 the masses of the projectile and the target atom, respectively. e is the electron charge and a_L the Lindhard screening potential (see [35]). Equation (2.6) illustrates that the sputtering yield is particularly dependent on the masses and atomic numbers of the projectile-target combination. Threshold energies given in this work taken from Eckstein [31] rely on this revised fitting formula, it is an improved description of the energy dependence at low incident energies near the threshold compared to previous fits.
When estimating the sputter yield of a material, not only the elemental composition of the target atoms is important but also their arrangement. For rough surfaces, it was observed that sputtering is reduced due to re-deposition of sputtered particles on the valleys of the 3D surface structure [36]. For layered targets, polycrystalline materials or alloys, preferential sputtering of elements or grains has to be considered.

Preferential sputtering: In case of a multicomponent target, i.e. the target consists of two or more different atomic species, sputtering becomes more complex. Different energy transfer of the incoming projectiles to the components of the targets causes preferential sputtering. This means that the components have different partial sputter yields, one component will get more effectively sputtered compared to the others. [31] gives an elaborate description of preferential sputtering, in the following section a summary is given.
To understand the consequences of different partial sputter yields in a multicomponent system, a binary alloy with homogeneously mixed species i and j is considered. Their respective concentrations are c_j and c_i so that $c_j + c_i = 1$. The components possess different partial sputter yields Y_i and Y_j with $Y_i \neq Y_j$. If one component i is sputtered preferentially during prolonged bombardment, this results in the surface being

enriched in the other component j. As a consequence the probability that j is sputtered increases. After irradiation with sufficiently high fluence a steady state is reached. At this state the ratio of sputtering yields equals the ratio of the bulk concentrations, i.e. it is stoichiometric as described in Equation (2.7).

$$\frac{Y_i}{Y_j} = \frac{c_i}{c_j} \tag{2.7}$$

The normalised ratio δ (see Equation (2.8)) is called sputter preferentiality.

$$\delta = \frac{Y_i}{Y_j}\frac{c_i}{c_j} \tag{2.8}$$

δ is predicted to depend on the masses $M_{i,j}$ and the surface binding energies $E_{sb_{i,j}}$ of the respective alloy species:

$$\delta = \frac{M_j}{M_i}^{2m} \frac{E_{sb_j}}{E_{sb_i}}^{1-2m} \tag{2.9}$$

Here the power exponent m describes the projectile-target inter-atomic interaction potential. The fluence until steady state is reached depends on the range from the surface into the material over which the composition is changed. This range in turn can be influenced by diffusion of the different components. It is important especially for irradiation at high fluences and when there is a significant difference between the components' masses in an alloy to take preferential sputtering into account. Further, the partial sputter yields may depend on the angle of incidence, leading to different steady state concentrations under different angles of incidence. The total sputter yield of a compound material is the sum of its partial sputter yields.

In the case of the light hydrogen isotope fuel ions, lighter elements are sputtered more easily than heavier ones, which leads to a modified stoichiometry in the projectile range. This is important for the W-based smart alloys, because the lighter alloying elements Cr and Y are sputtered much more easily than the heavy element W leading to an enrichment of W at the alloy's surface. Unlike WCrY smart alloys, Reduced Activation Ferritic Martensitic (RAFM) steel is mainly composed of Fe and Cr and only less than 1 at% is W. For this material as well, W is enriched at the surface during ion bombardment leading to reduced sputter yields [37].

Chemical erosion

In case of chemical reactions between thermalised projectiles and surface atoms leading to the production of volatile molecules, the process is called chemical erosion. Unlike physical sputtering, this type of erosion cannot be treated easily in the BCA model as the formation of compounds needs to be taken into account [31]. Chemical erosion is especially important for fusion research as it appears when carbon (C) or beryllium (Be) is bombarded with hydrogen, e.g. D or T atoms. As until some years ago C was considered to be the best option for PFC of future fusion devices, the chemical erosion for carbon-based materials has been studied in much detail. Due to heavy re-deposition in form of amorphous hydrogen-rich layers and therefore enhanced expected T inventory in a fusion reactor, the usage of C has been abandoned in favour of W. In case of W physical sputtering is the dominant erosion process.

Further mechanisms attributing to erosion

Besides the aforementioned types of erosion there are several more mechanisms attributing to the erosion of PFCs in fusion devices: during transient events such as ELMs excessive heat loads can cause melting of the material. Melt-layer motion and ejection of melt can significantly contribute to decreasing the lifetime of a PFC material and lead to plasma contamination [38]. Furthermore, uni-polar arcs between plasma and PFCs, triggered e.g. by high voltages across the plasma sheath, can result in increased erosion. This arc erosion manifests itself in form of micron range craters and depends on PFC material as well as cleanliness of the surface [39].
Generally, irradiation with high energy particles in the keV range leads to the formation of lattice defects. In a fusion reactor, neutron irradiation during plasma operation produces radiation-induced defects such as vacancies, interstitials or traps inside the PFC material. The resulting changes in the material's microstructure, e.g. voids or dislocation networks, or possibly also changes in the chemical composition by transmutation, degrade the material properties. It can lead to a decrease of the thermal conductivity or ductility as well as He embrittlement and even swelling in case of high radiation doses. Blistering describes the process of capturing atoms in under-surface gas bubbles. It occurs under certain experimental conditions during the exposure of material when H or He accumulates at material defects, i.e. grain boundaries, voids or even single vacancies. Great amounts of accumulated gas lead to high pressure and therefore mechanical stress which eventually leads to enhanced erosion.

2.2.2. Deposition, retention and surface morphology

Deposition

With a certain probability R, the particle reflection coefficient, a projectile incoming onto a target surface does not penetrate the target but can be reflected. All the particles which are not reflected are deposited and possibly lead to erosion. Particles reflected from metal surfaces are mainly neutralised. For higher energies of the impinging ions, the penetration depth inside the target is increased leading to a reduced energy deposition in the surface layers and thus reduced sputter yields. If only collisional and no chemical effects are considered, the deposition regime describes the case in which more atoms are implanted (in deeper target layers by increased projectile energy) than sputtered [31].

$$R = \frac{\text{number of reflected particles}}{\text{number of incident particles}}, \text{Deposition} = 1 - R \tag{2.10}$$

Besides incoming particles, particles eroded from the surface can also be deposited onto the target. This case is referred to as re-deposition. Normally, eroded particles start from the surface as neutrals and are ionised at some distance, the ionisation length λ_{ion}.

Due to the presence of the magnetic field, charged particles gyrate with a Larmor radius r_L. If the eroded particle returns to the surface within the first gyration, i.e. it gets ionised and thus attracted by the surface before the first Larmor radius is completed, this re-deposition is called prompt re-deposition. This is illustrated schematically in Figure 2.3. From the formulae written below it becomes clear that prompt re-deposition especially occurs for high-Z, Z being the atomic number, materials of high mass M like W. P_{prompt} is the probability for prompt re-deposition of a particle that has been eroded from a surface and therefore its condition is $P_{prompt} < 1$.

$$r_L = \frac{M * v_\perp}{q \cdot B}, \; \lambda_{ion} = \frac{v}{\langle \sigma v \rangle_{ion} \cdot n_e}, \; P_{prompt} = \frac{\lambda_{ion}}{r_L}, \tag{2.11}$$

with the perpendicular particle velocity v, the strength of the magnetic field B, the electric particle charge q and the ionisation probability $\langle \sigma v \rangle_{ion}$. Prompt re-deposition depends strongly on the plasma parameters. For scenarios with a high plasma density n_e and high electron temperature T_e it can reach up to 100 %. One has to take into account that when analysing e.g. the mass loss of a sample after plasma exposure, the number on the scale is the net erosion, not the gross erosion. By means of spectroscopy measurements during the exposure and totally calibrating the intensities of line radiation from eroded particles being ionised again, one can additionally estimate the gross erosion. Apart from deposition by implantation of energetic particles into or on top of a solid layer, another way of growing a deposition film onto a surface is by adsorption of thermal particles. This becomes important especially for gaseous species like O_2 or H_2. The adsorbates can be released by the surface again via thermal desorption, hence by heating up the surface, unless they form oxides.

Fuel retention

Tritium is radioactive with a half-life of about 12 years. For safety reasons the inventory of this radioactive hydrogen isotope is strictly controlled and e.g. limited to 700 g for the

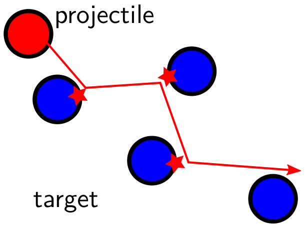

Figure 2.2.: Schematic illustration of path of projectile through target material in BCA model. Between the subsequent and independent binary collisions the projectile follows a straight path.

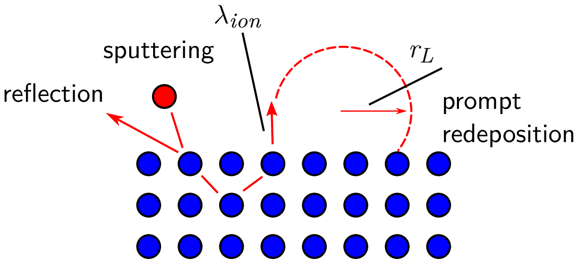

Figure 2.3.: Schematic illustration of reflection, physical sputtering and prompt re-deposition. The sputtered target neutral atom is ionised after the ionisation length λ_{ion} and promptly re-deposited.

maximum retention on the in-vessel components of ITER [40]. If this limit is reached, plasma operation is stopped and the wall has to be cleaned, therefore fuel retention should be kept at a minimum. There are different mechanisms of fuel retention present in the fusion reactor environment:

tritium can be adsorbed on the surface, either via physisorption (binding via van der Waals forces) or via chemisorption (binding via exchange of electrons). Atoms or molecules are bound at a solid surface until the wall is saturated. By heating the surface the adsorbed species can desorb from the surface into the gas phase again. Thus the retention by adsorption is transient. A permanent mechanism is retention resulting from implantation of energetic particles: for example the T is trapped by chemical bonding in the material at a certain depth where it comes to rest due to the strong binding between T and the solid atoms. This mechanism also saturates. At increased surface temperatures, fuel can diffuse into the bulk by thermal diffusion. This mechanism does not saturate but depends on the diffusion coefficient inside the PFC material.

Co-deposition is the process of deposition of eroded wall material together with fuel atoms. Layers can be formed in some regions of the fusion device if material is preferentially deposited at these regions and not at the positions where it got originally sputtered. If the built-up co-deposits grow too thick and become unstable, flaking can occur leading to the formation of T containing and hence radioactive dust inside the fusion device. Besides T coming from the fuel, a T inventory can be built up inside the PFCs by transmutation caused by nuclear reactions. Furthermore, the damage caused by neutron irradiation and the emerging defects can serve as additional trapping sites for T and hydrogen in general.

For experimentally investigating retention of fusion fuel in PFC materials, D or H is assumed to behave like T. Experiments take place loading samples with e.g. D instead of T so that no additional safety measurements for radioactive materials must be taken. For W exposure to low energy D plasma, [41] reports that the maximum amount of retained D depends on the incident ion flux at a given fluence and ion energy. It increases with increasing the ion flux. With increasing temperature lower amounts of D are retained.

In [42] it is stated that the amount of hydrogen retained in W is determined by defects as hydrogen solubility is generally low in W. Defects act as trap sites for hydrogen where it is retained after irradiation. Excess, solute hydrogen diffuses out of the material already at room temperature. The number of trap sites depends on the material's microstructure. Material defects such as the surface or grain boundaries act as trap sites, smaller grains hence lead to an increased number of trap sites. The mechanical alloying and the subsequent sintering of the WCrY smart alloys leads to the creation of material defects such as grain boundaries. For the smart alloy functioning during accidental scenarios it was found that smaller grains are beneficial for successful oxidation suppression [43].

[44] states that a higher intrinsic trap density in W-tantalum(Ta) alloys raises retention compared to pure W for exposure to D ion fluxes of the order of $1 \times 10^{19}\,\mathrm{D/(m^2s)}$, while [45] finds no difference in the amount of retained D between W and W-Ta for exposures to D ion fluxes of the order of $1 \times 10^{24}\,\mathrm{D/(m^2s)}$. Additionally, the number of traps can be increased by radiation damage, either caused by the incident hydrogen ions or by the fast neutrons from the D+T fusion reaction. While damage caused by ions is mostly

concentrated at the near-surface region due to the low penetration depth of ions, fast neutrons produce trap sites throughout the bulk.

Surface morphology changes

The bombardment by energetic ions or neutral particles usually has an impact on the outer appearance of the PFC material, too. Different effects are observed depending on the bombarding species and the target material: exposure of W to low energy D ions with an incident energy of a few ten eV is reported to modify the surface in diverse ways [41], [46]: existence and appearance of the modifications depend on the flux and fluence during the plasma ion irradiation. Further, the material microstructure and the sample temperature during the irradiation play an important role. [41] reports the formation of blisters ranging in size from a few tenth of nm to µm. The blister size depends on the temperature as well as on the ion flux density. In [46] is was found that blister size decreases with increasing ion flux. Besides blister formation, exposure of polycrystalline W samples leads to the formation of porous structures and ripples on the surface. Further, nano-structures of different shapes are formed on the surface. The structure formation often correlates with the grain orientation. The variation in morphology is reported to be mostly dominated by the flux differences.

During bombardment by He ions with energies below the threshold value for physical sputtering, holes and bubbles are generated in W for surface temperatures above 1600 K and a He ion fluence greater than $1 \times 10^{25}\,\mathrm{ions/(m^2s)}$ to $1 \times 10^{26}\,\mathrm{ions/(m^2s)}$. Below this temperature, at about 1200 K, the material surface is altered resulting in decreased optical reflectivity [47]. This decrease can be attributed to the formation of a submicron grass-like structure, so called W fuzz. Besides a decreased reflectivity this He-induced nanostructure formation leads to increased erosion and a lowered thermal conductivity. Other forms of surface modifications induced by plasma impact include recrystallization, a new ordering of the material's crystalline structure, due to high surface temperatures, surface roughening and implantation and deposition of impurities.

In case of multiphase materials, heterogeneous materials consisting of different crystallites representing different phases of different compositions and sometimes different crystal structures, the different phases can vary in their response to plasma impact. For instance grains representing a phase with a high sputtering yield will be eroded faster than those with lower yields. This results in the surface becoming enriched in low sputtering yield grains. This process is called selective sputtering [48]. WCrY consists of WCr grains with finely dispersed YO particles. These are smaller particles in the WCrY microstructure (see Chapter 3) containing mostly Y and additionally O. In the case of a varying W-Cr composition in the WCr grains, the grains with a higher W content are expected to have lower erosion yields. In [48] it is stated that selective sputtering of a multiphase material results in the development of a surface relief with features such as etch pits for medium ion fluences. At high ion fluences the interplay of selective sputtering and the formation of surface relief features finally converges to steady state conditions after erosion of a layer in the order of a few grain diameter.

[49] have exposed W to He plasma under DEMO first wall conditions in the linear plasma

device PSI-2. At incident ion energies of 75 eV, sample temperatures of around 800 K and a flux of $1.6 \times 10^{22}\,\mathrm{He/(m^2s)}$ a total fluence of $3 \times 10^{26}\,\mathrm{He/m^2}$ was accumulated. It was found that the crystal orientation has an impact on surface structural modification, such as the found nanoscale undulating surface structure, and erosion.

2.2.3. Thermally activated surface phenomena

Thermal diffusion

During the plasma operation of a fusion reactor, the material properties of the PFCs are not just subject to external ion or neutral bombardment but also to heat loads. Thus thermally activated processes play an important role as well, especially at the material's surface where the PWI mainly takes place.

Thermal diffusion is a thermally activated mechanism leading to changes in the material's composition. If a material is heated up, thus kinetic energy is given to the constituting atoms in form of heat, the atoms are given the possibility to change positions. This change of positions of the atoms in a crystal lattice relies on thermally activated jumps between the lattice positions. Thus there must be defects, such as voids or interstitials, present in the lattice. The WCrY alloys usually possess a lot of lattice defects, especially if the material is made up of small grains since each grain boundary is a lattice defect. Given the existence of lattice defects, diffusion of elements is caused by concentration gradients within a material. These lead to diffusion of elements in the direction of the gradient to counteract the concentration difference. Assuming the rate of composition change of the alloy microstructure, in particular the locations of lattice defects, to be slow compared to the diffusion process, the Arrhenius equation, used to describe the temperature dependence of reaction rates in equilibrium, can be applied in a first approximation.

An in-depth description of the processes governing diffusion is given in [50]. The equations describing diffusion are Fick's laws:

$$\text{Fick's first law: } J = -D\nabla C \tag{2.12}$$

$$\text{Fick's second law (diffusion equation): } \frac{\delta C}{\delta t} = \nabla \cdot (D\nabla C) \tag{2.13}$$

$$\text{Arrhenius equation for the diffusion coefficient: } D(T) = D_0 \cdot e^{\left(\frac{-E_a}{k_B T}\right)}, \tag{2.14}$$

here D_0 is the temperature-independent diffusion constant, E_a the activation energy and k_B the Boltzmann constant. D_0 and E_a are material-specific constants. They depend on the diffusion mechanism considered and (alloy) system and are not known for many materials, especially for alloys. Fick's first law (Equation (2.12)), here given for three dimensions, describes the flux of particles J (diffusion flux) caused by gradients in the concentration C. D is the factor of proportionality and is also called the diffusivity or the diffusion coefficient of the considered species. The second of Fick's laws describes the temporal evolution of the concentration of a certain species. It is a second-order partial differential equation and hence non-trivial to solve. If the diffusivity is composition-dependent ($D(C)$) it is called interdiffusion coefficient and solving for $C(t)$ cannot be done analytically. In cases for which the diffusivity is independent of concentration, e.g. for diffusion in ideal solid solutions, Fick's second law (Equation (2.13)) simplifies to $\frac{\delta C}{\delta t} = D \Delta C$, where Δ is the Laplace operator. This is then called the linear diffusion equation and one can find solutions if boundary and initial conditions are formulated. Diffusion increases exponentially with temperature and this relation is described by the Arrhenius equation for D in dependence of the temperature T (Equation (2.14)).

For low ion energies and especially for the light hydrogen ions of which the fusion fuel is made up of, ion bombardment does not cause additional lattice damage. Preferential sputtering of the lighter elements in an alloy leads to the build-up of concentration gradients and hence diffusion. Since the wall material is additionally heated up by the plasma impact and diffusion increases exponentially with temperature, the diffusion process induced by preferential sputtering is enhanced. As a consequence for smart alloys, the desired W enrichment at the surface can be suppressed by thermal diffusion counteracting the build-up of an element-enriched layer.

[51] describes the simultaneous effects of sputtering, implantation and solid-state diffusion for a tungsten–iron system under deuterium bombardment as model system for EUROFER. EUROFER is a reduced activation ferritic martensitic steel which is currently considered as first wall blanket material for DEMO [20]. The goal was to determine the surface profile of this mixed-material system at elevated temperatures which lead to enhanced atomic mobility. It was shown that the W surface concentration, which is of paramount importance for the material's sputter yield, strongly depends on ion energy, temperature and fluence as well as on the initial W concentration. Similarly, the coupled sputter-diffusion effects have to be considered when investigating the plasma impact on the WCrY smart alloys. This is achieved via SDTrimSP modelling (see Section 5.2 for model description), the diffusion mechanism used in this model is based on the physics described above.

Segregation

In contrast to thermal diffusion induced by concentration gradients, which leads to the equalisation of these gradients within a material, segregation can go uphill these gradients or even generate them. Segregation is the preferential enrichment of one component of a multicomponent system at a boundary or interface. The segregation process itself, namely the movement of the involved atoms, is governed by diffusion. Thus segregation can be understood as a special form of diffusion.

It is a common observation that in an initially interspersed homogeneously solid solution certain elements tend to accumulate at imperfections, such as grain boundaries, or segregate to free surfaces. The kinetics of segregation is controlled by diffusion of the segregating species in the bulk material and by the exact nature of the boundary conditions between the surface layer and the adjacent bulk. If evaporation from the free surface plays a role as well, then the resulting loss rate from the surface also has to be taken into account [52]. According to [53] there are two different forms of segregation:

equilibrium and non-equilibrium segregation. Equilibrium segregation occurs as a result of inhomogeneities in the solid which are responsible for the presence of sites for which solute atoms have a lower free energy. These sites are interfaces such as grain boundaries, the free surface as well as defect sites. Within these regions the concentrations of solute atoms differ from each other and from that of the bulk material. At a given temperature the solute concentration in each of the sites asymptotically approaches a unique equilibrium value at a diffusion-governed rate. In contrast, non-equilibrium segregation depends on rate processes and kinetic events and disappears with time as diffusion processes are allowed to reach equilibrium.

In the following paragraph the more common form of segregation, the segregation at equilibrium, as described in detail in [53] is introduced. For establishing the equilibrium segregation, the McLean method [54], which was specifically derived for grain boundaries but is also valid for free surfaces, is referred to. A boundary condition for the method is that the quotient of the concentration in the surface layer (called site 1) and the concentration in the immediately adjacent bulk (site 2) can be set to a constant value, the segregation enrichment factor. Further, this method is developed in analogy of the Langmuir gas adsorption on the free surface of a solid. Considering a simple binary system of elements A and B, $c_1(\mathrm{A})$ and $c_1(\mathrm{B})$ and $c_2(\mathrm{A})$ and $c_2(\mathrm{B})$ are the concentrations of elements A and B in the sites or layers 1 and 2. Now it is considered that element A is segregating in a matrix of element B. The Langmuir adsorption isotherm (see [53] for details) describes the limit of adsorption on a surface where all available sites are occupied by the adsorbed atoms. This limit corresponds to the surface being covered by a monolayer of adsorbed atoms at a certain surface concentration. The Langmuir-McLean relation is the grain boundary analogy to the Langmuir adsorption at free surfaces. This means that similar to adsorption on a surface, the limit of segregation corresponds to the grain boundary being covered by a monolayer of segregated atoms. Equation (2.15) is the Langmuir-McLean relation as derived in [53]:

$$\frac{c_1(\mathrm{A})}{c_1^0(\mathrm{A}) - c_1(\mathrm{A})} = \frac{c_2(\mathrm{A})}{1 - c_2(\mathrm{A})} \cdot e^{-\frac{\Delta G}{RT}}, \tag{2.15}$$

where $c_1^0(\mathrm{A})$ is the fraction of the grain boundary monolayer available for segregated atoms at saturation and $c_1(\mathrm{A})$ the actual fraction covered with segregant. $c_2(\mathrm{A})$ is the bulk solute fraction, R the gas constant and T the temperature. ΔG is the free energy of segregation per mole of solute. Equation (2.15) describes the equilibrium state of the system, i.e. the fraction covered with segregant $c_1(\mathrm{A})$ at which the energy of the system is minimised. According to [55] the surface segregation energy is the energy cost of transferring an impurity atom from the interior of a host crystal to its surface. It can therefore be understood as the difference in the total energies of the system with the impurity in a surface layer and in the bulk. Often ΔH, the enthalpy of segregation of a solute with unlimited solid solubility (i.e. $c_1^0(\mathrm{A}) = 1$), is used instead of ΔG and also referred to as segregation energy.

3. Smart Alloys

3.1. Motivation

Currently the heavy metal tungsten is the favoured PFC material for future fusion devices and therefore in the focus of PWI research. With a melting point of around 3700 K it can withstand high heat loads. While further advantageous properties such as low T retention and low sputter yields make W a suitable PFC material, its disadvantageous property of fast oxidation may disqualify it. W oxidises rapidly at temperatures of above 1000 K, above 1200 K sublimation of the oxide becomes significant [9]. This makes pure W a potential safety hazard if a Loss-Of-Coolant Accident (LOCA) with additional air ingress occurs. In that case the cooling system fails and the wall temperatures rise from 1200 K to 1500 K for a few days to several months, depending on the blanket design, due to nuclear decay heat [56]. W, having been activated by neutron irradiation during plasma operation, then forms radioactive WO_3. Sublimation of WO_3 leads to its mobilisation and thus the possible release of radioactive material out of the vacuum vessel. [57] states that assuming a W first wall area of $1000\,\mathrm{m}^2$ and an evaporation rate of $300\,\mathrm{m\,h}^{-1}$ at about 1200 K, radioactive W is mobilised at a rate of about $150\,\mathrm{kg\,h}^{-1}$. As a result, an activity of approximately $7.5 \times 10^{16}\,\mathrm{Bq\,h}^{-1}$ would be released into the environment. This safety hazard has to be prevented in order to ensure save operation of fusion reactors.

Advanced W-based materials are developed to counteract the aforementioned disadvantages of using pure W. This is done for example by adding alloying elements, varying the material's microstructure or by using different manufacturing techniques. To suppress the oxidation of W, self-passivating W-based alloys are developed. The development of smart alloys to be used in nuclear fusion was started at IPP Garching, the first work on the oxidation behaviour of W-based alloys was published by Koch and Bolt in 2007 [58]. A variety of different alloying elements was tested. Important points for the choice of alloying elements are, besides improving the oxidation resistance, benign activation behaviour and the alloy's stability. Research on W-based self-passivating alloys is currently carried out at multiple international locations. Additional to the group at IPP Garching, research on this topic has been published by a research group at CEIT in San Sebastian, Spain (see e.g. [59]) and Forschungszentrum Jülich (FZJ), Germany (see following references in this paragraph). So far the most promising alloy systems feature chromium (Cr) as well as small amounts of yttrium (Y). Just like in conventional steel, Cr serves as a passivating element diffusing to the surface when the material comes into contact with oxygen (O). A stable and dense Cr oxide layer is formed with the help of Y so that W oxidation is suppressed. Y facilitates the Cr transport towards the alloy's surface during oxidation, it adds to the stability of the oxide scale and supports the

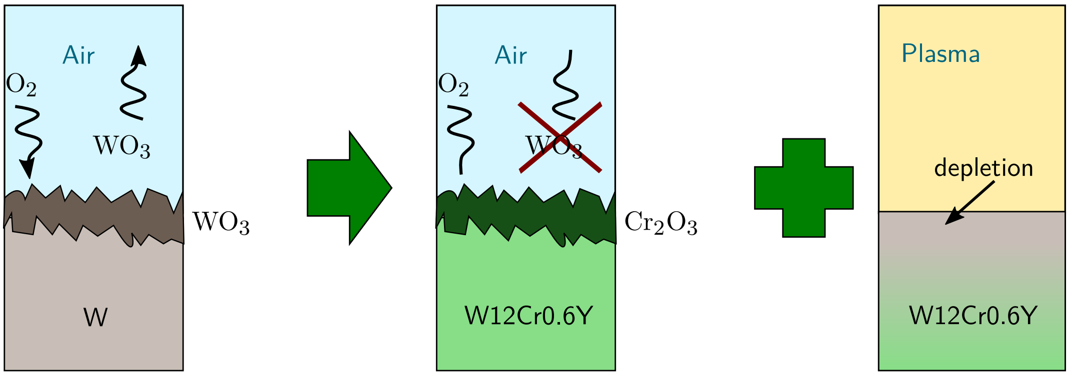

Figure 3.1.: The smart alloy concept consists in suppressing W oxidation during accidental conditions, while conserving W-like erosion behaviour during plasma operation.

formation of a continuously growing, well adhering and dense Cr_2O_3 layer [57].
Magnetron-sputtered WCrY thin films were used to carry out a Cr and Y composition scan at FZJ. The optimum composition for these WCrY thin film systems was found to be 88 wt% W - 11.4 wt% Cr - 0.6 wt% Y, they are described in detail in [57] and [60]. Here wt% stands for weight percent, the elemental fraction of the total alloy weight. Thus the material is with 88 wt% W mostly composed of W. The thin films demonstrated a significant oxidation suppression so that it was decided to produce bulk WCrY samples with the same composition. Details on the bulk material production are given in this chapter in Section 3.3.
The smartness of the WCrY alloys consists in their ability to adapt to two kind of reactor scenarios: on the one hand the oxidation of W should be suppressed during accidents, on the other hand smart alloys should behave like pure W during regular plasma operation. The preferential sputtering of the lighter alloying elements Cr and Y leads to an enrichment of W at the alloy surface. That way the plasma faces a pure W surface and the alloy benefits from low W erosion yields making it relatively resistant to erosion by plasma ion irradiation. The smart alloy concept is illustrated in Figure 3.1.

3.2. Oxidation and passivation

Oxidation generally describes any chemical reaction which increases the metal oxidation state, i.e. losing at least one electron by forming a compound such as an oxide. High temperature oxidation of metals is described in detail in [61]. An overview of the oxidation reaction and aspects relevant to this work is given in this section. Here the oxidation reaction of an alloy with oxygen is considered: at first, all reactive components of the alloy are in contact with oxygen. Some elements form more stable oxides than others, they are more active with oxygen. These elements will react with the oxygen first. Generally, the oxidation reaction between a metal M and oxygen O_2 is described in Equation (3.1).

$$\frac{x}{y}\mathrm{M} + \frac{1}{2}\mathrm{O_2} = \frac{1}{y}\mathrm{M_xO_y} \tag{3.1}$$

This reaction can be followed by measuring the consumption of metal or oxygen or by observing oxide accumulation over time. In case of WCrY the oxide is growing on top of the alloy [62] such that the reaction can be followed by monitoring the mass gain caused by oxide formation. For this purpose the sample is attached to a balance of appropriate sensitivity and then heated in oxygen containing atmosphere.

Alloying is a common method for increasing the oxidation resistance of a material. Common alloying passivating elements are Cr or aluminium (Al). Since nuclear reactions of the 14 MeV fusion neutrons with a PFC material containing Al would lead to long-term activation products [63], this element is not a suitable alloying element to be used in a fusion environment. In contrast, the neutron induced activation and transmutation of Cr is regarded as non-critical [63]. In most of the industrial iron (Fe) and nickel (Ni) alloys, oxidation resistance is achieved by the addition of Cr. The same applies for WCrY smart alloys. Here Cr is added to suppress the oxidation of W due to the formation of a passivating Cr containing oxide layer. Passivity is defined in [64] as the loss of chemical reactivity of a metal or alloy in an environment where the reaction ought to have occurred. When exposing the sample to the reaction environment, a continuous increase in oxidation is observed at first. This is followed by a sharp drop in the oxidation rate, which results from the formation of a thin oxidised protective layer on the sample surface. Cr is known to oxidise preferentially, and thereby form a protective oxide scale of Cr_2O_3 as stated by [65] and references therein. For further oxidation at the surface, metal ions need to diffuse through the dense scale. As the rate of oxidation is consequently determined by diffusion of metal ions through the scale, it follows a parabolic law: the mass gain Δm or oxide growth on a sample with the reacting sample area A is proportional to the square root of time t:

$$\left(\frac{\Delta m}{A}\right)^2 = k_1 t + k_2, \tag{3.2}$$

where k_1 and k_2 are constants. This diffusion-limited behaviour is termed self-passivation. In contrast, a linear oxidation behaviour can be explained by an albeit small but constant oxygen supply to the metal. In the case of WCrY, oxygen is supplied to W during the linear oxidation regime. The third main equation used to describe oxidation, besides linear and parabolic, is logarithmic. In many cases of metal oxidation at lower temperatures, oxidation follows a logarithmic behaviour, i.e. it initially proceeds rapidly and then slows considerably down. Moreover, there are mixed forms of oxidation behaviour. The oxidation performance of samples oxidised for this work is monitored by measuring the mass gain over time. Ideally the mass should not increase after the protective oxide layer has formed. If the oxidation of the sample slows down, mass increase slows down. [66] states that sample edges or other surface defects such as scratches are prone to the formation of W containing oxides. Thus samples with slightly different geometries may start off with a higher mass gain at the beginning of the oxidation process. Details on the sample geometry and the cutting and grinding process will be given in the subsequent section. Due to the fact that grinding from all sites and thus removing all remnants from wire erosion is not possible, conditions at the start of an oxidation test vary for samples used in this work. For this reason the gradient of the mass change per area is chosen as a measure of oxidation performance:

$$k_1 = \frac{\delta \left(\frac{\Delta m}{A} \right)^2}{\delta t} \tag{3.3}$$

If the mass remains constant, the gradient of the mass change becomes zero. Slowing down the mass gain results in the gradient of mass gain approaching a value close to zero. When a dense and closed oxide sale on the surface is formed and the sample is chemically approximately inactive (passive), self-passivation has been reached.

3.3. Sample production and preparation

The sample production process starts with mechanically alloying a powder mixed from W, Cr and Y powders. First the powders are weighed in to obtain the desired composition of 88 wt% W - 11.4 wt% Cr - 0.6 wt% Y. For convenience in this work the composition in at(atomic)% is used: 67.9 at% W - 31.1 at% Cr - 1.0 at% Y. The powder with the optimum composition is then milled for 60 h in a planetary ball mill. During this mechanical alloying step a homogeneous and fine particle distribution is obtained. After mechanical alloying, the powder is compacted using the Field assisted sintering technology (FAST) [67]. For one ingot, 25 g of powder are placed into a die which is clad on the inside with graphite foil. During the FAST process a pulsed DC current is applied while simultaneously applying a constant pressure until the maximum sintering temperature is reached. At this point the powder is compacted. Consequently the pressure is released and the obtained sintered ingot is cooled down by convection.
For the two WCrY samples exposed in experiment D220P (see 6.1.1 for the experiment description), FAST parameters are an uni-axial ramp of 200 K min^{-1}, a maximum pressure of 50 MPa and a holding time of 1 min at a maximum temperature of 1823 K. For all other WCrY samples the FAST parameters differ in a maximum temperature of 1733 K after which no holding time was applied. The last-mentioned FAST parameters were found to be the optimum parameters. Samples produced with these optimum parameters feature a fine microstructure of sub-micrometre sized grains and improved oxidation resistance as referred to in [60] compared to samples produced earlier. Since the smart alloy concept relies on achieving a good oxidation as well as plasma performance, optimisation of samples for oxidation purposes and testing of the plasma performance have to be performed simultaneously and supportingly. For this reason the sample production and preparation procedure of samples used for oxidation testing and samples used for plasma exposures is kept as similar as possible.
In Figure 3.2 Scanning Electron Microscopy (SEM) images of a cut orthogonal to the sample surface of a WCrY sample produced for experiment D220P (see Chapter 7) and a sample produced for experiment D120P (see Section 6.1) are shown. The sample produced for experiment D120P is characteristic for the samples produced for all experiments except D220P. The microstructure is characterised by grains containing mostly W and Cr and smaller particles containing mostly Y and additionally O. These particles are called YO particles throughout this work. The sample produced at a lower maximum

temperature and without holding time, D120P1-WCrY1, features smaller grains. For all samples presented in this work powder from the same milling procedure was used. More details of the sample production and the resulting microstructure can be found in [43]. After sintering, a cylindrical ingot with a height of about 5 mm and a diameter of about 20 mm is obtained. Wire erosion is used to cut the ingots so that they fit the geometry of the sample holders used for plasma exposure. These holders are described in Chapter 4. The sample geometry is cut from the middle of the ingot so that at least half a mm is cut from all sides. This is done to ensure removing inhomogeneities close to the surface and carbon impurities from the graphite foil used during sintering. A hole is added on top so that after plasma exposure samples can be hung in the furnace for oxidation. Figure 3.3 depicts the plasma geometry of WCrY and W samples. Wire erosion (also referred to as spark erosion) cutting is additionally used for cutting the W reference samples from a large piece of ITER-specified [68] W. The sample geometry of the W samples is similar to the one of the WCrY samples except for the hole.

In order to remove remnants from wire erosion cutting and have comparable surface conditions, the W and WCrY samples are manually ground. Grinding is performed using a rotating and planar grinding disk on which abrasive silicon carbide (SiC) paper is fixed. The abrasive paper is classified by grit size or average particle size of the SiC particles in microns. For example, a P1200 SiC paper has a nominal micron size of 15.3 µm, P800 is more coarse with a nominal micron size of 21.8 µm. Several consecutive grinding steps are performed for front and back side of the samples and using different SiC papers. Samples are glued equidistantly onto a metallic disc during all steps. If possible, at least three samples are glued onto the disk together to prevent tilting of the samples during the grinding. Back and front side should be as plane-parallel as possible after grinding. W and WCrY samples were not ground together to impede for example Cr particles being incorporated into the pure W sample surface. The metallic disc with the samples is pressed onto the grinding disk. For all samples used in this work the grinding procedure is performed as outlined in Appendix A. The SiC paper P1200 with a particle size of 15.3 µm used for the last step determines the surface roughness of the samples. This SiC paper is also used in the last grinding step for the samples meant for oxidation testing. After performing the consecutive grinding steps a reproducible surface finish

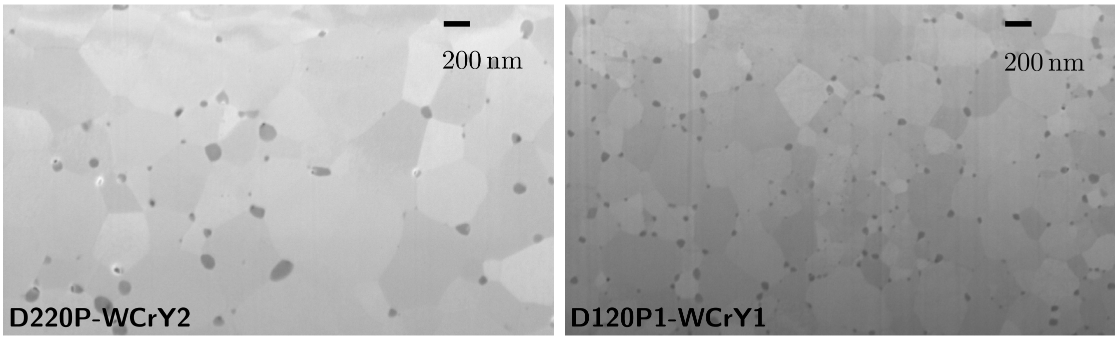

Figure 3.2.: SEM images of the microstructure of samples D220P-WCrY2 (left side) and D120P1-WCrY1 (right side).

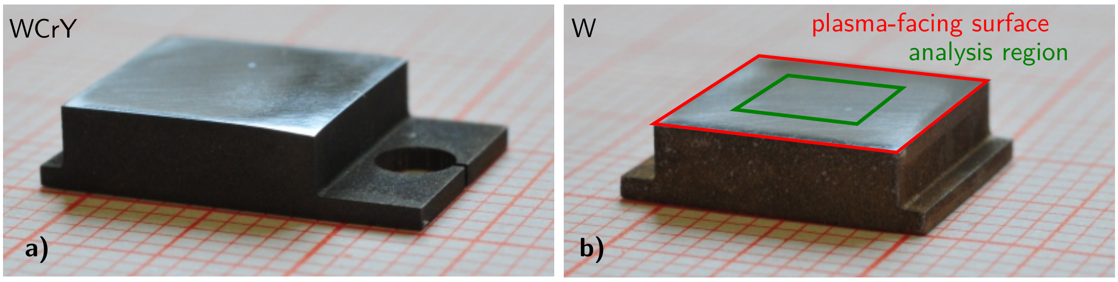

Figure 3.3.: Pictures of a WCrY and W sample showing the specific sample geometries. The plasma-facing surface and the region within which analysis is conducted are indicated.

for all samples resulting in a surface roughness R_a of about 30 nm (see Section 5.1.8 for definition of R_a) is obtained. For a W and a WCrY sample exposed in D120P1 (see Section 6.12), D120P1-WCrY3 and D120P1-W2, the SiC paper P800 with a particle size of 21.8 µm was used in the last grinding step to obtain a more rough surface finish. The accessible sample sides (plasma-facing surface and back of sample plus the sample sides, see Figure 3.3) are then ground by pressing them manually onto a SiC P1200 paper at a rotating speed of 60 rotations/min and under constant water supply. However, due to the sample geometry not all sides are accessible and on several locations on the sample dirt from wire erosion remains.

After the grinding process and removing the samples from the metallic disc, they are put into an ultrasonic bath with acetone (C_3H_6O) and then isopropanol (C_3H_8O) for about 15 min each for cleaning.

4. Experimental facilities

4.1. Linear plasma devices

In future fusion devices like ITER and even more DEMO, particle and heat loads will be substantially higher than in present facilities. Long pulse durations in steady state reactor conditions as well as transients will cause severe erosion of the PFM. PFM erosion is an important factor determining the lifetime of the reactor wall components. This, in turn, determines the cost-efficiency of a fusion power plant as deteriorated material has to be exchanged. Consequently, it is important to test the materials envisaged to serve as PFM in the future already now in relevant conditions. Further, it is of equal importance to isolate the effects caused by different PWI processes to understand their impact on material properties. Laboratory experiments are used for this purpose. Linear plasma devices offer the possibility for dedicated and controlled testing of new materials under fusion-relevant plasma edge conditions. Exposure to ion irradiation and laser pulses for simulating transients allow in-depth studies of plasma-wall interaction phenomena such as the evolution of the material's surface morphology and microstructure. Moreover, an extended particle flux and therefore accumulated fluence allow making predictions about the material's erosion in reactor-relevant conditions on longer time scales.
The plasma in a linear plasma device is first generated at the plasma source, where usually different gases can be introduced as plasma ion species. The plasma is then focussed and directed onto a target using magnetic coils. A bias voltage between source and target is applied to accelerate the plasma ions to different ion energies. High particle and heat flux densities can thus be obtained, leading to heating of the target material. The target is often additionally heated or cooled externally, e.g. by means of water cooling. Different diagnostics are employed to study either the plasma itself or the target material's evolution. For this work the two linear plasma devices PSI-2 and Magnum-PSI were used, both are described below.

4.1.1. PSI-2

The linear plasma device PSI-2 is located at the Institut für Energie und Klimaforschung, Plasmaphysik (IEK-4), Forschungszentrum Jülich GmbH, Germany. It is an upgraded version of PSI-1, which was operated until 2010 at the Humboldt University Berlin, Germany. Main operational parameters of PSI-2 are ion fluxes in the order of $1 \times 10^{21}\,\mathrm{ions/(m^2 s)}$ to $1 \times 10^{23}\,\mathrm{ions/(m^2 s)}$, which is similar to the expected average ion flux at the DEMO first wall (see Section 2.1.3), and an electron density n_e in the order of $1 \times 10^{16}\,\mathrm{m^{-3}}$ to $1 \times 10^{19}\,\mathrm{m^{-3}}$. Further, the electron temperature in pure D plasma ranges from 1 eV up to 25 eV, while the ion temperature is in the range of 0.5 eV to 5 eV.

More details of the PSI-2 operational space and on the device itself are given in [69]. Figure 4.1 is a sketch of the PSI-2 setup. Different gases can be introduced into the cathode chamber, where they get ionised to form a plasma. Most frequently D is used as working gas, additionally noble gases such as Ar or gas mixtures are possible. The working gas flow is varied between approximately 10 sccm and 100 sccm. Gas usage is monitored via gas flow controllers. Plasma is generated by an arc discharge between a heated lanthanum hexaboride (LaB_6) cylindrical cathode and a molybdenum (Mo) anode. The arc power can be tuned up to 26 kW. The geometry of the plasma source results in a radial-symmetric hollow plasma profile, which is illustrated in Figures 4.2 and 4.3. In total 6 magnetic field coils confine the plasma into a column with a diameter of 6 cm. The plasma chamber extends in total over 3 m. Whereas the plasma source is installed at a fixed position at one end of the device, the target holder for sample exposure is mounted on a movable manipulator. Mounting samples is carried out in a target exchange chamber, which is positioned behind the plasma dump and is not shown in the sketch, so that vacuum conditions in the source and target chamber are not degraded when samples are exchanged. The manipulator with the installed samples is moved towards the source into the target chamber, shown in Figure 4.1, for exposure. At the target exposure region a magnetic field of 100 mT is present, the plasma beam hits the target perpendicularly.

When a solid target, i.e. the sample mask, is placed into the PSI-2 plasma column, a Debye sheath develops. As already described in Chapter 2, this sheath is characterised by a spontaneously arising potential drop V_{sf} for a floating surface. In order to accelerate the plasma ions onto the target and specify different incident ion energies, an external negative bias voltage V_{bias} can be applied. The energy of the incident ions E_{in} is then given by Equation (4.1).

$$E_{in} = q(V_{bias} - V_P), \tag{4.1}$$

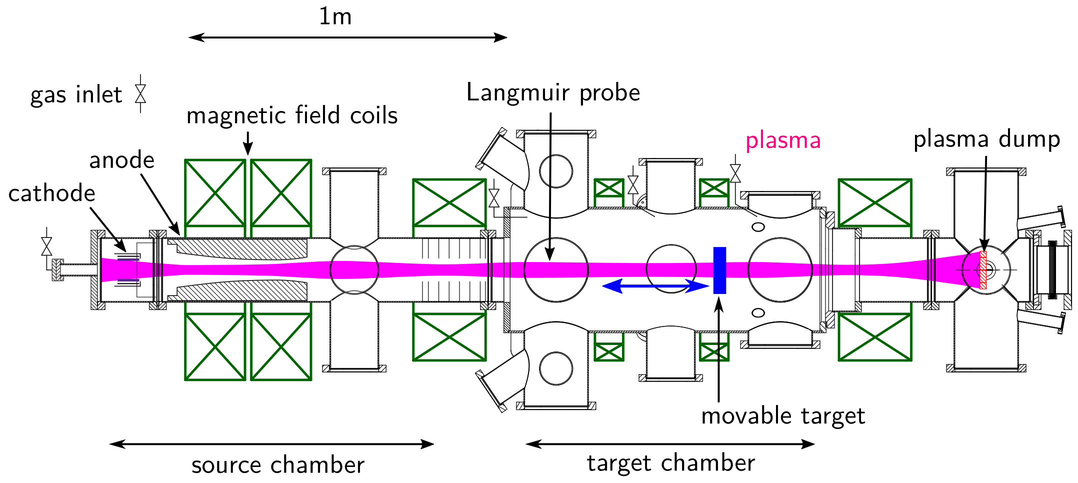

Figure 4.1.: Schematic top-view of PSI-2 setup.

with the ion charge q and the plasma potential V_P. In this work the incident ion energy is given in eV ($1\,\text{eV} = 1.602 \times 10^{-19}\,\text{J}$), q is given in multiples of the elementary electric charge e ($1\,e = 1.602 \times 10^{-19}\,\text{C}$). The plasma temperature in PSI-2 is low enough to consider only singly ionised ions. The plasma potential V_P describes the potential of the plasma compared to an arbitrary and fixed reference potential and is measured by the Langmuir probe as described below. If no bias voltage and hence no reference is applied, V_P is given by the floating potential V_{sf}.

Sample installation and diagnostics

The PSI-2 sample mask used for exposing WCrY samples can fit up to eight samples. These are placed at the maximum of the flux, 2.5 cm to 3.0 cm off the plasma axis, to ensure as similar plasma conditions as possible. Figure 4.3 is a picture of the mask during exposure. The sample mask is made from pure W to not have other re-deposition than that from W on the samples during plasma irradiation. Flexible graphite foil (Grafoil) as well as Cu spacers are placed between samples and mask to ensure good thermal contact. Additionally, a piece of W foil is placed behind each sample to avoid direct contact with the Grafoil and possible sticking of the samples to the Grafoil. One can see in Figure 4.3 that the samples' surfaces are sticking out a bit from the mask so that re-deposition of eroded mask material is reduced.

The mask can be installed onto different target holders, depending on the maximum temperature reached during the experiment and if additional cooling or heating of the mask is required. For experiments presented in this work target holder B was used, additional heating is possible with this holder. On the backside of one of the samples, the sample in the middle row and closest to the left side of the mask shown in 4.3, a thermocouple is installed. It allows monitoring the sample temperature and gives the possibility for calibration of the sample's emissivities together with the active heating of the sample holder. This is done by means of a FLIR SC700 infrared (IR) camera before plasma start. The camera is positioned near the plasma source and records all samples installed in the mask. Samples are heated to a certain temperature until thermal equilibrium has been reached. At this point the temperature measured by the thermocouple behind the mask and the temperature measured for the samples by the IR camera have to agree, temperatures shown by the IR software are now adjusted by changing the samples emissivities. These emissivities are then used during the exposure for monitoring the sample surface temperatures.

The target holder is placed onto a manipulator which allows varying the exposure position in PSI-2. During the conducted experiments the holder is located between magnetic coils four and five (see Figure 4.1). Measuring the sample temperatures with the IR camera is only possible at a certain position where there is a free line-of-sight onto the samples. Moving the sample holder to a position directly in front of the Optical Emission Spectroscopy (OES) window allows measuring line radiation intensities during exposure using imaging spectroscopy. An Acton Research Spectrapro 750 from Princeton Instruments with a resolution of $0.01657\,\Delta\lambda$/pixel is used. Line radiation is the discrete radiation emitted when an electron in an excited state falls back to a lower energetic state. For optically thin plasmas as in PSI-2, excitation is dominated by electron collisions (see Table 2.1 in Chapter 2). For the conducted experiments line radiation of neutral W (WI) at 429.46 nm and neutral Cr (CrI) at 427.48 nm in front of the target were monitored. Further, the D_γ line at 433.93 nm is always present in the spectra measured during exposure in D plasma. As the measurement is taken in the form of an overview spectrum with a width of 24 nm, all three lines are monitored simultaneously.

A movable Langmuir probe is used for characterising the plasma. For this purpose the probe moves down from above the plasma column radially to the centre of the plasma and back. This way the upper maximum of the plasma profile is measured twice. A symmetric profile is assumed for the second maximum at the lower side of the plasma profile. This is illustrated in Figure 4.2. The radial resolution of the Langmuir probe measurement is given by the size of the probe tip of 1.5 mm, the scanning frequency is 100 Hz. From the measured $I-V$-characteristics plasma parameters such as the electron density n_e, the electron temperature T_e, the plasma potential V_P and the parallel ion flux can be inferred.

Quadrupole Mass Spectrometry (QMS) data is recorded in the PSI-2 vacuum vessel at the top of the target chamber. Besides the working gas (mainly D in this work), a minute residual oxygen amount is present on the QMS data. The line radiation of the impurity oxygen in the plasma is too weak to be detected via OES measurements, similar to the spectroscopy measurements described in [70] for a plasma oxygen content of 0.2 % in the linear plasma device PISCES-B. Therefore, and based on simulation results described in detail in Section 6.1.3, the plasma oxygen impurity content is assumed to be around 0.2 % to 0.3 %.

When a plasma exposure of WCrY and pure W reference samples is conducted in PSI-2, samples are installed with the mask onto the sample holder about 2 h prior to exposure.

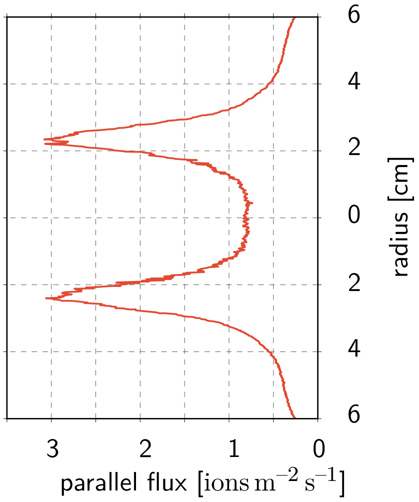

Figure 4.2.: Upper (and mirrored) half of parallel ion flux as measured by the Langmuir probe during experiment D120P1.

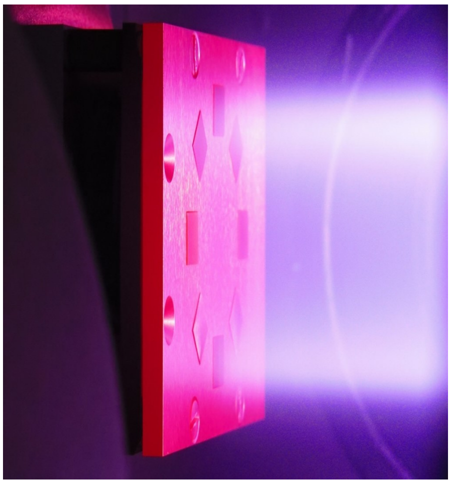

Figure 4.3.: Picture of sample mask during exposure to pure D plasma in D120P1.

Without plasma, a vacuum pressure of about 1×10^{-7} mbar is present in the PSI-2 device. During plasma operation, this pressure is increased due to the gas inlet at the plasma source to values in the range of 1×10^{-5} mbar to 1×10^{-4} mbar. A few hours after the experiment ended or the next day, the target holder and the samples are taken out to allow cooling down to room temperature.

4.1.2. Magnum-PSI

MAgnetized plasma Generator and NUMerical modeling for Plasma Surface Interaction (Magnum-PSI) is a linear plasma device located at the Dutch Institute For Fundamental Energy Research (DIFFER) in Eindhoven, the Netherlands. It is the successor experiment of Pilot-PSI, the linear plasma device previously operated at DIFFER. Magnum-PSI was officially opened in 2012. The device is designed to achieve plasma parameters relevant to high performance detached divertor operation in ITER [71], namely particle fluxes in the order of $1 \times 10^{23}\,\mathrm{m^{-2}\,s}$ to $1 \times 10^{25}\,\mathrm{m^{-2}\,s}$, and electron densities n_e of the order of $1 \times 10^{19}\,\mathrm{m^{-3}}$ to $1 \times 10^{21}\,\mathrm{m^{-3}}$among other design values stated in [71]. These extremely high fluxes, two orders of magnitude higher in comparison to PSI-2, are possible thanks to using a superconducting magnet with a strong magnetic field of the order of 1 T.

The Magnum-PSI setup is described in detail in [72]. Magnum-PSI is approximately 15 m long and consists of a water-cooled vacuum vessel with a cascaded arc plasma source mounted on the one end of a manipulator tube. The target holder is mounted on the other end. Target holder and plasma source can be brought within a distance of 1 m. At this position a plasma beam is generated between source and target with the aid of a magnetic field. A 3D model of the superconducting magnet with the plasma source and the (single-)target holder inside can be seen in Figure 4.4. Different types of a water-cooled cascaded arc source can be installed on the source manipulator depending on the envisaged plasma conditions. Just as in PSI-2, the working gas used for plasma generation and the cathode to anode current of the source can be changed. A gas flow of up to 4×10^4 sccm is possible, six power supply units, each with a power of $300\,\mathrm{V} \times 100\,\mathrm{A} = 3 \times 10^4\,\mathrm{W}$, are available for plasma source current and bias voltage. The plasma beam has a Gaussian electron density profile with the Full Width at Half Maximum (FWHM) ranging from about 1 to 2 cm. While a vacuum pressure of lower than 1×10^{-2} mbar is achieved at the target during plasma operation, this pressure is reduced to a value lower than 1×10^{-6} mbar in between operations to minimise contamination of the vessel. Similar to PSI-2, the level of impurity oxygen in Magnum-PSI is too low to be detected. Therefore, the plasma oxygen content is assumed to be significantly below 1 %.

On the end of the manipulator where the target holder is mounted, two holder types are available. For large targets with dimensions of several cm, a single-target holder is available, whereas a multi-target holder can fit up to 5 smaller targets. Both holders are water-cooled with a flow of up to $50\,\mathrm{l\,min^{-1}}$. By adjusting the shape and the thickness of the material between the target and holder, typically Grafoil, the heat conductance is varied.

The target voltage during plasma exposure can be varied by connecting power supplies to the target. Thus a bias voltage for accelerating ions onto the target can be applied. Just as in PSI-2 the energy of the incident ions E_{in} is then given by Equation (4.1). In Magnum-PSI the electron temperature T_e is very low, typically around 1 eV or 2 eV near the target. At these low temperatures the plasma potential amounts only to a few eV [12]. As a consequence it can be neglected compared to the much higher bias voltage used in the experiments presented in this work and the incident ion energy simplifies to Equation (4.2):

$$E_{in} = qV_{bias}. \tag{4.2}$$

Similar to PSI-2, only singly ionised ions are considered in Magnum-PSI (only D^+ as in Magnum-PSI exposures took place in pure D plasma), thanks to the low plasma temperature. When tuning the plasma source to the preferred plasma conditions, a beam dump is moved in front of the plasma source to prevent target exposure. This is not possible in PSI-2. However, in both plasma devices significant sputtering of target material only occurs once the bias voltage is applied to the target.

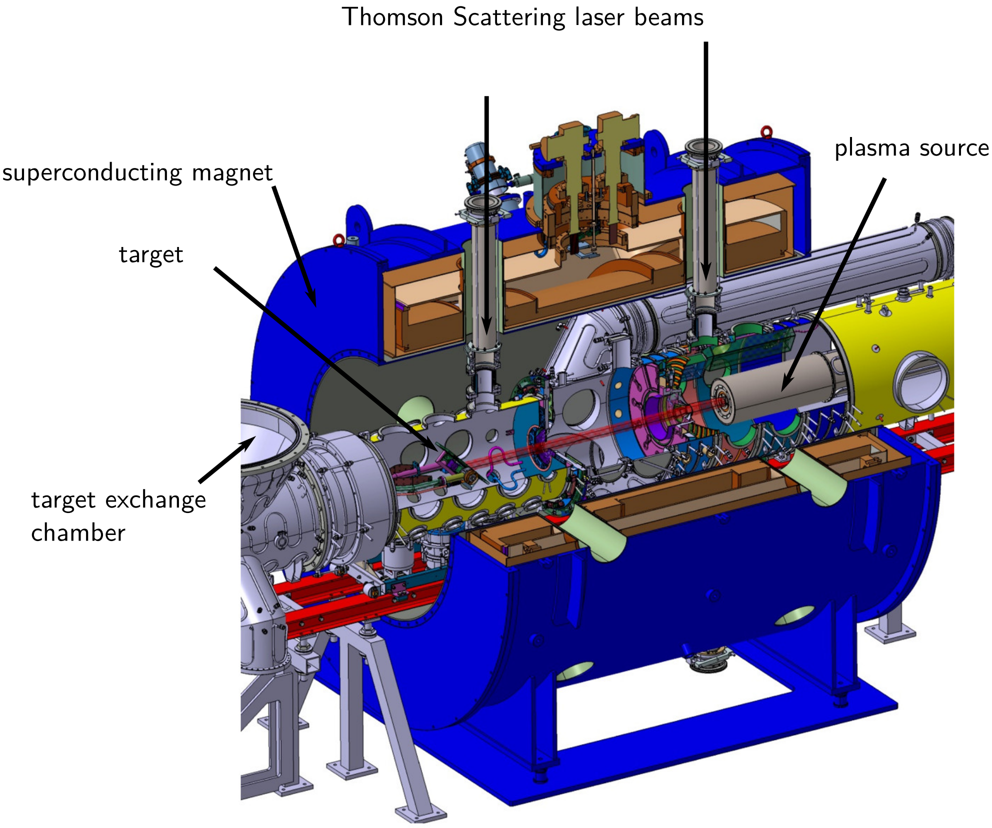

Figure 4.4.: 3D model of Magnum-PSI exposure region with target and plasma source.

Sample installation and diagnostics

For the experiments reported in this work, the multi-target holder fitting up to 5 samples was used. The plasma beam hits the target at normal incidence. The target holder with the installed samples is shown in Figure 4.5. A customised mask was fabricated for the typical geometry of the WCrY and W samples (see Figure 3.3) so that only the plasma-facing surface of 1 cm × 1 cm was accessible by the plasma and the sample surfaces are elevated with respect to the mask. Additionally, the ring around the samples is coated with W to minimise re-deposition from other materials onto the samples. The outer clamping ring is made out of tantalum. Grafoil was used for thermal insulation between the backside of the samples and the mask. Here care was taken to not tighten the screws of the clamping ring with too much force to avoid sticking of the Grafoil to the samples. Due to the beam geometry it is only possible to expose one sample at a time. Between the exposures, the target holder is rotated to have another sample centred in the maximum of the beam profile.

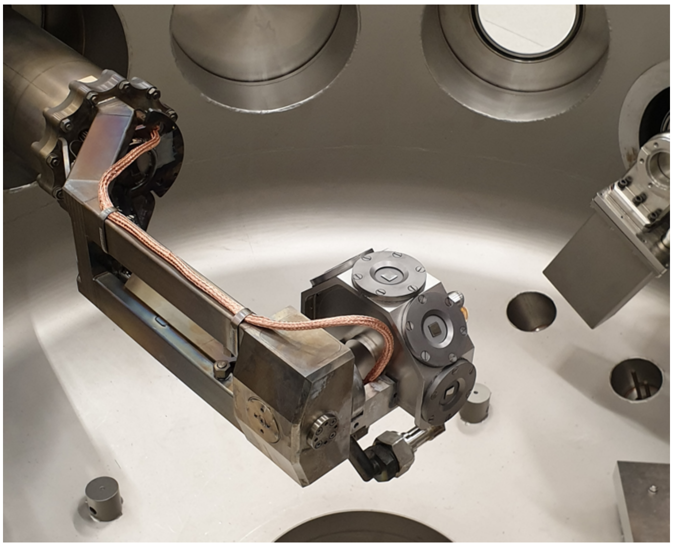

Figure 4.5.: Multi-target holder with W and WCrY samples installed inside the target preparation chamber of Magnum-PSI.

In the control room, which is separated from the laboratory, the complete experimental installation, including the diagnostics, is operated and monitored. The diagnostics are described in detail in [71]. A summary of the diagnostics utilised during the experiments presented in this work is given in this paragraph. The most important diagnostic for characterising the plasma is Thomson Scattering (TS). TS determines the profiles of n_e and T_e at a distance of about 2 cm in front of the target with a spatial resolution of 1.6 mm and a repetition period of 1 s. Figure 4.6 shows a n_e and a T_e profile acquired during the exposure of D120M-W1. Using wide spectral OES, information on the plasma composition in front of the target is obtained. This enables observing the excitation and hence presence of sputtered target atoms in this plasma region. A fast IR camera (FLIR SC7500-MB) with a frame rate of 30 kHz in combination with a multi-wavelength spectroscopic pyrometer (FARSpectro Pyrometer model FMPI) are used to monitor the sample surface temperature during plasma exposure. Since the pyrometer starts reliably working at temperatures of above 700 K and the sample temperature during conducted experiments was set to about 900 K, no calibration of the emissivities for the IR camera was necessary. It is not possible to enter the laboratory where the linear plasma device is installed. Therefore, a fast visible light camera (Phantom) with a frame

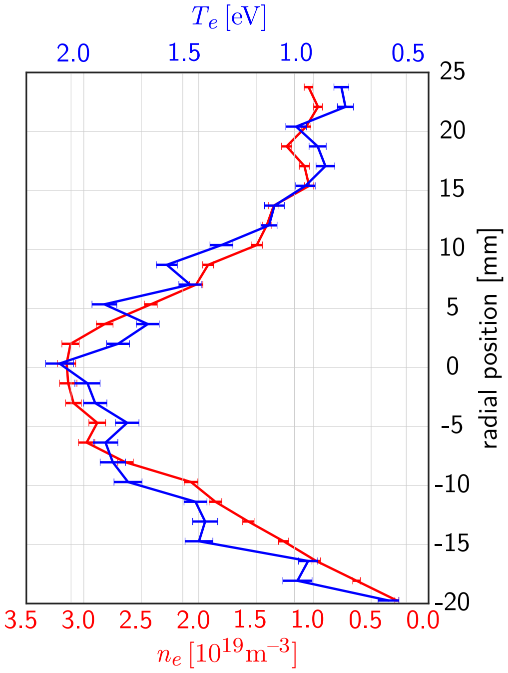

Figure 4.6.: n_e and T_e profile acquired by TS in front of the target during exposure of D120M-W1.

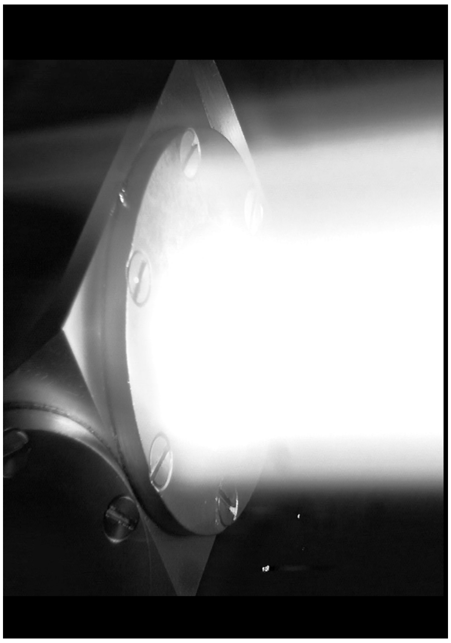

Figure 4.7.: Picture of sample D120M-W1 during exposure in Magnum-PSI.

rate of up to 1 MHz is available to look at the target during exposure. This is shown in Figure 4.7. Biasing of the target leads to broadening of the beam due to the geometry of the biasing cable at the target holder so that the W-coated ring around the sample is partly exposed to plasma as well. The IR camera was used to ensure that the beam maximum is focussed onto the sample.

4.2. ASDEX Upgrade

ASDEX (axisymmetric divertor experiment) Upgrade (AUG) is a fusion experiment based on the tokamak principle (see Chapter 2) located in Garching near Munich, Germany. It has been operated by the Max-Planck-Institut für Plasmaphysik Garching since 1991 [73]. Since the 2007 experimental campaign it is operated with W coated PFCs [74]. The aim of fusion research at AUG is preparing the physics base for ITER and DEMO. For this purpose essential plasma parameters such as the plasma density, plasma pressure and the wall load are matched to the conditions in a future fusion power plant [73]. Consequently, AUG can serve to test newly developed PFC materials in a more-realistic fusion environment compared to e.g. linear plasma devices where single parameters such as the plasma ion flux are chosen to match fusion-relevant values. Within the framework of this PhD work, a WCrY smart alloy sample and a reference W sample were installed at the inner upper divertor of AUG for long-term exposure in fusion-relevant conditions. Details on AUG can be found in [73] or [74]. A short summary of its main operation

technical data	
major plasma radius	1.6 m
minor plasma radii	0.5/0.8 m
plasma shape	D-shape; upper and/or lower divertor
magnetic field	3.9 T
plasma current	2 MA
pulse length	10 s
plasma heating	27 MW
plasma mixture	hydrogen, deuterium

Table 4.1.: AUG technical data from [73].

characteristics is given in the text below, technical data is given in Table 4.1.
The plasma in AUG is confined by a magnetic field essentially generated by 16 large copper magnet coils placed around the ring-shaped plasma vessel, alongside with 17 auxiliary coils for the divertor. There are three different methods available for plasma heating: neutral particle injection with a power of max. 20 MW, high-frequency heating with 6 MW and microwave heating with 4 MW. Up to 40 diagnostics are used to investigate the plasma, some of which determine the plasma properties while others focus on the PFC behaviour. AUG can be operated with an upper and/or a lower divertor configuration, allowing the formation of two X-points. Due to the form of the vacuum vessel in combination with the coil setup the plasma is D-shaped. In the divertor, especially along the strike points where the magnetic field lines intersect the PFC material, wall heat and particle loads are highest and hence erosion is most intense. In contrast, particle fluxes at the first wall are considerably lower, resulting in the main chamber being a strong net-deposition region for W [75]. Although WCrY smart alloys are designed for the first wall or main chamber of DEMO, exposure in the main chamber of AUG would probably just lead to an accumulation of sputtered and re-deposited material making it impossible to study the sample erosion behaviour. On the other hand, exposure directly at the strike line could lead to additional effects such as local overheating or excessive erosion. Therefore, it was decided to install the WCrY and the W reference sample at the upper inner baffle. This region does not come into direct contact with the strike line, yet erosion is expected to be stronger than in the top part of the device. The view inside the vacuum vessel with the lower divertor at the bottom is shown in Figure 4.8.

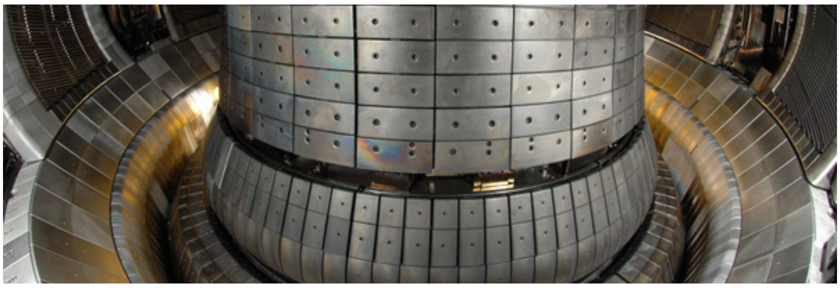

Figure 4.8.: View inside the AUG vacuum vessel clad with PFC tiles. The lower divertor can be seen at the bottom. Image from [73].

5. Analysis methods

This chapter is devoted to describing the different analysis methods used within the present work. First the experimental analysis techniques for sample characterisation and investigating the plasma impact are presented. Following this, an introduction to SDTrimSP modelling is given. The model used for simulating the impact of the plasma ion irradiation and therefore serving as a semi-empirical analysis method is described.

5.1. Experimental analysis techniques

5.1.1. Energy-dispersive X-ray Spectroscopy (EDX)

Energy-Dispersive X-ray analysis (EDX) allows to identify and quantify the elements of the beam-excited interaction volume within the probed sample. For the EDX analysis in this work, the detector included in the FIB-SEM Crossbeam XB540 setup, whose main purpose is SEM analysis as described in Section 5.1.2, is used. Within this setup the sample is irradiated with an energetic electron beam. The element-specific X-rays are a product of the interaction of this primary electron beam with the sample [76]: energetic beam electrons excite the atoms of the sample within the interaction volume (see Figure 5.1). Once these atoms relax, characteristic X-ray photons possessing defined energies specific to each atom species are emitted. Additionally, a continuous X-ray spectrum, caused by the electrons' bremsstrahlung is generated. The spatial resolution of the EDX analysis is limited on the one hand by the fact that X-rays originate from a large fraction of the electron interaction volume. Further, the background due to bremsstrahlung X-rays needs to be removed for quantification of the characteristic X-ray energy peaks. Depending on the sample's composition and the beam energy, the beam-excited interaction volume dimensions range from approximately 100 nm to 10 µm. The beam electron

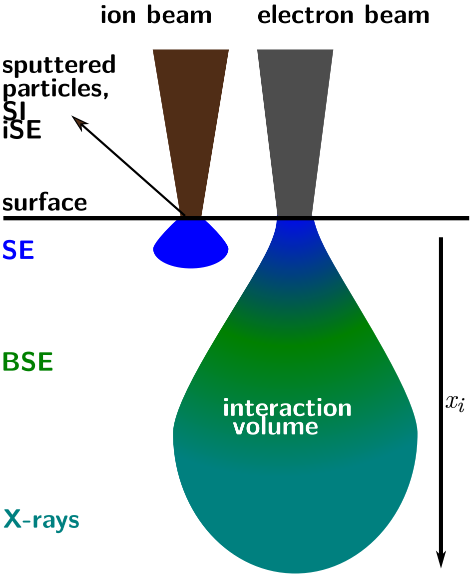

Figure 5.1.: Interaction volumes of ion and electron beam with a solid surface. Reaction products are SIs, iSEs, SEs, BSEs and X-rays.

energy E_0 must exceed the electron binding energy, i.e. the critical ionisation energy E_c for any specific electron shell, in order to generate characteristic X-rays. Efficient excitation is obtained in case this excitation energy is exceeded more than twice: $E_0 > 2\times E_c$. Hence at higher incident beam energies, electrons on higher levels can be excited, which yields more characteristic peaks extending to higher energies in the obtained spectrum and thus helps identifying the elements present in the sample. Yet, the interaction volume increases for higher incident beam energies leading to a decrease in spatial resolution.

Figure 5.1 shows the interaction volumes of an electron beam as well as of an ion beam with a solid target. The maximum penetration range from [77], i.e. the lateral extension of the interaction volume, is given in Equation (5.1):

$$x_i\,[\mathrm{nm}] = 27.6\frac{A}{Z^{0.89}\rho}E_0^{1.67}, \tag{5.1}$$

with the atomic weight A [g/mol], the incident beam energy E_0 [keV], the atomic number Z and the atomic density ρ [g/cm^3]. Using an incident energy E_0 of 5 keV yields a maximum penetration depth x_i of about 80 nm in W. As WCrY is made up of about 70 at% W and 30 at% Cr, and Cr has a lower density and atomic number Z compared to W, x_i for WCrY is assumed to be of approximately 100 nm at this incident energy. Further, from the Lambert-Beer law given in Equation (5.2), the depth d from which a certain fraction $\frac{I}{I_0}$ of the initial X-ray intensity I_0 can still escape can be inferred.

$$\frac{I}{I_0} = e^{-\frac{\mu}{\rho}\rho d}, \tag{5.2}$$

with the initial X-ray intensity I_0, the escaping intensity I, thickness d and the material-specific X-ray mass attenuation coefficient $\frac{\mu}{\rho}$ [cm^2/g]. The X-ray mass attenuation coefficient $\frac{\mu}{\rho}$ is indicated with a value of about 5.5 cm^2 g^{-1} for X-rays with energies of 5 keV in W by [78]. At a ratio of $I/I_0 = 0.95$, d amounts to approximately 0.5 mm. Consequently, the information depth is limited by the penetration depth or mean free path of the electrons into the sample and not the X-ray escaping depth. Thus in this work the EDX analysed layer is assumed to extend to a depth of approximately 100 nm below the WCrY sample surface.

5.1.2. Focussed Ion Beam - Secondary Electron Microscopy (FIB-SEM)

The Focussed Ion Beam - Secondary Electron Microscopy (FIB-SEM) setup is a dual-beam instrument, which is besides a SEM equipped with a focussed ion beam (FIB). For this thesis a Carl Zeiss Crossbeam XB540 FIB-SEM setup was used.

A SEM is an instrument used to create magnified images of microscopic-scale information of a variety of material properties such as size, shape, composition and crystallography [76]. The main working principle, which is described in more detail in [76] and summarised below, relies on first creating a finely focussed beam of electrons, which are emitted from an electron source. For the Crossbeam XB540 a Schottky emitter, a tungsten tip coated with a layer of zirconium oxide, is used as field emission gun. The electron beam gets accelerated typically to energies in a range from 0.1 keV to 30 keV, which is also the case for the Crossbeam XB 540, and is further modified by electrostatic or magnetic apertures and lenses or magnetic coils. This serves to focus the beam to a smaller beam diameter and to scan it in a raster pattern over a rectangular area across the sample. The raster is a pattern of discrete locations where the electron beam interacts with the sample. As a result of this interaction two electron products are created: some electrons are elastically scattered and deflected by the electric fields of the sample's atoms. These electrons are Backscattered Electrons (BSEs), they conserve a large amount of their incident energy after the interaction with the sample and stem from sub-surface regions. Besides this elastic scattering of the beam electrons, there is inelastic scattering leading to the emission of Secondary Electrons (SEs) from the sample. These have usually low kinetic energies in the range of 0 eV to 50 eV and can thus only escape the sample from shallow depths. The interaction volume of the electron beam within the sample depends on the incident energy of the electron beam as well as on the atomic number of the sample's material (see Figure 5.1 and Equation (5.1)). There exist detectors specifically for acquiring SE or BSE signals, as they are sensitive to different electron energy ranges. With a beam current of 300 nA down to 10 pA the Crossbeam XB540 allows to acquire images with a resolution of below 10 nm.

The SE detector allows to create high-resolution images of the surface topography since due to their low energies SEs escape only from very shallow depths: by increasing the angle of incidence of the probing electron beam the interaction volume increases and on one side of the beam the distance the SEs need to travel to escape the sample decreases. According to [76], the secondary electron coefficient increases monotonically with increasing specimen tilt angle. Moreover, if the electron beam is located close to a sample edge, additional surface area that lies within the SE escape range is available. Thus more SEs are emitted from the sample at steep surfaces and edges making them appear brighter than flat sample regions. Further, an energy-selective BSE detector allows to obtain sub-surface information on the nano-scale composition of the sample. The information on the sample's composition can be obtained as elements backscatter electrons more effectively the higher the atomic number Z is and therefore appear brighter on the image. In order to minimise scattering of the beam electrons as well as the BSEs or SEs with atmospheric atoms and molecules, the sample chamber of the Crossbeam XB540 is operated at a pressure of the order of 1×10^{-6} mbar. Samples need to be electronically conducting and are glued with conductive silver glue to the sample holder to ground the sample and thus to avoid accumulating electric charge on the surface.

Thanks to the addition of the focussed ion beam gun to the SEM setup, it is possible to prepare samples for SEM imaging in different ways. Most commonly, cross sections, i.e. cuts orthogonal to the sample surface, are created to view the sub-surface material microstructure. For this purpose a liquid metal ion source is used in the Crossbeam XB540 setup. It creates positively charged gallium (Ga) ions, which can be accelerated onto the sample to energies ranging from 0.5 kV to 30 kV. The beam current can be varied between 1 pA and 100 nA and can be moved in a raster pattern across the sample surface for the milling process. As the beam also produces SEs when hitting the sample, the signal from the sputtered ions or from these SEs is collected for imaging. The rate at which material is eroded from the sample depends on the beam current and on the sample material. To erode or mill a large amount of material a high current is used while at very low currents and at 30 kV incident beam energy the resolution of the Ga focussed ion beam can reach 3 nm. This allows the creation of nano-scale patterns and in-depth micro-structural analyses.

An additional erosion measurement, besides mass loss of the samples by weighing them before and after plasma exposure, is obtained with the help of the FIB-SEM setup: the surface recession d_e, the distance over which the surface receded during a plasma or ion irradiation experiment. For this purpose a crater featuring an orthogonal cut relative to the sample's surface is created by means of the Focussed Ion Beam (FIB) technique prior to plasma exposure. In Figure 5.2 such a cut on a WCrY sample is shown. Equidistant marker lines, typically with a spacing of 1 µm, are milled onto that orthogonal cut so that d_e can be inferred directly by comparing the distance from the surface to the uppermost marker line after plasma exposure. This is shown on the right hand side in the figure. The FIB crater and therefore measurement of d_e is located in the middle of the sample surface. To obtain a single value for the surface recession of one sample, d_e is measured five times and the average is taken. Error bars for d_e in the erosion graphs (see for example Figure 6.1) indicate the range of d_e measurements. For a sample exposed in experiment D220P (see Chapter 7) an additional crater was milled at the corner of the sample.

5.1.3. Laser Scanning Confocal Microscopy (LSCM)

A confocal microscope, such as a Laser Scanning Confocal Microscope (LSCM), serves as a high-resolution optical microscope, while at the same time it can be used as a non-contact optical profilometer [79]. For LSCM analysis presented in this work a device of type Olympus LEXT OLS4000 at the Max-Planck-Institut für Plasmaphysik (IPP) in Garching, Germany, was used.

The basis working principle is described in detail in [80], a short summary is given in the following paragraph: image formation in a confocal microscope differs fundamentally from the method of a conventional wide field light microscope, where the entire sample is exposed to the light source. In a confocal microscope, one or more focussed beams of

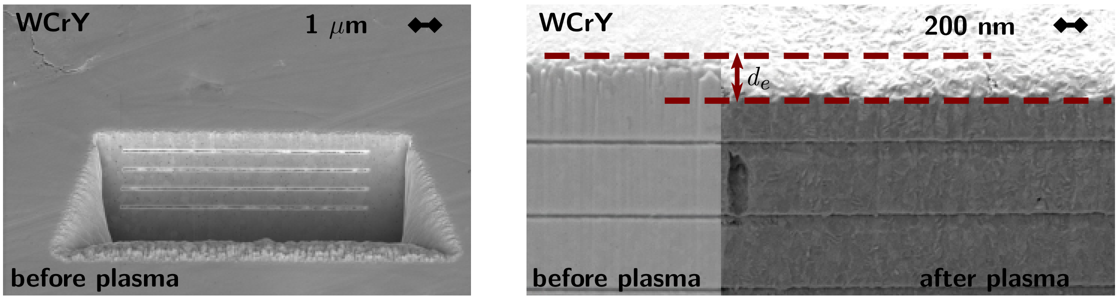

Figure 5.2.: SEM image of a prepared FIB crater on a WCrY sample before exposure (left) and the direct comparison of the uppermost marker lines before and after exposure (right).

light, laser light in case of a LSCM, is scanned across the sample. Reflected light from the laser-illuminated and diffraction-limited point on the sample is detected by a photomultiplier behind a pinhole. The output is then built into an image by the computer. Imaging of large areas of the sample is achieved by scanning the beam across the sample in a raster pattern. The LSCM is built around a conventional light microscope, which is essential for efficiently finding the region of interest by eye before scanning in confocal mode. This is very useful since the strength of the confocal microscope of eliminating out-of-focus information can make it difficult to locate a region in the confocal mode. Mounting the whole apparatus on an anti-vibration air table makes this configuration stable. Compared with the conventional wide field light microscope, both maximum lateral resolution (0.5 µm vs. 0.25 µm) and maximum axial resolution (1.6 µm vs. 0.7 µm) are increased for the LSCM, so that high quality images from samples prepared for the light microscope can be produced.

5.1.4. Low Energy Ion Scattering (LEIS)

Among the various available ion beam material analysis methods, Low-Energy Ion Scattering (LEIS) is used to probe the first few atom layers of a sample. Low-energy ions in the range of 1 keV to 8 keV are used for this purpose. A detailed description of the method can be found in [81]. The energy distribution of ions scattered from a solid surface provides information on the mass and number of surface atoms. This information is derived from the energy position and magnitude of corresponding peaks in the obtained spectrum, respectively. Within the LEIS setup a relatively small ion source with an ion energy ranging from 0.5 keV to 10 keV is used during the measurement. Usually noble gases like He, Ne or Ar are accelerated as ions onto the probed sample where they are scattered. By employing an ion mass filter an isotopic clean ion beam can be achieved. The scattered ions are then detected using an energy analyser. Scattering kinematics are in detail described in [82], crucial points for the LEIS analysis are summarised in the following paragraph.

In the binary collision model, the scattering of a projectile particle with mass M_1, velocity v_1 and initial energy E_0 at a target particle with mass M_2 can be described as an elastic collision assuming conservation of energy and momentum. Defining the mass ratio of the target and projectile particles as $\mu = M_2/M_1$ and introducing an additional term Q to account for inelastic energy loss, the scattering angle θ of the projectile is given by Equation (5.3).

$$cos\,\theta = \frac{1}{2}\sqrt{\frac{E}{E_0}}(1+\mu) + \frac{1}{2}\sqrt{\frac{E_1}{E_0}}\left(1 - \mu\left(1 - \frac{Q}{E_0}\right)\right), \tag{5.3}$$

where E is the energy of the projectile particle after scattering. Rewriting Equation (5.3) in polar coordinates yields a circular function:

$$cos\,\theta = \frac{1}{2}r\frac{1}{x} + \frac{1}{2}\frac{1}{r}\frac{x^2 - R^2}{x}, \tag{5.4}$$

with the radius of the circle R and the distance from the origin to the centre of the circle x. Comparing Equations (5.3) and (5.4), the coordinate r can be identified with $(\frac{E}{E_0})^{1/2}$. Fixed mass ratios μ for a scattered particle with initial energy E_0 and detected energy E after backscattering are represented as circles centred at a distance $x = 1/(1+\mu)$. The whole set of equations can be found in [82]. For experiments in this work, He ions backscattered at an angle of 140° are used for analysis. The reason for this becomes evident when looking at the graph in Figure 5.3. Here the scattering kinematics of 1000 eV He ions on W, Cr, Y and O are displayed. At a scattering angle θ of 140°, the energies of 1000 eV He ions are 926 eV, 853 eV, 762 eV and 405 eV when backscattered from a W, Y, Cr and O target atom, respectively.

Since scattering takes place mainly in the first atomic surface layers, the fact that only scattered ions are analysed is the reason for the surface sensitivity of LEIS. For the presented work the LEIS setup, called Auger, LEED, Ion scattering (ALI) and presented in [83] was used. Within this setup, ions from an electron ionisation ion source are accelerated to an ion energy of 1000 eV and focussed onto the sample where a beam diameter of about 1 mm is achieved. Experiments are carried out in an ultra-high vacuum chamber with a base pressure of below 5×10^{-10} mbar to avoid collisions of the probing ions with atmospheric particles and to keep the surface clean and well-defined during analysis. The sample to be probed is mounted on a sample holder permitting resistive heating up to about 1200 K. The sample holder's temperature is hence regulated by changing the current through the resistive heater. Samples can be cleaned, e.g. from residual oxygen, with the aid of a sputter ion gun before measurement. 500 eV Kr^+ ions are used for the sputter-cleaning. The same sputter ion gun can also be used with other gases, in this work D_2 is employed for irradiating the sample surface with 250 eV D^+

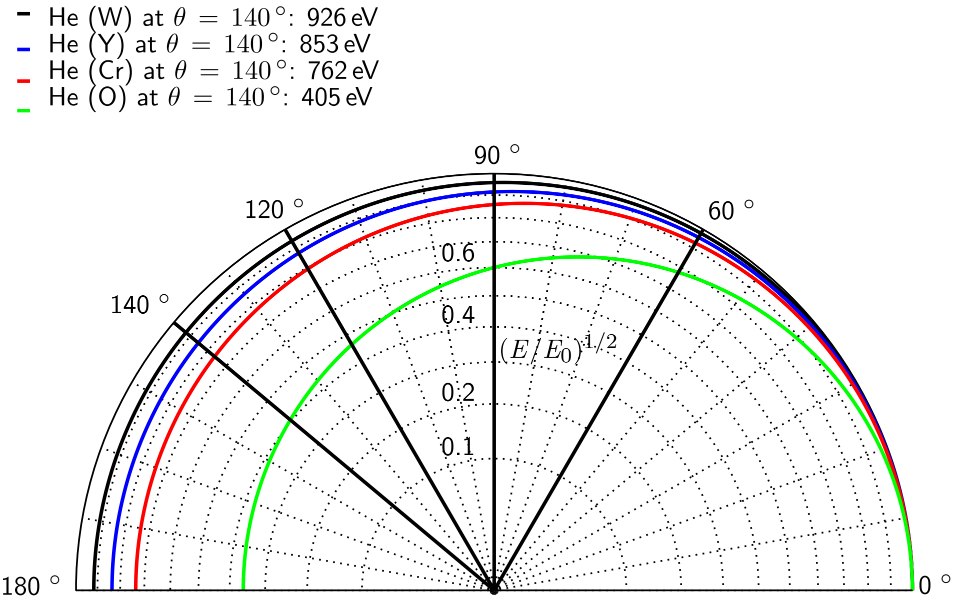

Figure 5.3.: Scattering kinematics of 1000 eV He ions on W, Y, Cr and O. Fixed mass ratios $\mu = M_2/M_1$ can be drawn as circles using polar coordinates in the binary collision model.

ions. To obtain high spatial resolution and avoid shadowing effects, samples probed by LEIS must be polished.

5.1.5. Mass loss and density measurement

To infer the mass loss during plasma exposures, samples are weighed before and after an experiment. This is done using a Sartorius MSA225P microbalance with a resolution of 10 µg. Samples are weighed three times before and after the plasma exposure, and the average over the three measurements is taken. Error bars for Δm in the erosion graphs (see for example Figure 6.1) indicate the range of the three single measurements. With the aid of the Archimedes principle the density of the samples ρ_f can be obtained by immersing them into a fluid. Here ethanol is used. According to Archimedes the weight of the fluid which is displaced by the immersed object is equivalent to the object's buoyant force. This buoyant force F_b can be expressed as the difference between the weight of the sample measured on air, m_a $(= \rho_a V_d g)$ and the weight of the sample when immersed into the fluid m_f. Since F_b further equals the weight of the fluid's volume V_d displaced by the object, $m \times g$, and $\rho_f = m_f / V_d$, one obtains:

$$\rho_a = \frac{m_a}{m_a - m_f} \cdot \rho_f, \tag{5.5}$$

where g is the gravitational constant and ρ_f is the density of the fluid.

5.1.6. Nuclear Reaction Analysis (NRA)

Nuclear Reaction Analysis (NRA) is a nondestructive, isotopically sensitive method belonging to the group of Ion Beam Analysis (IBA) techniques. It is used to investigate a material's elemental composition and features high-mass resolution. The method is described in detail in [81]. Here the authors state that NRA is mostly used for detecting light elements, such as H or D. For the analysis procedure, ions with energies of a few MeV are focussed onto the material to be sampled where they excite target nuclei and form compound nuclei. Subsequently, these nuclei decay and the elemental composition can be determined from the detection of the decay products (usually γ-rays but also particles). With a depth resolution in the nm range trace elements with a concentration of down to 1 ppm can be detected not only in near-surface regions but also in interfaces and the bulk.

The NRA setup used for this thesis is a µm-NRA setup with a 4.5 MeV ^{3}He ion beam for D detection via the nuclear reaction D(^{3}He,p)α. Using this setup it is possible to infer D retention up to a concentration of 1×10^{-6}. Further, it allows to distinguish between the retention in the subsurface layer, extending up to a depth of 3 µm, and a second layer extending from a depth of 3 µm to 8 µm.

5.1.7. Secondary Ion Mass Spectrometry (SIMS)

Secondary Ion Mass Spectrometry (SIMS) is used to determine the isotopic, elemental or molecular composition of a solid's surface region. A detailed description of this technique and the underlying physical principles is given in [84]. A short summary is given in this paragraph. Information on the solid's composition is derived from the ions that are emitted from the solid's surface due to energetic ion impact. The impacting ions are called primary ions, here most commonly a focussed beam of between about 0.1 keV and 50 keV is used. The emitted ions are referred to as secondary ions, these are the ions which are then analysed by mass spectrometry. The basis SIMS equation written down below describes the emission of the secondary ions:

$$I_s^x = I_p C_x S \gamma F, \tag{5.6}$$

with I_s^x : the secondary ion current of species x, I_p : the primary ion beam current, C_x : the concentration of species x, S the sputter ion yield of x, γ the ionisation efficiency, i.e. the probability that the detected species forms negative or positive ions, and F the transmission [85]. In general, the SIMS analysis stands out due to its high sensitivity allowing the detection of small concentrations of species in the probed sample.

The SIMS setup used for analyses within this work is a Time-of-Flight (ToF) SIMS device of the type IonTof IV (pre-analysis of experiments in Magnum-PSI and experiments in PSI-2, except post-analysis for DHeAr120P) and a device of type IonTof V.NCS (post-analysis for DHeAr120P and post-analysis of experiments in Magnum-PSI), both produced by the IONTOF GmbH in Münster, Germany. In order to obtain the elemental composition along the depth, dynamic SIMS measurements are performed. For this purpose two alternating beams are used: a pulsed Bi_3^+ as the primary ion beam or analysis beam analyses the surface by producing secondary ions while a Cs^+ or O_2^- ion beam, also called sputter beam, sputters the surface following each analysis step. The energy of the analysis ion beam is typically in the range of 20 to 30 keV, while the energy of the sputter ion beam ranges from 0.5 to 2 keV. Ion emission of the surface depends on the sample chemistry, which can be dedicatedly altered by the sputter beam. Cs enhances the ionisation of electronegative elements such as halogens, whereas O enhances the ionisation of electro-positive elements such as metals. Generally, the ion yield, i.e the SIMS ionisation efficiency or the production efficiency for secondary ions (γ in Equation (5.6)), varies over many orders of magnitude for different elements. For quantitative SIMS analysis, therefore, relative sensitivity factors depending on the concentration of the elements to be detected must be defined.

While the sputtered area amounts to 300 µm × 300 µm, the size of the analysed area is 50 to 50 µm × 60 to 60 µm to ensure that only the sputtered surface area is analysed. Signals obtained during the analysis step with Bi_3^+ are integrated over the quadratic raster area. The depth resolution is determined by the amount of material eroded during a sputter step, which in turn depends on the sputter beam current. For homogeneous materials the sputter depth scales linearly with the sputter time. Hence if after the analysis procedure the depth of the sputtered crater is measured, sputter time and sputter depth can be correlated and the depth-resolved sample composition is obtained. In the present SIMS device the sputter ion beam employed for depth profiling and the analysis ion beam are installed on the two opposite sites of the flight tube, which is used for mass separation of the secondary ions (see explanation below). Both, the sputter and the analysis ion beam are directed at an angle of 45° at the surface. One has to take into account that in case

of surface roughness the area irradiated by the sputter beam is not necessarily the same as the area irradiated by the analysis beam, as would be the case for an ideal mirror-like surface. Thus especially directly at the surface, interpretation of the obtained signals is complicated by the surface structure as the sputter beam needs some time to equilibrate.
In Figure 5.4 an image of a sputtered crater is shown. On the right side it can be seen that the surface at the bottom of the crater is an imprint of the surface morphology before sputtering.
For the ToF SIMS setup, the mass of the secondary ions emitted during the analysis step is separated by accelerating them into a flight tube and measuring the time needed for them to reach the detector, i.e. their time of flight within the tube. As particles of the same electric charge but possessing different masses fly at different speeds, the characteristic mass and thus the atom or molecule species can be determined. ToF SIMS allows acquiring the whole mass spectrum at high mass resolution. Quantification of the sample's composition is difficult due to the variation in the ion yield of an element contained in different matrices (matrix effect). This is especially challenging for multicomponent materials.

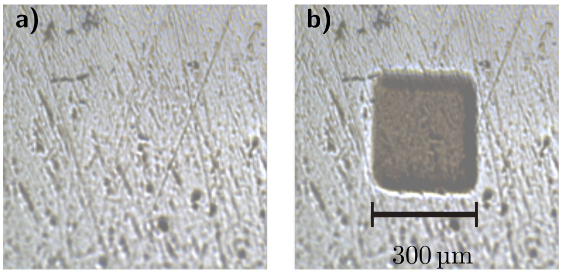

Figure 5.4.: Image of plasma-exposed surface of D120M3-WCrY a) prior to and b) with sputtered crater with a size of approximately 300 µm × 300 µm.

Samples used in this work are given to SIMS analysis before and after plasma exposure. The analysis is carried out inside the sputtered region, approximately in the middle of a sample as shown in Figure 3.3. On average the SIMS analysis extends up to a depth in the order of 1 µm into the bulk. Based on the enhanced sensitivity for metals, an O_2^- ion beam at an energy of 2 keV is used for the analysis presented in this work. Differences in the sensitivity of detecting W, Cr and Y can be seen when looking at Figure 5.5. This figure shows the as-measured signals before and after plasma exposure of sample D120P2-WCrY1 (see Section 6.1). It becomes evident that it is very difficult to infer plasma-induced changes when displaying the as-measured signals all in one graph (on a log-scale). For this reason and since no calibration was available, the as-measured intensities were normalised to be one in the bulk, at the largest analysed depth. Implicitly using this normalisation it is assumed that there is no change in the secondary ion production cross sections during the analysis. The bulk signal intensity is the average of the last 10 obtained data points. The top graph in Figure 5.6 shows the bulk-normalised W, Cr and Y intensities at full scale. Since changes induced by low-energy plasmas are expected mainly at the surface, the first 100 nm below the surface are zoomed in on for analysis. This is shown in the bottom graph of Figure 5.6. The above-described procedure is followed for all SIMS analyses presented in this work. Only a qualitative conclusion about the individual signal evolution towards the surface and not a comparison of the intensity of different elements is possible due to the normalisation. Furthermore, one can see that there are instabilities of the analysis ion current

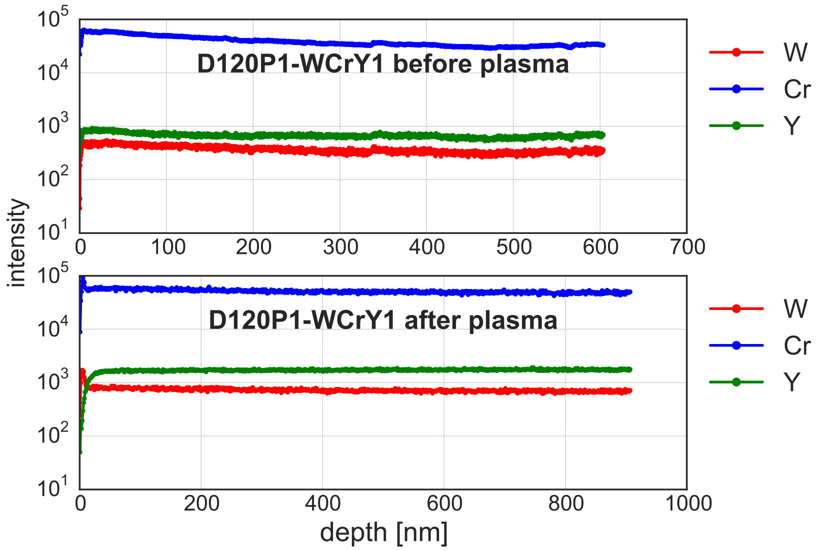

Figure 5.5.: As-measured SIMS-signals for sample D120P2-WCrY1 before (top) and after (bottom) plasma exposure.

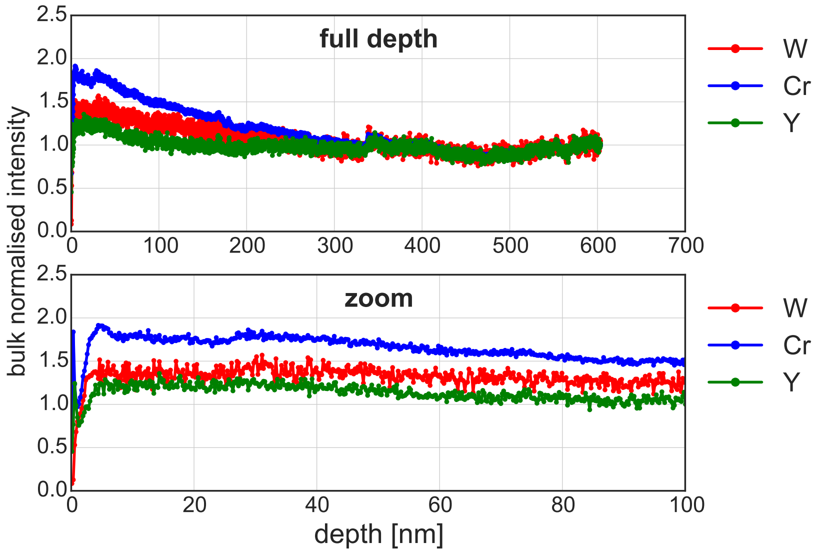

Figure 5.6.: Bulk-normalised SIMS-signals for sample D120P2-WCrY1 before plasma at full scale (top) and zoomed onto the first 100 nm below the surface.

impacting all measured intensities, for instance at a depth of about 350 nm in the top graph of Figures 5.5 and 5.6.

5.1.8. Surface profilometry and surface roughness

Characteristic surface parameters such as the surface roughness, waviness, step heights or deposited film thickness can be inferred by measuring a solid's surface with a surface profilometer [86]. For this thesis a Dektak 6M Stylus Profilometer from Veeco is employed. A measurement is carried out by means of contacting and scanning a sharp stylus across the surface in a line scan. Depending on the surface tip diameter, steps with a size of below 100 Å and roughness in the sub-nanometer range can be measured [87]. During the measurement procedure the diamond-tipped stylus gets displaced as it is mechanically drawn across the surface. During this process a set force is applied by the stylus onto the surface. Selecting a force in the range from 1 mg to 15 mg allows profiling of soft or hard surfaces. The stylus is connected to a displacement sensor, a Linear Variable Differential Transformer (LVDT). Surface variations cause the stylus to be translated vertically, which is translated into electrical signals by the LVDT. Signals are then digitalised and saved as height versus scanning length data on the connected computer. For this thesis the arithmetic average height R_a is used to parametrise the surface roughness. Is is defined as the sum of absolute deviations of each measured height value $|y_i|$ from the mean line over the sampling length:

$$R_a = \frac{1}{n}\sum_{i=1}^{n}|y_i| \tag{5.7}$$

In order to separate the waviness or non-planarity of the surface from the roughness of the surface profile, linear fitting and discrete Fourier transformation are applied before R_a is calculated. Waviness is a wider surface texture superimposed on the surface roughness and usually originates from the sample machining process. Slopes on the sample surface can for example be created during the grinding process resulting in an overall tilt of the line scan or the addition of waves. An overall tilt can be compensated by subtracting a linear slope from the line scan. For compensating waves, a discrete Fourier transformation is applied: while roughness corresponds to signals of higher frequency when Fourier-transformed, the wider wave-like structures correspond to signals of low frequency. Thus a cut-off frequency can be defined to separate waviness from roughness. The appropriate cut-off frequency or wavelength depends on the application, i.e. the size of waviness structures induced during machining. Veeco recommends to set the cutoff wavelength to be 1/5 of the scan length for the Dektak6M [87]. For roughness calculations in this work the cut-off frequency is adapted to the sample preparation procedure. The procedure for inferring a sample's surface roughness is described in the following paragraphs.

Several line scans with different orientations are carried out in the analysis region of the sample (see Figure 3.3). For each line scan the following procedure, here as an example shown for sample D120P2-WCrY3 (see Section 6.1) before plasma exposure, is applied to infer the average arithmetic height R_a: first a linear fit is carried out to remove tilting of the surface profile (see left side of Figure 5.8). Following this, the roughness is separated from the waviness of the surface profile. Every non-linear signal can be described as a sum of periodic sine and cosine signals of varying frequencies, amplitudes and phases. Thus, by transforming the surface profile from the spatial to the frequency domain using the Fourier transform, one can identify amplitude and phase of these signals. This enables us to filter certain wavelength ranges before transforming back to the spatial domain. First the discrete fast Fourier transform (DFT) of a real sequence implemented in the python [88] module scipy as scipy.fftpack.rfft [89] is used to transfer the measured and linear-fitted signal of finite duration to the frequency domain. The obtained frequency spectrum is displayed on the upper right side in Figure 5.9. For filtering the wavelengths ascribed to the waviness of the signal a cut-off frequency below which values of the Fourier transformed signal (rfft(y)) are set to zero is defined. This aims at excluding surface features significantly bigger than those induced by the grinding procedure. Scratches induced by grinding are assumed to be approximately of the size of a SiC particle d_{SiC} (see Section 3.3). Since the surface wavelength λ is equal to $1/f$, with f being the spatial frequency, the cut-off frequency f_c is defined as the inverse of the cut-off wavelength λ_c.

$$(1/\lambda_c =) f_c = 1/4 \cdot d_{SiC}\ [1/\mu\text{m}] \tag{5.8}$$

The filtered signal in the frequency domain is displayed in the lower right corner of Figure 5.9. For the SiC paper mostly used as the last step of sample preparation, P1200, the grinding paper particle size is $d_{SiC} = 15.3\,\mu\text{m}$ and the cut-off frequency corresponds to $2 \times 10^{-2}\,\mu\text{m}^{-1}$. After filtering the signal it is transformed back to the spatial domain using the inverse fast Fourier transform scipy.fftpack.irfft. The resulting filtered signal can be seen in the lower left corner of the same figure. Lastly another linear fit, fit2 displayed in the upper right image of Figure 5.8, is carried out before R_a is calculated according to Equation (5.7). This procedure is carried out for each line scan resulting in mean value and standard deviation of R_a for one sample. The result for D120P2-WCrY3 before plasma exposure is shown in Figure 5.7.

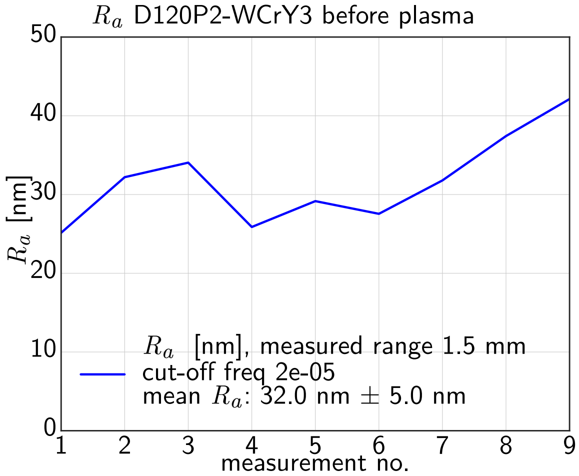

Figure 5.7.: Distribution of roughness R_a values measured on D120P2-WCrY3 before plasma.

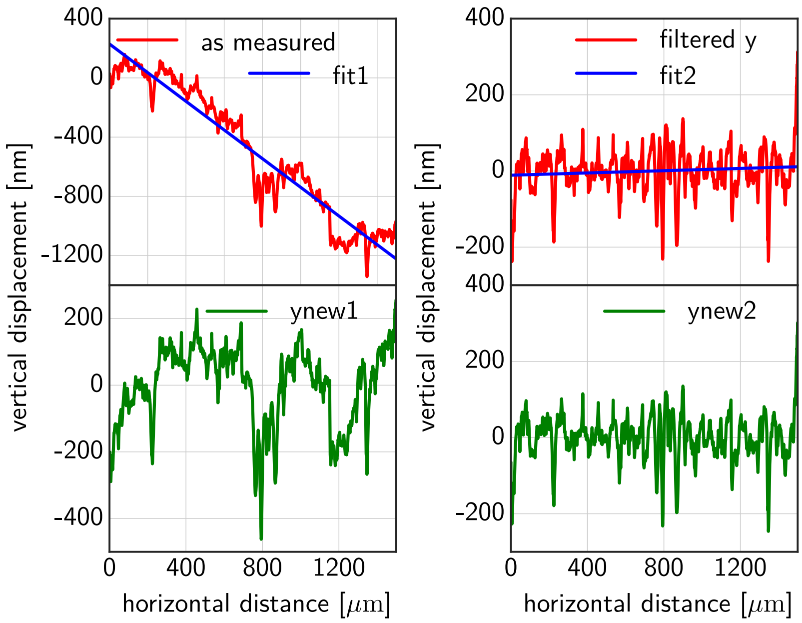

Figure 5.8.: Surface roughness profile before and after first linear fit on the left side and before and after second linear fit (performed after fft-filtering) on the right side.

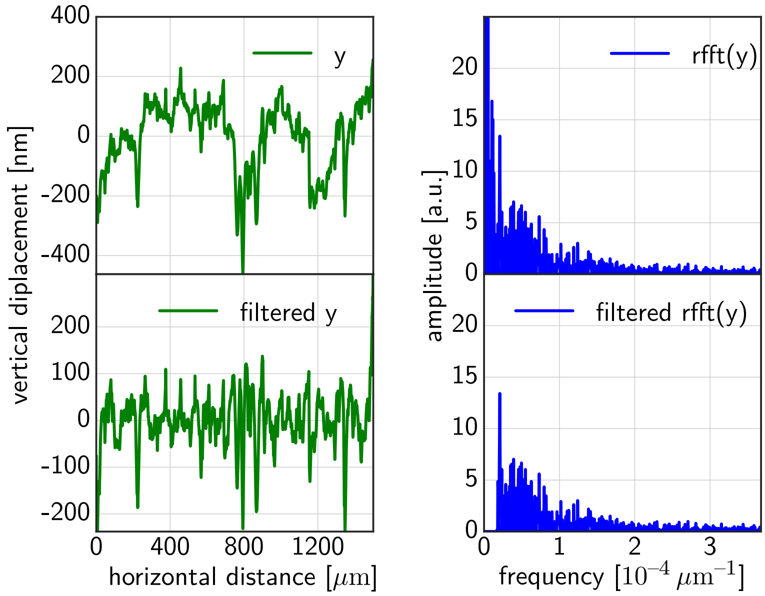

Figure 5.9.: Surface roughness profile before and after fft-filtering on the left side, and the respective signals in the frequency domain on the right side.

5.1.9. Thermogravimetric analyser

The Thermogravimetric Analyser (TGA) TAG-16/18 from SETARAM is the setup used for evaluating the oxidation performance of samples. This analyser is built as a dual furnace, one furnace containing the investigated sample and the other containing an inert product with the same volume as the sample to counteract buoyancy effects. The temperature and the atmosphere inside the furnace can be controlled. Sample and inert product are hung into the furnace tubes using platinum wires, both are shown in Figure 5.10. The oxidation rate of a sample is determined by measuring the mass increase, as oxygen from the atmosphere reacts with the sample (see Section 3.2). Oxidation experiments presented in this work took place at 1273 K in an atmosphere containing 80 vol% Ar and 20 vol% O at 1 bar. Under steady state conditions, i.e. once the temperature at which the oxidation shall take place is reached, the drift in the mass measurements amounts to only 0.1 µg h^{-1}. The temperature variation can be up to 4 K. For the tubes used in this setup with a diameter of 2.2 cm, the laminar gas flow is 10 ml min^{-1}. While the heating rate during experiments is approximately 10 K min^{-1}, the reactive gas O_2 is only fed into the furnace after the desired experimental temperature has been reached. During cool down of the furnace at a rate of 30 K min^{-1}, it is flushed with Ar at a flow rate of 100 ml min^{-1}. Details on the oxidation mechanism and measuring oxidation rates are given in Chapter 3. More details on the setup can be found in [43].

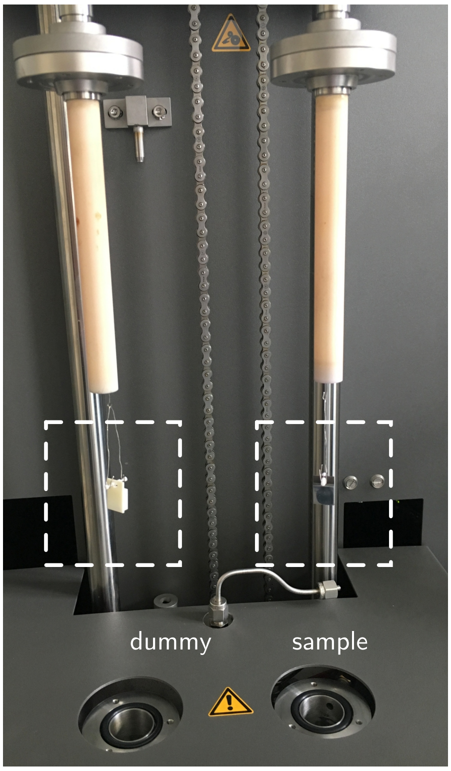

Figure 5.10.: Picture of the inert product and the sample installed in the TGA.

5.1.10. X-ray Photoelectron Spectroscopy (XPS)

One of the most commonly used electron spectroscopies is X-ray Photoelectron Spectroscopy (XPS). XPS is used to define the elemental and chemical composition within the first 10 nm beneath a solid's surface. In [90] the technique's principles are described in detail, a short summary is given in the following paragraph.

The basis for the XPS analysis is the emission of photoelectrons (photoemission) from the core levels of atoms of the probed sample's surface. For this purpose an X-ray beam with a discrete incident energy $h\nu$ (see Equation (5.9)) is directed onto the sample. The process of photoemission can be divided into three steps: firstly, the X-ray photons excite the core electrons for which they need to overcome the electron's binding energy E_b(1. photoexcitation). Secondly, the excited electrons, called photoelectrons, are transported to the sample's surface (2. transport to the surface) and thirdly, given their energy is sufficient to escape the sample, the photoelectrons leave the solid into the vacuum (3. transmission) and can subsequently be detected. The minimum energy required for an electron to escape the solid's surface is represented by the work function Φ_w. As the sample and the analyser of the XPS setup are electrically connected, in place of Φ_w the analyser work function Φ_A, i.e. the analyser's potential, needs to be overcome by the electrons. The remaining kinetic energy E_{kin} (w.r.t. the vacuum level of the analyser) of the detected photoelectrons is then measured. Equation (5.9) is the principal formula used for XPS analysis:

$$E_{kin} = h\nu - E_b - \Phi_A \tag{5.9}$$

This kinetic energy E_{kin} is discrete since the binding energy E_b, which depends on the specific element, the analyser's work function Φ_A and the X-ray beam energy are discrete values. Consequently, the elements emitting the photoelectrons can be identified by measuring E_{kin} of the detected photoelectrons. Using XPS, all elements from lithium (Li) to uranium (U) can be identified and quantified, given they exist at $> 0.05\,\mathrm{at\%}$ within the sampled volume.

H and He are not detectable due to their low photoelectron cross sections. Additionally, H does not have core electrons, the electrons of H atoms are valence electrons which participate in chemical bonding. Binding energies of valence electrons change with the chemical environment, they are not discrete as is the case for core electrons. This is why any H signal overlaps with signals from excitation of other surface atoms and it is not possible to distinguish between valence electrons of the H atom and those of other elements [91].

X-rays can penetrate micrometres below the surface. The information depth of the XPS signal is limited by the depth from which the photoelectrons can escape before losing a too large fraction of their energy. The attenuation function of the intensity $I(z)$ emitted from a depth z follows in a first approximation an exponential decay according to Equation (5.10).

$$I(z) = I(z=0)e^{-\frac{z}{\lambda cos\theta}}, \tag{5.10}$$

with the emission angle θ to the surface normal and the attenuation length λ. In general, the attenuation length is about 10 % less than the inelastic mean free path of the photoelectrons λ_{imfp} [92] as it includes also elastic scattering. Some authors, however, do not make a clear distinction between λ and λ_{imfp}. At a sampling depth of $z = 3\lambda$, 95 % of the photoemission intensity is still detected for emission normal to the target surface. [93] uses a value of about 2 nm for λ_{imfp} in W (W $4f_{7/2}$ with the peaks of W $4f_{7/2}$ and W $4f_{5/2}$ at the biding energies of 31.3 eV and 33.4 eV, respectively), hence $3\lambda_{imfp}$ corresponds to a depth of about 6 nm. Given the varying surface composition of the analysed WCrY samples (e.g. due to plasma exposure or heating) and the fact that λ is generally less than λ_{imfp}, an estimate of $z = 5\,\mathrm{nm}$ is used for the XPS-sampled depth in this work.

XPS analysis for this thesis was carried out by two different XPS devices: on the one hand a PREVAC XPS setup equipped with a monochromatic aluminium (Al) K_α X-ray source at an energy of 1.4867 keV was used for experiments investigating the temperature dependence of the surface composition of smart alloy samples (Chapter 8). On the other hand a Phi5000 VersaProbe II device from ULVAC-Phi Inc. USA with a monochromatic X-ray Al K_α source was used for depth-profiling in Section 6.1 and Chapter 7. Information on the depth-resolved composition is for both devices obtained with the help of an Ar ion sputter beam at 1 kV. The effect of preferential sputtering of the alloy due to the Ar ion beam is discussed in Section 6.1.2. Whereas the sputtered area amounts to 5 mm × 5 mm and the analysis spot measures 1.6 mm × 5 mm for analysis with the PREVAC device, the sputtered area is 3 mm × 3 mm and the diameter of the circular analysis spot is 200 µm for the ULVAC device. The base pressure in the respective sampling chambers of the XPS devices is of the order of 1×10^{-9} mbar.

5.2. SDTrimSP Modelling

5.2.1. Modelling particle-solid interactions

A variety of different codes exist for modelling particle-solid interactions. Each of them relies on a different ansatz for the treatment of the potentials between the interacting particles. There is a multiscale modelling approach for plasma-surface interactions. One chooses a model based on the desired material resolution, down to the atomic level or coarser on micrometre-scale. Further, the time scale of the material evolution is chosen depending on the available computational resources. If in-depth understanding of e.g. the ab-initio electronic structure is desired, it will not be possible to get a model representing a couple of seconds or not even microseconds, rather just pico- up to nanoseconds.

As already stated in Chapter 2, the Binary Collision Approximation (BCA) model is used for successively treating independent binary collisions between atoms. There are several codes which use this model for considering amorphous targets, i.e. the atoms in the target are randomly positioned and do not follow a certain order. These codes are for example TRIM, TriDyn, or SDTrimSP. MARLOWE instead is a code which also relies on the BCA model but can simulate atomic collisions in crystalline targets, hence the atoms can be arranged in a specific order. All of the aforementioned codes are Monte Carlo methods, meaning that they rely on repeated random sampling to obtain numerical results. In that way, a large number of particles, which means high fluences of incoming projectiles, can be considered.

In contrast to this, the group of Molecular Dynamics (MD) codes does not rely on random sampling. For this approach the forces from all atoms on each other in a specified surrounding are taken into account to numerically solve Newton's equation of motion on an atomistic model. This results in long computational times and therefore a problem with good statistics [31]. As an advantage one has the possibility to calculate emission of molecules and clusters. Moreover, according to [29] classical dynamics calculations are more appropriate in the low eV range. It is stated that the binary collision model fails starting at several tens of eV. The failure becomes serious in the eV range where

many-body effects and chemical bonds become important.
Another code belonging to the Monte Carlo group is ERO. ERO does not only treat the pure ion-solid interaction, but also part of the transport of the emitted particles into the plasma. Unlike e.g. TRIM, ERO considers re-deposition of material. Thus one can estimate the net erosion, which can be directly compared to the experimental mass loss values. Other codes are only able to calculate the gross erosion so that direct comparison to the experiment often is not possible if re-deposition plays a role.
In this work SDTrimSP modelling is carried out in addition to plasma exposures where re-deposition is negligible. This code allows investigating the impact of the plasma ion irradiation on the near-surface composition evolution of the multicomponent WCrY targets.

5.2.2. Model description

The Monte-Carlo code SDTrimSP [94] makes use of the BCA to simulate ion irradiation of amorphous targets. The underlying physics is described in [29]. In the dynamic version, a one-dimensional target made up of dynamically thickening or shrinking layers is employed. The ion projectiles successively shot into the target create recoils which in turn lead to reordering of atoms. Eventually, sputtering of atoms in the surface layer is caused if the energy transferred to these atoms is greater than the surface binding energy and the transferred momentum is pointing in the outward target direction. Concentration gradients are induced in case of preferential sputtering for mixed materials. This means that the sputter yield, the number of atoms sputtered per incoming projectile, for one atomic species is higher than the yield of the other atomic species of the mixed material. With diffusion added to the model, the depleted element is transported towards the surface to counteract the build-up of these gradients. Using the dynamic version enables reproducing the evolution of the alloy's near-surface composition during ion bombardment. Since a one-dimensional target model is used, the specific microstructure of the WCrY material is not reproduced, instead an amorphous target structure with a composition of 67.9 at% W - 31.1 at% Cr - 1.0 at% Y is assumed. The target is initially subdivided into equidistant 2.5 Å thick layers of the same composition as shown in Figure 5.11. In a calculation step, a certain number of projectile ions, i.e. a certain fluence, is shot onto the target and their impact is calculated. After each such fluence step the target composition is updated according to the change in the number of the respective atomic species in each layer. If the composition is changed due to implantation or reordering of the recoils, this, in turn, causes a change in the atomic density. Implantation and recoils further result in an increase or, in case of sputtering, a decrease of the layer thickness. Summing over the changes in thickness of all layers leads to growth or shrinkage of the target. If erosion dominates the summation results in shrinkage, i.e. the surface recesses. For the calculations, normal incidence of the bombarding ions is assumed. The samples' surface roughness of about 30 nm cannot be reproduced with the one-dimensional model. This should not have a large impact on the erosion results for the case of normal incidence irradiation.
In SDTrimSP, thermal diffusion between adjacent target layers can be included into the

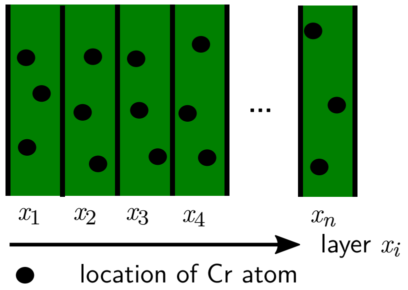

Figure 5.11.: Model target structure with slabs of initially the same composition and width.

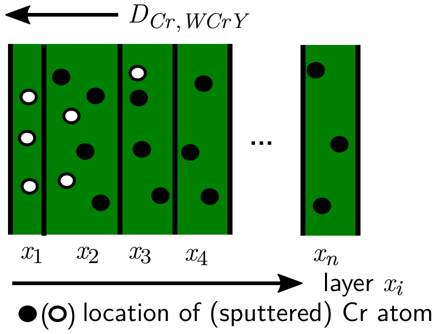

Figure 5.12.: Model target structure where projectile ions shot on the target lead to Cr concentration gradients between slabs and therefore induce Cr diffusion.

model. For this purpose the temperature-dependent diffusion coefficients must be specified. Generally, diffusion is induced by concentration gradients of an element within a material (Figure 5.12). This is expressed by Equation (5.11), which depicts the evolution of the element(i)-specific concentration c at layer x. The diffusion coefficient in Equation (5.12) increases exponentially with temperature T (see also Chapter 2). Diffusive transport across the surface boundary is set to zero, surface atoms can only leave the target by sputtering. However, if atoms of the first layers get sputtered, the induced concentration gradient initiates diffusion from subsurface layers. The physical sputtering process within the model depends solely on the number of ions arriving at the target and not on the time as collisions are treated successively. In contrast, diffusion is a time-dependent process. Therefore, the ion flux, i.e. the number of ions arriving at the target per second, enforces a time dependence. The time for a fluence step results from Equation (5.13), this time is then used to calculate a diffusion step. Calculated recoils result in changes of the concentrations c of the elements i within each layer x. Based on this concentration change, the overall layer-specific diffusion coefficient $\eta(x,i)$ (see Equation (5.14)) is calculated. This is done by summing over the concentrations and diffusion coefficients of element i within material j for all elements j.

$$\frac{\partial c(i)}{\partial t} = -\frac{\partial(\eta(x,i)\cdot\frac{\partial c(x,i)}{\partial x})}{\partial x} \tag{5.11}$$

$$D(i,j) \;=\; D_0(i,j)\cdot\exp(-\frac{Q_a(i,j)}{k_B T}) \tag{5.12}$$

$$\Delta t = \frac{\Delta \mathit{fluence}\ [\mathrm{m}^{-2}]}{\mathit{flux}\ [\mathrm{m}^{-2}\mathrm{s}^{-1}]} \tag{5.13}$$

$$\eta(x,i) = \sum^{j} c(x,j)\cdot D(i,j) \tag{5.14}$$

According to Equation (5.12), two material-specific parameters have to be specified to assign a diffusion coefficient $D(i,j)$ for element i in element j: the activation energy Q_a and the diffusion constant $D_0(i,j)$. Both are not known for the alloy WCrY. In order to vary only $D_0(i,j)$ for the simulations, Q_a (see [50] for detailed explanation) is not specified but instead set to be zero so that the exponential function equals one. Therefore, the simulations are only valid for the sample temperature present in the experiment. In that way a parameter scan for $D_0(i,j)$ can be performed. For the simple physical sputtering process, temperature is not taken into account within the BCA. The implementation of the algorithm solving the diffusion equation and further details are described in [51].

Lighter alloy elements are preferentially sputtered, which leads to a continuous change of the surface stoichiometry during ion irradiation until a steady state is reached [95], as explained in Section 2.2. For this state, the ratio of the sputter yields is stoichiometric [31]. This means for dynamical SDTrimSP runs, partial sputter yields converge with increasing fluence. In order to save computational time, simulations were carried out up to a certain fluence and then extrapolated to the experimental fluence. Simulations in this work calculate up to 1×10^{25} ions/m^2, which corresponds for instance to 10 % of the experimental fluence of D220P (see Chapter 7), assuming steady state has approximately been reached at this point. The last 10 values of this simulation are then used to linearly extrapolate the surface recession: the slope of a line intersecting these last 10 values is assumed to be constant until 100 % of the experimental fluence (see Section 6.1.3).

The mass loss is obtained from the simulation output by integration of the partial yield curves. Mass loss values were extrapolated using the partial sputter yields of W, Cr and Y at the last fluence step.

6. Plasma exposure at ion energies below the W sputter threshold

Particle and heat loads with different energy spectra and synergistic effects of both affect the material properties of PFCs of a fusion device. The fuel is composed of the hydrogen isotopes D and T. For safety reasons, solely D is mostly used in fusion-relevant experiments to simulate the fuel. In contrast to the thermal particle energy distribution in future fusion devices such as DEMO, the ions in the linear devices such as PSI-2 and Magnum-PSI (see Chapter 4 for detailed description) are close to mono-energetic during plasma exposure, as determined by the applied bias voltage. Thus, a single incident ion energy is chosen for an experiment. As according to [29] the sputter threshold for D on W is around 220 eV, no W sputtering is expected in pure D plasma for the expected DEMO ion energies of around 100 eV at the plasma edge. However, minute amounts of residual oxygen and other impurities are present in the vacuum vessel of a fusion reactor and also in linear devices. The sputter threshold for O on W of 44 eV [96] is considerably lower than that for D on W. Therefore, sputtering will be caused be residual oxygen. To see the effect of particle irradiation at energies mainly below the sputter threshold, pure D plasma at an incident ion energy of 120 eV was chosen for the exposures. Since wall temperatures for the DEMO first wall should not be much higher than around 900 K (see Section 2.1.3), the sample temperature was chosen to be in this range during the experiments. The exposures took place in PSI-2 at fluxes in the order of 1×10^{21} ions/(m^{2}s) and fluences in the order of 1×10^{26} ions/m^2, while for exposures in Magnum-PSI fluxes were in the order of 1×10^{23} ions/(m^{2}s) and fluences in the order of 1×10^{26} ions/m^2 to 1×10^{27} ions/m^2. Assuming an average ion flux of about 1×10^{21} ions/(m^{2}s) for the DEMO first wall [28], PSI-2 fluxes are DEMO-relevant fluxes. Consequently, fluences reached in PSI-2 correspond to a couple of hours of operation in DEMO whereas fluences in Magnum-PSI correspond to several days to weeks of operation.

This chapter starts with the presentation of the PSI-2 experimental results. Experimental details are given before presenting the experimental as well as SDTrimSP modelling results. This section is followed by a section on the experimental details and results of the exposures in Magnum-PSI. In both sections the results are discussed alongside with their presentation. The chapter is concluded with a summary.

6.1. Exposure of WCrY and reference W in PSI-2

6.1.1. Experimental details

In PSI-2, two exposures at ion energies below the W sputter threshold were carried out, they are called D120P1 and D120P2. Pure D was used as working gas for the exposures, the residual oxygen content is assumed to be around 0.2 % to 0.3 % (see Section 4.1.1). The electron temperature T_e was around 8 eV for the conducted experiments, while the plasma electron density n_e was of the order of $3 \times 10^{17}\,\mathrm{m}^{-3}$. Further experimental parameters are given in Table 6.2.

Samples used for the two experiments, as well as all other experiments presented in this work, are manufactured and prepared as described in Section 3.3. Magnetron-sputtering was used for one pure W sample in D120P1, D120P1-W4, to coat half of the surface with a WCrY layer of about 4 µm thickness (see Figure 6.11). The composition of this layer is about 89 wt% W - 10 wt% Cr - 1 wt% Y. Due to having a pure W layer directly next to a WCrY layer, it is possible to study Cr sputtering and re-deposition in more detail. All samples used for D120P1 and D120P2 are listed in Table 6.1. WCrY and reference W samples are exposed simultaneously on the same sample holder as described in Chapter 4.1.1.

6.1.2. Experimental results and discussion

Erosion

A critical parameter for the lifetime of PFC is the material's erosion. Two different measurements are performed to compare the erosion performance of the WCrY samples to that of the W reference samples. The samples are weighed before and after plasma, as

sample name	experiment	material	density	further comments
D120P1-W1	D120P1	W	> 98.0 %	
D120P1-W2		W	> 98.0 %	
D120P1-W3		W	> 98.0 %	
D120P1-W4		W	> 98.0 %	half of the sample coated with WCrY
D120P1-WCrY1		WCrY	98.7 %	
D120P1-WCrY2		WCrY	98.4 %	
D120P1-WCrY3		WCrY	98.6 %	
D120P2-W1	D120P2	W	> 98.0 %	
D120P2-W2		W	> 98.0 %	
D120P2-W3		W	> 98.0 %	
D120P2-WCrY1		WCrY	98.5 %	
D120P2-WCrY2		WCrY	98.4 %	

Table 6.1.: Samples used for plasma exposures in pure D with the main plasma ion species under the W sputtering threshold. The density as determined using the Archimedes principle (see Section 5.1.5) is given in % of the theoretical density.

experiment	plasma[a]	ion energy [eV]	ion flux [ions/m^{2}s]	ion fluence [ions/m^2]	sample temperature [K]
D120P1	1 D	120	2.7×10^{21}	1.0×10^{26}	890 - 970
D120P2	1 D	120	4.3×10^{21}	1.7×10^{26}	890 - 970

[a]: neglecting residual impurities such as oxygen

Table 6.2.: Parameters of plasma exposures in PSI-2 with main plasma ion energies below the W sputter threshold. The plasma ion composition is given in fractions of the total plasma ions neglecting possible impurities such as oxygen.

described in Section 5.1.5, and the mass loss Δm is obtained. Additionally, the FIB-SEM device is used to infer the surface recession d_e as described in Section 5.1.2. Average results for W and WCrY samples exposed in D120P1 and D120P2 are displayed in Figure 6.1. The results are not normalised to a single fluence. In case of preferential sputtering after irradiation with sufficiently high fluence, a steady state is reached and sputter yields converge to stable values, as described in Section 2.2. According to SDTrimSP simulations presented in Section 6.1.3, this state is already reached approximately at a fluence of 0.2×10^{25} ions/m^2. From then on erosion of WCrY should be linear assuming only physical sputtering. In case thermal diffusion plays a role, steady state is reached at a later stage (Sections 6.1.3 and 7.3). Erosion results are not normalised to prevent excluding these effects when comparing the experiments performed at different fluences. Unfortunately, no mass loss results were obtained for samples exposed in D120P1. In this experiment the samples (partly) stuck to the graphite foil used for thermal insulation so that the sample weights measured after plasma exposure were falsified. This is why, as already mentioned in Section 4.1.1, in all subsequent experiments a piece of W foil was placed between sample and graphite foil so that sticking could be avoided. Further, the error bars of the mass loss results for D120P2 are increased since unfortunately measurements of the sample weight and the density, using the Archimedes principle and immersing the sample into ethanol, were carried out simultaneously. Consequently, ethanol evaporating from the sample surface during the weight measurements led to variations in the sample weight.

Since the plasma-facing area amounts to $1\,\mathrm{cm}^2$ for all samples, it is relatively straightforward to directly compare the values obtained for the surface recession d_e, i.e. the thickness of the eroded layer, for W and WCrY samples. In the top graph it gets evident that in terms of surface recession the erosion of W and WCrY is similar. When comparing the mass loss results for W and WCrY, one has to take into account the different densities of the two materials. While for pure W the material density (ρ_W) is $19.25\,\mathrm{g\,cm^{-3}}$, it amounts to only $15.87\,\mathrm{g\,cm^{-3}}$ (ρ_{WCrY}) for the WCrY smart alloys. For a fixed volume of eroded material at 100 % of the theoretical density and using the relation $m = \rho V$, Equation (6.1) can be used to compare the mass losses of WCrY and W samples.

$$\frac{\Delta m_{WCrY}}{\Delta m_W} = \frac{\rho_{WCrY}}{\rho_W} \approx 0.82. \tag{6.1}$$

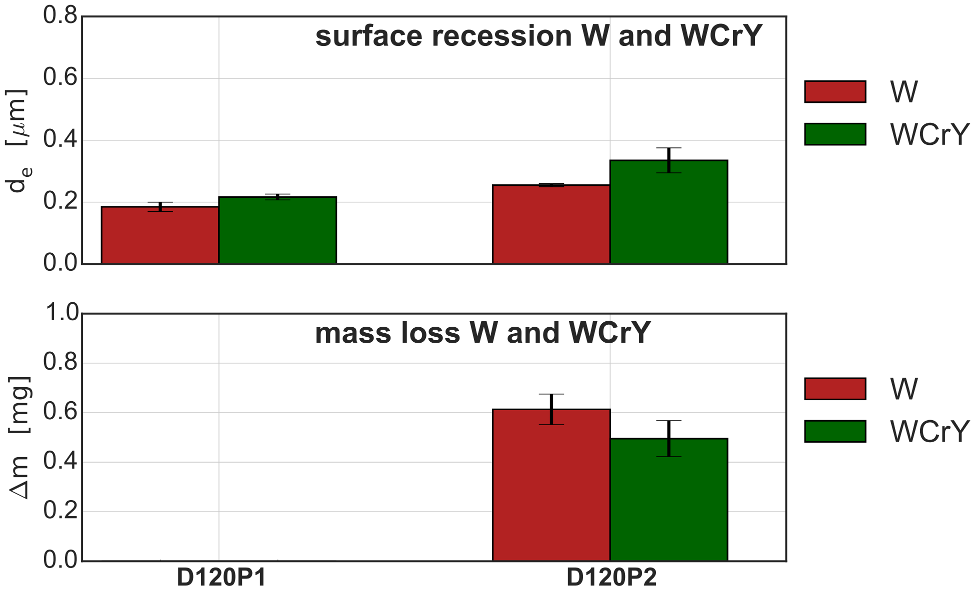

Figure 6.1.: Measured average surface recession d_e (top graph) and mass loss Δm (bottom graph) of W and WCrY samples exposed in D120P1 and D120P2. Measurement procedures are described in Sections 5.1.5 and 5.1.2.

Hence at a fixed volume, the mass loss is reduced for WCrY due to the alloy's lower density. The theoretical mass ratio assuming the same volume loss, which corresponds to approximately the same number of sputtered particles per material, is 0.82. Making this comparison is not possible for experiment D120P1 since no mass loss results are available. The ratio of mass losses in D120P2 gives $\Delta m_{WCrY}/\Delta m_W \approx 0.66 \pm 0.10$. Here one has to take into account the uncertainties introduced in the mass loss measurements as described above. Still, this value is slightly below the theoretical mass ratio of 0.82 and further supports the statement that, as seen for the surface recession results in both D120P1 and D120P2, erosion of WCrY is not increased against that of W during plasma exposure below W sputter threshold in PSI-2.

Spectroscopy measurements (see diagnostic description in Section 4.1.1) were taken during

D120P1 and D120P2, the line radiation of neutral W (WI) at 429.5 nm and neutral Cr (CrI) at 427.5 nm were monitored. Due to the low sputtering rates in a plasma consisting mainly of D at ion fluxes in the order of 1×10^{21} ions/(m^{2}s), the integration time is of the order of several tenths of seconds to minutes. Further, plasma parameters are adjusted at the beginning of the exposure so that no statement on the time evolution of the W and Cr sputtering behaviour can be made. In D120P1, at an integration time of 50 s, the detected signal was too low to be evaluated. In D120P2 the integration time was increased to 60 s, additionally the plasma ion flux is slightly higher compared to D120P1. Consequently in D120P2, starting from approximately half an hour after the exposure start and under steady plasma conditions, W and Cr sputtering could be detected. There was no significant change in the signal intensities, which is a sign of W and Cr sputtering till the end of the exposure.

Mass loss and surface recession measure the sample's net erosion during the exposure, possible re-deposition during the exposure cannot be inferred. The ionisation length λ_{ion} (see Section 2.2.2) serves as a good first approximation to evaluate the importance of re-deposition depending on the plasma conditions. Since $\lambda_{ion} = v/(\langle\sigma v\rangle_{ion} n_e)$, the velocity v of the sputtered particles, the ionisation probability $\langle\sigma v\rangle_{ion}$ and the plasma density n_e have to be assessed first. v can be inferred via $E = (1/2)mv^2$ from the energy distribution of the sputtered particles. The SDTrimSP code (see Section 5.2) was used to simulate the irradiation of a pure W target with $\mathrm{D} + 0.23\,\%\,\mathrm{O}$ ions at an energy of 120 eV at normal incidence. The resulting energy distribution summed over all exit angles (polar and azimuthal angle) is displayed in Figure 6.2. The polar angle runs from 0°, direction parallel to the surface, to 90°, direction normal to the surface, whereas the azimuthal angle runs from 0° to 180° describing a circle parallel to the surface. Figure 6.3 displays the resulting angular distribution summed over all energies. A mean kinetic energy of around 7.0 eV leads to an average velocity v of $2.7 \times 10^3\,\mathrm{m\,s^{-1}}$ for the sputtered W atoms, which is in agreement with experimentally found values for sputtered W in PSI-2 [97]. The polar exit angle shows a wide distribution with an average of approximately 50°, whereas the azimuthal angle distribution is homogeneous and shows no preferred direction. These findings agree well with ERO simulations for low energy W sputtering in PSI-2 [98]. The ionisation probability depends on the electron temperature T_e and is taken from [99]. At an electron temperature T_e of 8 eV, $\langle\sigma v\rangle_{ion}$ is indicated with $1.3 \times 10^{-13}\,\mathrm{m^3\,s^{-1}}$. Taking n_e to be $3 \times 10^{17}\,\mathrm{m^{-3}}$ yields $\lambda_{ion} \approx 1 \times 10^{-1}\,\mathrm{m}$ in PSI-2. Based on the angular distribution one can say that most of the sputtered atoms leave the target at an angle of 40° from the surface normal (corresponding to 50° from the direction parallel to the surface) and are ionised after a distance of $\lambda_{ion} \approx 1 \times 10^{-1}\,\mathrm{m}$ in the plasma. Since the peak width of the radial maxima in the PSI-2 plasma beam profile (see Figure 4.2) amounts to less than 2 cm, which is significantly less than λ_{ion}, ionisation of the sputtered atoms in the plasma in front of the target and therefore re-deposition can be neglected in a first approximation.

Elemental composition

The depth-resolved elemental composition of the WCrY samples is measured before and after plasma exposure using SIMS and XPS (see Sections 5.1.7 and 5.1.10 for the respective analysis descriptions). W samples are analysed by SIMS as well, mainly to check for the presence of impurities either due to sample preparation or due to the plasma impact. Additionally, EDX (see Section 5.1.1) surface analysis was carried out on a WCrY sample in D120P2. The main purpose of the elemental composition analysis of WCrY samples is to see changes in the subsurface profiles of W and the alloying elements Y and Cr, i.e. enrichment and depletion. First, the SIMS results will be presented. This is followed by the presentation of the results obtained with XPS and finally the EDX results.

The relative change of elemental composition of smart alloy samples D120P1-WCrY1 and D120P2-WCrY1 along the respective depths towards the surface (depth = 0 nm)

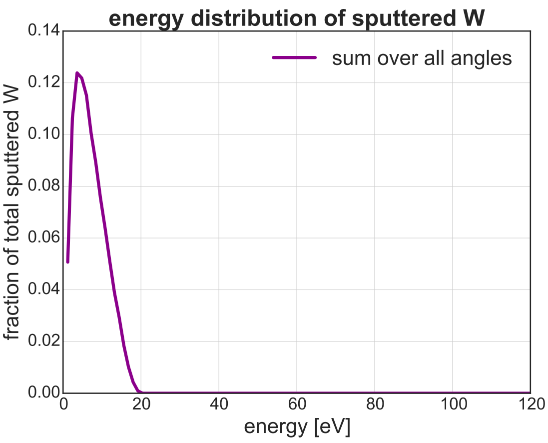

Figure 6.2.: Energy distribution of sputtered W summed over all angles (polar angle from 0° to 90° and azimuthal angle from 0° to 180°). The distribution is obtained by static SDTrimSP simulations for 99.77 % D + 0.23 % O ion irradiation at normal incidence on pure W target.

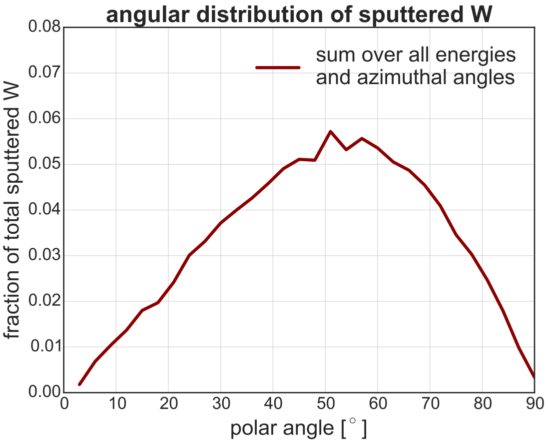

Figure 6.3.: Polar angular distribution of sputtered W summed over all azimuthal angles and energies (azimuthal angle from 0° to 180° and energy from 0 eV to 120 eV). The distribution is obtained by static SDTrimSP simulations for 99.77 % D + 0.23 % O ion irradiation at normal incidence on pure W target.

measured by SIMS and normalised according to the procedure described in Section 5.1.7 is shown in Figures 6.4 and 6.5. It is remarked that for the SIMS analysis after plasma exposure in D120P2 the new device described in Section 5.1.7 was used, which explains the improved signal-to-noise ratio. Again it is stressed that since no intensity calibration was carried out, only statements on changes of the signal evolution of a single element and not between the different elements within a graph can be made. In both figures the intensity of the Y signal is slightly increased towards the surface before plasma exposure. After plasma exposure a distinct depletion up to a depth of about 40 nm is evident. The intensity of the W signal measured in D120P1-WCrY1 after plasma increases towards the surface, starting also from a depth of around 40 nm, indicating enrichment of W. Furthermore, comparing the Cr intensity evolution before and after plasma for this sample, a shallow depletion is visible here, too. Whereas the Y signal intensity in D120P2-WCrY1 (Figure 6.5) behaves similarly to the one in D120P1-WCrY1, Cr and W show a contrary behaviour: at about 10 nm below the surface both W and Cr intensities peak. It is assumed that W and Cr intensities close to the surface do not result from the plasma impact on the samples, but are rather a result of sample storage on atmosphere and the analysis method: the measurement after plasma exposure for experiment D120P2 was performed not earlier than half a year after the experiment took place due to an upgrade of the SIMS device used for analysis. In contrast, all other post-plasma SIMS measurements were conducted two to three weeks after exposure. Oxidation of the sample surface affects the detection sensitivity as explained in Section 5.1.7. Y, in

contrast to W and Cr, is already oxidised during the metallurgical production process of the bulk WCrY samples. Therefore, it is suspected that Y is less affected by surface oxidation during the transport or storage on air before SIMS measurements take place. Another WCrY sample exposed in D120P2 was analysed by XPS. This XPS analysis supports the aforementioned assumption. Results are shown in the next paragraph.
Next, results of the sputter-XPS analysis will be shown. First the sputter-XPS analysis of an unexposed WCrY sample is shown on the left of Figure 6.6. Again, the elemental composition is plotted against the depth, starting from the surface at a depth of 0 nm. Unlike the SIMS analysis where the signals are normalised, here the concentration is

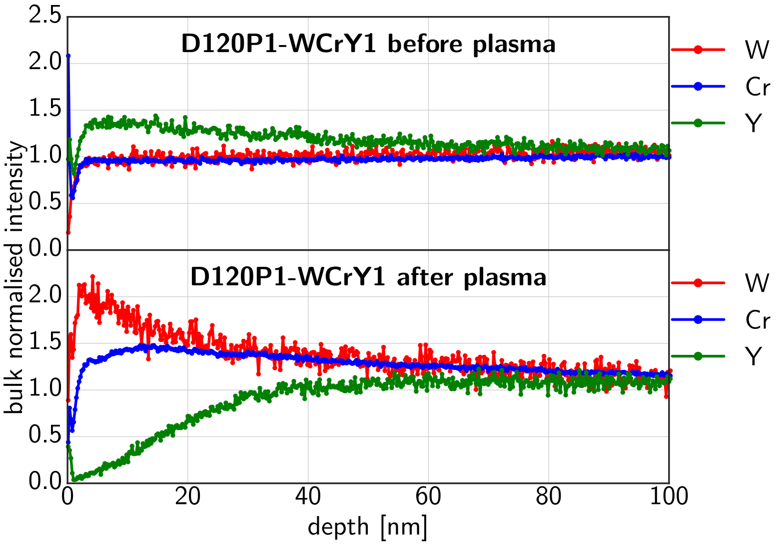

Figure 6.4.: SIMS analysis of sample D120P1-WCrY1

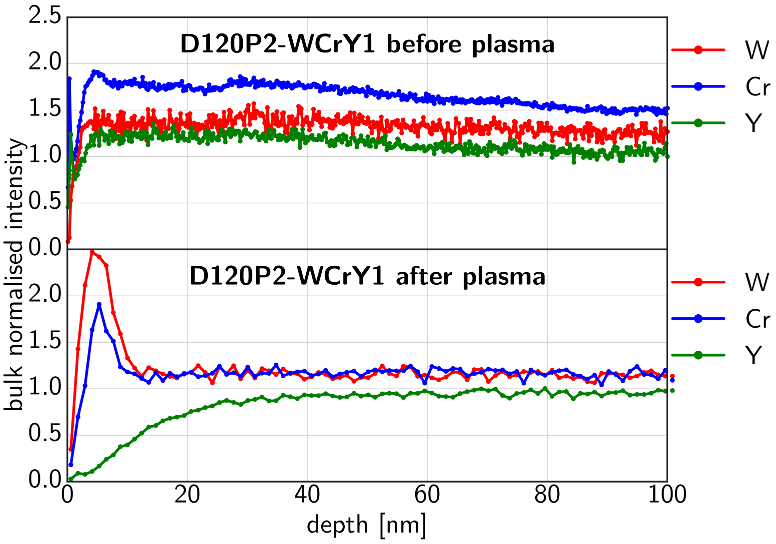

Figure 6.5.: SIMS analysis of sample D120P2-WCrY1

given in at%. The device-specific empirical relative error of the measured concentrations is 15 %. One should note that the measured concentrations are a combination of the effect of the Ar ion beam used for the sputter-XPS analysis and the actual alloy composition. Depth evolutions resulting from a dynamic SDTrimSP simulation of the 1 keV Ar irradiation of a WCrY target with a composition of 67.9 at% W - 31.1 at% Cr - 1.0 at% Y are displayed on the right side of Figure 6.6. Here it can be seen that after reaching a fluence of approximately 2×10^{20} ions/m^2, corresponding to an eroded layer of less than 5 nm thickness, steady state is reached. Before reaching this fluence, preferential sputtering by the Ar sputter beam during the XPS analysis is evident. After this point the surface concentration is stable with a W content of 85 at%, a Cr content of 15 at% and an Y content of 1 at%. This matches well with the surface concentrations found by sputter-XPS for the unexposed sample: here, at a depth of around 5 nm, the elemental concentrations converge to the stationary surface concentrations found by the simulation. The same trend is found for the exposed samples at a depth greater than 50 nm.

In Figure 6.7 sputter-XPS results of D120P1-WCrY1 and D120P2-WCrY2 after exposure are shown. Due to the low Y content of about 1 at% in the alloy, the detected Y concentration is just slightly above the noise level. Despite the fact that the absolute concentrations are affected by the Ar sputtering as explained above, W enrichment accompanied by Cr depletion extending to a depth of about 30 nm to 40 nm is clearly visible. Since according to SDTrimSP simulations in Figure 6.6 the surface concentrations are stable below a depth of 5 nm and no longer are changes induced by the Ar sputtering during the XPS analysis, these gradients of W and Cr concentrations are a result of the plasma exposure. Enrichment and depletion are visible for both samples. They are slightly more pronounced for D120P2-WCrY2, which has been exposed to a higher fluence at the same plasma conditions compared to D120P1-WCrY1. The XPS

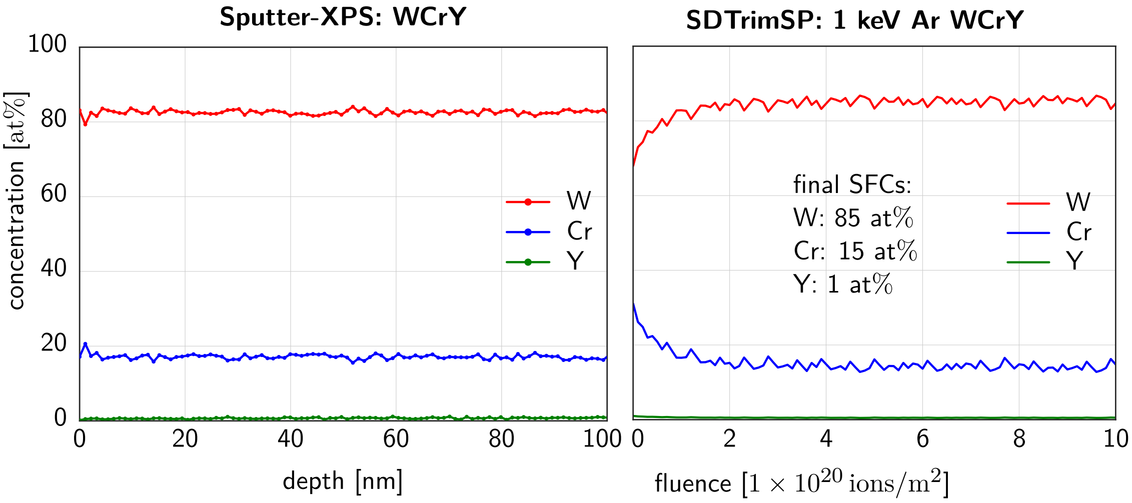

Figure 6.6.: Sputter-XPS analysis of unexposed WCrY (left) and SDTrimSP (see Section 5.2) analysis of WCrY under 1 keV Ar irradiation (right). After a fluence of 10×10^{20} ions/m^2 a depth of approximately 18.4 nm has been eroded in the simulation.

analysis of D120P2-WCrY2 supports the assumption that the increased W and Cr signals found by SIMS in the plasma-exposed samples in D120P2 are an artefact of the measurement and sample storage (see two previous pages).

Further insight into the depletion of alloying elements was obtained using EDX. Figure 6.8 is an EDX surface map of a region of sample D120P2-WCrY1 after plasma exposure. The probed depth for WCrY amounts to about 100 nm (see Section 5.1.1). As the size of the YO particles amounts to typically a few tenths of nm in the WCrY microstructure, the small black holes on the surface are assumed to be preferentially sputtered YO particles. Further, bigger holes are assumed to be caused by the superficial depletion of Cr. EDX results show Y and Cr beneath the small black hole and bigger crater, respectively. It is suspected that prior to preferential sputtering the hole and the crater were mainly filled with Y and Cr, respectively, which is why these EDX results support the assumptions of depletion of Y and Cr at the surface.

D retention of a WCrY sample and a W sample exposed in D120P1 and respectively in D120P2 was measured using NRA (see Section 5.1.6). As a result the measured D concentration is given in Table 6.3 for the subsurface layer extending from the surface to

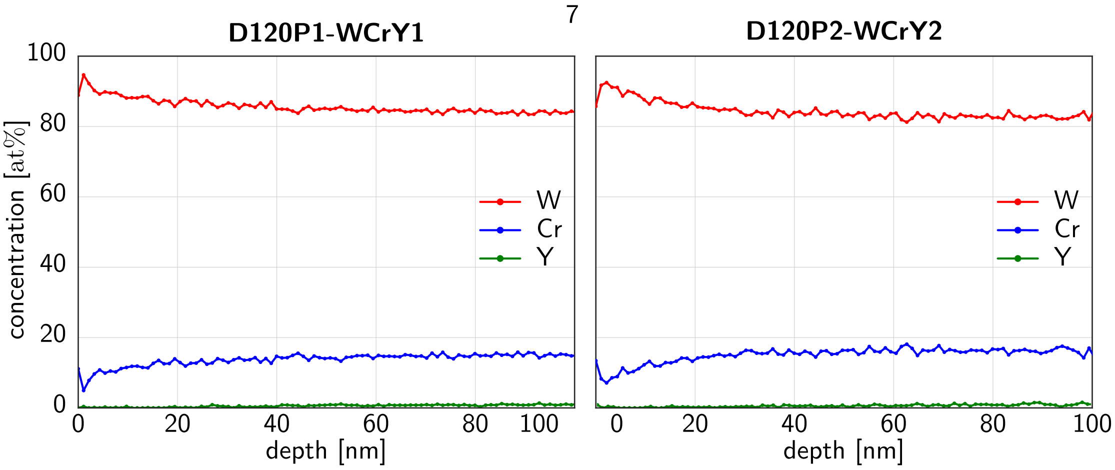

Figure 6.7.: Sputter-XPS analysis of samples D120P1-WCrY1 and D120P2-WCrY2.

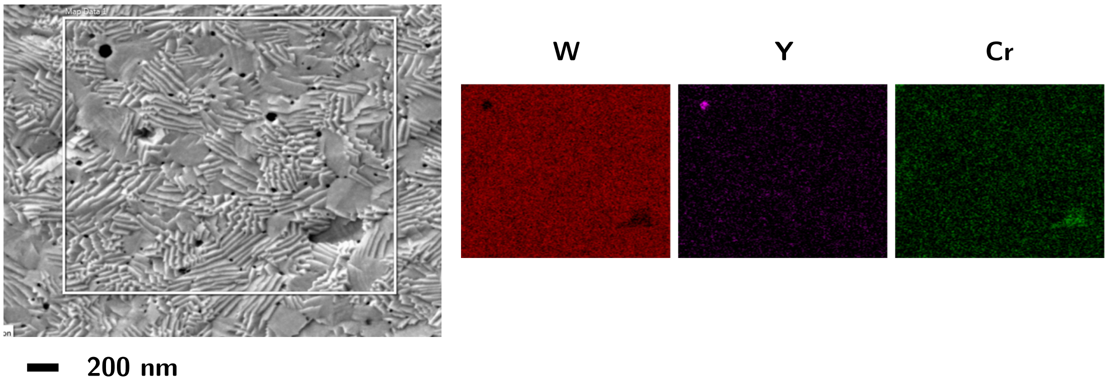

Figure 6.8.: EDX surface map of sample D120P2-WCrY1 plasma

experiment	sample	D concentration layer 1	D concentration layer 2
D120P1	D120P1-WCrY2	8×10^{-6}	6×10^{-6}
	D120P1-W3	2×10^{-6}	2×10^{-6}
D120P2	D120P2-WCrY2	4×10^{-6}	5×10^{-6}
	D120P2-W1	$<1 \times 10^{-6}$	$<1 \times 10^{-6}$

Table 6.3.: Retained D concentration in layer 1 (0 µm to 3 µm) and layer 2 (3 µm to 8 µm) of plasma-exposed samples in D220P1 and D120P2.

a depth of 3 µm (layer 1) and in the second layer extending from 3 µm to 8 µm (layer 2), respectively. Generally, all the detected D amounts are very close to the detection limit of 1×10^{-6}, which is to be expected since at the high sample temperatures of around 900 K D gasses out easily again and not much D is retained after the exposure [100]. In D120P1 retention in both layers is increased by a factor of 3 to 4 for WCrY in comparison to pure W. In D120P2 retention is increased for WCrY up to a factor of 5.

Chromium re-deposition

The positions of the EDX spectra on the coated and the uncoated half of D120P1-W4 are shown in Figure 6.9. In Figure 6.10 the results of the EDX spectra acquired within the indicated locations are given. The measured surface concentrations of W and Cr are shown. Y concentration was too low to be detected. The figures are indicative of Cr re-deposition next to the coating edge as a Cr content could only be measured in spectrum 2 after plasma exposure. Re-deposited material is also visible on the SEM image, on which the positions of the numbered spectra are indicated, directly at the right side of the edge. The small amount of re-deposited material is only visible very close to the 4 µm thick WCrY coating edge. This re-deposited material is assumed to stem either from the side of the coating or from the very top edge.
From SDTrimSP simulations of the irradiation of a WCrY target with D + 0.23 % O ions at an energy of 120 eV at normal incidence (similar to the calculations presented above for pure W) the energy distribution of Cr sputtered from WCrY (summed over all azimuthal and polar angles) is inferred. The energy distribution of the sputtered Cr is shown in Figure 6.12. A mean kinetic energy of about 4.7 eV leads to an average velocity v of $5.4 \times 10^{3}\,\mathrm{m\,s^{-1}}$. At an electron temperature T_e of 8 eV, $\langle \sigma v \rangle_{ion}$ of Cr is indicated

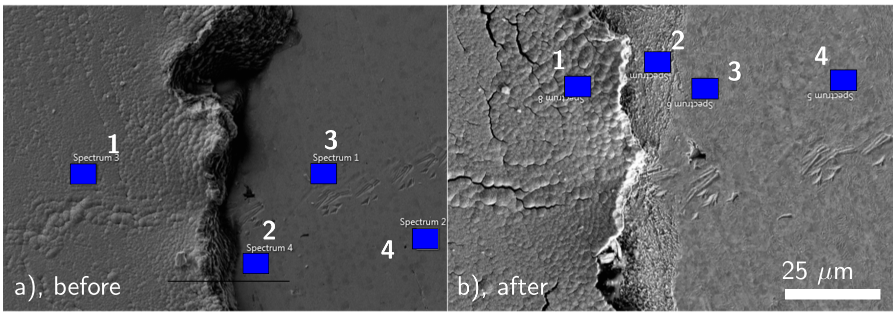

Figure 6.9.: Indicated positions of EDX spectra on D120P1-W4 (WCrY-coated W sample) a) before and b) after plasma. Left side of sample with position of spectrum 1: deposited WCrY.

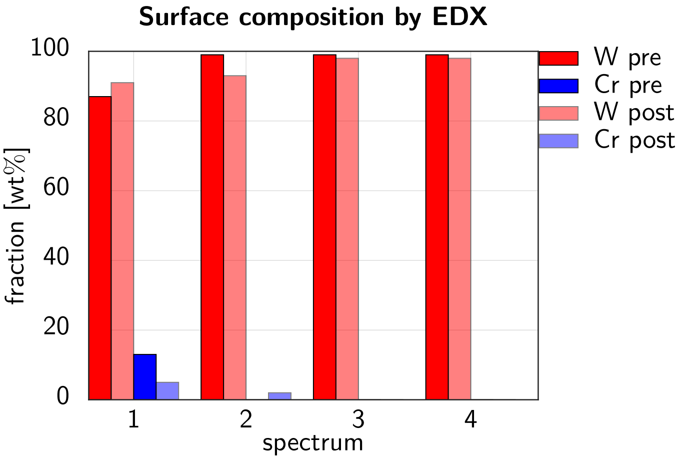

Figure 6.10.: EDX spectra 1-4: surface composition of W and Cr in wt%, not displayed O- and C-content add up to 100 wt%.

with $1.4 \times 10^{-13}\,\mathrm{m^3\,s^{-1}}$ by [99]. Taking n_e to be $3 \times 10^{17}\,\mathrm{m^{-3}}$ yields $\lambda_{ion} \approx 1 \times 10^{-1}\,\mathrm{m}$ (via $\lambda_{ion} = v/(\langle\sigma v\rangle_{ion} n_e)$) for the sputtered Cr, which is the same value as previously obtained for W. The distribution of λ_{ion} for the sputtered Cr in shown in Figure 6.13. It can be seen that the ionisation length is of the order of several centimetre, which is expected for the relatively low plasma density in PSI-2. Hence the detected locally re-deposited Cr can be attributed to stem from Cr sputtered from the side of the coating edge. This is illustrated in Figure 6.11: the angular distribution of the sputtered particles leads to re-deposition directly next to the edge. Material sputtered from the top of the coating is mostly not ionised in the plasma close to the target surface, which is why no re-deposition is seen beyond the vicinity of the coating edge. The ionisation length of W was found to be as well in the order of $\lambda_{ion} \approx 1 \times 10^{-1}\,\mathrm{m}$. Thus λ_{ion} of W and Cr is relatively large in comparison to the diameter of the plasma maximum of the order of $1 \times 10^{-2}\,\mathrm{m}$. This explains why the re-deposition of the W mask onto the samples can be neglected in a first approximation. Moreover, one should keep in mind that outside the plasma maximum, the plasma density is even lower, leading to an even larger ionisation length.

At the same time, the Cr content on the surface of the WCrY-coating decreased during plasma operation (spectrum 1), which again shows Cr depletion due to preferential sputtering.

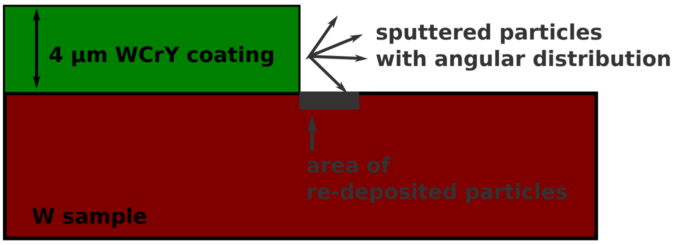

Figure 6.11: Schematic drawing of W sample coated by magnetron sputtering with 4 µm thick WCrY layer. The area where particles re-deposit next to the coating edge is indicated.

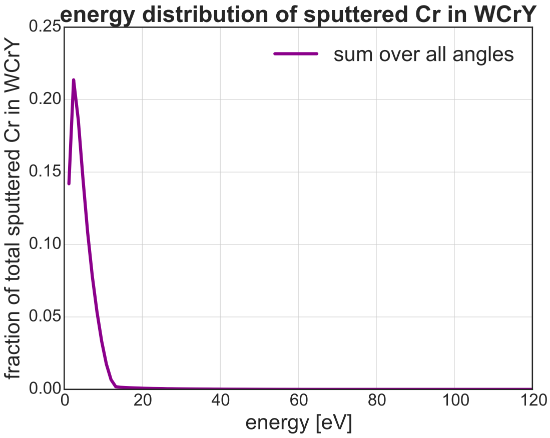

Figure 6.12.: Energy distribution of sputtered Cr in WCrY summed over all angles (polar angle from 0° to 90° and azimuthal angle from 0° to 180°). The distribution is obtained by static SDTrimSP simulations for 99.77 % D + 0.23 % O ion irradiation at normal incidence on a WCrY target with the optimum composition.

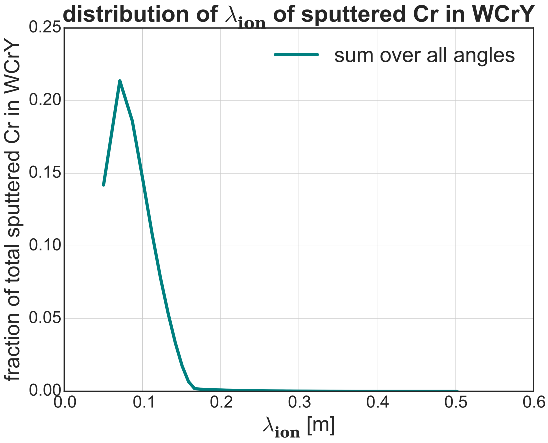

Figure 6.13.: Distribution of λ_{ion} of the sputtered Cr in WCrY obtained via $\lambda_{ion} = v/(\langle\sigma v\rangle_{ion} n_e)$ and $E = (1/2)mv^2$ from the energy distribution in Figure 6.12. There are no sputtered Cr particles with $\lambda_{ion} <\approx 0.05\,\mathrm{m}$, since the SDTrimSP energy distribution of sputtered Cr particles does not contain values below 1.2 eV.

Surface morphology

SEM images (see description of the used device in Section 5.1.2) of the sample surfaces are taken before and after plasma exposure for investigating plasma-induced morphology changes. Shown below are surface images taken at two different magnifications. First the images of WCrY, then those of W samples are presented.

In Figures 6.14 and 6.15 unexposed WCrY samples, at different surface roughnesses R_a, are shown. Figures 6.16 to 6.18 are images of the samples after plasma. Generally, one should note that the SEM images are not taken at the same locations. Results of the R_a roughness measurements carried out with the surface profilometer as described in Section 5.1.8 are given in Table 6.4. With the usual sample preparation described in Section 3.3, a surface roughness R_a of about 30 nm (see Table 6.4 for average and Appendix B for detailed roughness results). Except for some scratches from grinding, the surface looks smooth and homogeneous as can be seen in Figure 6.14. Scratches and other marks from grinding mainly determine the surface roughness. The sample shown in Figure 6.15 has been ground with a more coarse SiC paper in the last grinding step (see Section 3.3 for details on the sample preparation) resulting in a surface roughness of more than 300 nm. Compared to Figure 6.14, which has the same magnification, the surface looks much less smooth as grinding induced bigger artefacts such as scratches and loose material.

Based on the SEM images of WCrY after plasma exposure in D120P1 and D120P2, three main statements can be made: firstly, the surface roughness is still mainly dominated by

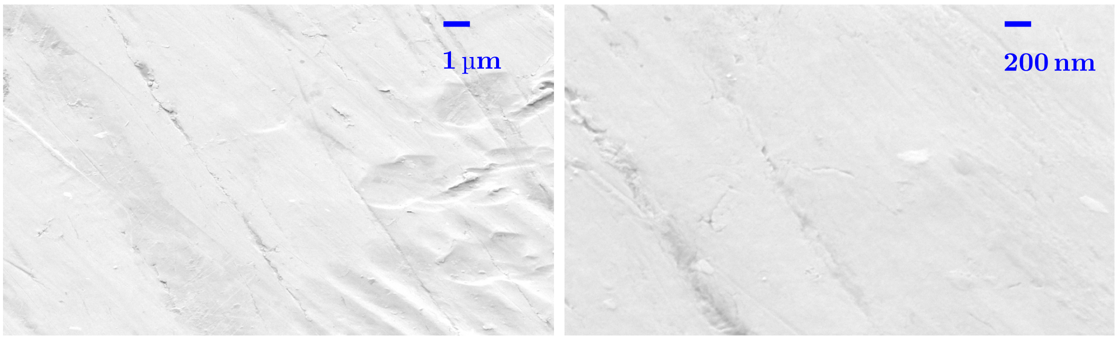

Figure 6.14.: SEM images of an unexposed WCrY sample (surface roughness $R_a \approx 30\,\text{nm}$).

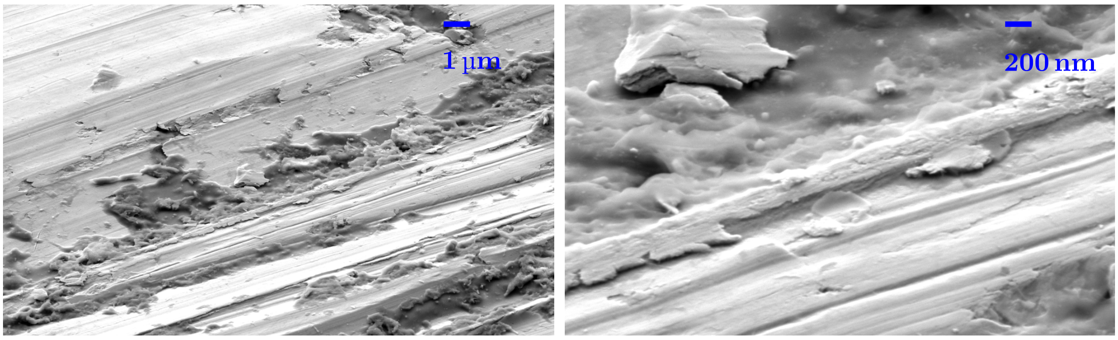

Figure 6.15.: SEM images of unexposed rough WCrY sample (surface roughness $R_a > 300\,\text{nm}$).

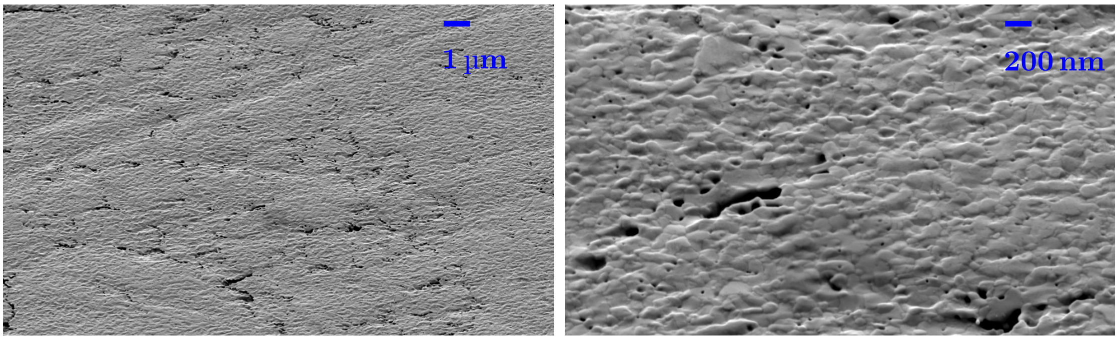

Figure 6.16.: SEM images of D120P1-WCrY2 after plasma.

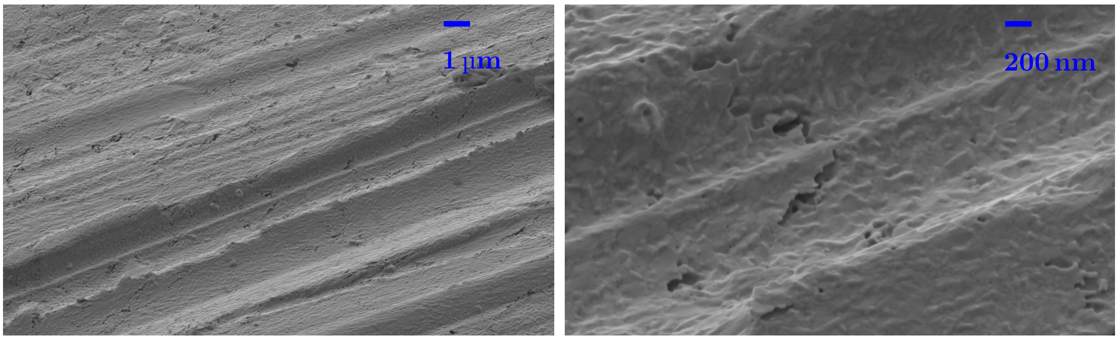

Figure 6.17.: SEM images of D120P1-WCrY3 (rough) after plasma

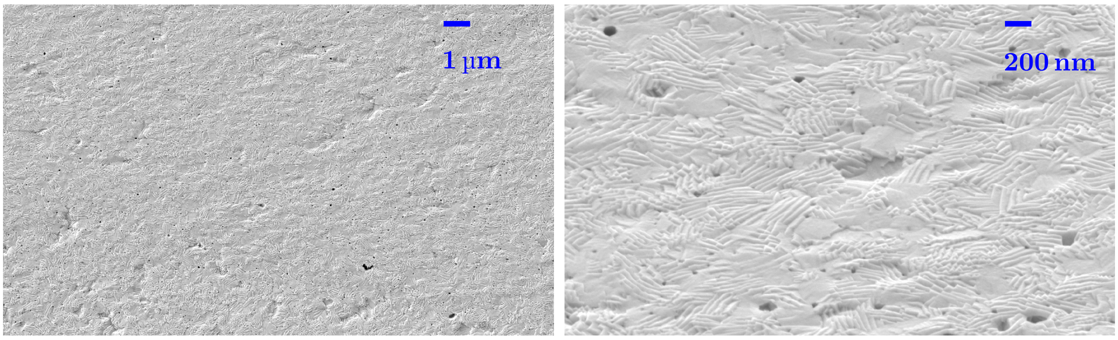

Figure 6.18.: SEM images of D120P2-WCrY1 after plasma.

the grinding process as the surface profile with the grinding scratches keeps its shape. This becomes especially clear when comparing the images of the rough WCrY sample before and after plasma (Figures 6.15 and 6.17) and is also reflected by the just marginal increase in surface roughness in Table 6.4. Secondly, after plasma exposure in both D120P1 and D120P2, some small black holes of the size of tenths of nm and bigger holes or craters, especially along the grain boundaries, of the order of hundreds of nm are visible. As already explained above, these surface features are attributed to the depletion of Y and Cr. Thirdly, wave-like structures correlating with the grain orientation can be seen on all exposed WCrY samples after plasma exposure. They are more pronounced in experiment D120P2 than in D120P1. A reason for this could be the about 1.6 times enhanced ion fluence in D120P2 compared to D120P1.

Wave-like structures or ripples are also found on all exposed W samples (Figures 6.21 to 6.23). According to [101] the formation of quasi-periodic height modulations on the nm-scale such as ripples has widely been observed for the irradiation of surfaces with a broad ion beam. This reference states that for polycrystalline metal surfaces the surface roughness progressively increases due to the variation of the sputter yield between different grains. The oblique ion bombardment of the rough surface then leads to varying local incidence angles and consequently to local variations of the flux and sputter yield. This finally translates to an anisotropy in the surface morphology evolution which is characterised by a pronounced ripple pattern for a sufficiently large incidence angle of the ion beam ($> 80°$). Surface diffusion counteracts the roughening acting as a smoothing term. An all-embracing model for these surface structure formation on a nm-scale during ion irradiation has not been formulated yet. However, the presence of these structures, with wavelengths of the quasi-periodic height modulations of the order of tenths of nm, on the W and WCrY samples evidence grain-dependent sputter yields during exposures. As W and WCrY samples are prepared in the same way, a W sample before exposure looks just like a WCrY sample before exposure. W samples before exposure are shown in Figure 6.19 with a smooth surface finish of about 30 nm and in Figure 6.20 with a rough surface finish of more than 500 nm. Neither holes nor craters were found on the W samples after plasma. Pure W samples are sputtered down homogeneously as they only consist of one element, unlike the WCrY samples where Cr and Y are sputtered preferentially.

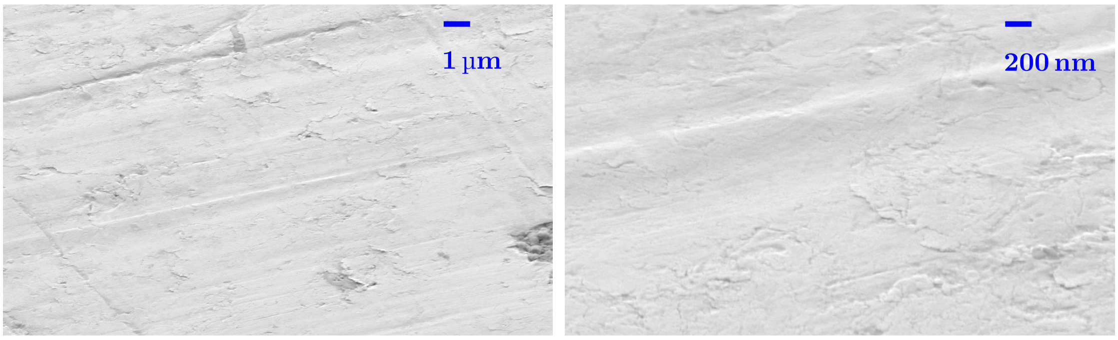

Figure 6.19.: SEM images of unexposed W (surface roughness $R_a \approx 30\,\mathrm{nm}$).

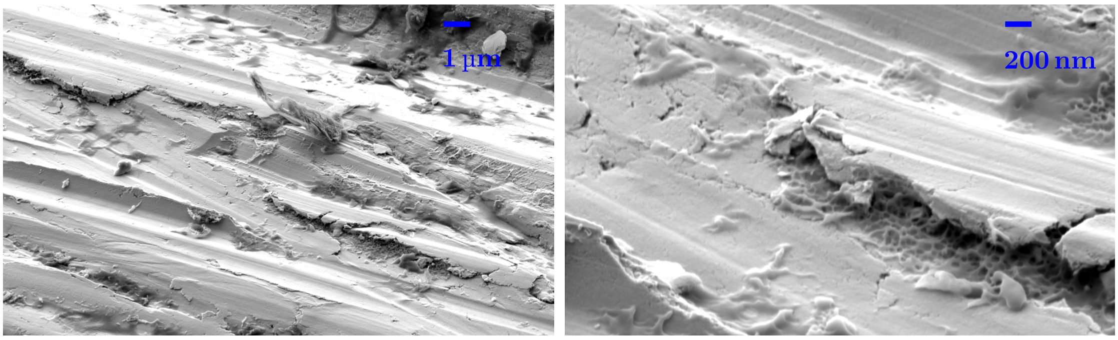

Figure 6.20.: SEM images of unexposed rough W (surface roughness $R_a > 500\,\mathrm{nm}$).

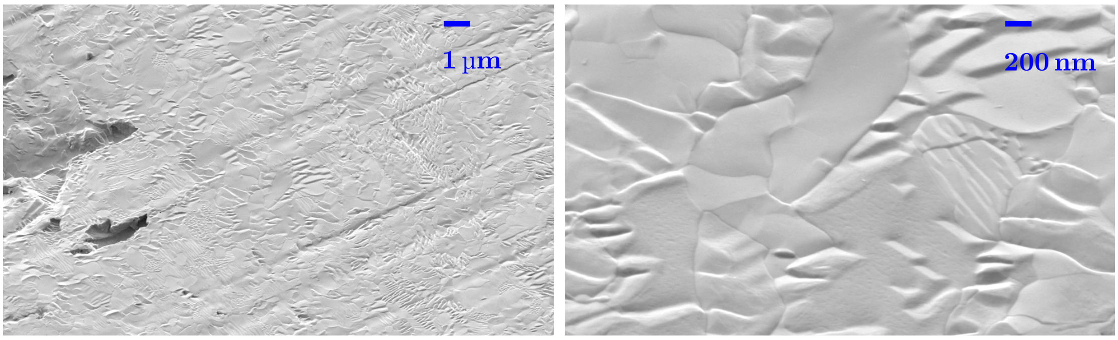

Figure 6.21.: SEM image of D120P1-W3 after plasma.

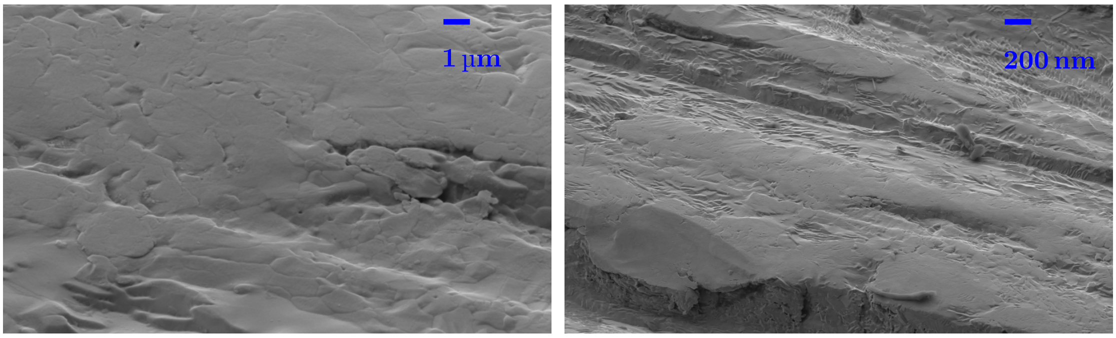

Figure 6.22.: SEM images of D120P1-W1 (rough) after plasma.

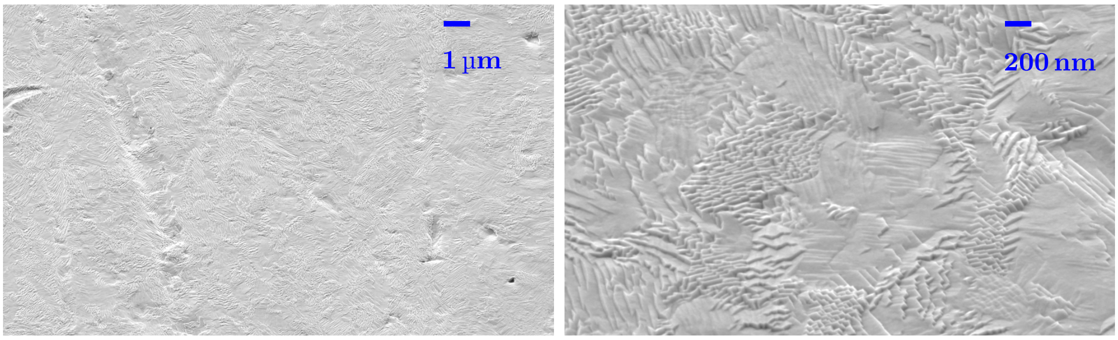

Figure 6.23.: SEM images of D120P2-W1 after plasma.

The surface roughness R_a of all samples was measured before and after plasma exposure with the surface profilometer Dektak 6M as described in Section 5.1.8. Average roughness results are given in Table 6.4. It can be inferred that on average the roughness does remain at a stable value or increases slightly within the margin of the error bars. It is assumed that the ion-induced ripple formation on a nm-scale is, in comparison to the roughness stemming from the sample preparation procedure, too small to be detected with the surface profilometer. Detailed roughness results for all samples are given in the Appendix.

6.1.3. SDTrimSP modelling results and discussion

SDTrimSP modelling is used to gain insight into the material evolution under plasma ion irradiation. The model and the underlying physics are described in Section 5.2. Cr transport to the surface is described by thermal diffusion in the model, which is induced by concentration gradients within the material. Modelling results for experiments D120P1 and D120P2 are presented in this section.

Erosion is heavily dependent on the plasma composition and especially for mixed D+Ar/He plasmas, small variations in the plasma composition lead to large changes of the materials' erosion yields. In pure D plasma, the residual oxygen content of the plasma plays a crucial role. Simulations were carried out at an incident ion energy of 120 eV and at a plasma oxygen content of 0.23 %. Without taking into account diffusion of alloying elements in case of WCrY, this leads to an extrapolated surface recession

experiment	sample	R_a before [nm]	R_a after [nm]
D120P1	$\overline{\text{W}}$ without rough sample	29 ± 8	29 ± 5
	$\overline{\text{WCrY}}$ without rough sample	38 ± 14	47 ± 34
	rough W sample	532 ± 60	584 ± 36
	rough WCrY sample	306 ± 33	319 ± 15
D120P2	$\overline{\text{W}}$	32 ± 12	33 ± 11
	$\overline{\text{WCrY}}$	24 ± 8	24 ± 6

Table 6.4.: Average roughness R_a results over the W ($\overline{\text{W}}$) and WCrY ($\overline{\text{WCrY}}$) samples exposed to pure D plasma in D120P1 and D120P2.

of 188.2 nm for W and 215.6 nm for WCrY at a fluence of 1.0×10^{26} ions/m^2. For a fluence of 1.6×10^{26} ions/m^2 extrapolated surface recessions are 300.9 nm for W and 345.0 nm for WCrY, as displayed in Figure 6.24. These surface recession results agree with experimentally found values (see Section 6.1.2). The sputter yield evolution simulated up to a fluence of 1.0×10^{25} ions/m^2 is shown in Figure 6.25. Extrapolated mass losses for WCrY are 345 µg at a fluence of 1.0×10^{26} ions/m^2 and 531 µg at a fluence of 1.6×10^{26} ions/m^2. Simulations for pure W yield a mass loss of 363 µg at a fluence of 1.0×10^{26} ions/m^2 and 560 µg at a fluence of 1.6×10^{26} ions/m^2 (experimental fluence of D120P1, see Table 6.2). Mass loss results of W and WCrY agree with the experimental values in D120P2 at a fluence of 1.6×10^{26} ions/m^2 (experimental fluence of D120P2), around 500 µg for WCrY and about 600 µg for W as displayed in Figure 6.1. Mass loss results for D120P1 are not available for comparison.

Further simulations were executed at an ion energy of 120 eV and an oxygen content of 0.23 % with the diffusion coefficient $D_{Cr,WCrY}$ set to 1×10^{-17} m^2/s. This value was found to be a suitable value for the diffusion coefficient in experiment D220P described in Chapter 7. Simulations with added diffusion, shown on the right side of Figure 6.25, yield an extrapolated mass loss of 868 µg and a surface recession of 716 nm for WCrY at a fluence of 1.6×10^{26} ions/m^2. These erosion values exceed the experimentally found ones, regarding both mass loss and surface recession. Hence diffusion has a less significant impact on the erosion of WCrY during D120P1 and D120P2. A more detailed explanation is given alongside with the SDTrimSP results in Chapter 7.

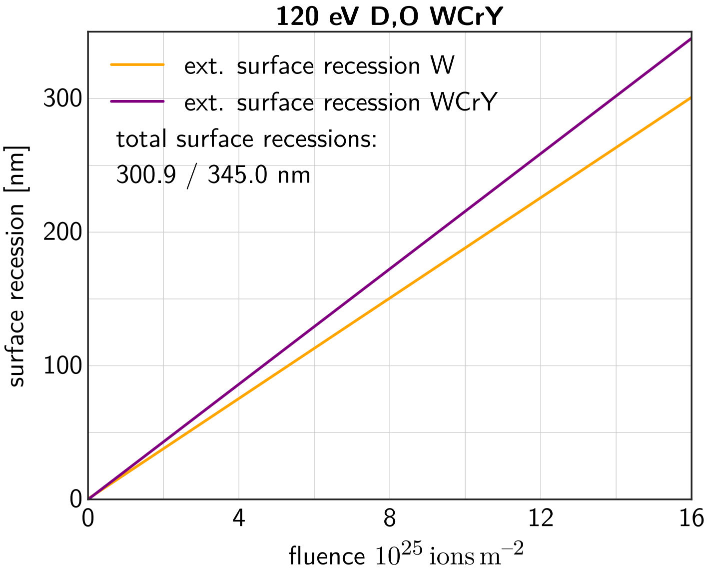

Figure 6.24.: Simulated surface recession of W (yellow graph) and of WCrY (purple graph) without diffusion.

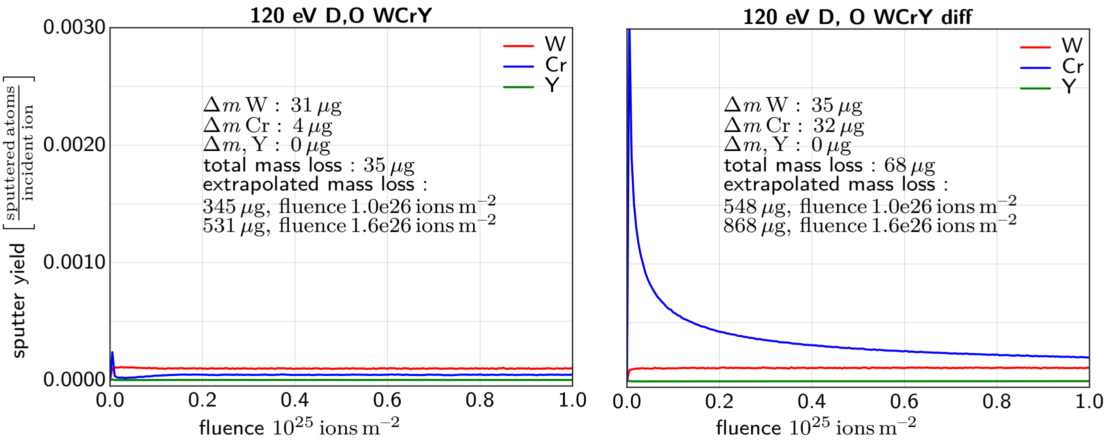

Figure 6.25.: Simulated partial sputter yields of W, Cr and Y for WCrY without diffusion on the left and with the diffusion coefficient of Cr in WCrY, $D_{Cr,WCrY}$, set to 1×10^{-17} m^2/s on the right. The mass loss per element is obtained via integration of the partial yield curves. Mass losses obtained by extrapolating the sputter yields at the last fluence steps are 345 µg and 531 µg for a fluence of 1.0 ions/m^2 and 1.6 ions/m^2, respectively, without diffusion. The addition of diffusion leads to mass losses of 548 µg and 868 µg for a fluence of 1.0×10^{26} ions/m^2 and 1.6×10^{26} ions/m^2, respectively.

6.2. Exposure of WCrY and reference W samples in Magnum-PSI

6.2.1. Experimental details

In Magnum-PSI in total 8 samples, 4 WCrY and 4 W samples, were exposed to ion energies below the W sputter threshold, namely to pure D plasma at 120 eV. Similar to PSI-2, the plasma oxygen content is assumed to be significantly below 1 %. Four different fluences were chosen, each time a WCrY and a W sample were exposed to the same fluence. Since samples are exposed subsequently (see the facility description of Magnum-PSI in Section 4.1.2), exposing 8 samples means 8 consecutive experiments. The experiments were carried out at fluences of 0.1×10^{27} ions/m^2, 0.5×10^{27} ions/m^2, 1.0×10^{27} ions/m^2 and 2.0×10^{27} ions/m^2 and are called D120M1-W/WCrY, D120M2-W/WCrY, D120M3-W/WCrY and D120M4-W/WCrY, respectively. Whereas a fluence of 0.1×10^{27} ions/m^2 equals approximately the fluence achieved in PSI-2, the highest achieved fluence in Magnum-PSI equals 20 times the PSI-2 fluence and corresponds to about one month of DEMO operation. Compared to PSI-2 conditions, the plasma temperature T_e is lower with 2 eV and the electron density higher with $n_e = 2 \times 10^{20}$ m^{-3} in Magnum-PSI. All experiments and the samples used, which are manufactured and prepared as described in Section 3.3, are listed in Table 6.5.

experiment	plasma[a]	ion energy [eV]	ion flux [ions/m^{2}s]	ion fluence [ions/m^2]	sample temperature [K]	material	density
D120M1-W	1 D	120	2.9×10^{23}	0.1×10^{27}	900 - 940	W	> 98.0 %
D120M1-WCrY	1 D	120	2.3×10^{23}	0.1×10^{27}	900 - 940	WCrY	98.3 %
D120M2-W	1 D	120	1.9×10^{23}	0.5×10^{27}	900 - 940	W	> 98.0 %
D120M2-WCrY	1 D	120	1.9×10^{23}	0.5×10^{27}	900 - 940	WCrY	98.3 %
D120M3-W	1 D	120	0.9×10^{23}	1.0×10^{27}	900 - 940	W	> 98.0 %
D120M3-WCrY	1 D	120	1.7×10^{23}	1.0×10^{27}	900 - 940	WCrY	98.3 %
D120M4-W	1 D	120	1.9×10^{23}	2.0×10^{27}	900 - 940	W	> 98.0 %
D120M4-WCrY	1 D	120	1.7×10^{23}	2.0×10^{27}	900 - 940	WCrY	98.3 %

[a]: neglecting residual impurities such as oxygen

Table 6.5.: Experiment parameters of plasma exposures in Magnum-PSI with main plasma ion energies below the W sputter threshold together with the respective samples. The plasma ion composition is given in fractions of the total plasma ions neglecting possible impurities such as oxygen. The density as determined using the Archimedes principle (see Section 5.1.5) is given in % of the theoretical density.

The sample temperature was monitored with the pyrometer to make sure it stays around 900 K. The magnetic field at the target position was set to 0.8 T. Due to the high flux density in Magnum-PSI, samples are significantly heated by plasma impact. After exposing a sample for more than 1 h, the whole target holder structure has heated up and the water cooling is not sufficient any more to keep the sample temperatures in the desired range. As a consequence, the source current and therefore the incident plasma flux onto the sample needed to be adjusted to avoid overheating of the samples: once the sample temperature came close to 940 K, the flux was reduced to obtain again a sample temperature of around 900 K. Thus, for the experiments with the highest fluence the flux had to be increasingly reduced during the experiment resulting in longer exposure times. Exposure times ranged from a couple of minutes for the experiments at lowest fluence (M1) up to several hours for the highest fluence (M4). The flux given in Table 6.5 is the average flux during the experiments. In all experiments the flux varied between a minimum value of 0.7×10^{23} ions/(m^{2}s) and a maximum value of 3.0×10^{23} ions/(m^{2}s).

6.2.2. Experimental results and discussion

Erosion

Erosion results, average surface recession d_e and weight loss Δm of W and WCrY samples, are displayed in Figure 6.26. The surface recession is slightly increased for WCrY or equals the W surface recession: d_e for W and WCrY is similar within error bars. The mass loss is reduced for WCrY for all of the 4 different fluences at which experiments were conducted. Using Equation (6.1) to obtain the ratio of mass losses yields $\Delta m_{WCrY}/\Delta m_W \approx 0.60 \pm 0.03$ in D120M1, $\approx 0.89 \pm 0.03$ in D120M2, $\approx 0.83 \pm 0.01$ in D120M3 and $\approx 0.82 \pm 0.01$ in D120M4. A ratio of $\approx 0.79 \pm 0.16$ is obtained when averaging over the mass losses of all experiments. Hence the theoretical mass ratio of $\Delta m_{WCrY}/\Delta m_W \approx 0.82$, assuming the same eroded volume for W and WCrY, is approximately matched, especially at higher fluences. This means that erosion of WCrY is on average similar to that of W, and most similar in the experiment conducted with the highest fluence. In the experiments conducted at the lowest fluence, D120M1-W and D120M1-WCrY, the uncertainty whether the same fluence has been achieved for both samples is highest due to the short duration of the exposure of only several minutes.

When comparing these erosion results to the ones presented earlier for PSI-2 experiments under the W sputter threshold, it is notable that although fluences were increased up to a factor of 20 for exposures in Magnum-PSI, neither mass loss Δm nor surface recession d_e did scale accordingly. A possible reason for this is a slightly different oxygen content in the Magnum-PSI plasma. However, there are no measurements of the oxygen content in Magnum-PSI available. Another possible explanation is the fact that Δm and d_e can only serve as measures for the net erosion and not the gross erosion during an experiment. Consequently, these values do neglect the effect of re-deposition. Similar to PSI-2, the ionisation length λ_{ion} of W serves as a good first approximation to evaluate the importance of re-deposition based on the plasma conditions in Magnum-PSI. Again v is inferred from the energy distribution (see Figure 6.2) via $E = (1/2)mv^2$. Further, the Thomson Scattering (TS)-measured plasma temperature T_e was 2 eV, which implies an ionisation probability $\langle \sigma v \rangle_{ion}$ of $6.2 \times 10^{-15}\,\mathrm{m}^3$ from [102], at an electron density of about $n_e = 2 \times 10^{20}\,\mathrm{m}^{-3}$ during experiments. Inserting all these values into $\lambda_{ion} = v/\langle \sigma v \rangle_{ion} \cdot n_e$, yields an ionisation length of $\lambda_{ion} \approx 2 \times 10^{-3}\,\mathrm{m}$ in Magnum-PSI. Comparing this to the plasma beam FWHM of about 2 cm (see Figure 4.6), it becomes evident that every eroded particle is likely to be ionised close to the target and consequently re-deposition and self-sputtering play an important role. Calculating the

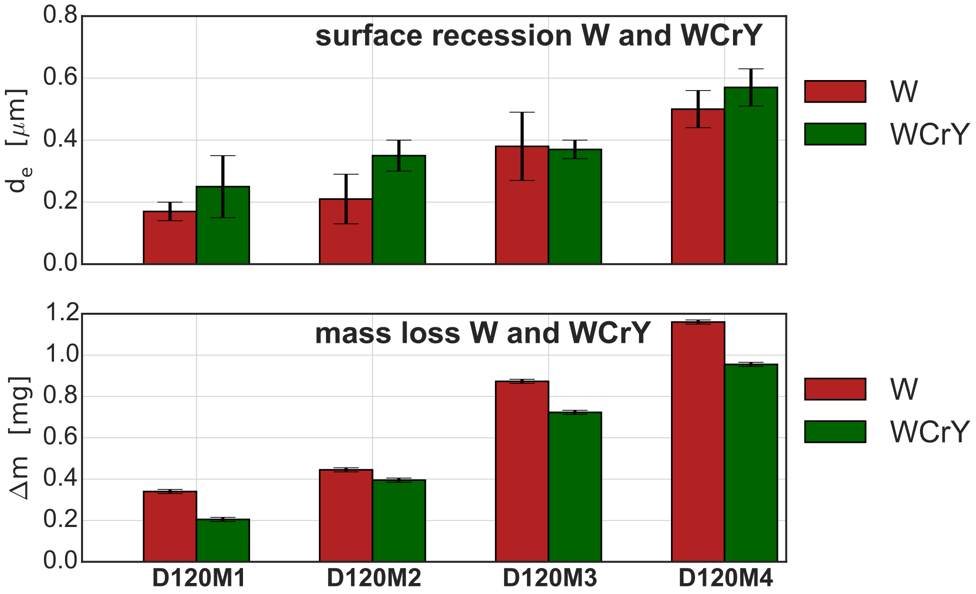

Figure 6.26.: Measured average surface recession d_e (top graph) and mass loss Δm (bottom graph) of W and WCrY samples exposed in D120M1, D120M2, D120M3 and D120M4. Measurement procedures are described in Sections 5.1.5 and 5.1.2

probability for prompt re-deposition P_{prompt} of W, i.e. re-deposition of the eroded particle before completing its first Larmor radius r_L, via $P_{prompt} = \lambda_{ion}/r_L$ (see Equation (2.11)), yields $P_{prompt} = 1/3$, with $r_L \approx 6 \times 10^{-3}$ m. Hence (prompt) re-deposition is very probable to be a reason for the reduced net-erosion in Magnum-PSI compared to experiments in PSI-2.

Since re-deposition cannot be taken into account in SDTrimSP modelling, no simulations were carried out for experiments conducted in Magnum-PSI.

Using the OES system at Magnum-PSI (see description in Section 4.1.2) the line radiation of neutral W (WI) at 400.88 nm as well as neutral Cr (CrI) at 427.48 nm were monitored. Thanks to the two order of magnitude higher fluxes and the resulting accordingly higher sputtering rates in Magnum-PSI plasmas in comparison to PSI-2, signal integration times of fractions of a second are possible. As a consequence the time-evolution of the line radiation detected in front of the target, focussing on the excitation of sputtered neutral W and Cr atoms, helps investigating the (preferential) sputtering behaviour in the course of a sample's exposure. For this purpose the focus was on the spectra obtained in the wavelength range from 400 nm to 440 nm. The NIST database [103] was used to identify the peaks in the acquired spectra. Since there exists no absolute calibration of the line radiation intensities, the D Balmer line at 433.93 nm (D_γ) was used for normalising the acquired counts. Another reason for this normalisation is that instabilities in the D plasma ion beam are taken into account as well as the degradation of the transmission of the window through which the OES system monitors the radiation as a result of deposition of sputtered material throughout an exposure. The D Balmer lines are clearly visible once the D plasma is switched on and can hence be used as an indicator for the plasma start. Normalised spectra of the monitored range are shown in Figures 6.27 and 6.28. These spectra were obtained by setting the D_γ intensity to be 1.0 and scaling all other intensities accordingly. The spectra were acquired during the exposure of a W respectively WCrY sample. On the graphs the D_δ transition at 410.06 nm and the D_γ transition at 433.93 nm, used for normalisation, are visible. Additionally, the wavelengths for strong neutral W lines at 400.88 nm, 407.44 nm and 429.46 nm and strong neutral Cr lines at 425.44 nm, 427.48 nm and 428.97 nm are indicated in red and blue. Whereas peaks corresponding to W line radiation are visible on both graphs, peaks corresponding to Cr line radiation are identified above the noise level only in Figure 6.28. The maximum height of the strongest W peak, at 400.88 nm, and the maximum height of the strongest Cr peak, at 425.44 nm, are inferred for each spectrum to investigate the time evolution over the acquired spectra in the course of an experiment. These maxima are then plotted against the time at which the respective spectra were acquired alongside with the D_γ signal. The time of 0 s corresponds to the first series of spectra acquired with the plasma switched on, as indicated by the then clearly visible D Balmer lines. The OES is triggered to acquire a series of spectra in between time intervals where no measurements take place. During an acquisition period, 10 or 250 spectra are obtained with an integration time of 0.05 s for each spectrum. The time interval between acquisition periods is a couple of minutes. This is why in Figures 6.29 to 6.32, where the time evolution of the maxima is shown, sequences with a high frequency of data points are followed by time intervals with no data points. Regarding the Cr signal evolution in 6.29,

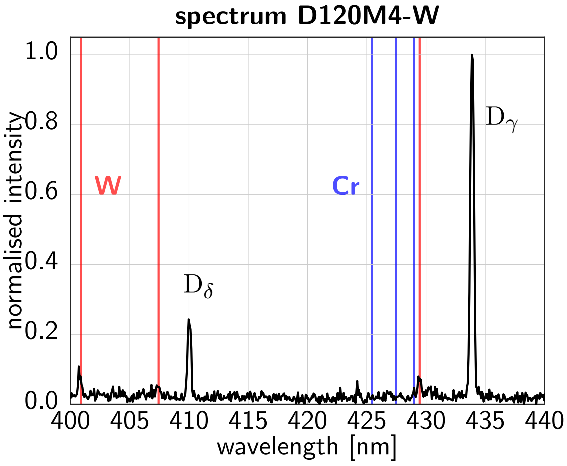

Figure 6.27.: Normalised spectrum of the line radiation in the range of 400 nm to 440 nm acquired in front of the target during D120M4-W in Magnum-PSI.

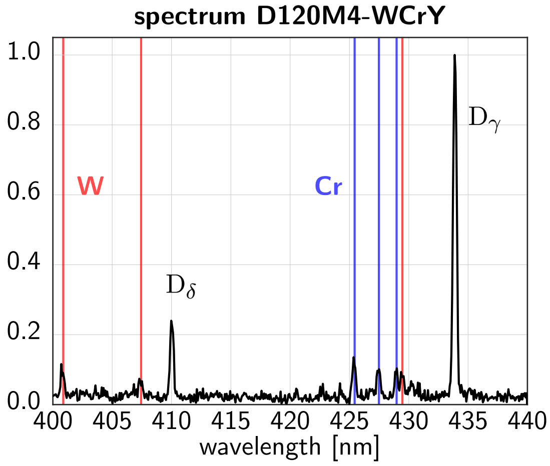

Figure 6.28.: Normalised spectrum of the line radiation in the range of 400 nm to 440 nm acquired in front of the target during D120M4-WCrY in Magnum-PSI.

one should note that although there is no Cr peak distinguishable at the indicated wavelength in Figure 6.27, there are some noise peaks visible. Hence the maximum height values of the noise peaks at this wavelength are inferred and plotted for consistency. During the exposure of D120M4-W (Figure 6.29), the W peak signal strength is constantly at a value of about 0.1, hence at around a tenth of the D_γ signal strength. The

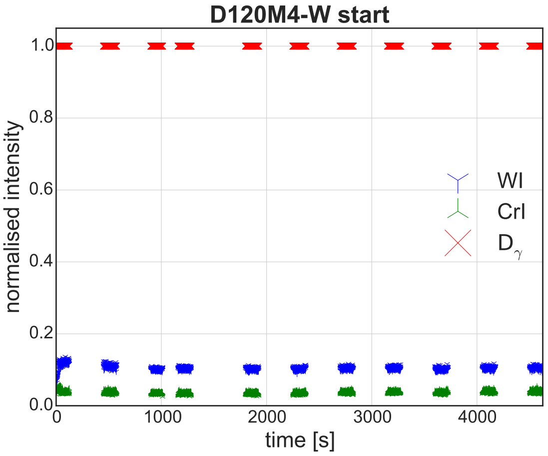

Figure 6.29.: Time evolution of normalised maximum W peak at 400.88 nm and Cr peak at 425.44 nm as well as D_γ peak at 433.93 nm during the exposure of D120M4-W. Spectra acquired during acquisition period: 250, integration time: 0.05 s.

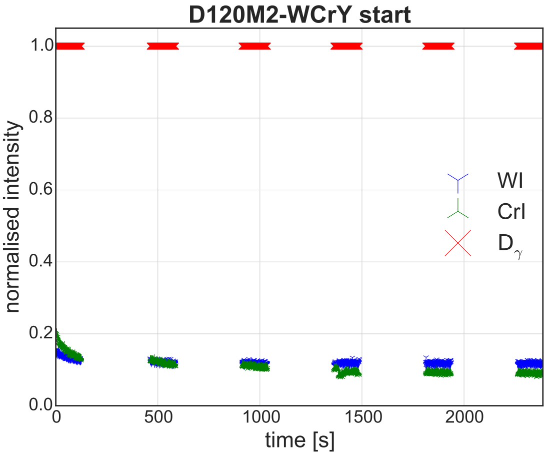

Figure 6.30.: Time evolution of normalised maximum W peak at 400.88 nm and Cr peak at 425.44 nm as well as D_γ peak at 433.93 nm during the exposure of D120M2-WCrY. Spectra acquired during acquisition period: 250, integration time: 0.05 s.

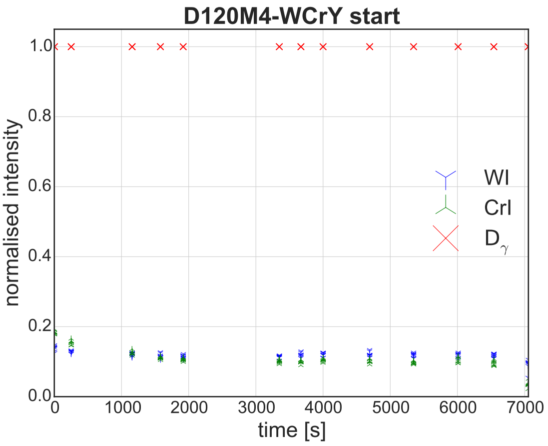

Figure 6.31.: Time evolution of normalised maximum W peak at 400.88 nm and Cr peak at 425.44 nm as well as D_γ peak at 433.93 nm during the first part of exposure of D120M4-WCrY. Spectra acquired during acquisition period: 10, integration time: 0.05 s.

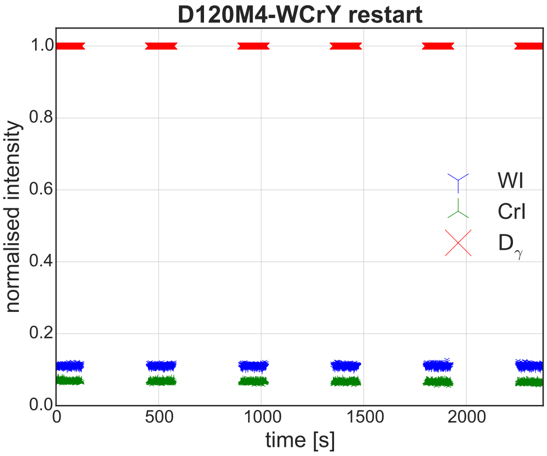

Figure 6.32.: Time evolution of normalised maximum W peak at 400.88 nm and Cr peak at 425.44 nm as well as D_γ peak at 433.93 nm during the restarted exposure of D120M4-WCrY. Spectra acquired during acquisition period: 250, integration time: 0.05 s.

plotted Cr signal strength is constantly at the noise level as during the exposure of a pure W sample no Cr is sputtered. In Figure 6.30 one can see that during the exposure of a WCrY sample, D120M2-WCrY, both W and Cr sputtering are observed. At the exposure start, the Cr signal is increased compared to W, after about 500 s both signals are at the same signal strength. At later times the Cr signal goes below the W signal. This behaviour is similarly seen for D120M4-WCrY (Figure 6.31): at first Cr is increased against W before levelling off and falling beneath it. D120M4-WCrY was the longest exposure carried out (see Table 6.5), it was stopped in between and restarted the next day. The restarted exposure is shown in Figure 6.31. Here one can see that now from the restart of the exposure onwards the Cr signal lies clearly below the W signal. This behaviour suggests that Cr has been preferentially sputtered and therefore depleted during the first part of the exposure and is sputtered much less afterwards. The decrease in the Cr signal in Figures 6.30 and 6.32, which was seen for all WCrY samples, supports this assumption. Yet, when comparing Figures 6.29 and 6.32, it is noticeable that the Cr signal level during the restarted D120M4-WCrY is higher than that acquired during D120M4-W. Thus, although Cr sputtering significantly decreases during the exposure, it is still detectable and above the noise level throughout the full length of exposure. Cr is sputtered by the D plasma ions at the incident ion energies of 120 eV since the threshold energy for D on Cr is 35 eV. In contrast, W is only sputtered by the residual O as sputter thresholds for O on W and Cr are 44 eV and 15 eV, respectively (see Table 2.2 in Chapter 2).

The W signal evolution in Figures 6.30 and 6.31 suggests that W sputtering is increased at the start of the exposure of a WCrY sample, when still a significant fraction of the surface is composed of Cr. During the course of the experiment, when less Cr is present at the surface due to being preferentially sputtered, also the W signal strength decreases. This observation hints at enhanced W erosion in the vicinity of Cr at the alloy surface.

Elemental composition

Changes in elemental composition after plasma exposure are investigated using SIMS depth-profiling as well as EDX surface analysis.

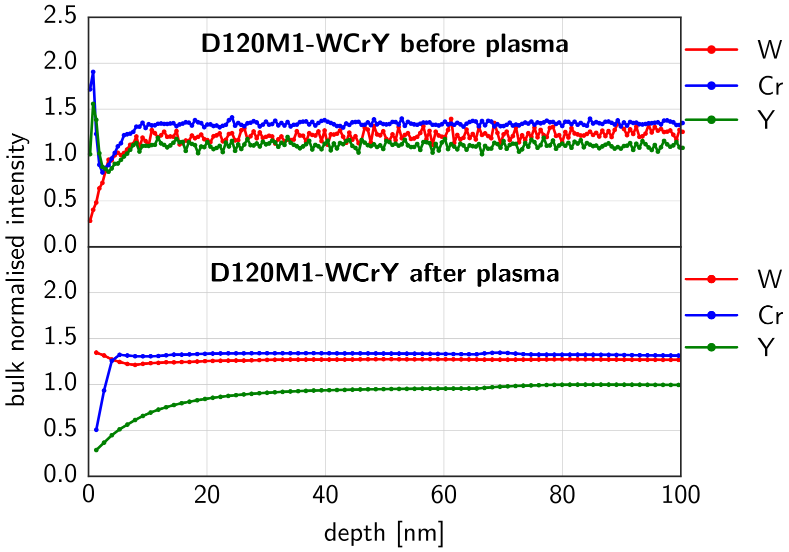

Figure 6.33.: SIMS analysis of sample D120M1-WCrY

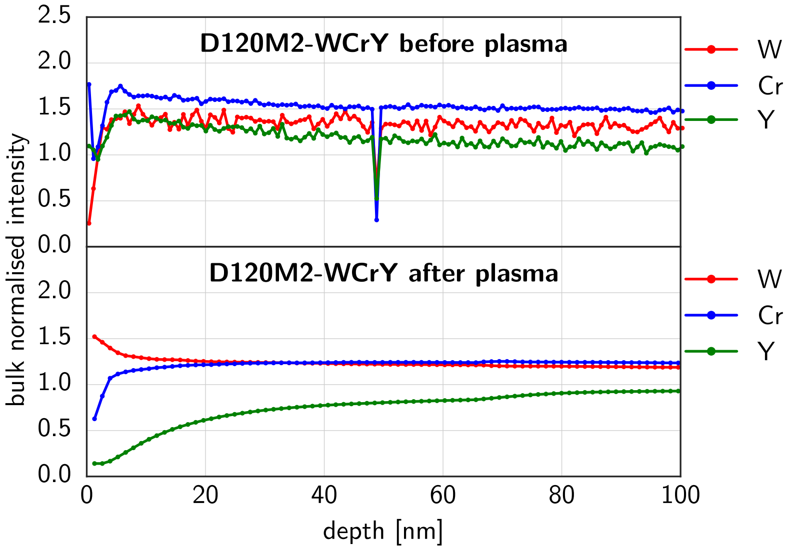

Figure 6.34.: SIMS analysis of sample D120M2-WCrY

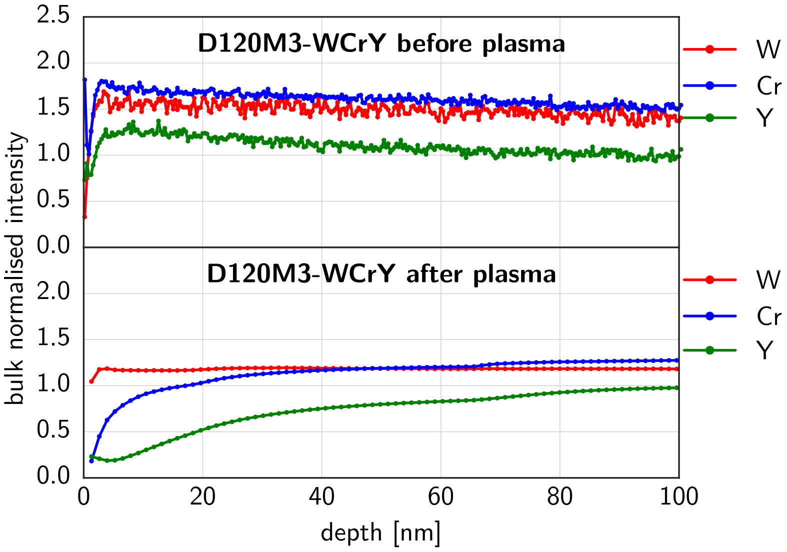

Figure 6.35.: SIMS analysis of sample D120M3-WCrY

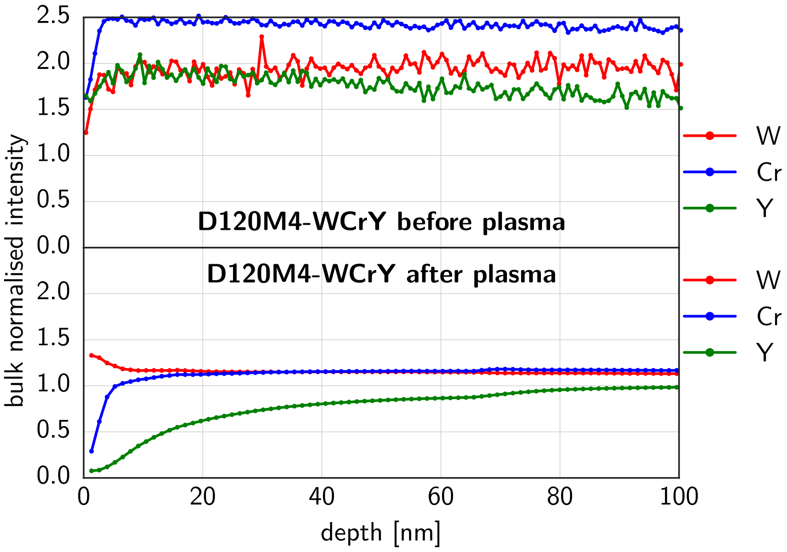

Figure 6.36.: SIMS analysis of sample D120M4-WCrY

The depth-resolved elemental composition of the WCrY samples measured before and after plasma exposure using SIMS are shown in Figures 6.33 to 6.36. Measurements after plasma were acquired with the new SIMS setup (IonTof V NCS, see Section 5.1.7), whereas the measurements before plasma were acquired using the old setup (IonTof IV). Thanks to an increased signal-to-noise ratio with the updated system, graphs showing the signal evolution after plasma are smoother. In all figures, the W, Cr and Y signal evolution is constant towards the surface except for surface artefacts due to non-equilibrium conditions of the sputter beam or surface roughness. The overall increased signal level in Figure 6.36 is caused by an overall decrease in the sputter current throughout the analysis. After plasma, all figures show a distinct decrease in the Y signal intensity towards the surface. Further, a shallow increase in the W signal intensity as well as a decrease in the Cr signal intensity is visible. This behaviour is less distinct for the lowest fluence in experiment D120M1. Whereas the Y signal is decreased extending to a depth of about 60 nm, the increase and W and decrease in Cr signal intensities is limited to a depth of about 20 nm. Consequently, a distinct Y depletion as well as a shallow Cr depletion and W enrichment is detected in all experiments. No strict fluence dependence is observed, yet depletion of Y and Cr and enrichment of W is less distinct for the experiment conducted at the lowest fluence, D120M1-WCrY.

EDX was employed as further means of detecting changes in the elemental (sub-)surface composition. With a 5 kV electron beam a surface area of approximately 200 µm × 200 µm was analysed. The analysed depth in WCrY at this energy extends to about 100 nm (see analysis description in Section 5.1.1). In Figure 6.37, the measured W, Cr and Y surface concentrations of the exposed WCrY samples, given in wt%, are displayed. Two non-exposed WCrY samples were measured as reference, these reference values (including error margins) are indicated by the dotted lines. Whereas in all experiments the Cr content after plasma is significantly decreased compared to the WCrY reference samples, the Y concentration is significantly increased. The W surface concentration is increased, however, the change is less significant compared to the change in Cr surface concentration.

When comparing the EDX results to the previously presented SIMS analysis, one should keep in mind that the EDX-measured surface concentrations are averaged over a depth of

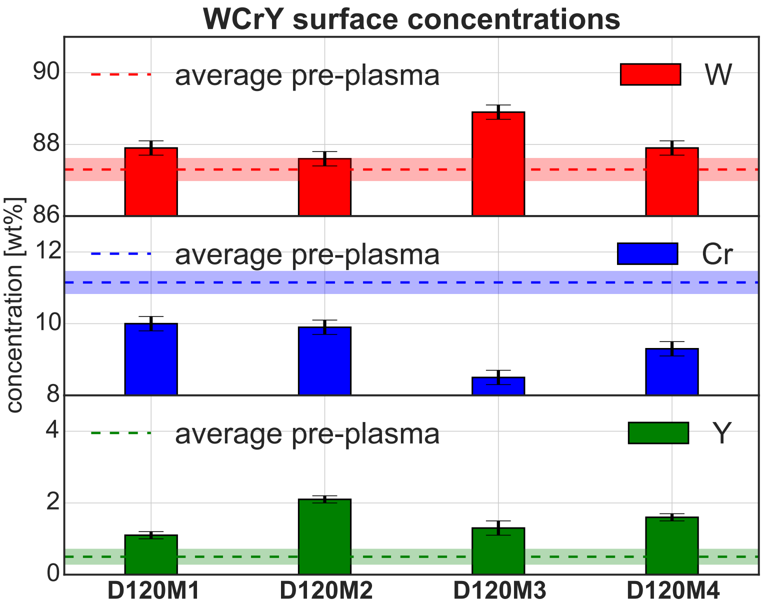

Figure 6.37.: Surface concentrations of WCrY samples after exposure to D120M1, D120M2, D120M3 and D120M4 as measured by EDX at an incident beam energy of 5 kV over a surface area of approximately 200 µm × 200 µm. The red, blue and green shaded area around the respectively coloured dotted lines represent the error margins.

around 100 nm. Taken both together, the results suggest that, while the Y concentration declines directly at the surface, the Y concentration in the approximately 100 nm below the surface is increased compared to the non-exposed reference samples. On the opposite, the Cr concentration in the approximately 100 nm below the surface has fallen off compared to the non-exposed reference samples and additionally there is a shallow drop observed close to the surface. Additional to the plasma ion irradiation, thermally activated Cr and Y transport processes, such as diffusion and (surface) segregation are assumed to affect the subsurface alloy composition. For instance strong Y segregation to the subsurface layer could lead to an overall increase of the Y content in the EDX-detected layer, whereas directly at the surface Y is sputtered preferentially. Diffusion of Cr could lead to smearing out the gradients induced by preferential Cr sputtering, which is why on average the Cr content in the EDX-detected layer is decreased. In the two WCrY exposures with the highest fluence and thus longest duration, D120M3-WCrY and D120M4-WCrY, the average flux was decreased: 1.7×10^{23} ions/(m^2s) in these two experiments compared to 2.3×10^{23} ions/(m^2s) in D120M1-WCrY and 1.9×10^{23} ions/(m^2s) in D120M2-WCrY. For both these experiments with decreased flux, the Cr depletion in the EDX-detected layer is more significant compared to the two other WCrY experiments with higher average flux. This more significant depletion is assumed to be a result of the decreased flux which results in more time for the thermally activated processes diffusion and segregation to impact the concentrations beneath the alloy surface. Both the EDX and the SIMS analysis techniques hint at W enrichment at the surface.

Due to the delay of the Magnum-PSI experiments of more than a year, neither XPS nor NRA analysis were carried out within this work for these experiments. However, since the sample temperatures were kept at around 900 K during the exposures, no significant amount of retained D is expected, similar to D retention results for PSI-2 exposures.

Surface morphology

Figures 6.38 to 6.45 show SEM images of WCrY and W samples exposed in D120M1 to D120M4 at two different magnifications. As the sample preparation procedure resulting in a surface roughness R_a of about 30 nm is the same as for all other samples used for plasma exposures in this work, Figures 6.14 and 6.19 are referred to for surface images prior to exposure.

Generally, on all exposed samples, WCrY as well as W, wave-like structures or ripples, just like those already seen after experiments in PSI-2 (Section 6.1.2), are visible. They are increasingly pronounced and increase in size towards higher fluences, at the highest fluence in D120M4 they are well elaborated, especially on the W sample. The W sample exposed in D120M3, D120M3-W, shows slightly blackened areas on the surface. EDX analysis revealed that compared to all other samples there is an increased amount of oxygen present. This sample was among the 8 samples the first one to be exposed to the plasma. The masks specifically manufactured for exposing the WCrY and W reference samples in Magnum-PSI had not been exposed previously. Thus it is assumed that the increased oxygen content on D120M3-W is a result of exposing the mask for the first time to plasma. The high temperatures of about 900 K during the exposure

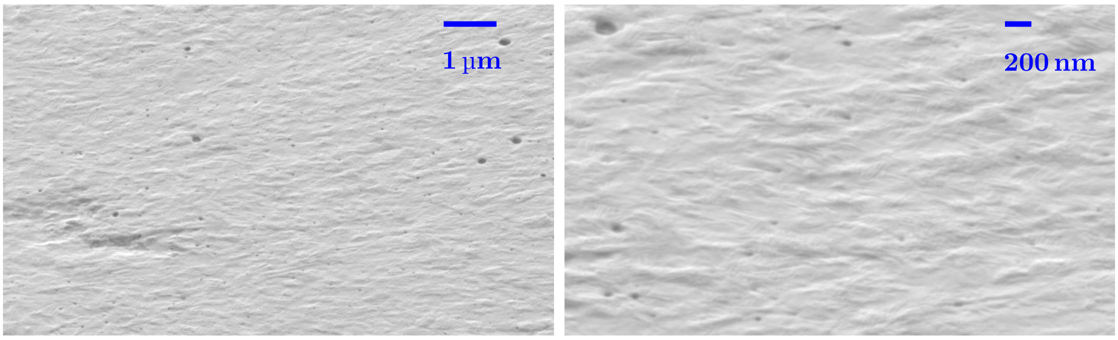

Figure 6.38.: SEM images of D120M1-WCrY after plasma.

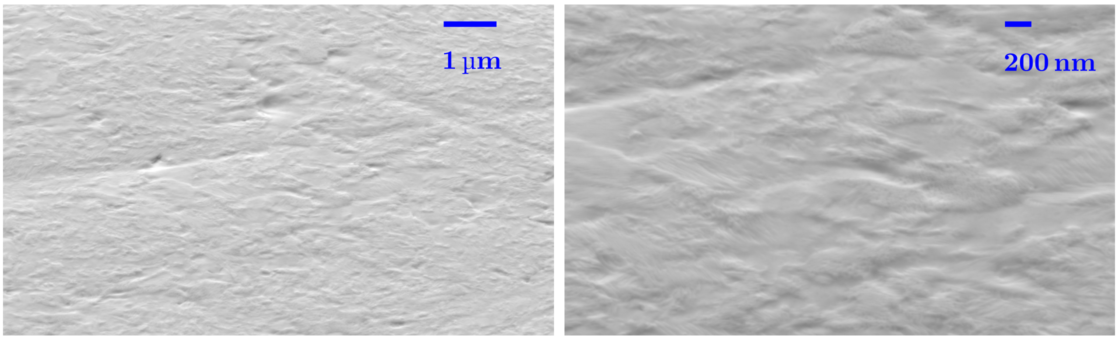

Figure 6.39.: SEM images of D120M1-W after plasma.

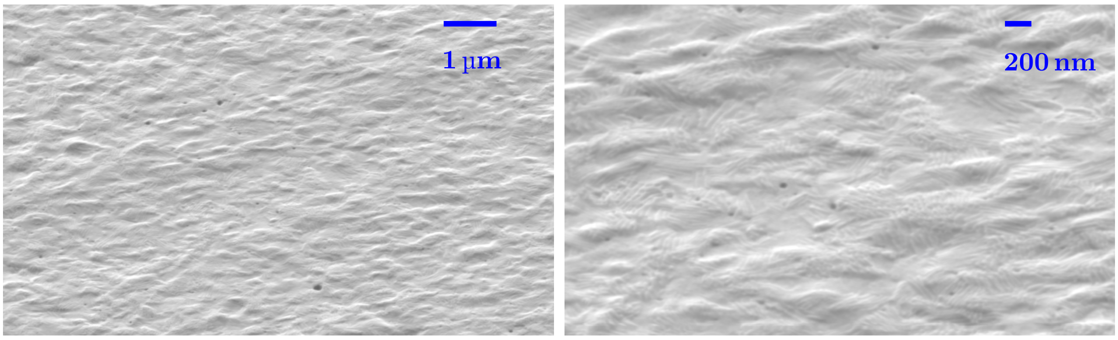

Figure 6.40.: SEM images of D120M2-WCrY after plasma.

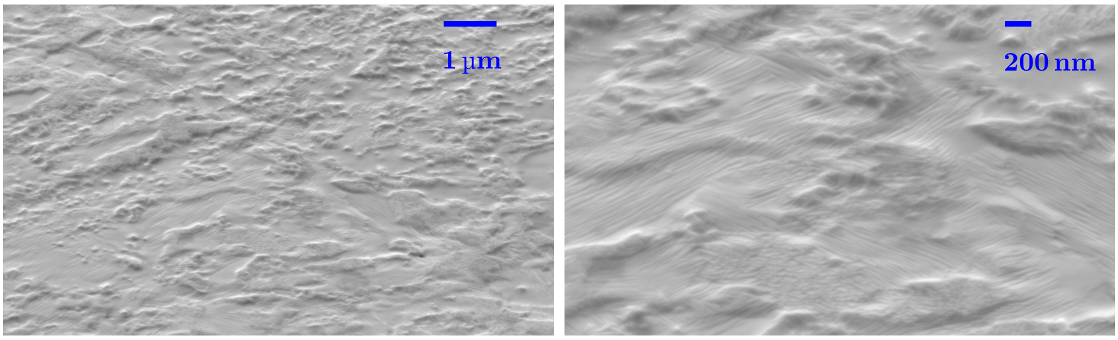

Figure 6.41.: SEM images of D120M2-W after plasma.

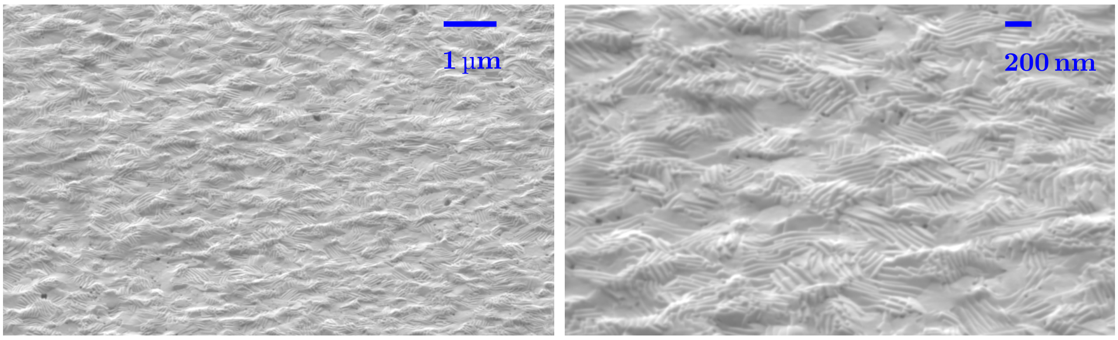

Figure 6.42.: SEM images of D120M3-WCrY after plasma.

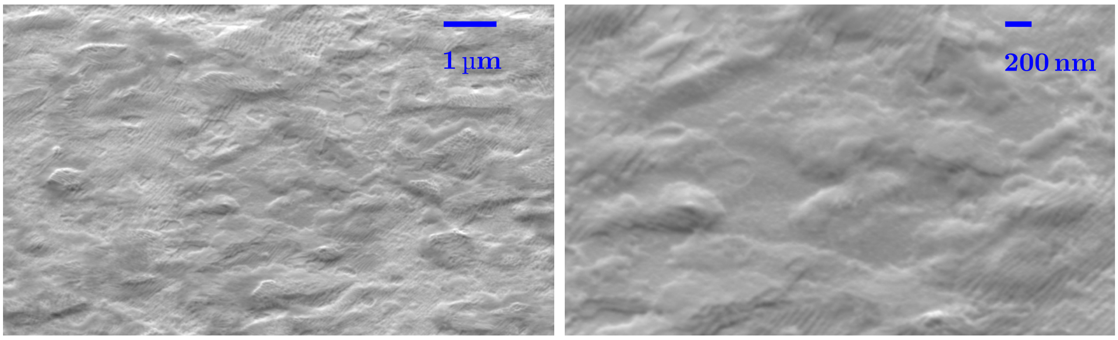

Figure 6.43.: SEM images of D120M3-W after plasma.

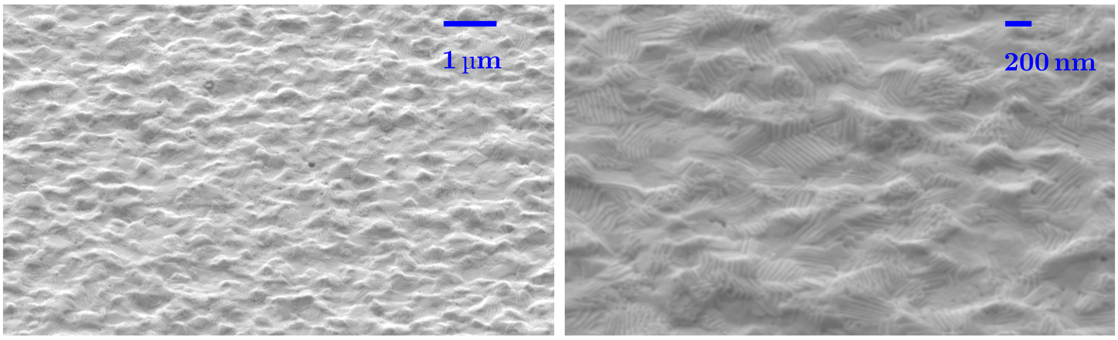

Figure 6.44.: SEM images of D120M4-WCrY after plasma.

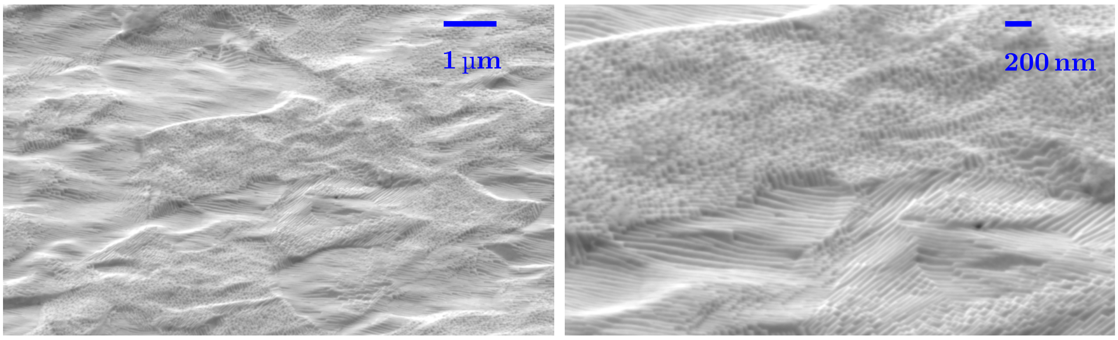

Figure 6.45.: SEM images of D120M4-W after plasma.

experiment	sample	R_a before [nm]	R_a after [nm]
D120M	$\overline{\mathrm{W}}$	23 ± 3	30 ± 9
	$\overline{\mathrm{WCrY}}$	27 ± 5	29 ± 2

Table 6.6.: Average roughness R_a results over the W ($\overline{\mathrm{W}}$) and WCrY ($\overline{\mathrm{WCrY}}$) samples exposed to pure D plasma in D120M1-M4.

are assumed to lead to oxygen desorption from the mask and consequently oxygen deposition on the sample. After exposure, on the WCrY samples some small black holes, corresponding to Y depletion, are visible. However, compared to exposures in PSI-2 there are fewer holes visible and they are less distinct. Elongated craters predominantly along the grain boundaries as found earlier are not visible on the WCrY samples exposed in Magnum-PSI. The fact that the WCrY surfaces show more similarities to the W surfaces after exposure, further hints at significant re-deposition of especially W in the Magnum-PSI plasma conditions.

The average surface roughnesses R_a measured before and after plasma exposure are presented in Table 6.6. Detailed results are given in the Appendix (Table B.3). On average, R_a is slightly increased when measured after plasma or remains constant compared to measurements carried out prior to the exposures. This is in agreement to what was found for the exposures below the W sputter threshold in PSI-2. There is no fluence dependence recognisable.

6.3. Chapter summary

Experiments aiming at investigating the plasma response of WCrY and reference W samples at ion energies below the W sputter threshold were conducted in the linear plasma devices PSI-2 (experiments D120P1 and D120P2) and Magnum-PSI (experiments D120M1-M4) in pure D plasma at an ion energy of 120 eV at normal incidence. Whereas in PSI-2 experiments WCrY and W samples were exposed simultaneously, exposures in Magnum-PSI were conducted subsequently due to the target holder geometry. The sample temperature was kept at around 900 K, fluxes and fluences were varied ranging from 1×10^{21} ions/(m^{2}s) to 1×10^{23} ions/(m^{2}s) and from 1×10^{26} ions/m^2 to 1×10^{26} ions/m^2 to 2×10^{27} ions/m^2, respectively.

Erosion results for exposures in PSI-2, mass loss Δm and surface recession d_e, support the statement that erosion of WCrY is not increased against that of W during plasma exposure below the W sputter threshold. The same result is obtained for exposures in Magnum-PSI: erosion of WCrY is on average similar to that of W and most similar in the experiment conducted with the highest fluence. In both devices, OES was used to investigate the time evolution of W and Cr sputtering throughout the exposure. Based on the low plasma and flux density in PSI-2, integration times are in the order of about a minute and the signal strength is too low to allow assessing the time evolution of the sputtering. Yet, spectroscopy in D120P2 could confirm that during the entire exposure W and Cr were constantly sputtered. Thanks to integration times in the order of fractions of seconds in Magnum-PSI, it was possible to observe a decrease in the signal of sputtered Cr from values initially above to values below the signal of sputtered W during exposure of WCrY. Hence preferential sputtering of Cr is confirmed. Additionally, decreased W sputtering is observed after Cr depletion at the surface, which hints at enhanced W erosion in the vicinity of Cr at the alloy surface.

Calculations show that the increased plasma density in Magnum-PSI leads to significant re-deposition, which explains reduced erosion at the same fluence compared to experiments in PSI-2. Additionally, a different residual plasma oxygen content could lead to differences in the speed of erosion among the two linear devices. A higher oxygen content leads to faster sputtering at the same flux magnitude. However, the oxygen content cannot be assessed experimentally for both devices. In contrast to the plasma conditions in Magnum-PSI, re-deposition can be neglected in PSI-2 experiments. Here the energy and angular distribution, calculated for the purpose of estimating the significance of re-deposition, are in agreement with experimental observations for W sputtering and ERO calculations. Experimentally, re-deposition could not be detected except for a minute Cr re-deposited area next to a coating edge. This occurred by prompt re-deposition resulting from the edge geometry.

Thanks to this insignificance of re-deposition in PSI-2, it is possible to compare experimental results to results obtained by SDTrimSP modelling. Assuming a plasma oxygen content of 0.23 %, experimental and simulation erosion results match for D, O ion irradiation at an energy of 120 eV at normal incidence and without adding thermal diffusion of Cr to the model. Since re-deposition and self-sputtering cannot be taken into account within the SDTrimSP model, no simulations were carried out for comparison with exposures in Magnum-PSI.

In both linear devices, the depletion of Y and Cr accompanied by an enrichment of W is detected via analysis of the elemental composition of the plasma-exposed WCrY samples. SIMS analysis reveals a shallow depletion of Cr and enrichment of W up to a depth of about 10 nm to 20 nm, Y depletion is extended to a depth of 40 nm to 60 nm. There is no strict fluence dependence recognisable in the investigated range, yet for Magnum-PSI exposures, depletion of Y and Cr and enrichment of W is less distinct for the experiment conducted at the lowest fluence.

EDX analysis on the surface of the WCrY samples exposed in Magnum-PSI, extending to a depth of 100 nm, shows a significantly decreased Cr and increased Y content and a less significantly increased W content. Thus although Y is depleted due to preferential sputtering in the subsurface atomic layers (SIMS analysis results), the overall Y content in the near-surface region is increased. Oppositely for Cr, both the layers directly beneath the surface (as shown by SIMS analysis) and up to a depth of 100 nm show depletion. Thermally activated Cr and Y transport processes, such as diffusion and (surface) segregation are assumed to affect the subsurface alloy composition in addition to the plasma ion irradiation. The XPS analysis carried out for plasma-exposed samples in PSI-2 further hints at depletion of W and Cr up to a depth of 30 nm to 40 nm, which is more pronounced for the experiment with higher fluence, D120P2. Y is not detectable due to its low concentration in the alloy.

NRA analysis carried out for samples exposed in PSI-2 reveal concentrations of retained D close to the detection limit of 1×10^{-6}. This low D retention was expected since at the sample temperatures of about 900 K D is easily released and based on the low D solubility in W.

Changes in surface morphology were analysed with the help of SEM images taken before and after plasma exposure and by measuring the surface roughness R_a. It is found that the roughness is predominantly determined by the previous grinding procedure for exposures in both devices. R_a is slightly increased when measured after plasma or remains constant compared to measurements carried out prior to the exposures. No fluence dependence is recognisable. Generally, on all exposed samples, WCrY as well as W, wave-like structures or ripples are visible. They are increasingly pronounced and increase in size towards higher fluences, at the highest fluence in D120M4 in Magnum-PSI they are well elaborated, especially on the W sample. WCrY samples exposed in PSI-2 show small black holes and bigger elongated craters on the surface along the grain boundaries. Analysis of an EDX-obtained surface map for experiment D120P2 in PSI-2 confirms that these features correspond to depletion of Y and Cr localised at the grain boundaries. They are less visible on the rough WCrY surface. On WCrY samples exposed in Magnum-PSI, some small black holes are visible. However, compared to exposures in PSI-2 there are less of the holes visible and they are less distinct. Elongated craters predominantly along the grain boundaries as found in PSI-2 are not visible on the WCrY samples exposed in Magnum-PSI. The fact that the WCrY surfaces show more similarities to the W surfaces after exposure, further hints at significant re-deposition of especially W in the Magnum-PSI plasma conditions.

7. Plasma exposure at ion energies at or above the W sputter threshold in PSI-2

Besides fuel ions with energies mainly below the W sputter threshold during steady state plasma operation, other scenarios have to be considered for evaluating the qualification of a PFC material.

On the one hand seeding impurities are introduced in a fusion reactor with the aim of cooling the plasma edge (see Chapter 2). These seeding impurities have a higher atomic number Z and therefore sputter the PFC material already at lower energies compared to the fuel ions. Ar is one of the candidates foreseen as seeding species in future fusion devices. Based on the considerations in Section 2.1.3 a seeding level of 1 % of Ar in D plasma was used for a mixed D+Ar plasma while the incident ion energy was kept at 120 eV. He, a product of the D+T fusion reaction, will always be present in a fusion plasma. A further experiment was therefore carried out in a mixed D+5 % He+1 % Ar plasma. On the other hand, in case DEMO is operated in limited configuration, fuel ion energies at the plasma edge will be sufficiently high to cause W erosion. Additionally, CX neutrals with incident energies above the W sputter threshold will cause W erosion. For the pure D plasma exposures at ion energies below the W sputter threshold, sputtering is assumed to be caused mainly by the residual oxygen present in the plasma. To have W erosion caused also by D sputtering and not only by residual O, an ion energy of 220 eV was chosen for an experiment in pure D plasma. Comparing the sputter thresholds in Table 2.2 in Section 2.2, it can be said that D ion energies of 220 eV and He ion energies of 120 eV are just about at the sputter threshold of W, whereas Ar ion energies of 120 eV are clearly above the sputter threshold.

For all the three experiments at ion energies at or above the W sputter threshold, the sample temperature was again kept around 900 K, based on estimates for the DEMO first wall. The experiments were carried out in the linear plasma device PSI-2 at fluxes in the order of $1 \times 10^{21}\,\mathrm{ions/(m^2s)}$ and fluences in the order of $1 \times 10^{25}\,\mathrm{ions/m^2}$ to $1 \times 10^{26}\,\mathrm{ions/m^2}$.

In this chapter, first experimental details for the three experiments are presented, before giving experimental as well as SDTrimSP modelling results. For the exposure in pure D plasma at an ion energy of 220 eV, extensive SDTrimSP modelling was carried out; it serves as an exemplary case for investigating the impact of different model parameters. Eventually, the chapter is concluded with a summary.

experiment	plasma[a]	ion energy [eV]	ion flux [ions/m^{2}s]	ion fluence [ions/m^2]	sample temperature [K]
D220P	1 D	220	5.5×10^{21}	1.0×10^{26}	890 - 940
DAr120P	0.99 D, 0.01 Ar	120	2.8×10^{21}	0.2×10^{26}	890 - 970
DHeAr120P	0.94 D, 0.05 He, 0.01 Ar	120	5.7×10^{21}	0.5×10^{26}	890 - 970

[a]: neglecting residual impurities such as oxygen

Table 7.1.: Experiment parameters of plasma exposures in PSI-2 with main plasma ion energies at or above the W sputter threshold. The plasma ion composition is given in fractions of the total plasma ions neglecting possible impurities such as oxygen.

7.1. Experimental details

For all the three experiments, which were carried out using WCrY and reference W samples in the linear plasma device PSI-2 (see Section 4.1.1), a plasma oxygen impurity content of around 0.2 % to 0.3 % (see Section 6.1.1) is again assumed. One experiment was carried out in pure D plasma at an ion energy of 220 eV and is called D220P. Two experiments were carried out in a mixed D plasma at an ion energy of 120 eV. The plasma composition was D+1 % Ar and D+5 % He+1 % Ar, they are called DAr120P and DHeAr120P, respectively. The plasma temperature T_e ranged from 8 eV to 10 eV, while the plasma density n_e was of the order of $1 \times 10^{17}\,\mathrm{m}^{-3}$. Further experimental parameters are given in Table 7.1.

All samples used for the experiments are listed in Table 7.2, the manufacturing and preparation procedure is described in Section 3.3. Based on the low density of the porous samples DAr120P-WCrY2 and DAr120P-WCrY3 it was decided to reuse a previously exposed non-porous WCrY sample. The plasma-facing surface of D120P1-WCrY2 was reground; a layer of 0.5 mm thickness was removed.

7.2. Experimental results and discussion

7.2.1. Erosion

Erosion results, average surface recession d_e and mass loss Δm of W and WCrY samples, are displayed in Figure 7.1. Three out of four W samples exposed in DAr120P (see Table 7.2) were deformed after plasma exposure as shown in Figure 7.2. The surface looks as if it had been pushed in, the FIB generated marker lines are non-parallel. Measuring the surface recession d_e was not possible for these samples. It is suspected that the deformations arise from mechanical stresses induced during the production of the W plate from which the samples are cut. Samples are not annealed to release stresses prior to exposure since no additional heat treatment should be applied to the WCrY samples and there should be no difference in the sample preparation of W and WCrY samples. Fortunately, these kind of deformations were not detected for any other conducted experiment.

Whereas the surface recession shown in the upper graph in Figure 7.1 is approximately

sample name	experiment	material	density	further comments
D220P-W1	D220P	W	> 98.0 %	
D220P-W2		W	> 98.0 %	
D220P-WCrY1		WCrY	98.2 %	additional FIB crater at the corner
D220P-WCrY2		WCrY	98.5 %	
DAr120P-W1	DAr120P	W	> 98.0 %	damaged after experiment
DAr120P-W2		W	> 98.0 %	
DAr120P-W3		W	> 98.0 %	damaged after experiment
DAr120P-W4		W	> 98.0 %	damaged after experiment
DAr120P-WCrY1		WCrY	98.6 %	
DAr120P-WCrY2		WCrY	91.2 %	porous
DAr120P-WCrY3		WCrY	93.2 %	porous
DAr120P-WCrY4		WCrY	98.4 %	reground D120P1-WCrY2
DHeAr120P-W1	DHeAr120P	W	> 98.0 %	
DHeAr120P-W2		W	> 98.0 %	
DHeAr120P-W3		W	> 98.0 %	
DHeAr120P-WCrY1		WCrY	97.9 %	
DHeAr120P-WCrY2		WCrY	97.9 %	

Table 7.2.: Samples used for plasma exposures in pure D and mixed D with the main plasma ion species at or above the W sputtering threshold. The density as determined using the Archimedes principle (see Section 5.1.5) is given in % of the theoretical density.

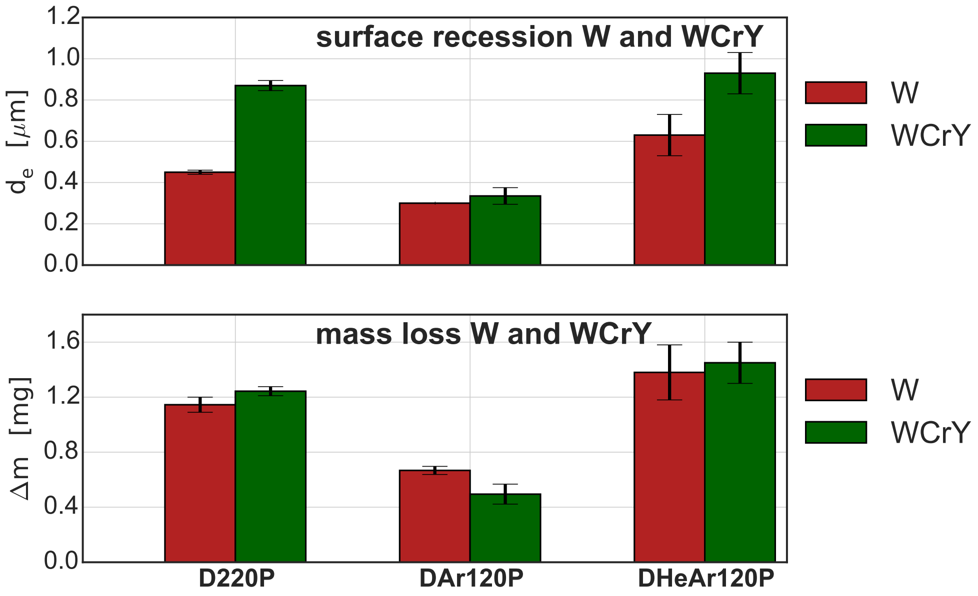

Figure 7.1.: Measured average surface recession d_e (top graph) and mass loss Δm (bottom graph) of W and WCrY samples exposed in D220P, DAr120P and DHeAr120P. Measurement procedures are described in Sections 5.1.5 and 5.1.2.

equal for W and WCrY in DAr120P, it is on average increased for the WCrY samples in D220P and DHeAr120P. Similarly, the mass loss is only reduced for WCrY in DAr120P, whereas it is approximately the same in D220P and DHeAr120P. Using Equation (6.1) to obtain the ratio of mass losses yields $\Delta m_{WCrY}/\Delta m_W \approx 1.08 \pm 0.06$ in D220P, $\approx 0.75 \pm 0.11$ in DAr120P and $\approx 1.05 \pm 0.19$ in DHeAr120P. The values obtained in D220P and DHeAr120P are above the theoretical mass ratio of 0.82, assuming the same volume loss was obtained for both materials. Thus for both the experiments where the ion species mainly responsible for sputtering (D in D220P and He in DHeAr120P) are close to the sputter threshold of W, erosion is increased for the WCrY samples compared to that of W.

It is worth noting that the erosion results are not scaled to the respective fluences of the experiments, since linear up-scaling would require assuming constant erosion rates (see also Section 6.1.2). Hence it is remarked that adding Ar to a pure D plasma at 120 eV significantly enhances erosion. When comparing the results of the mixed plasma exposures to the ones of in pure D plasma, it becomes evident that especially the addition of Ar severely increases erosion. In DAr120P surface recession for W as well as WCrY samples is about 0.3 µm after a fluence of 0.2×10^{26} ions/m^2. Similar surface recession was reached in D120P2 (see Figure 6.1), but just after a fluence of about 1.7×10^{26} ions/m^2. In comparison to the results obtained in D120P1 and D120P2 (see Section 6.1.2), erosion is enhanced by approximately a factor of 7.

Usually, one single FIB crater (see analysis description in Section 5.1.2) is cut in the middle of the sample surface for inferring the surface recession d_e. With the aim of judging the homogeneity of the erosion, on one WCrY sample in D220P, D220P-WCrY1, two FIB craters were cut and evaluated: one FIB crater was located at the usual position in the sample centre and yielded a surface recession of 0.84 µm ± 0.17 µm, the additional FIB crater located at the corner of the sample yielded 0.90 µm ± 0.21 µm (see Table B.4 in Appendix). As these two results agree within error bars, one can conclude that the plasma erosion of the samples is homogeneous across the surface. This is further supported by the fact that results for d_e among the W samples and among the WCrY samples are consistent.

Using the spectroscopy setup at PSI-2, the line radiation of neutral W (WI) at 429.5 nm and neutral Cr (CrI) at 427.5 nm were monitored. Due to the low sputtering rates in a plasma consisting mainly of D at the PSI-2 ion fluxes of the order of 1×10^{21} ions/(m^{2}s), signal integration times were set to 30 s for DAr120P and DHeAr120P. Radiation intensities are not absolutely calibrated and depend on the plasma conditions. Moreover, since plasma parameters are adjusted in the first minutes of the experiment, with the target already being exposed, and since due to the large integration time the changes cannot be captured, the time evolution of the sputtering behaviour is not inferable. Yet, spectroscopy measurements were taken at time intervals of at least an hour during the experiments DAr120P and DHeAr120P. For these experiments continuous line radiation of neutral W and Cr and thus continuous erosion of W and Cr from the target were detected. It was again observed that starting from approximately half an hour after the exposure start, under steady plasma conditions there was no significant change in the signal intensities till the end of the exposure. There is no spectroscopy data available for D220P.

Since the plasma conditions during the here reported experiments are very similar to the ones reported in Section 6.1 with respect to the plasma temperature T_e and the plasma density n_e, re-deposition can be neglected in a first approximation.

7.2.2. Elemental composition

The depth-resolved elemental compositions of samples D220P-WCrY1, DAr120P-WCrY1 and DHeAr120P-WCrY2, starting from the surface at a depth of 0 nm, measured by SIMS are shown in Figures 7.4, 7.5 and 7.6.

As described in Section 5.1.7, the signal intensities of the W, Cr and Y signals are normalised to be one in the bulk, i.e. the average over the 10 deepest measured data points. Here it is assumed that the initial elemental properties of the bulk material are reached, thus only the relative change and no quantitative information is displayed. Again, the impact of the surface roughness as well as impurity and oxide deposition at the surface have to be taken into account for the interpretation of the signals close to a depth of 0 nm. This issue is further discussed in Chapter 10.

For D220P-WCrY1, the Y intensity increases starting from about 20 nm to 30 nm below the surface before plasma (see top graph of Figure 7.4). This behaviour can be attributed to the accumulation of YO particles in the subsurface layer (see Figure 7.3), which is damaged by manual grinding and agrees well with the size of the YO particles. Whereas the Y signal intensity decreases closer to the surface after plasma exposure (bottom graph of Figure 7.4), both the W and Cr intensities do not show significant deviation from the pre-plasma elemental composition. For W, the signal is a bit elevated in the first approximately 5 nm below the surface indicating a shallow enrichment. A clear depletion of Y only is inferable from the SIMS analysis.

The Y and the Cr signal intensities of DAr120P-WCrY1 (Figure 7.5) prior to plasma exposure show a sharp increase towards the surface. These two or three measured data points at the surface are considered to be artefacts from the analysis such as non-equilibrium conditions of the sputter beam or surface roughness. These peaks have

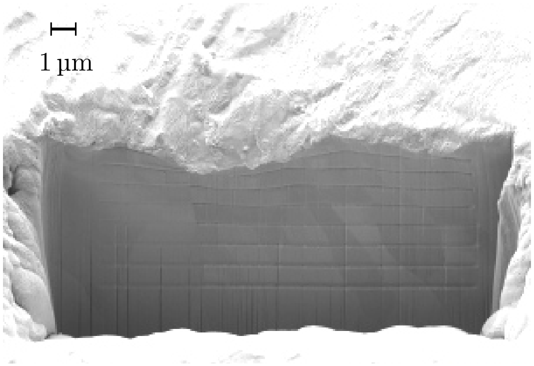

Figure 7.2.: SEM image of FIB cross section of damaged sample DAr120P-W3 after exposure.

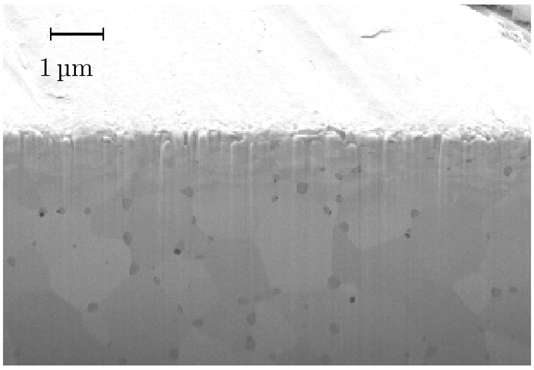

Figure 7.3.: SEM image of FIB cross section of ground sample D220P-WCrY1 before exposure.

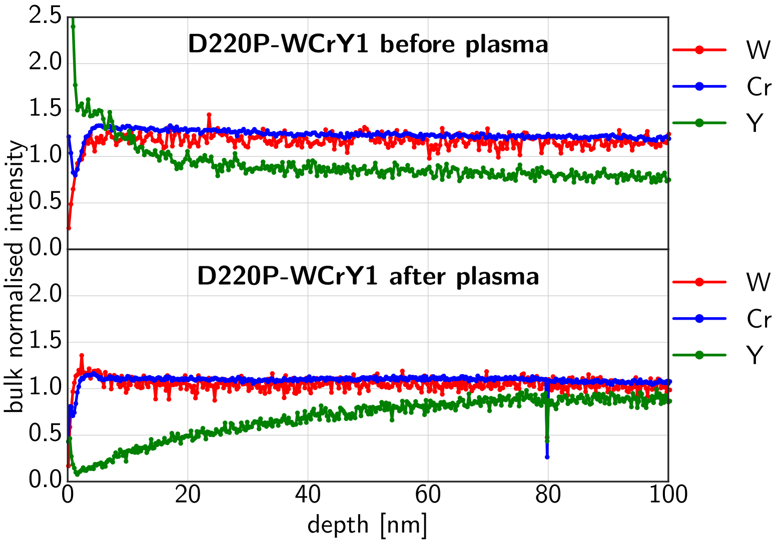

Figure 7.4.: SIMS analysis of sample D220P-WCrY1.

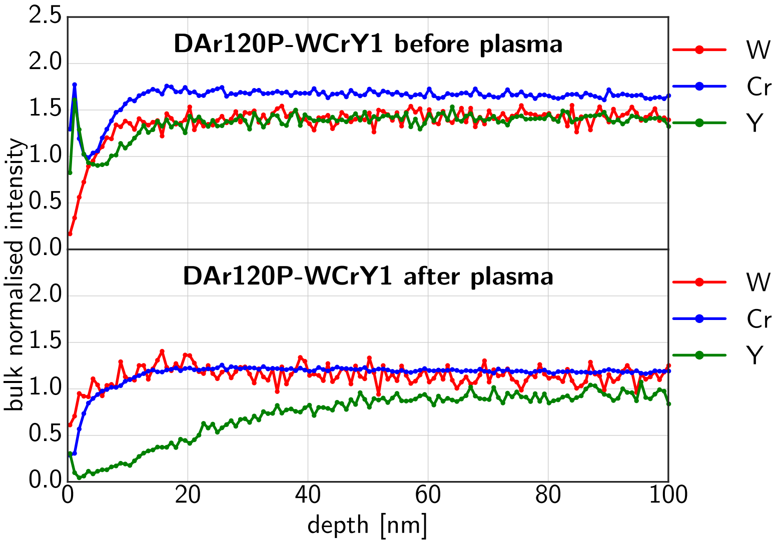

Figure 7.5.: SIMS analysis of sample DAr120P-WCrY1.

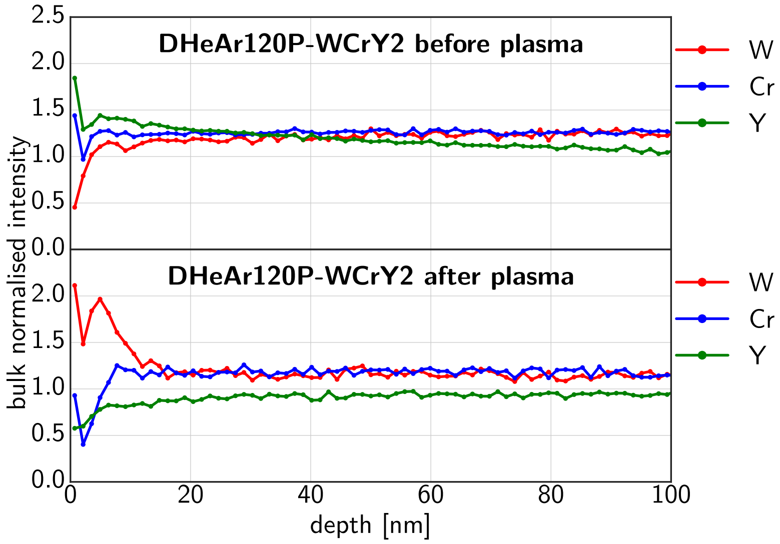

Figure 7.6.: SIMS analysis of sample DHeAr120P-WCrY2.

vanished after plasma exposure. Whereas Y after plasma shows significant depletion, no distinct enrichment of W and only a very shallow depletion of Cr can be detected.

The bulk normalised depth-resolved intensities of W, Cr and Y in sample DHeAr120P-WCrY2 are shown in Figure 7.6. The Y signal decreases in the first 20 nm below the surface after plasma exposure. Moreover, a slight depletion of Cr and enrichment of W is visible. Compared to results reported for PSI-2 exposures below the W sputter threshold (6.1.2), depletion of Cr and enrichment of W is less shallow or not detectable. Still, one has to be aware that the surface roughness, which is about 30 % increased for DHeAr120P after plasma, more than for D220P and DAr120P (see Table 7.4), complicates surface analysis with SIMS.

Sputter-XPS was used as another means to obtain the depth-resolved alloy elemental composition after plasma. As already explained in Section 6.1.2, the profiles obtained are a combination of the plasma ion impact during the experiment and the Ar ion impact during the analysis itself. No sputter-XPS profiles were obtained for exposure D220P. Results of DAr120P-WCrY3 and DHeAr120P-WCrY2 are displayed in Figure 7.7. Enrichment of W and depletion of Cr is visible for both samples. For DHeAr120P-WCrY2 the increase of W and accordingly the Cr decrease towards the surface are more sharp than for DAr120P-WCrY3. Here the W increase and Cr decrease respectively are more gradually extending up to a depth of more than 100 nm. In contrast, profiles of DHeAr120P-WCrY2 show a pronounced change up to a depth of around less than 40 nm. These findings of steeper gradients in the W enrichment and Cr depletion in DHeAr120P compared to DAr120P is in agreement with the SIMS results. The detected Y signal again is very close to the noise level because of the low Y content.

As previously shown in Section 6.2.2, EDX was used as further means of detecting changes in the elemental (sub-)surface composition for WCrY samples exposed in DHeAr120P. Using a 5 kV electron beam a surface area of approximately 200 µm × 200 µm was anal-

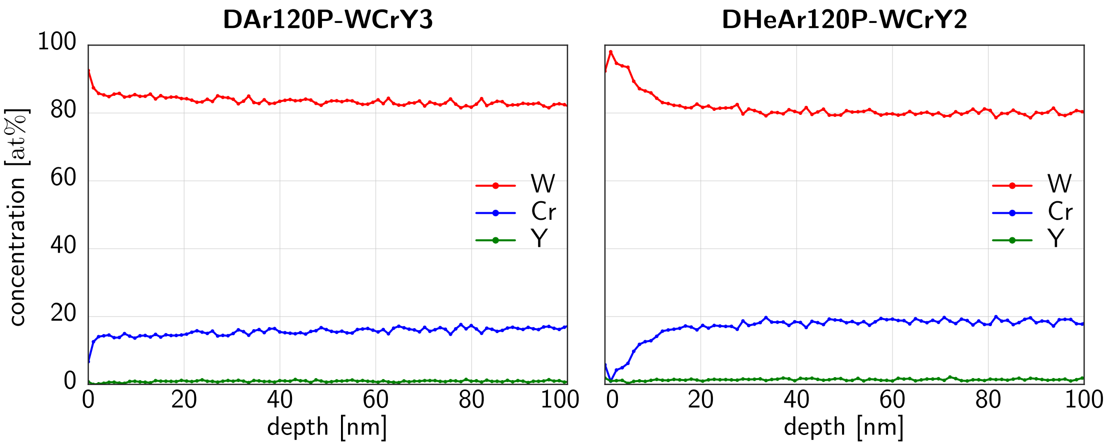

Figure 7.7.: Sputter-XPS analysis of samples DAr120P-WCrY3 and DHeAr120P-WCrY2.

ysed extending to a depth of about 100 nm in WCrY. The measured W, Cr and Y surface concentrations given in wt% are displayed in Figure 7.8. The same non-exposed WCrY samples as already used previously in Section 6.2.2 are taken as reference and indicated by dotted lines.

In the uppermost graph of Figure 7.8 a significant rise in the W surface concentration is observed, while the Cr surface concentration is significantly decreased in the middle graph. The Y concentration is just slightly increased compared to the reference values in the bottom graph. Comparison of these results with the ones obtained by SIMS and

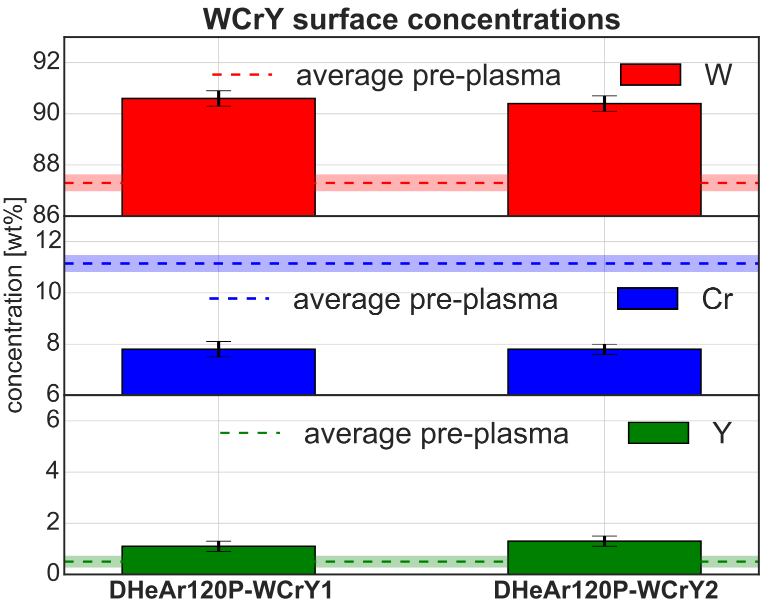

Figure 7.8.: Surface concentrations of samples DHeAr120P-WCrY1 and DHeAr120P-WCrY2 after exposure as measured by EDX at an incident beam energy of 5 kV over a surface area of approximately 200 µm × 200 µm.

XPS suggests that the average enrichment of W and depletion of Cr extends over the first 100 nm beneath the surface. The Y concentration in this layer is on average increased, at the same time the SIMS profiles show a decline closer to the surface. Further, the EDX results in Figure 7.8 show the same W, Cr and Y behaviour as the EDX results for the samples exposed in Magnum-PSI (Figure 6.37). Similarly, it is assumed that thermally activated processes impact the subsurface Cr and Y concentration in addition to the preferential sputtering due to plasma ion irradiation.

The NRA setup described in Section 5.1.6 was used for detection of retained D after plasma exposure. Results are presented in Table 7.3. For D220P no exposed W sample was measured. On average, all the detected concentrations of retained D are very close to the detection limit of 1×10^{-6}. This general trend is to be expected since at the high sample temperatures of around 900 K D is easily released. After the exposure at 220 eV in pure D and the exposure to mixed D+Ar+He plasma, the retained D concentration in WCrY is increased in layer 1 by about a factor of 5 to 10 compared to the available W concentrations.

7.2.3. Surface morphology

Surface images of one sample exposed in DAr120P and one unexposed WCrY reference sample were taken with the LSCM (analysis description in Section 5.1.3). In Figure 7.9 these images are shown. On both surfaces scratches from the grinding procedure are visible, including after plasma exposure in DAr120P. This implies that even after plasma exposure the grinding procedure has an impact on the measured surface roughness R_a and explains why R_a is just slightly increased after plasma or stays approximately constant (see Table 7.4) when measured with the Dektak surface profilometer (see analysis description in Section 5.1.8). The size of the structures induced by plasma (see SEM images further below) is in the nanometre range and therefore most probably too small to be detected with this method. Further, on the plasma-exposed sample the alloy's grain boundaries are visible as if the sample surface has been etched and the grain boundaries were especially attacked. This finding suggests that during plasma exposure the grain boundaries are preferentially sputtered, which in turn implies that the lighter alloying elements are predominantly located at the grain boundaries.

To have a closer look on the surface, SEM images were taken before and after plasma exposure at different magnifications. For images of the surface of a WCrY and a W sample before exposure, Figures 6.14 and 6.19 in Section 6.1.2 are referred to, since all

experiment	sample	D concentration layer 1	D concentration layer 2
D220P	D220P-WCrY2	5×10^{-6}	1×10^{-6}
DAr120P	DAr120P-WCrY2	$<1 \times 10^{-6}$	$<1 \times 10^{-6}$
	DAr120P-W1	2×10^{-6}	2×10^{-6}
DHeAr120P	DHeAr120P-WCrY2	9×10^{-6}	$<1 \times 10^{-6}$
	DHeAr120P-W3	$<1 \times 10^{-6}$	$<1 \times 10^{-6}$

Table 7.3.: Retained D concentration in layer 1 (0 µm to 3 µm) and layer 2 (3 µm to 8 µm) of plasma-exposed samples in D220P, DAr120P and DHeAr120P.

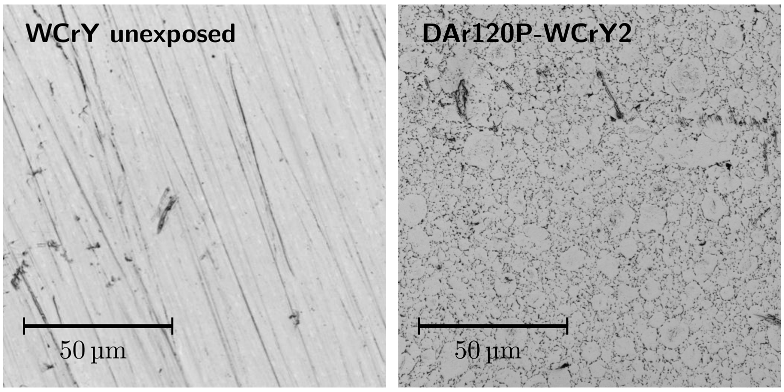

Figure 7.9.: Surface image taken with the LSCM on unexposed WCrY sample (left) and DAr120P-WCrY2 (right) after plasma exposure.

samples are prepared according to the same procedure described in Section 3.3 with a surface finish of $R_a \approx 30\,\mathrm{nm}$. The SEM images taken of the WCrY and subsequently those of the W samples exposed in D220P, DAr120P and DHeAr120P are shown in Figures 7.10 to 7.15.

The surface imaged by SEM of D220P-WCrY1 is shown in Figure 7.10. D220P-WCrY1 is characterised by a coarser microstructure featuring bigger YO particles as well as WCr grains as a result of different parameters during the sintering process (see Figure 7.3 and

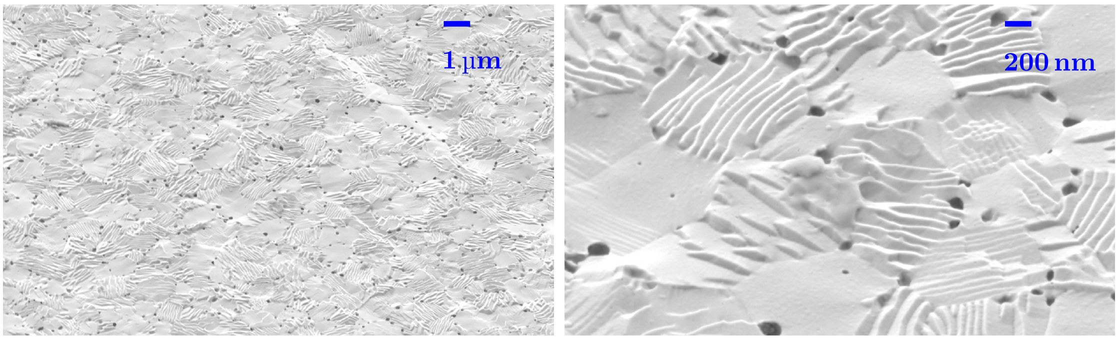

Figure 7.10.: SEM images of D220P-WCrY1 after plasma.

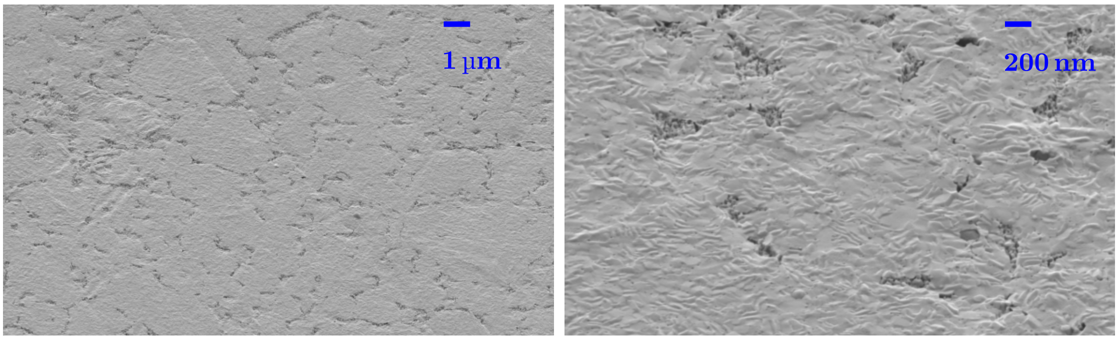

Figure 7.11.: SEM images of D120ArP-WCrY2 after plasma.

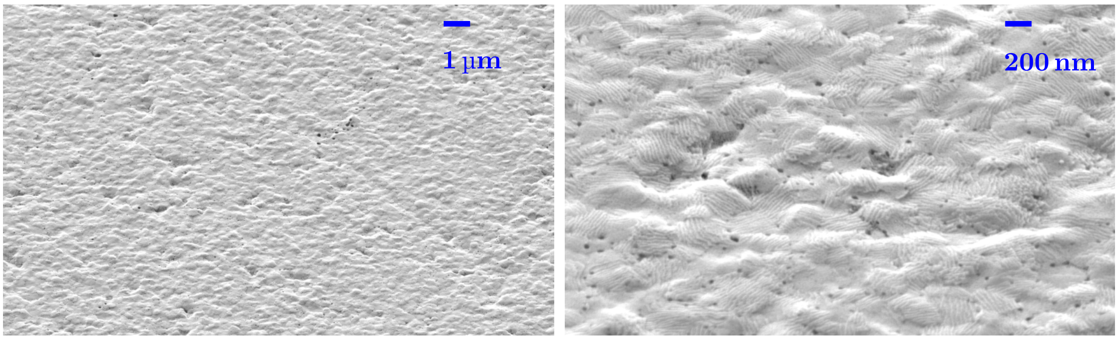

Figure 7.12.: SEM images of DHeAr120-WCrY2 after plasma.

Section 3.3). For this sample the small black holes, signs of superficial Y depletion, but no bigger elongated craters, signs of superficial Cr depletion, are visible on the surface. SEM images of WCrY exposed in DAr120P and DHeAr120P can be seen in Figures 7.11 and 7.12. The surface of DAr120P-WCrY2 shows elongated craters along the grain boundaries and small black holes on the surface. These are very similar but not as pronounced as for the sample exposed to sub-threshold pure D plasma in PSI-2 in the previous section. Adding He to the D+Ar plasma (DHeAr120P-WCrY2) results in an increased number of small black holes and less shallow craters. Hence it is assumed that due to the less pronounced Cr depletion, the depletion of Y (small back holes) becomes more visible.

On all exposed W and WCrY samples, wave-like structures with a wavelength in the order of tenths of nm correlating with the grain orientation can be seen. These waves or ripples are smaller for the samples exposed in DAr120P and DHeAr120P with smaller grains, compared to the sample exposed in D220P with bigger grains. The addition of 1 % of Ar in DAr120P leads to more pronounced ripples. In comparison, adding 5 % of He to the mixed D+Ar plasma, makes the ripples look more smooth and fine (DHeAr120P-WCrY2 and DHeAr120P-W2). On DHeAr120P-WCrY2 it can be seen that although the craters along the gain boundaries mentioned earlier and seen for example on the surface of DAr120P-WCrY2, are less pronounced, the overall surface seems more homogeneously attacked, more rough. This could be a result of the enhanced W sputtering in the vicinity of Cr at energies close to the W sputter threshold (see Figure 7.19 in Section 7.3). Due to this enhanced W sputtering no sharp edge or crater develops at the location where Cr is preferentially sputtered since the edges surrounding the crater consist of W.

The surface roughness was measured before and after plasma exposure according to the description in Section 5.1.8. In D220P and DAr120P, the surface roughness remained approximately constant or increased slightly, similarly to the results found for the PSI-2 exposures in pure D plasma below the W sputter threshold, D120P1 and D120P2. In contrast, the mean surface roughness of W and WCrY samples is about 30 % increased after plasma exposure in DHeAr120P. As displayed in Table 7.4 for W, R_a rises from 25 nm ± 8 nm to 37 nm ± 11 nm, for WCrY it rises from 37 nm ± 17 nm to 58 nm ± 12 nm.

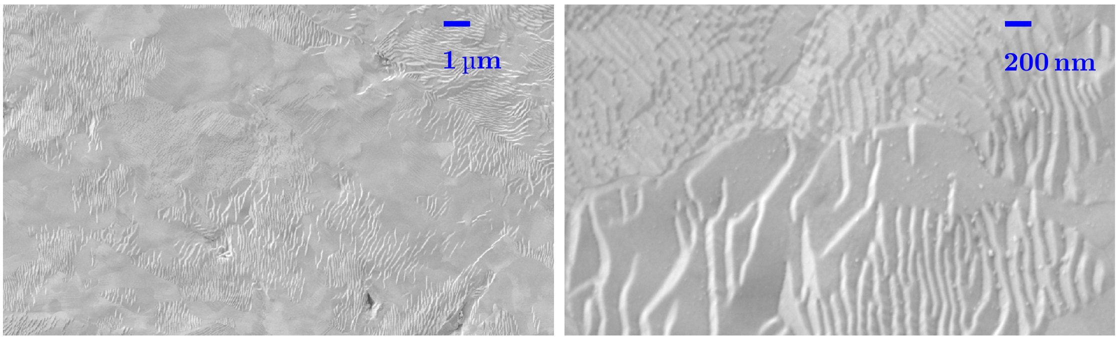

Figure 7.13.: SEM images of D220P-W2 after plasma.

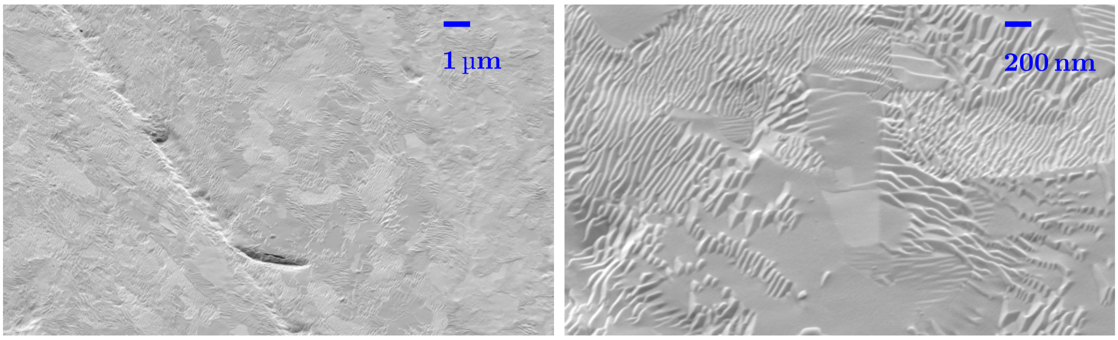

Figure 7.14.: SEM images of DAr120P-W2 after plasma.

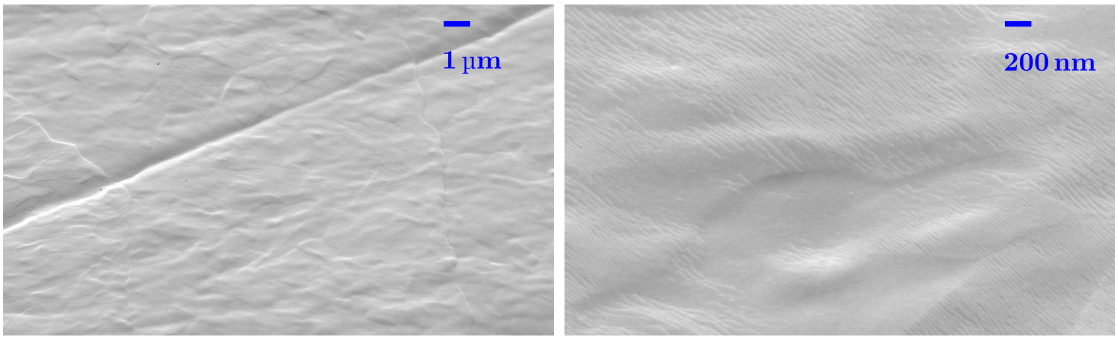

Figure 7.15.: SEM images of DHeAr120P-W2 after plasma.

experiment	sample	R_a before [nm]	R_a after [nm]
D220P	$\overline{\text{W}}$	35 ± 14	40 ± 15
	$\overline{\text{WCrY}}$	27 ± 9	30 ± 13
DAr120	$\overline{\text{W}}$	29 ± 8	34 ± 15
	$\overline{\text{WCrY}}$	32 ± 13	28 ± 9
DHeAr120	$\overline{\text{W}}$	25 ± 8	37 ± 11
	$\overline{\text{WCrY}}$	37 ± 17	58 ± 12

Table 7.4.: Average roughness R_a results over the W ($\overline{\text{W}}$) and WCrY ($\overline{\text{WCrY}}$) samples exposed in D220P, DAr120P and DHeAr120P.

7.3. SDTrimSP modelling results and discussion

In this section the SDTrimSP modelling (see description in Section 5.2) results for experiments D220P, DAr120P and DHeAr120P are presented. The SDTrimSP model and the methods to obtain surface recession and mass loss are described in detail in Chapter 5.2.

7.3.1. D plasma at an ion energy of 220 eV

Plasma exposure D220P serves as an exemplary modelling case since experimental results hint at enhanced erosion of lighter alloying elements: defining ρ_e, the density of the sputtered material, to be the quotient of mass and volume loss yields

$$\begin{aligned}\rho_e &= \Delta m/\Delta V = \Delta m/(d_e \cdot A) \\ &\approx 1200\,\mu\text{g}/(850\,\text{nm} \cdot 1\,\text{cm}^2) \approx 14.1\,\text{g}\,\text{cm}^{-3}.\end{aligned}$$

With an initial alloy composition of 67.9 at% W - 31.1 at% Cr - 1.0 at% Y, the initial theoretical density of the smart alloy is $\rho_{i,0} = 15.9\,\text{g}\,\text{cm}^{-3}$. Measurements according to the Archimedes principle confirmed an initial density of more than 98 %. Thus the minimum initial density ρ_i of WCrY in D220P is $15.9\,\text{g}\,\text{cm}^{-3} \cdot 0.98 = 15.6\,\text{g}\,\text{cm}^{-3}$. If the material is sputtered without significant mixing of material, the density of the eroded material ρ_e must approximately equal the initial material density ρ_i. Since the value of ρ_e is smaller than ρ_i, one can conclude that more lighter elements were eroded than initially present in the eroded volume. To investigate this enhanced erosion of lighter alloying elements and therefore transport of these to the surface, it was decided to include thermal diffusion of Cr in WCrY in the simulation. As only 1.0 at% of the alloy is Y, the Y transport to the surface was neglected. Several simulations with varying parameters, such as the oxygen content of the plasma or the diffusion coefficient of Cr in WCrY, were carried out. For adapting the diffusion coefficient $D_0(i,j)$ (see Equation (5.12) in Section 5.2), experimental values are used for benchmarking: the experimentally obtained surface recession d_e (see Figure 7.1) is taken to be 450 nm for pure W and 850 nm for WCrY. Mass loss Δm reference values for W and WCrY are 1.1 mg and 1.2 mg, respectively. Both the measured mass loss and the surface recession are subject to measurement uncertainties, which is considered for determining the model parameters. Neither preferential sputtering nor diffusion have to be considered for the erosion yield of pure W samples.

Simulations for the exemplary case D220P were carried out with 220 eV ions at normal incidence. In the following subsections, the effects of D ion irradiation, oxygen plasma content and Cr diffusion are presented according to their order of implementation in the model. Subsequently, effects of D retention, surface binding energies and possible other factors are looked upon. Following this, two-dimensional SDTrimSP simulations are presented, which aim at qualitatively investigating the effect of diffusion occurring predominantly along the grain boundary.

The last part of this section is devoted to the presentation of the main simulation results of the exposures to mixed D+Ar/He plasmas.

Pure D irradiation

Sputter thresholds for pure W, Cr and Y calculated with SDTrimSP in static mode (see description in Section 5.2) are shown in Table 7.5. The thresholds for W and Cr are about 220 eV and 35 eV, respectively, and are approximately in agreement with the threshold values as presented in [104], 216 eV for W and 34 eV for Cr. Thresholds given by [31] in Table 2.2 for D are 230 eV on W and 35 eV on Cr. Oxygen sputter thresholds are considerably lower. According to SDTrimSP thresholds for O are 45 eV on W and 20 eV on Cr. Especially at D ion energies close to or below the threshold, the effect of impurity oxygen becomes important [105]. Consequently it can be expected that already small amounts of O in the target ion flux have a large impact on the material's erosion. Surface recession results for W (yellow line) and WCrY (purple line) in pure D are shown in Figure 7.16, the first data point at $x = 0$ corresponds to an oxygen amount of 0 % in the plasma. For W, the simulated surface recession amounts to only below 1 nm. This is far below the experimental value of 450 nm (red dotted line). Consequently, by simulating the plasma exposure with irradiation of pure D ions at 220 eV the experimental erosion results cannot be matched, neither for W nor for WCrY.

Mixed D,O irradiation

The plasma oxygen content was varied in a next step. This value likely amounts to a few tenths of one percent in PSI-2 (see Section 4.1.1). Surface recession versus varying oxygen content is displayed for both pure W and WCrY in Figure 7.16. Experimental surface recession of pure W (450 nm) is reproduced assuming a plasma composition of 99.73 % D and 0.23 % O, here the red dotted and yellow line intersect. Hence, this composition was used for further calculations. By including oxygen-induced erosion, the experimentally obtained surface recession of pure W can be rendered at 0.23 % O, whereas the WCrY surface recession is with about 565 nm far below the experimental value. Hence some factor increasing the erosion of WCrY against that of W at the same plasma conditions must be included in the model.

Mixed D,O irradiation including diffusion

To increase the sputtering of lighter alloying elements during the ion bombardment, these must be transported to the surface. The transport process was simulated by including

target	bombarding ion species		
	D	O	Ar
W	220	45	35
Cr	35	20	20
Y	60	15	20

Table 7.5.: Thresholds [eV] for pure elements W, Cr and Y sputtered by D, O and Ar as calculated with SDTrimSP at normal incidence using surface binding energies E_{sb} of 8.79 eV, 4.10 eV and 4.26 eV for W, Cr and Y, respectively.

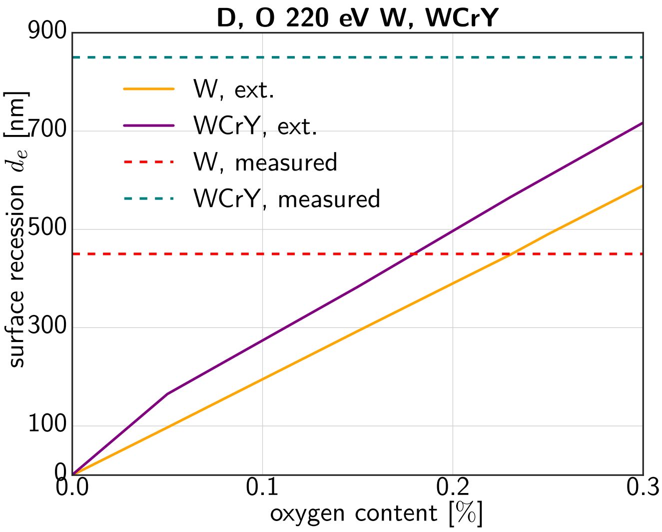

Figure 7.16.: Surface recessions [nm] under D, O 220 eV ion bombardment: simulated and extrapolated values for pure W and WCrY with variation of the oxygen content O. Experimentally measured values for the surface recession d_e of W and WCrY are indicated by horizontal dotted lines.

thermal diffusion (see model description in Section 5.2). For varying the diffusion coefficient of Cr in WCrY, $D_{Cr,WCrY}$, the oxygen content of the plasma is fixed to 0.23 %. In order to calculate besides the surface recession also the mass loss from the simulations, the partial sputter yields are used. The evolution of the partial sputter yields of W, Cr and Y is displayed in Figure 7.18 up to a fluence of 1×10^{25} ions/m^2 for the diffusion coefficient $D_{Cr,WCrY}$ set to 5×10^{-18} m^2/s (right hand side) and without dif-

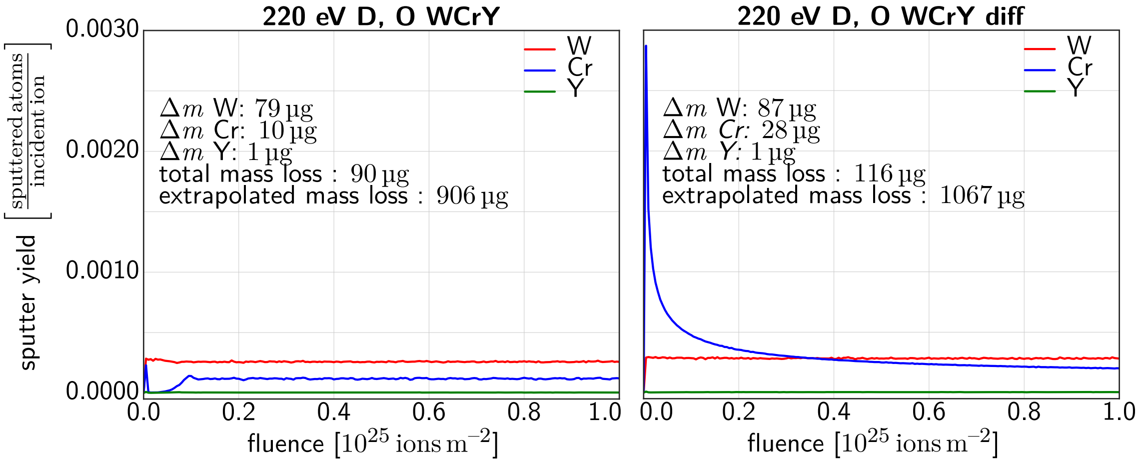

Figure 7.17.: Simulated partial sputter yields of W, Cr and Y for WCrY without diffusion on the left and with the diffusion coefficient of Cr in WCrY, $D_{Cr,WCrY}$, set to 5×10^{-18} m^2/s on the right. The mass loss per element is obtained via integration of the partial yield curves.

fusion (left hand side). The mass loss is extrapolated to the experimental fluence of 1×10^{26} ions/m^2. All yield curves show an asymptotic trend towards increasing fluence, i.e. the sputter yields converge. The total mass loss is the sum of the partial mass losses for W, Cr and Y. Up to the calculated fluence the mass loss is obtained via integration of the yield curves, the yield obtained for the last fluence step is used for extrapolating the mass loss up to higher fluences. Mass loss caused by Y erosion is insignificant compared to mass loss caused by W and Cr, since only 1 at% of the alloy consist of Y and Y diffusive transport is neglected. On average, most of the mass loss is caused by W sputtering. Without taking diffusion into account, the W sputter yield is the highest yield throughout the whole simulation. In contrast to this, taking diffusion into account leads to Cr sputtering being dominant at the beginning of the irradiation. The Cr partial sputtering yield is increased compared to the end of the simulated fluences for both cases, because at first Cr is present at the surface and preferentially sputtered. If diffusion is neglected the Cr sputter yield then decreases as Cr is depleted before reaching a steady level at a fluence of about 0.1×10^{25} ions m^{-2}. At this fluence enough W has been sputtered by the D, O ions so that Cr is accessed again. For the non-diffusion case the extrapolated weight loss stays with 906 µg below the experimental value of about 1200 µg. If diffusion is taken into account, the Cr sputter yield is higher than W and Y yields and decreases below the value of W only after a fluence of about 0.4×10^{25} ions m^{-2}. Moreover, both the erosion yields for W and Cr are increased compared to the non-diffusion case. This leads to an accelerated and non-linear surface recession as can be seen in Figure 7.18. In this figure the simulated (and not extrapolated) surface recession evolutions of WCrY without diffusion and with diffusion at the diffusion coefficient $D_{Cr,WCrY}$ set to 5×10^{-18} m^2/s are shown. Simulating 10 % of the experimental fluence,

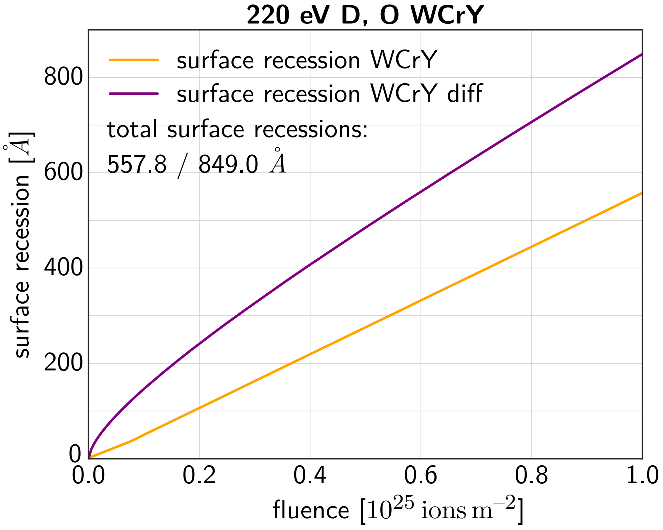

Figure 7.18.: Simulated surface recession of WCrY without diffusion (yellow graph) and with diffusion at a diffusion coefficient $D_{Cr,WCrY}$ set to 5×10^{-18} m^2/s (purple graph). 85 nm corresponds to 10 % of the experimentally measured WCrY surface recession.

1.0×10^{25} ions/m^2, yields a surface recession of around 56 nm without and 85 nm with diffusion. The latter value corresponds to 10 % of the experimentally measured WCrY surface recession.

In case Cr gets preferentially sputtered in the course of the irradiation, at some point less Cr atoms are present at the surface so that then more W is sputtered since the probability for a projectile ion to hit a W target atom is increased. Adding diffusion to the model leads to Cr transport towards the surface in case preferential sputtering creates Cr concentration gradients. For a higher diffusion coefficient the Cr transport towards the surface is stronger, provided a Cr concentration gradient exists. Stronger diffusion results in less Cr depletion at the alloy's surface, up to a higher fluence the sputter yield of Cr is higher than that of W. Thus the overall mass loss is increased as the mass loss caused by Cr as well as for W is increased. The increased W sputtering stems from the effect of more effective W sputtering in the vicinity of Cr atoms: according to BCA the maximum elastic energy transfer between two colliding atoms 1 and 2 is

$$\gamma = 4m_1m_2/(m_1+m_2)^2 \tag{7.1}$$

$$\gamma_{D,W} \approx\ 0.04,\ \gamma_{D,Cr} \approx\ 0.14,\ \gamma_{Cr,W} \approx\ 0.69 \rightarrow\ \gamma_{D,Cr,W} \approx\ 0.10$$

With an intermediate Cr-W collision instead of the direct energy transfer from D to W, the energy transfer factor γ is increased from 0.04 to 0.10. Thus in the vicinity of Cr atoms W sputtering is augmented. This is also evident from Figure 7.19 where the sputter yields of W and Cr in a WCr system with the Cr concentration varying from 0.0 (where the W concentration is 1.0) to 1.0 (where the W concentration is 0.0) under irradiation of 220 eV D ions are shown. For increasing Cr content in the WCr system, the W sputter yields increases up to a Cr content of about 0.6 where it reaches its maximum of about 1.4×10^{-2}. Increasing the Cr content beyond this point leads to a decreasing W sputter yield as less W is accessible to be sputtered.

In case diffusion is taken into account, the non-linear evolution of the surface recession (see Figure 7.18) complicates the extrapolation of simulation results. With the aim of investigating the error induced by extrapolation, one calculation for W and one for WCrY, with $D_{Cr,WCrY}$ set to 5×10^{-18} m^2/s, were performed up to a fluence of 1×10^{26} ions/m^2 (100 % of the experimental fluence). These non-extrapolated simulations are compared to simulations which were calculated to 10 % and then extrapolated. Both are displayed for WCrY in Figure 7.20: while at 1×10^{25} ions/m^2, 10 % of the experimental surface recession, 85 nm, are met by both the extrapolated and the non-extrapolated simulation, results converge for larger fluences. The extrapolated simulation yields a value of 723 nm (green line), which is below the experimental value of 850 nm (teal dotted line). The non-extrapolated simulation results are represented by the yellow line and purple line for W and WCrY, respectively, in Figure 7.20. The non-extrapolated simulation yields a value of 660 nm (purple line), which is below the extrapolated value of 723 nm (green line). In case diffusion does not play a role, hence for W, the surface recession behaves linear and extrapolated and non-extrapolated curves lie on top of each other. Yet, for WCrY both the extrapolated (teal line) and the non-extrapolated (purple line) simulation results at 100 % of the experimental fluence stay with 660 nm and 723 nm below

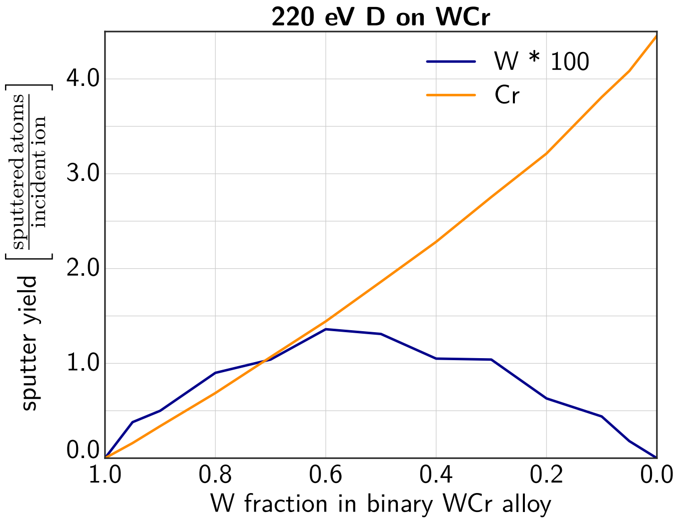

Figure 7.19.: Simulated sputter yields of W and Cr in a WCr system with varying Cr content during 220 eV D ion irradiation.

the experimental value of about 850 nm. At the same time these results support setting the diffusion coefficient to a value greater than $5 \times 10^{-18}\,\mathrm{m}^2/\mathrm{s}$. The convergence of the extrapolated and non-extrapolated simulation results can be explained by the fact that the yield curves have not fully reached stationary conditions at the end of the simulated fluence. Since the surface recession is not yet strictly linear for WCrY at a fluence of $1 \times 10^{25}\,\mathrm{ions/m}^2$ for a diffusion coefficient in the order of $1 \times 10^{-17}\,\mathrm{m}^2/\mathrm{s}$, the model results deviate for later steps. Thus for more exactly determining the numerical value of the diffusion coefficient, simulations should be extended to 100 % of the experimental fluence. Yet, this would require computation times of several weeks. Moreover, one has to take into account that the experimental surface and mass loss values are subject to measurement uncertainties which have an impact on the exact value of the diffusion coefficient as well. Consequently for assigning a conclusive value to the diffusion coefficient, both the surface recession and the mass loss were considered.

Diffusion can be increased either by an increased diffusion coefficient or by increased sample temperatures. However, the temperature was not varied in the simulations as for this purpose detailed knowledge on material-specific parameters like the activation energy Q_a of Cr in WCrY has to be known. Consequently, the diffusion coefficient was varied over several orders of magnitude. Surface recession values are calculated up to a fluence of $1 \times 10^{25}\,\mathrm{ions/m}^2$ and then extrapolated, results are shown in Figure 7.21. The blue shaded bar indicates the range for the diffusion coefficient in which extrapolated simulation results either exactly match the experimentally found surface recession d_e (left edge of the blue shaded bar) or the experimentally found mass loss Δm (right

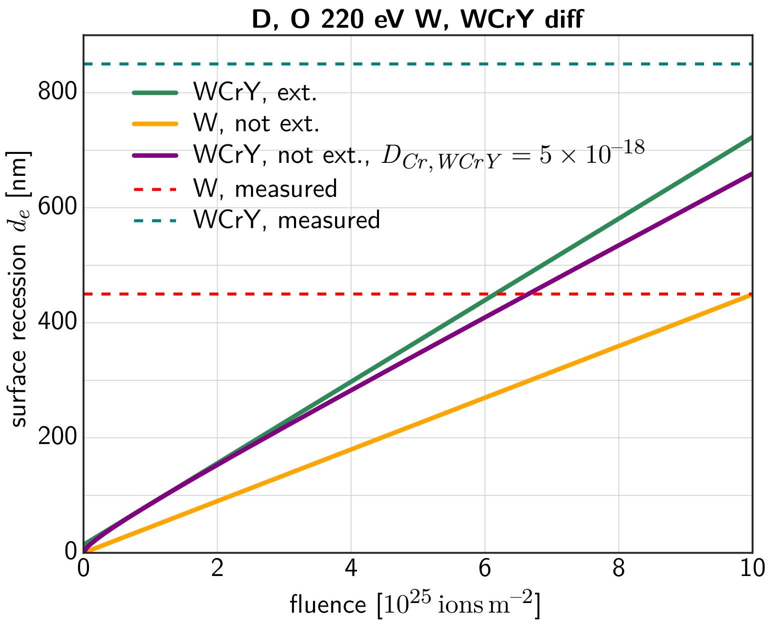

Figure 7.20.: Surface recession of pure W and WCrY (including diffusion with $D_{Cr,WCrY} = 5 \times 10^{-18}\,\mathrm{m^2/s}$) calculated for the experimental fluence of $1 \times 10^{26}\,\mathrm{ions/m^2}$ and not extrapolated (W and WCrY not ext.) and calculated for a fluence of $1 \times 10^{25}\,\mathrm{ions/m^2}$ and then extrapolated to the experimental fluence (WCrY ext.). Experimentally measured values for the surface recession d_e of W (in red) and WCrY (in teal) are indicated by horizontal dotted lines.

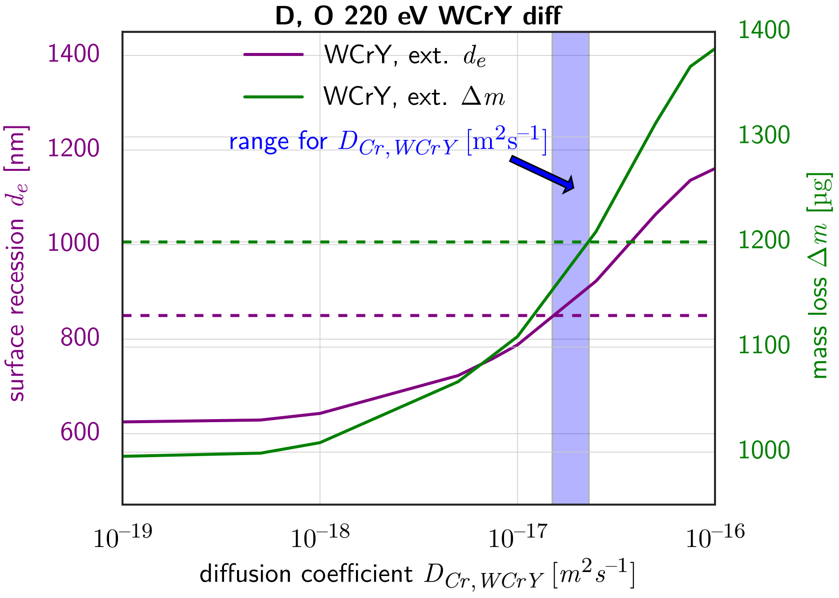

Figure 7.21.: Extrapolated (ext.) surface recession (d_e) and mass loss (Δm) for WCrY with varying diffusion coefficient under D, O (0.23 % O) 220 eV ion bombardment. Experimentally measured values for the surface recession d_e (in purple) and the mass loss Δm (in green) of WCrY are indicated by horizontal dotted lines.

edge of the blue shaded bar). The diffusion coefficient has to be set to a value within the blue-shaded range in Figure 7.21, 2 to $3 \times 10^{-17}\,\mathrm{m^2/s}$, so that both d_e and Δm are matched within measurement uncertainties.

Role of surface binding energy and retention

A further factor influencing the erosion yield of a material is the surface binding energy E_{sb}. This is the energy that a target surface atom needs to overcome to get sputtered (see Chapter 2). Surface binding energies of the constituent elements can differ from those of the pure elements [48]. A lower E_{sb} value leads to increased erosion. Thus a lower binding energy of the WCrY constituent element W could be another possible cause of the enhanced erosion of WCrY in comparison to pure W. For W the default value in SDTrimSP tables is 8.79 eV. Lowering of E_{sb} to 6 eV for W in WCrY at a plasma oxygen content of 0.23 % leads to an extrapolated surface recession of about 3 µm at a mass loss of about 4.7 mg. This would mean a density of the eroded material of $\rho_e = 15.7\,\mathrm{g\,cm^{-3}}$, which is about the initial density of the alloy. Hence, a much lower surface binding energy of W in a mixed material may contribute to enhanced overall erosion. Yet, for explaining the reduced density of the eroded material, transport of lighter alloying elements such as Cr to the surface is necessary.

For evaluating the suitability of PFCs, it is important to consider D retention. At the high sample temperatures of about 900 K during the experiments, D is easily released and its content is hence very low when measured afterwards. As stated in Section 2.2.2 it is still an open question whether and in which way retention is altered due to a higher intrinsic trap density in alloyed materials. D retention was found to be just slightly increased for WCrY compared to W when measured after the exposure. Still, for a moment it may be present in the target during the exposure and hence influence the sputtering behaviour. When including D retention into the SDTrimSP model, the target density is reduced with increasing number of retained light D atoms. In that case less W is located at the target surface leading to a reduced W sputter yield. However, since there is no measurement of D retention during plasma exposure, the model is used to qualitatively assess the influence of D retention on erosion yields. [106] states that an increase in the surface fraction of D in W material leads to a decrease in the surface binding energy E_{sb} for the W-D system compared to pure W. The reduction of E_{sb} in turn leads to an enhancement of the sputter yields of W bombarded by D in the low energy region. This reduction in E_{sb} is not considered in the SDTrimSP model.

In [107] and [108] a reduced energy threshold for oxidised W sputtered by light ions as compared to pure W is reported. This results from a decrease in the binding energy of tungsten oxide molecules compared to tungsten metal. In SDTrimSP only binary atom collisions are considered, so the effect of possible oxide formation is not taken into account.

Two-dimensional model

With the purpose of better rendering the changes induced in the surface morphology, the two-dimensional version of SDTrimSP [109] was employed to model the effect of D, O ion irradiation on WCrY. In contrast to the one-dimensional model, where the amorphous target is described just by atomic densities, here it is possible to define a target structure and areas of different atomic composition (see top graph of Figure 7.22). The target is made up of quadratic (size 50 nm × 50 nm) WCr grains (70 at% W and 30 at% Cr) and 5 nm wide channels containing Y: 67.9 at% W - 31.1 at% Cr - 1.0 at% Y (corresponding to the WCrY smart alloy composition). Inside the channels, which are coloured in light green in Figure 7.22, Cr diffusion is enhanced by the presence of Y by a factor of 1.5: $D_{Cr,WCrY\,channel} = D_{Cr,WCrY} * (1 + 50 * \mathrm{Y}\,[\text{at fraction}])$, where $D_{Cr,WCrY} = 4 \times 10^{-20}\,\mathrm{m}^2\,\mathrm{s}^{-1}$ is the diffusion coefficient of Cr in WCrY. This simulation aims at qualitatively understanding the effect of Cr diffusion channels on the surface morphology. Results are displayed in Figure 7.22: the initial target structure is shown in the top graph, the middle graph shows the target evolution after a simulated fluence of 2.5×10^{24} ions/m^2 while the bottom graph displays the target after the end of the simulation, at a simulated fluence of 1×10^{25} ions/m^2. Further model parameters such as an oxygen fraction of 0.3 % of the ion flux are chosen such that the simulated surface recession matches the experimentally found values for W and WCrY. The increased diffusion coefficient in the 2D model compared to the 1D model results from e.g. the

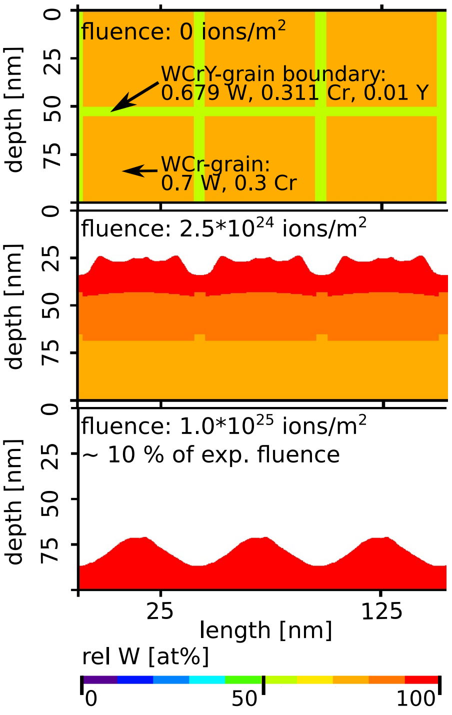

Figure 7.22.: 2D SDTrimSP Results for D220P

choice of the channel width, the diffusion enhancement caused by the presence of Y and the Y concentration in the channels. Since two-dimensional simulations are very time-consuming, only few simulations and no extensive scan varying the afore-mentioned parameters was carried out.
In Figure 7.22 it can be seen that with increasing fluence the surface recesses. After a fluence of 1×10^{25} ions/m^2 the surface has recessed approximately 75 nm. At the same time the composition of the alloy surface has changed. As a result of the Cr diffusion predominantly along grain boundaries (=channels containing Y), W-enriched hills gradually evolve on the surface. At the grain boundaries Cr is depleted and therefore valleys evolve. At the end of the simulation (bottom graph) the first 25 nm of the alloy surface consist solely of W. Hence from comparing the experimental results to the 2D simulation the conclusion can be drawn that diffusion is likely to occur along the grain boundaries. This causes the characteristic surface structure of W enriched elevated areas surrounded by lower locations, i.e. the grain boundaries, where the lighter alloying elements Cr and Y were preferentially sputtered.

7.3.2. Mixed D+Ar/He plasmas at an ion energy of 120 eV

For simulations of mixed D, Ar, He (and residual O) plasmas in DAr120P and DHeAr120P at an incident ion energy of 120 eV, the oxygen content was varied in a first step and then set to 0.3 % to not underestimate the effect caused by oxygen sputtering against that of the seeding species Ar and He. It is assumed that the usage of multiple gas inlets during exposures in mixed plasmas might increase the oxygen content in the PSI-2 plasma source. W erosion results were used for comparison. At an oxygen content of 0.3 % at a fixed Ar and He content, simulation results matched the experimental values. Key results of the W and WCrY simulations, with and without taking into account diffusion at $D_{Cr,WCrY} = 1 \times 10^{-17}$ m^2/s in case of WCrY, are given in Table 7.6.
When comparing the values for d_e and Δm in the table for DAr120P, one can see that at an oxygen content of 0.3 % and without taking into account diffusion they agree with the experimental values given in Figure 7.1: d_e of about 300 nm for W and WCrY and Δm of about 600 µg for W and about 500 µg for WCrY. Yet due to the rather low experimental fluence of 2×10^{25} ions/m^2, the results with and without taking into account

experiment	case	fluence [ions m^{-2}]	ext. surface recession [nm]	ext. mass loss [μg]
DAr120P	W	0.2×10^{26}	289	559
	WCrY	0.2×10^{26}	301	481
	WCrY diff	0.2×10^{26}	406	625
DHeAr120P	W	0.5×10^{26}	723	1400
	WCrY	0.5×10^{26}	777	1241
	WCrY diff	0.5×10^{26}	997	1559

Table 7.6.: Extrapolated (ext.) simulation results of surface recession d_e and mass loss Δm for W, WCrY without taking into account diffusion and WCrY with taking into account diffusion at $D_{Cr,WCrY}$ set to 1×10^{-17} m^2/s.

diffusion are close to each other. However, in case of D220P a distinct difference between the results with and without diffusion at this order of magnitude was already visible at a fluence of 1×10^{25} ions/m^2.

In contrast, when looking at the simulated values in Table 7.6 for DHeAr120P and comparing them to experimental results from Figure 7.1, d_e of about 600 nm for W and 900 nm for WCrY and further, Δm of about 1400 µg for W and about 1500 µg for WCrY, no good agreement is obtained without diffusion. Simulated results approach the experimental ones only when diffusion is added to the model.

The evolution of sputter yields, with and without diffusion, is shown for DAr120P in Figure 7.23 and for DHeAr120P in Figure 7.24. Looking at the sputter yield evolution for both experiments without diffusion, one can see that at the very beginning Cr is sputtered preferentially and then depleted, which is why there is an increase in W sputtering. Following this, sputter yields converge to steady state and W sputtering is dominant, as most of the alloy consists of W and sputter thresholds for Ar and O on W are below the incident ion energy of 120 eV. The sputter threshold for He on W is just about the incident ion energy (see Table 2.2 in Chapter 2). Besides the addition of He to the D+Ar plasma, model parameters are the same for DAr120P and DHeAr120P. This is the reason why generally, results for the simulations of these, with and without diffusion, are very close regarding surface recession and mass loss and just slightly increased for DHeAr120P. Here, similarly as pointed out earlier for D on W at 220 eV (see Section 7.3.1), the effect of enhanced W sputtering in the vicinity of Cr plays a role since the incident He ion energy is close to the W sputter threshold. W is more effectively sputtered in the vicinity of Cr due to an intermediate He-Cr collision and the resulting increased energy transfer γ:

$$\gamma_{He,W} \approx 0.08, \; \gamma_{He,Cr} \approx 0.27, \; \gamma_{Cr,W} \approx 0.69 \rightarrow \; \gamma_{He,Cr,W} \approx 0.19 \; .$$

7.4. Chapter summary

Experiments investigating the plasma response of WCrY and reference W samples at ion energies at or above the W sputter threshold were conducted in the linear plasma device PSI-2. Experiment D220P was conducted in pure D plasma at an ion energy of 220 eV. In the second and third experiment, DAr120P and DHeAr120P, plasma compositions were D+1 % Ar and D+5 % He+1 % Ar, respectively, at an ion energy of 120 eV. In all three experiments the ions hit the samples, which were exposed simultaneously, at normal incidence. The sample temperature was kept at around 900 K, fluxes were in the order of 1×10^{21} ions/(m^{2}s) while the fluence ranged from the order of 1×10^{25} ions/m^2 to 1×10^{26} ions/m^2.

D ion energies of 220 eV and He ion energies of 120 eV are just at about the sputter threshold of W, whereas Ar ion energies of 120 eV are clearly above the sputter threshold. It was found that the WCrY erosion is increased against that of W in experiments D220P and DHeAr120P. Comparing the results of the mixed plasma exposures at 120 eV to the ones in pure D in Section 6.1, it becomes evident that especially the addition of Ar severely increases the erosion. In DAr120P erosion is enhanced by approximately a

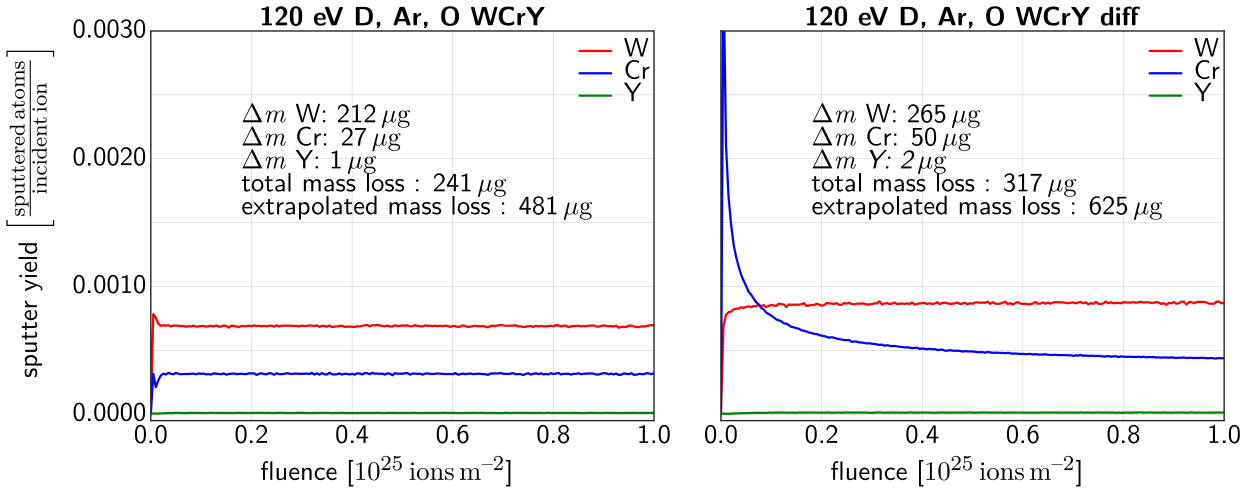

Figure 7.23.: Simulated partial sputter yields of W, Cr and Y for WCrY without diffusion on the left and with the diffusion coefficient of Cr in WCrY, $D_{Cr,WCrY}$, set to 1×10^{-17} m^2/s on the right. The mass loss per element is obtained via integration of the partial yield curves. The extrapolated mass loss is given for a fluence of 0.2×10^{26} ions/m^2

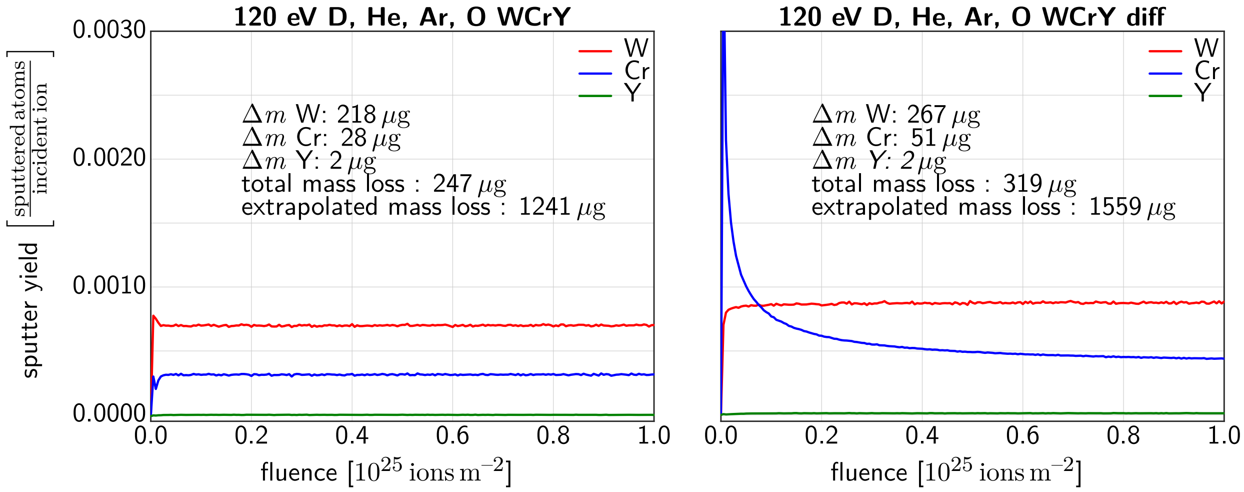

Figure 7.24.: Simulated partial sputter yields of W, Cr and Y for WCrY without diffusion on the left and with the diffusion coefficient of Cr in WCrY, $D_{Cr,WCrY}$, set to 1×10^{-17} m^2/s on the right. The mass loss per element is obtained via integration of the partial yield curves. The extrapolated mass loss is given for a fluence of 0.5×10^{26} ions/m^2

factor of 7 compared to D120P2. Still, erosion of WCrY is not significantly enhanced compared to that of W at the experimental fluence of 1×10^{25} ions/m^2. From the surface recession d_e measured at two FIB craters on the same sample in D220P and among the samples in general, homogeneous erosion across the sample surface(s) is concluded. Spectroscopy measurements taken in between time intervals of at least an hour suggest that under steady plasma conditions both W and Cr were constantly sputtered till the end of the exposure in DAr120P and DHeAr120P. No spectroscopy data is available for D220P.

Plasma-induced changes of the elemental composition are analysed using SIMS and XPS depth-profiling as well as EDX surface analysis. SIMS results show a distinct depletion of Y for all experiments, up to a depth of 40 nm to 50 nm. Depletion of Cr and enrichment of W is only detected for DHeAr120P, here both extend up to a depth of about 10 nm. XPS analysis suggests a depletion of Cr and W for DAr120P and DHeAr120P, while no data is available for D220P. The findings support the SIMS results of a more pronounced W enrichment and Cr depletion in DHeAr120P. The more gradual depletion respective enrichment in case of DAr120P might be the reason why it is not clearly detected using SIMS analysis. No Y is detected during XPS analysis due to the low Y alloy content. The EDX subsurface analysis, which was done for DHeAr120P and extends up to a depth of 100 nm, implies enrichment of W and a depletion of Cr as well as a moderate enrichment of Y in the analysed layer. Thus as a general result for the elemental composition after plasma it can be concluded that enrichment of W and depletion of Cr extend over the first 100 nm beneath the surface. Further, the Y concentration in this layer is on average increased with a gradient directly at the surface.

Regarding the D retention measured in layer 1 extending from the surface up to a depth of 3 µm and in layer 2 extending from 3 µm to 8 µm by NRA after plasma exposure, all concentrations of retained D are very close to the detection limit of 1×10^{-6}. This general trend is to be expected since at the high sample temperatures of around 900 K during the exposure, D is easily released and based on the low D solubility in W. After the exposure in pure D at 220 eV and the exposure to mixed D+Ar+He plasma, the retained D concentration in WCrY is increased by about a factor of 5 to 10 in layer 1. Oppositely, in the mixed D+Ar experiment, D retention is increased by a factor greater than 2 for W in layers 1 and 2.

Changes in surface morphology are best seen on the SEM images taken before and after exposure. The small black holes already reported in Chapter 6, and corresponding to preferential sputtering of YO particles, are visible on the WCrY samples after all plasma exposures. Whereas on WCrY samples in D220P and DHeAr120P only very shallow or hardly any bigger holes or elongated craters corresponding to Cr depletion are visible, these can be easily found on the WCrY sample exposed in DAr120P. Here they are very similar but not as pronounced as for samples exposed to sub-threshold pure D plasma in PSI-2. The small black holes found on samples in DHeAr120P and D220P are increased in number and more distinct in comparison to DAr120P. Hence, it is assumed that, due to the less pronounced Cr depletion, the depletion of Y (small back holes) becomes more visible.

On all exposed W and WCrY samples wave-like structures correlating with the grain orientation can be seen. These are more pronounced or coarse when adding Ar in DAr120P, while the addition of Ar+He in DHeAr120P makes them appear smoother and finer. Generally, the overall surface looks more attacked in DHeAr120P. Here the surface roughness is increased by about 30 % after plasma exposure, whereas it remained approximately constant or increased just slightly in D220P and DAr120P. On an LSCM image of a sample exposed to DAr120P, the surfaces scratches from the grinding procedure are still visible after plasma exposure. This implies that the grinding procedure has an impact on the measured surface roughness R_a even after plasma and explains why R_a stays approximately constant. Further, in the image it can be seen that the craters or ditches in the surface formed during plasma exposures, supposedly due to preferential sputtering, are located at the grain boundaries. This implies that the lighter alloying elements are predominantly located there.

SDTrimSP modelling was carried out for all three experiments, plasma exposure D220P serves as an exemplary modelling case. Here experimental results hint at enhanced erosion of lighter alloying elements, which implies the transport of these to the surface during the exposure. This transport is simulated by including thermal diffusion into the model. At a plasma oxygen content of 0.23 %, which was obtained by comparison of the simulated and experimental erosion results for the pure W samples, the diffusion coefficient of Cr in WCrY, $D_{Cr,WCrY}$, was varied. It has to be set to a value of the order of $1 \times 10^{-17}\,\mathrm{m}^2\,\mathrm{s}^{-1}$ so that experimental and simulation erosion results for WCrY match.

Including diffusion into the model leads to a change in the partial sputter yield evolution of W, Cr and Y in the WCrY alloy. On average, most of the mass loss is caused by W sputtering. Without taking diffusion into account, the W sputter yield is the highest yield throughout the whole simulation. Taking diffusion into account leads to Cr sputtering being dominant at the beginning of the irradiation. Moreover, the partial yields converge to steady-state at a higher fluence compared to the non-diffusion case. Due to enhanced W sputtering in case Cr is present at the surface, both the erosion yields for W and Cr are increased compared to the non-diffusion case. Additionally, a lower W surface binding energy due to alloying and the increased presence of D during the exposure could lead to an enhanced erosion for WCrY. However, these values cannot be assessed experimentally and are only discussed qualitatively in the model.

With the purpose of better rendering the changes induced in the surface morphology, the two-dimensional version of SDTrimSP was used. Results imply that diffusion is likely to occur along the grain boundaries, which causes the characteristic surface structure of W enriched elevated areas.

Simulation results of experiment DHeAr120P suggest that here diffusion is a probable reason for the enhanced erosion of WCrY, similar to the findings in D220P. In case of DAr120P, experimental results could be matched in case diffusion was not included. However, the fluence in DAr120P is quite low so that results with and without taking into account diffusion are close.

8. Temperature dependence of the WCrY smart alloy surface composition

During plasma exposure there are two effects impacting the alloy's surface composition: ion bombardment leads on the one hand to (preferential) sputtering, on the other hand to heating of the samples. Supplying energy in form of heat to the target atoms can trigger thermally activated processes such as diffusion and segregation. The importance of taking into account the transport of the lighter alloying elements to the surface, especially Cr, has already been pointed out in Section 7.3. To experimentally answer the question if erosion of WCrY smart alloys is temperature-dependent, a series of experiments with different sample temperatures under the same plasma conditions were carried out in PSI-2. These experiments were part of a master thesis supervised during this PhD. The results of the experiments conducted during the master thesis are displayed in Figure 8.1. Detailed results can be found in [110]. All other results presented here are not part of this master thesis. The two graphs plotted in Figure 8.1 are an evidence of the temperature dependence of WCrY erosion. Here the average erosion results of W and

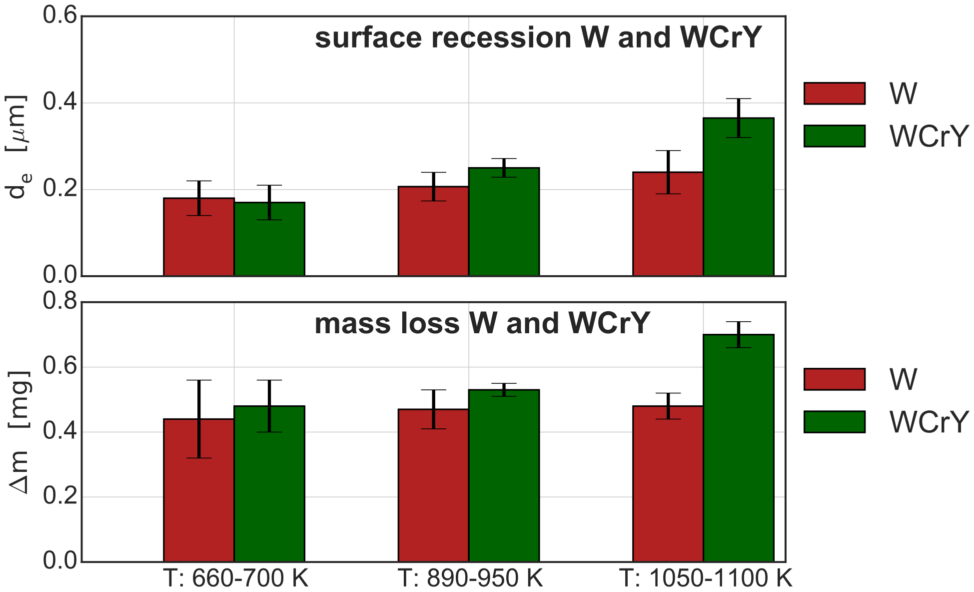

Figure 8.1.: Measured average surface recession d_e (top graph) and mass loss Δm (bottom graph) of W and WCrY samples exposed at different sample temperatures T. The exposures took place in PSI-2 in a mixed D+1 %Ar plasma at an incident ion energy of about 75 eV at an average ion flux of about 5×10^{21} ions/(m^{2}s) and a fluence of 5×10^{25} ions/m^2.

WCrY samples exposed at sample temperatures T ranging from 660 K to 1100 K are displayed. Flux and fluence for the here presented experiments are approximately the same, with values of 5×10^{21} ions/(m^{2}s) and 5×10^{25} ions/m^2, respectively. The energy of the plasma ions, which hit the target at normal incidence, was set to ion energies of about 75 eV. Compared to previous exposures at 120 eV, at this lower ion energy the sputter yields of Ar on W and Cr differ more from each other. Hence gradients induced by preferential sputtering, which in turn induce diffusion of the preferentially sputtered species to the surface, are expected to be stronger. Both the graphs in Figure 8.1 show clearly that whereas erosion is approximately constant throughout the experiments for the W samples, it increases with temperature for the WCrY samples. This is true for the surface recession d_e as well as for the mass loss Δm. The difference in erosion is significant where the range of the sample temperatures was highest with values ranging from 1050 K to 1100 K. Physical sputtering is not temperature-dependent for temperatures far below the melting point of the sputtered material as long as the surface binding energy E_{sb} is constant [31]. There is, however, a small change in E_{sb} (heat of sublimation) at the solid-liquid transition. An increased erosion of the WCrY alloy at higher temperatures, yet far below the melting point, hints at diffusion of lighter alloying elements to the surface. There they get sputtered and subsequently more of them is transported from the bulk alloy to the surface.

Static SDTrimSP runs (see Section 5.2 for model description) were carried out for the different exposures in PSI-2 to see the distributions of projectile and recoil particles within the target. Results for these distributions in D220P and DHeAr120P (see Chapter 7 for experimental description) are shown in Figures 8.2 and 8.3, respectively. At the low ion energies of 220 eV respective 120 eV during the reported plasma exposures, the penetration depth of the projectile ions and the triggered recoils extends to at maximum 10 nm below the surface. The interaction of the plasma ions and the target atoms,

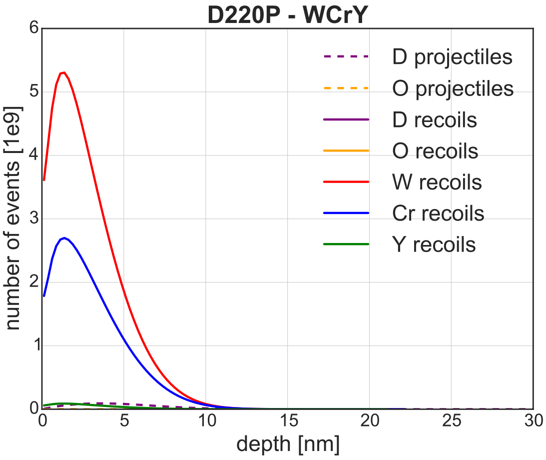

Figure 8.2.: Distribution of projectiles and recoils obtained with static SDTrimSP simulations of D220P.

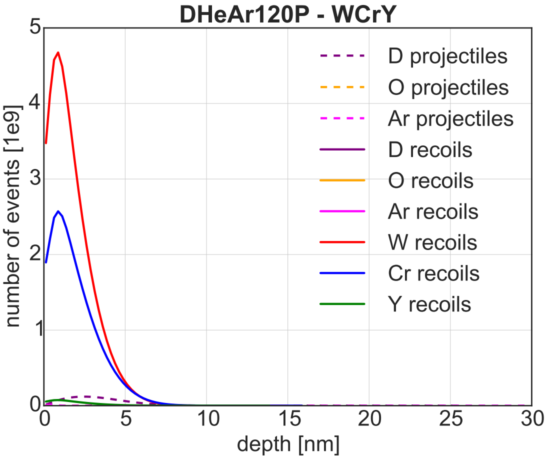

Figure 8.3.: Distribution of projectiles and recoils obtained with static SDTrimSP simulations of DHeAr120P.

as well as other processes triggered by this interaction, takes thus place in this region. However, Y depletion for instance extends to a depth of several 10 nm (see experimental results in Section 6.1.2), thus beyond the interaction range. This further underlines the presence of thermally activated transport processes such as diffusion and segregation since these lead to changes of the target composition also in layers not directly affected by the plasma ions. Thermal diffusion only counteracts compositional changes such as concentration gradients induced by preferential sputtering and thus extends the depth of the zone of altered composition. Surface segregation, in contrast, can produce compositional changes on its own. Hence this process enforces or weakens existing concentration gradients induced by preferential sputtering at the surface provided its rate is sufficiently high [48]. Therefore, the rates of the specific processes, i.e. (preferential) sputtering, thermal diffusion and (surface) segregation are of paramount importance for the resulting alloy composition in the interaction range and beyond.

For more detailed analysis of the processes induced by plasma ion irradiation and sample heating, it is first important to look in detail on the near-surface region and secondly to decouple these two processes. LEIS is a unique IBA method to study the composition of the topmost surface layer and enables us to gain understanding of the afore-mentioned processes. Further, the setup described in Section 5.1.4 allows heating the sample as well as irradiating it with ions of a defined energy. Using LEIS no information on the chemical composition of the probed surface is obtained. Moreover, just the topmost surface layer (probed depth $< 1\,\mathrm{nm}$) is analysed. For this purpose, XPS, described in Section 5.1.10 with a probed depth of about 5 nm and the possibility to obtain information on the chemical composition, is employed additionally. This chapter presents and discusses first the experimental procedure and results of the analysis carried out with LEIS before reporting on the XPS analysis.

Similar to the plasma impact during exposures, it is often not possible to strictly distinguish or separate the effects caused by thermal diffusion and segregation. Sometimes the compositional changes are even a result of the combination of these two processes. Equilibrium segregation described in Section 2.2.3 does not necessarily need preferential sputtering to occur. In LEIS measurements the enrichment of the surface in one of the components in comparison to the bulk concentration is investigated. The measurements are mostly carried out without previous preferential sputtering. Therefore, segregation is deemed the dominant process in changing the surface concentration. For the XPS analysis, Ar ion irradiation and consequently preferential sputtering induces compositional changes in the alloy, which is why in this case thermal diffusion is deemed the dominant process.

With an alloy content of just 1.0 at%, Y is difficult to be detected. Further, the effects induced by Y transport to the surface are less pronounced than those induced by Cr as the Cr alloy content amounts to 31.1 at%. For this reason, the analysis of the alloy surface composition's temperature dependence is mostly focussed on detecting changes in W and Cr concentrations.

8.1. Low-Energy Ion Scattering analysis

The ALI setup, which was used for the LEIS analysis presented here, is described in Section 5.1.4. A polished and non-plasma-exposed WCrY sample was used for the analysis. Two series of experiments were conducted:

Series 1
: Stepwise heating of the sample to 980 K, measuring the surface composition at each temperature step.

Series 2
: Irradiation of the sample with 250 eV D^+ ions at room temperature (about 300 K) and heating the sample to 980 K after irradiation, measuring the surface composition before and after the irradiation and at different time steps after heating.

The LEIS method consists in detecting low energy ions backscattered from a surface at a fixed angle. As explained in Section 5.1.4, 1000 eV He ions are used for analysis in the present work. At an angle of 140°, energies of the backscattered He ions are 926, 853, 762 and 405 eV for W, Y, Cr and O as backscattering target atoms, respectively. The obtained spectrum of backscattered ions is drawn in Figure 8.4. To identify the peaks caused by scattering of the He ions on W, Y, Cr and O target atoms, peak fitting and background subtraction must be applied. As described in [83], the background arises from re-ionisation by W. Using non-linear least squares via the python module scipy.optimize.curve_fit (see [111]), a Gaussian fit is applied to each of the four peaks.

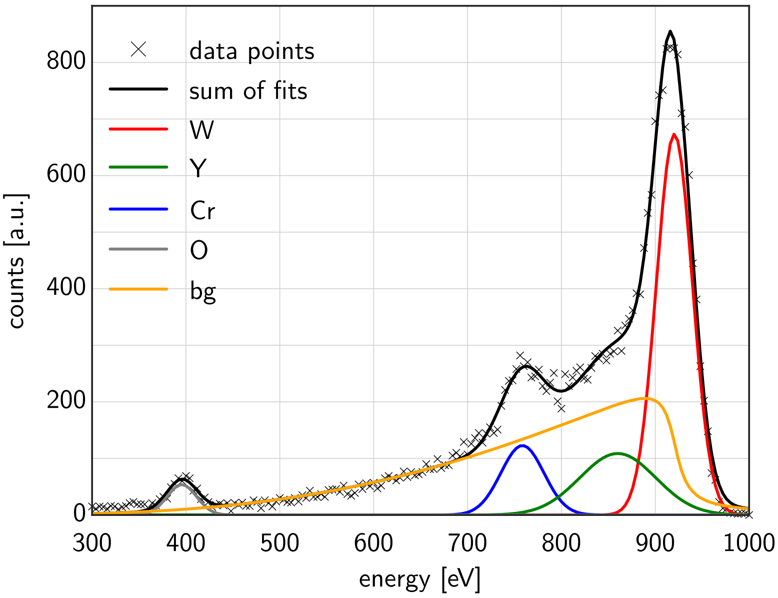

Figure 8.4.: LEIS spectrum acquired by scattering of He at the surface of polished WCrY. Shown are the obtained data points, the respective fits for the background (bg) and the four peaks corresponding to backscattering at W, Y, Cr and O as well as the sum of all fits.

The background is fitted based on the semi-empirical equation taken from [112]. Measured data points and fitted curves are drawn in Figure 8.4 for a spectrum of the polished WCrY acquired at room temperature. The intensity of a peak, i.e. the scaling factor of the Gaussian, is identified as the (non-calibrated) surface concentration of this species. It scales with the number of events of an incident He ion being scattered at target atoms of a specific species. All experimental results presented in this section are based on this analysis procedure.

Series 1

For this experimental series, the sample was heated up starting at room temperature (about 300 K) up to a temperature of 980 K. At each temperate step of about 50 K to 100 K a spectrum was acquired. The time interval between measurements is approximately half an hour to allow the set temperature to equilibrate. Surface concentrations of O, Y, Cr and W are obtained according to the fitting procedure described above for the consecutive temperature steps. These are displayed in Figure 8.5. In this graph it can be seen that with rising temperature the W surface concentration $c(W)$ decreases, while both the Cr and the Y surface concentrations increase. At the same time, the oxygen surface concentration remains constant. The biggest change in surface composition is observed after surpassing a temperature of about 700 K. At this point the predominant species at the surface switches from W to Cr. Here one should note that the signal

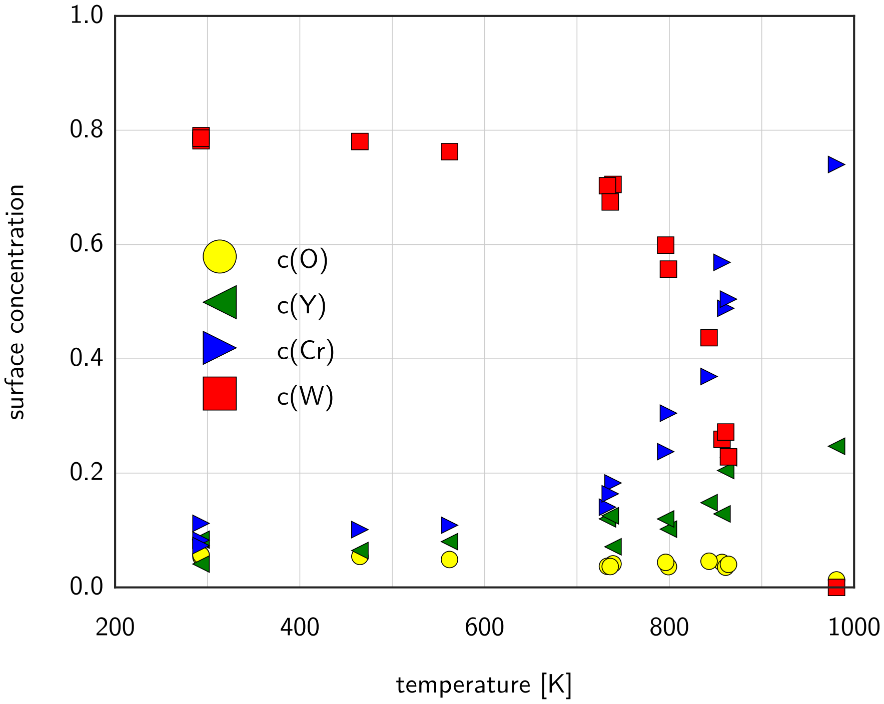

Figure 8.5.: Surface concentrations of O $c(O)$,Y $c(Y)$, Cr $c(Cr)$ and W $c(W)$ resulting from the fitted spectra acquired at different temperatures.

intensities and thus the surface concentrations are not calibrated but rather represent intensity ratios normalised to yield 1.0 in total.

In order to describe the temperature dependence of the enrichment of one alloy constituent at the alloy's surface, i.e. the constituent's surface segregation, the Langmuir-McLean relation, which is given as Equation (2.15) in Section 2.2.3, can be used. This has been done [113] and is applied here in the same way to describe the temperature dependence of the surface concentration of the segregating Cr ($c(Cr)$) with segregation energy ΔH according to Equation (8.1) from [113]:

$$\frac{c(Cr)}{1-c(Cr)} = \frac{c_{bulk}(Cr)}{1-c_{bulk}(Cr)} \cdot e^{-\frac{\Delta H}{k_B T}}, \tag{8.1}$$

with the Cr bulk concentration $c_{bulk}(Cr)$, the Boltzmann constant k_B (in units of eV K^{-1}) and the temperature T (in units of K). Taking the natural logarithm ln on both sides of the equation and reordering the equation yields Equation (8.2).

$$\ln\left(\frac{c(Cr)}{1-c(Cr)}\right) = \left(-\frac{\Delta H}{k_B}\right) \cdot T^{-1} + \ln\left(\frac{c_{bulk}(Cr)}{1-c_{bulk}(Cr)}\right). \tag{8.2}$$

This equation is linear and can thus be described as $y = m \cdot x + b$, with the gradient m being $\left(-\frac{\Delta H}{k_B}\right)$. Consequently, by plotting $\ln\left(\frac{c(Cr)}{1-c(Cr)}\right)$ versus T^{-1} and performing a linear fit, as shown in the Arrhenius plots in Figure 8.6, the segregation energy ΔH can be determined. This was done for the surface concentrations of Y, $c(Y)$ (left graph), and Cr, $c(Cr)$ (right graph), in WCrY. In each graph two separate linear regression lines were fitted to the data. The green dotted one describes the segregation in the inverse temperature range of about 1.0×10^{-3} to below 1.5×10^{-3} K^{-1} (corresponding to temperatures of 1000 K to 700 K). In the inverse temperature range of above 1.5×10^{-3} to

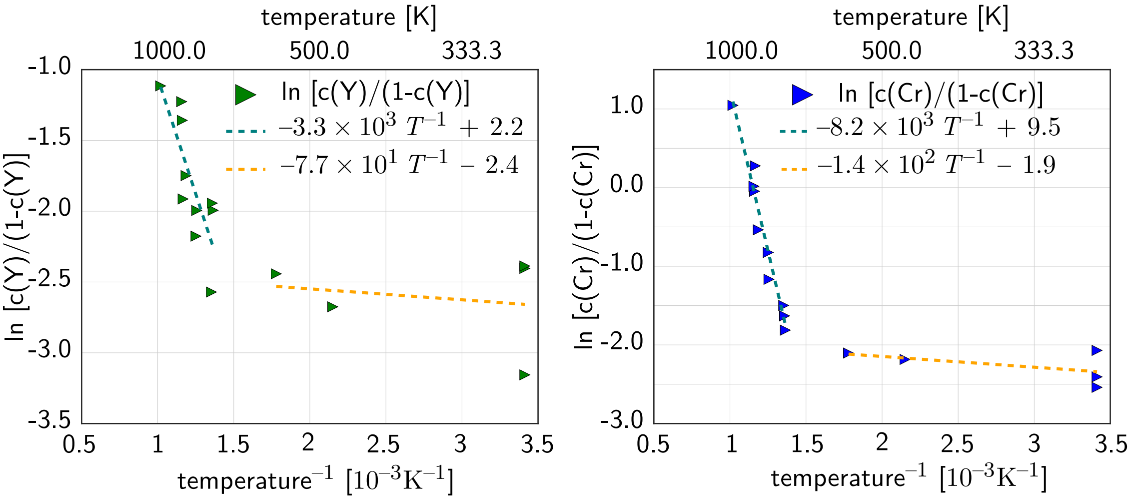

Figure 8.6.: Left: Arrhenius plot of the surface Y concentration $c(Y)$ taken from Figure 8.5. Right: Arrhenius plot of the surface Cr concentration $c(Cr)$ taken from Figure 8.5. Both graphs include linear fits to determine the respective segregation energies ΔH for Cr and Y in WCrY.

below $3.5 \times 10^{-3}\,\mathrm{K}^{-1}$ (corresponding to temperatures of 700 K to 300 K) the fit is displayed by the yellow dotted line. It must be pointed out that the temperature axes of both graphs in this figure as well as in Figure 8.5 are mirrored. A Cr segregation energy ΔH_{Cr} of about 0.7 eV and a Y segregation energy ΔH_Y of about 0.3 eV is obtained above 700 K. This temperature range includes the sample temperature of about 900 K during plasma exposures. Here segregation is much stronger compared to the lower temperature range, the determined Cr segregation energy is more than double the determined value of the segregation energy of Y. According to [55], segregation with surface segregation energies of solute metal impurities in the range of 0.3 eV to 0.7 eV is classified as strong segregation.

Series 2

In Series 2 the sample was irradiated with 250 eV D^+ ions at a flux of 1×10^{18} ions/(m^2s) up to a fluence of 5×10^{21} ions/m^2 at room temperature (about 300 K), then it was heated to 900 K. Figure 8.7 shows the respective spectra on its left side. Whereas there is a small Cr peak visible at about 760 eV before irradiation, this peak has vanished after irradiation. The entire surface is covered by W and additionally O. The O peak is assumed to be caused by O being introduced into the system by the D gas can used for irradiation. Further, the overall background signal is increased after irradiation, which means an increased re-ionisation of the scattered He. This is caused on the one hand due to the increased W fraction in the first atomic surface layers, and could additionally be caused by the rise in oxygen at the surface. Neither before nor after irradiation an Y peak is present. Heating the sample to 980 K in a third step leads to a sharp rise of the Cr peak as well as the appearance of the Y peak. The W peak nearly vanishes. Most of the surface is now covered by Cr. The O peak also diminishes, since during the heating step the valve connecting the D can to the analysis chamber is closed.

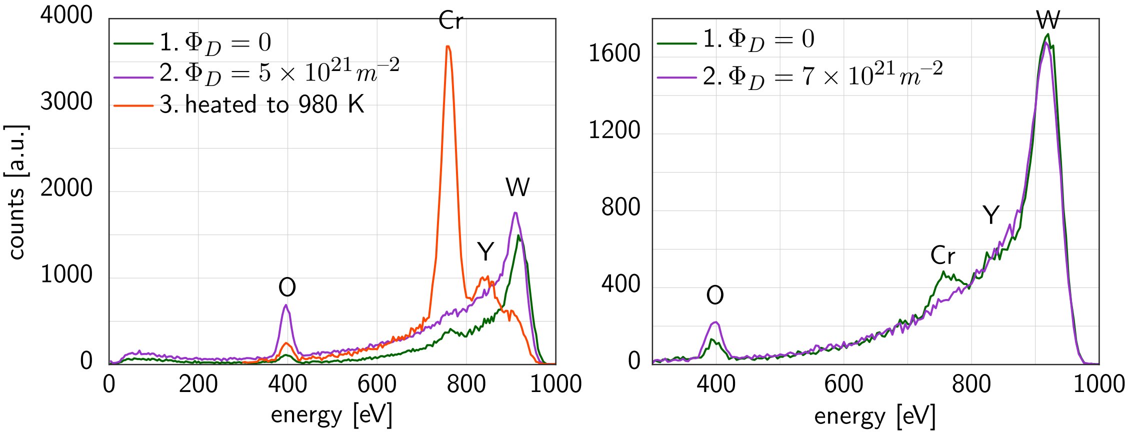

Figure 8.7.: (Preferential) sputtering by 250 eV D+ performed at room temperature without (left graph) and with (right graph) cryo trap installed in front of gas inlet. Shown are the spectra before and after irradiation and for the left graph additionally after heating to 980 K.

The presence of the O, assumed to be introduced into the system by the D, was only noticed after conducting experimental series 2. In order to verify that O mainly originates from the connected D can, a second irradiation was carried out, this time with a cryo trap installed at the D gas inlet. On the right side of Figure 8.7, the obtained spectra before and after irradiation with 250 eV D^+ and the cryo trap installed up to a fluence of 7×10^{21} ions/m^2 are displayed. The O peak is significantly reduced. The remaining minute O content is assumed to be residual O surface contamination from e.g. storage of the sample in air and has also been observed for other LEIS measurements using the ALI setup in [83]. Again Cr is only distinguishable before irradiation. Except for the minute O amount the surface is entirely covered by W after irradiation due to preferential sputtering of Cr (and Y). At about 850 eV a small Y peak is barely visible, however, it is hard to detect due to its low concentration in the alloy. Hence the obtained spectra before and after D irradiation without cryo trap (green and purple curves in left graph of Figure 8.7) are very similar to those obtained with cryo trap (green and purple curves in right graph of Figure 8.7) except for the difference in O surface content.

After heating the sample to 980 K and acquiring the spectra shown on the left of Figure 8.7, the sample was kept at this temperature and irradiated with 250 eV D+ ions up to a fluence of 5×10^{21} ions/m^2. Subsequently several spectra were acquired at different times without any additional treatment of the sample. The respective non-calibrated surface concentrations resulting from the above described fitting procedure of the spectra are shown in Figure 8.8. The first spectrum corresponding to the data points of the surface concentrations most on the left was acquired 240 s after preferential sputtering at 980 K. This is the minimum time interval needed to rotate the sample from the sputter ion gun into the direction of the analysis ion gun and then acquire a spectrum. As evident in

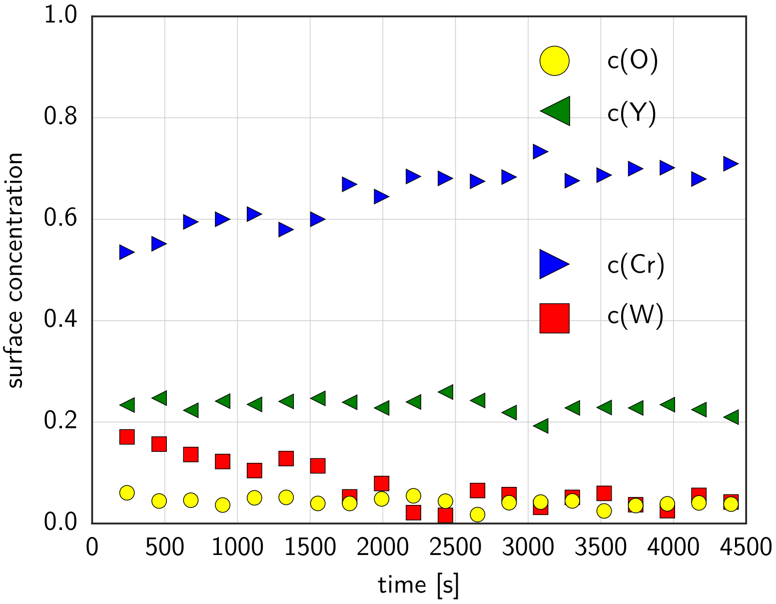

Figure 8.8.: Surface concentrations of O $c(O)$,Y $c(Y)$, Cr $c(Cr)$ and W $c(W)$ resulting from fitted spectra acquired at different times after preferential sputtering at 980 K.

Figure 8.8 and contrarily to the spectrum in Figure 8.7 after D^+ irradiation at room temperature with the same fluence (purple curve), the surface consists mostly of Cr after D^+ irradiation at 980 K. Going forward in time, the Cr concentration on the surface rises further while the concentration of Y decreases slightly and that of O stays approximately constant. The W surface concentration $c(W)$ decreases to the same extent $c(Cr)$ increases. From an acquisition time of 3000 s till the end of the measurement the surface composition is approximately stable, the surface is mostly covered by Cr.

8.2. X-ray Photoelectron Spectroscopy analysis

XPS is used to obtain information on the elemental and chemical composition of the surface of a WCrY sample before and after preferential Ar sputtering and heating to 900 K. Of special interest is the question whether the detected W and Cr are mostly present in the form of oxides or in pure metallic forms and the changes to this state induced by heating and Ar sputtering.

For this purpose one piece of a WCrY sample was used, ground according to the usual procedure used for plasma exposure. First an SEM image (Figure 8.9 a)) was taken, the sample was put into the XPS device and the surface composition was measured (Figure 8.10 a)). Following this, the sample was heated to 900 K for 1 h, taken out and another SEM image was taken (Figure 8.9 b)). Then the sample was put into the XPS device again and sputter-cleaned using 5 keV Ar ions at a fluence of 7×10^{21} ions/m^2 before the surface composition was again analysed (Figure 8.10 b)). Subsequently, the sample was heated to 900 K for 3 h and another XPS analysis was carried out (Figure 8.10 c)). Eventually, the sample was taken out and another SEM image was taken (Figure 8.9 c)). One should note that the SEM pictures are not taken at exactly the same position. In Figure 8.11, spectra of the region around W4f (transition with principal quantum number $n = 4$ (N shell) and orbital angular momentum quantum number $l = 3$ (f orbital)) and Cr2p (transition $n = 2$ (L shell) and $l = 1$ (p orbital)) corresponding to the XPS-analysis results displayed in Figure 8.10 are shown in the top and bottom row, respectively. The signal-to-noise ratio in the Cr spectra is increased compared to those obtained for W as the former ones are taken from an overview energy scan. Unfortunately, no detailed energy scans of the region around Cr2p were carried out.

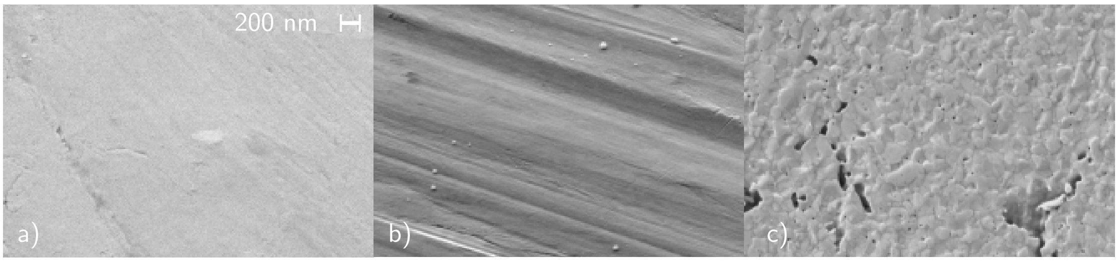

Figure 8.9.: SEM images of the surface of the WCrY sample a) untreated, b) after heating to 900 K for 1 h and c) after Ar sputtering and subsequent heating to 900 K for 3 h.

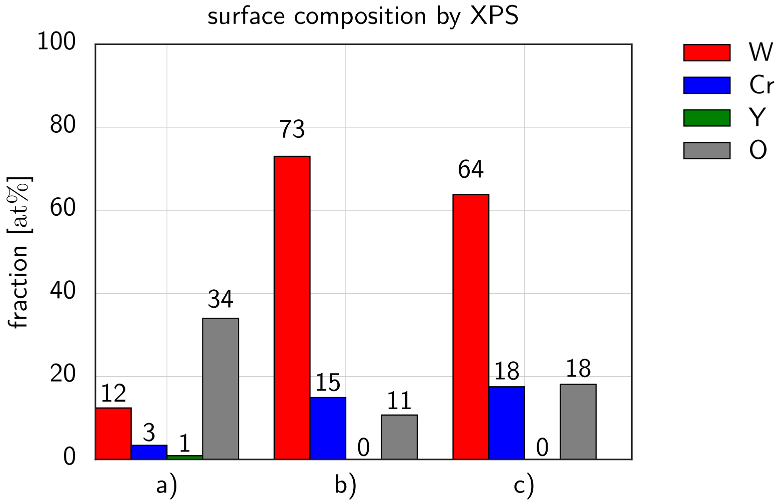

Figure 8.10.: XPS-measured surface composition of the WCrY sample a) untreated, b) after heating to 900 K for 1 h and subsequent Ar sputtering and c) subsequent heating to 900 K for 3 h. Other elements (in at%) are: a) 26 C, 23 F, b) 1 Mo and c) 1 Mo. The measurement error is approximately 1 at%.

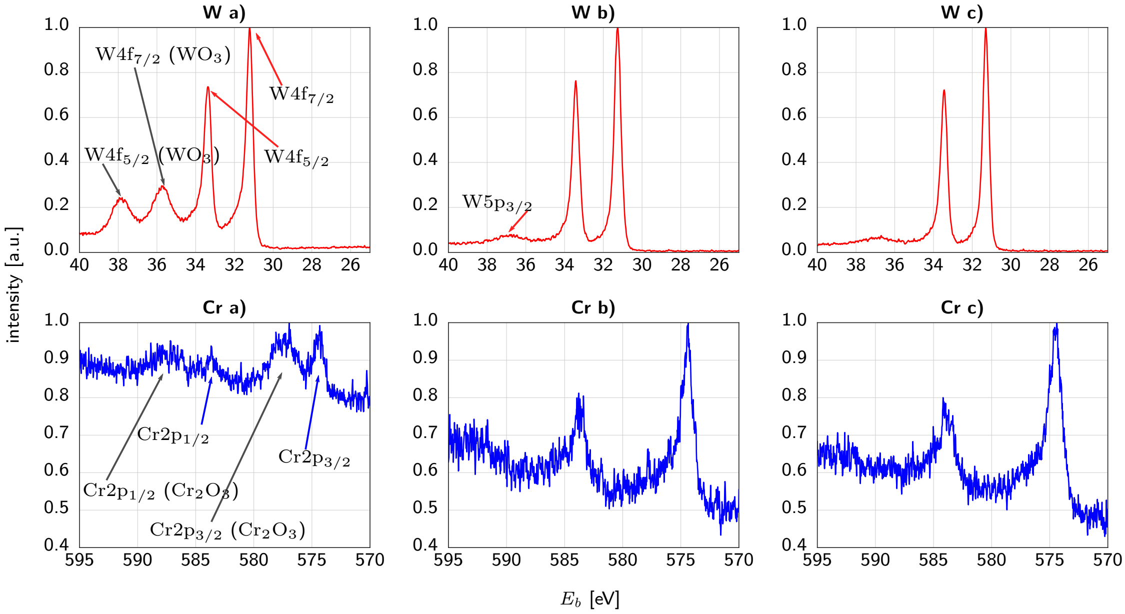

Figure 8.11.: XPS spectra of W4f (top row) and Cr2p (bottom row) of the WCrY sample a) untreated, b) after heating to 900 K for 1 h and subsequent Ar sputtering and c) subsequent heating to 900 K for 3 h. Electron transitions (see Section 5.1.10) are described by the principal quantum number n (electron shell or energy level of an electron) and orbital angular momentum quantum number l (subshell, magnitude of orbital angular momentum) and the total angular momentum quantum number j (magnitude of total angular momentum) according to nl_j. The red and blue arrows indicate metal W and Cr, respectively.

The elongated scratches on the untreated sample surface in Figure 8.9 a) stem from the grinding process during sample preparation. It can be seen from Figure 8.10 a) that there are residual impurities on the surface. Oxygen is mostly found as oxide or hydroxide bound to W and Cr, in spectra W a) and Cr a) of Figure 8.11 peaks corresponding to WO_3 and Cr_2O_3 are indicated. The measured molybdenum (Mo) stems from the sample holder inside the XPS device. As the sample piece has dimensions of 4 mm × 10 mm and is thus only slightly larger than the measurement spot of size 1.5 mm × 6 mm (see device description of the PREVAC setup in Section 5.1.10), the analysis region can easily contain parts of the sample holder. Yet, it is assumed that this does not have an impact on the information about the W and Cr content of sample surface and the respective oxidation states. Further, fluorine (F) was detected. This element has also been found by other analysis methods for samples produced and prepared around the same time. It is assumed that this F stems from residual impurities on the equipment used for ultrasonic cleaning. The SEM image in Figure 8.9 b) shows that heating does not lead to substantial changes of the surface. The 5 keV Ar sputtering then leads to removing impurities from the surface and further to a characteristic surface morphology (Figure 8.9 c)). Less oxygen is present on the surface (Figure 8.10 b)). W and Cr are now mostly found as metals (see Figure 8.11 W b) and Cr b)). The Ar sputtering leads not only to a removal of an approximately 3 nm thick surface layer, but also to a characteristic surface morphology of small holes and elongated craters along the grain boundaries, which is caused by preferential sputtering of lighter elements (see for instance reported results of plasma exposure in Section 6.1.2). These surface artefacts can still be seen on the SEM picture in Figure 8.9 c) taken after heating of the sample for 3 h. It can be excluded that these features stem from heating the sample to 900 K since they are not observed in Figure 8.9 b) after heating to this temperature for 1 h.

The Y content of the sample (1.0 at%) is close to the detection limit of the XPS analysis and not detectable after the Ar sputtering (Figure 8.10 b)) due to preferential sputtering. The XPS analysis results after heating for 3 h are displayed in Figure 8.10 as c) and in Figure 8.11 as W c) and Cr c). The W surface coverage decreased and the oxygen as well as slightly the Cr surface coverage increased after heating. Compared to the XPS measurement prior to heating and sputtering, the W and Cr signals are again predominantly metallic just as was the case after sputtering. Only a minor fraction of W and Cr is oxidised as can be seen in spectra W c) and Cr c) of Figure 8.11, the slightly increased signal at values of E_b of about 595 eV to 590 eV in spectrum Cr c) suggest that Cr is slightly more oxidised after annealing than before (see [114] for comparison). Since the Y content is generally very low and too low to be detected after sputtering, information about the oxidation state of the Y in the alloy is not available from XPS. Y generally is very reactive with oxygen and therefore mostly found in oxidised state. Hence, (part of) the oxygen measured by XPS in Figure 8.10 may be bound to Y. Here it is remarked that the spectra are acquired at normal incidence. Provided the low oxygen content is basically located at the very surface, XPS measurements under a grazing angle of incidence might allow a more accurate determination of the oxide composition. According to [115] Cr is oxidised prior to W in the WCrY system due to the lower Gibbs free energy of Cr. Hence since the Cr content as well as the O content of the surface are increased, it is assumed that Cr diffuses to the surface to form oxides so that less W is present. Comparing this to the surface concentrations measured by LEIS (analysed depth $< 1\,\mathrm{nm}$) after heating to 980 K in the previous section, it is assumed that the segregation of Cr to the surface, where it forms oxides, is especially strong in the first atomic surface layers. As XPS analyses the first approximately 5 nm beneath the surface and the contribution to the detected signal intensities decreases exponentially with depth, this effect of strong surface segregation is less distinct by averaging over a deeper extending layer. In particular, since XPS data is acquired under normal electron emission in the present work, there is a greater difference in the depth resolution between XPS and LEIS.

8.3. Chapter summary

This chapter reports on dedicated experiments, carried out additionally to the plasma exposures and based on LEIS as well as XPS analysis, investigating the temperature dependence of the WCrY surface composition. Before presenting the results obtained by the two analysis methods, the experiments are motivated. First, erosion results of PSI-2 experiments exposing W and WCrY samples at the same plasma conditions and varying temperatures are reported. These experiments were carried out in the framework of a master thesis, which was supervised during this PhD project. The here presented analysis of these experiments was not part of the master thesis. The fact that erosion results suggest increased erosion for WCrY with increasing temperature, again highlights the need for investigating thermally activated processes in more detail. Serving as a further motivation, results of static SDTrimSP calculations on the extent of the interaction range in WCrY during plasma exposure are shown. The experimentally detected changes in the alloy composition extend deeper than this range, which implies that transport processes from deeper layers play a significant role. Whereas surface segregation, the enrichment of one of the alloy components on the surface, does not necessarily need preferential sputtering to occur, thermal diffusion counteracts concentration gradients induced by preferential sputtering. Generally, both processes impact the surface composition during plasma exposure simultaneously.

Using the ALI setup for LEIS analysis, two series of experiments were conducted. In series 1 a polished WCrY sample was heated up from 300 K to 980 K in steps of 50 K to 100 K. Here the analysed surface layer extends to a depth of about less than 1 nm. The W surface concentration decreases with temperature, while both the Cr and Y surface concentrations increase. Surpassing a temperature of 700 K, the predominant species on the surface switches from W to Cr. Since the Cr concentration increases to a value above the initial alloy concentration, this phenomenon is called surface segregation. The Langmuir-McLean relation was used to estimate the segregation energy ΔH for the Cr segregation to the surface. A Cr segregation energy ΔH_{Cr} of about 0.7 eV is obtained for the temperature range above 700 K, where segregation is much stronger compared to lower temperatures. In similar manner an Y segregation energy ΔH_Y of 0.3 eV is obtained for the temperature range above 700 K.

In series 2 the polished WCrY sample was irradiated with 250 eV D^+ ions up to a fluence of 5×10^{21} ions/m^2 at a temperature of 300 K and afterwards heated to 980 K. After irradiating the sample, its surface is almost entirely covered by W, Cr has been preferentially sputtered. When heating the sample to 980 K after the irradiation, the surface coverage changes from almost pure W to almost pure Cr. Additionally, Y segregates to the surface. Irradiation of the sample with 250 eV D^+ ions up to a fluence of 5×10^{21} ions/m^2 at a temperature of 980 K does not yield depletion of Cr and Y. After preferential sputtering at this temperature the surface consists almost entirely of Cr and Y.

XPS analysis, in combination with taking SEM images, was used to further investigate the composition of the surface of a heated and Ar sputtered WCrY sample. The analysed surface layer extends to a depth of about 5 nm. Prior to heating and sputtering by 5 keV Ar ions up to a fluence of 7×10^{20} ions/m^2, W, Cr and O, besides other impurities, can be found on the surface. W and Cr are mostly present in the form of oxides. The Y concentration is too low to be detected. Ar sputtering leads to a removal of oxygen and impurities as well as to a characteristic surface morphology due to preferential sputtering. The latter is concluded from the comparison to previously reported plasma exposures. When the sample is heated to 900 K after the preferential sputtering, the Cr and O content on the sample surface are increased. At the same time the W content is decreased. After Ar sputtering and heating of the sample, both W and Cr are mostly found in metallic form and are only partly oxidised. It is assumed that Cr diffuses to the surface, where it partly forms oxides, so that less W is present on the surface. The effect of Cr enrichment at the surface is less distinct for the XPS results in comparison to LEIS measurements as XPS analysis averages over a deeper extending surface layer (5 nm compared to < 1 nm).

9. Oxidation of plasma-exposed samples

In case of a reactor accident with additional air ingress as described in Chapter 3, smart alloys should be able to suppress W oxidation after being exposed to plasma during regular operation. For this reason it is important to investigate the oxidation performance of the plasma-exposed WCrY samples and draw a comparison to non-exposed WCrY samples.

Complementary to testing the plasma performance of the produced WCrY samples, specific oxidation testing varying sample production parameters as well as oxidation parameters has been carried out outside this work. The work on the optimisation of the oxidation performance of WCrY smart alloys is described in [115] and [43]. In case of a reactor wall accident with additional air ingress and failure of the cooling system, the wall temperature will be above 1200 K for several weeks [56]. The main testing scenario for the oxidation performance of the WCrY alloys is dry synthetic air with the composition of 80 vol% Ar and 20 vol% O at 1 bar and 1273 K.

After previously developing W-Cr alloys with the addition of Ti, Y was first used as third alloying element in thin films produced by magnetron-sputtering. In [57] it was found that a Cr content of more than 8 wt% in the alloy is needed for effective passivation. Due to the limited thickness of a few µm and Cr reservoir in thin films, these can only effectively passivate for a few hours. In contrast, bulk WCrY samples produced with the optimum composition have a thickness of a few mm, successful passivation is achieved for several days. After approximately two days of oxidation, the oxide starts to sublimate at a measurable rate [43]. At this point the oxide scale on top of the alloy surface has a thickness of several µm, the internal oxides formed inside the bulk material extend several µm deep. If additionally to air ingress water leakage into the reactor occurs during the accident, sublimation rates will increase. Still, just as in dry air, the efficient supply of Cr to the alloy surface for forming a protective Cr_2O_3 oxide scale is crucial also for successful passivation in humid air.

It was found (see e.g. [43]) that the surface roughness R_a has a crucial impact on the oxidation performance. The oxidation rate of samples with a surface roughness R_a of about 0.6(1) µm was increased about an order of magnitude in comparison to that of the standard samples.

9.1. Experimental details

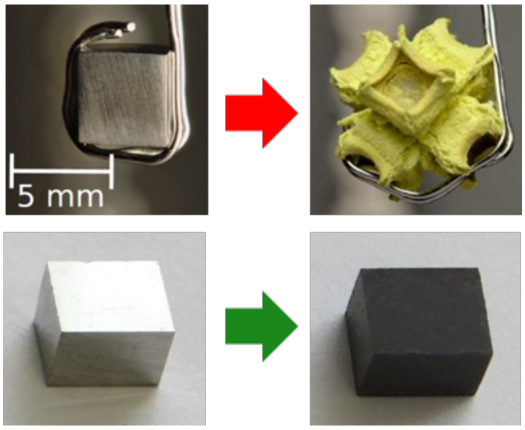

Figure 9.1.: Pictures of cubic W and WCrY samples (top and bottom) before and after oxidation (left and right).

In this work, oxidation experiments were performed in the dual furnace setup described in Section 5.1.9. They were conducted in dry synthetic air at 1273 K in an atmosphere containing 80 vol% Ar and 20 vol% O at 1 bar. Due to the geometry used for PSI-2 experiments, it is not possible to grind the samples meant for plasma exposure from all sides (see Figure 3.3). Smart alloy samples not meant for plasma exposure but specifically for determining oxidation rates have a standardised cubic shape and are ground from all sides as shown in the pictures on the left side in Figure 9.1. Wire erosion leads to deposition of the wire material onto the samples. Not all remnants from wire erosion cutting can be removed during grinding. Moreover, sample edges or other surface defects such as scratches are prone to the formation of W-containing oxides. Thus a sample with many edges and on top with remaining dirt from wire erosion is expected to show a degraded oxidation behaviour. For this reason, two WCrY reference samples with the PSI-2 geometry were oxidised without having been exposed to plasma before so that the oxidation rates of non-plasma-exposed and plasma-exposed samples can be compared. The surface area and therefore slightly varying sample geometries or differences induced by manual grinding have a great impact on the oxidation behaviour. In order to better compare the performance of the different samples, the gradient of mass change, described in detail in Section 3.2, is used.

9.2. Experimental results

On the left side of Figure 9.2 the oxidation performance of a cubic pure W sample is compared to that of a cubic WCrY sample with the optimum composition of 67.9 at% W - 31.1 at% Cr - 1.0 at% Y. On the right sight, with an increased scale, the performance of the cubic WCrY sample is compared to that of non-exposed and plasma-exposed WCrY samples with PSI-2 geometry (see Figure 9.3).

On the left, the W first shows a sharp decrease in the gradient of mass change as the oxide layer is rapidly formed and oxidation slows down. After about less than 2 h however, the gradient increases. At this point the oxidation rate speeds up again as a bigger surface area is accessible to the oxygen due to falling apart of the sample: the sample fails and loses its initial cubic shape which is shown in the top row in Figure 9.1. After about 9 h the oxidation was stopped. In contrast, the gradient of the WCrY sample starts at a value of nearly 0. At this scale, which was chosen to display both, the graphs

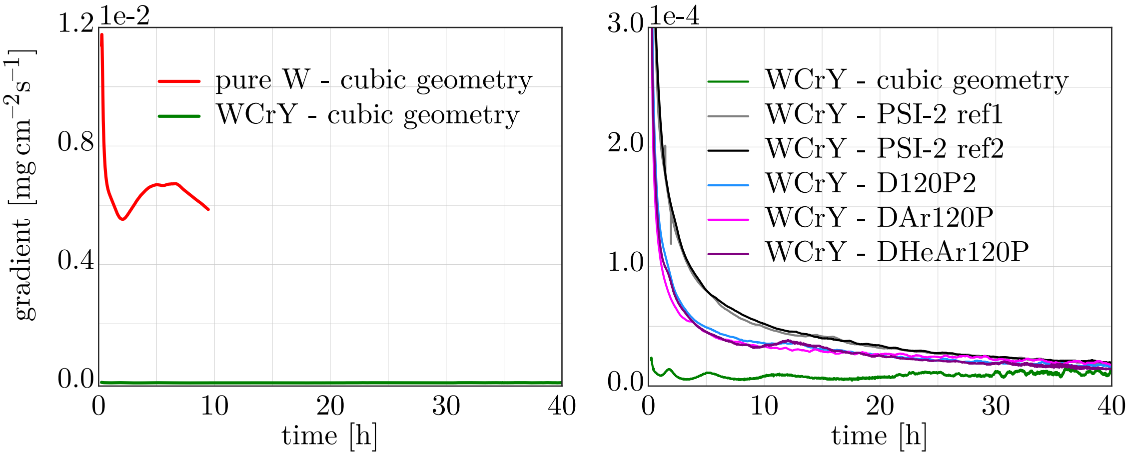

Figure 9.2.: Gradient of mass change in mg cm^{-2} s^{-1} during isothermal oxidation in dry air at 1273 K in an atmosphere containing 80 vol% Ar and 20 vol% O at 1 bar. On the left, the oxidation graphs of a pure W and a WCrY sample with cubic geometry are shown. Samples exposed in D120P2, DAr120P and DHeAr120P as well as two WCrY reference samples with PSI-2 geometry and not exposed to plasma (ref1 and ref2) are shown on the right.

of W and WCrY, the graph of WCrY is very close to the x-axis and hardly visible. In comparison to the pure W sample, oxidation is suppressed by 3 orders of magnitude. The oxidation performance is shown for up to 40 h. During this time the gradient remains approximately constant at about 2×10^{-5} mg cm^{-2} s^{-1}, which can be seen more clearly on the right. Unlike the W sample, where the rising gradient after about 2 h indicates a sudden increase of the oxidation rate by sample failure, the WCrY graph does not rise again. Here the stable gradient denotes a constant oxidation rate. A dense oxide scale has formed resulting in a steady and slow mass gain.

On the right side of Figure 9.2, the oxidation performance of the WCrY sample with cubic geometry is compared to that of plasma-exposed and non-exposed reference WCrY samples of the PSI-2 geometry. One can see that right at the start the shown gradient of mass change decreases rapidly for all PSI-2 samples. A sudden change of the gradient means a significant change in the oxidation rate, e.g. at the beginning the oxidation rate is rapidly decreased by the formation of a passivating layer. After 20 h all PSI-2 graphs start to converge and reach a value of about 2×10^{-5} mg cm^{-2}s$^{1-1}$ at 40 h, where they meet the graph of the cubic WCrY sample. Here again the stable gradient denotes a

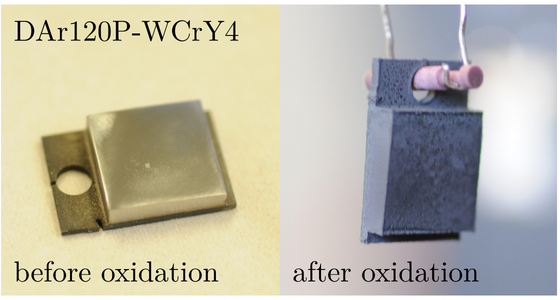

Figure 9.3: Pictures of sample DAr120P-WCrY4 before and after oxidation (left and right).

constant oxidation rate due to the formation of a dense oxide scale. The increased mass gain and hence gradient at the beginning can be deduced to edge effects and the wire erosion remnants. After about 20 h these initial effects do not play a significant role any more. It is suspected that the plasma-exposed samples perform slightly better in the beginning than the reference samples because some of the dirt at the edges of the plasma-exposed samples has been removed by physical sputtering. Pictures of the sample exposed in DAr120P after plasma exposure and before oxidation and after oxidation are shown in Figure 9.3. The sample has kept its shape, the surface appears black due to oxide formation.

9.3. Chapter summary

In this chapter the oxidation performance of plasma-exposed WCrY samples is investigated and compared to non-exposed samples. Experiments took place at 1273 K in an atmosphere containing 80 vol% Ar and 20 vol% O at 1 bar. Usually, in the experiments testing the oxidation performance of WCrY alloys, a cubic geometry ground from all sites is used. For better comparison of WCrY samples with the plasma geometry, where not all remnants from wire erosion can be removed by grinding, here the gradient of mass change was used to evaluate the oxidation performance. It could be shown that plasma-exposed WCrY samples show constantly low oxidation rates during the entire experiment of 40 h duration. Plasma-exposed and reference samples of the same geometry show an increased gradient of mass gain at the beginning of the oxidation compared to the standard cubic WCrY sample, however, at the end of the oxidation all gradients converge to the same value.

The surface roughness has a significant impact on the oxidation behaviour. In Chapters 6 and 7 it was shown that the surface roughness stays approximately constant or just increases slightly after plasma exposure. The surface roughness is still after plasma exposure mainly determined by the grinding procedure during the sample preparation. Thus no degradation of the oxidation performance due to surface roughening is expected. Still, since the plasma-irradiated area of 1 cm^2 makes out only about one fourth of the total sample surface area and edge effects play a crucial role, the plasma geometry is not well suited to test the oxidation performance. A geometry suitable for both oxidation and plasma performance testing needs to be developed.

Plasma-induced changes were seen to extend to, at maximum, a few 100 nm (Chapters 6 and 7). Since after some hours of oxidation the affected layer extends several µm deep into the alloy, the compositional changes induced by the plasma do not play a significant role. This is confirmed by the experimental results: after some hours of oxidation the performance of all tested samples assimilates. An alloy Cr content of more than 8 wt% is of paramount importance for successful oxidation. Thus as long as there is no decrease in the Cr alloy content beneath this value for a depth of at least several µm, the effect of plasma exposure on the oxidation in a reactor accident lasting for several days can be neglected.

10. General Discussion

In this chapter the results which are in detail reported in Chapters 6, 7, 8 and 9 are collectively discussed and balanced against each other. First possible plasma inhomogeneities during the exposures in the linear devices and their effect on the erosion results are discussed. This is followed by a section connecting the erosion results to the investigations of temperature dependence of the surface concentration. Here, first experimental findings of the exposures to main plasma ion energies below the W sputter threshold are discussed, before examining those at energies at or above the W sputter threshold. Eventually, the interdependency of erosion and diffusion rates during plasma exposure of WCrY is evaluated. Possible implications for oxidation of plasma-exposed samples are pointed out.

10.1. Plasma inhomogeneities and possible impact on erosion results

Evaluation of the erosion performance of WCrY samples relies to a large extent on comparing samples exposed either simultaneously, but at different locations in the case of PSI-2 exposures, or at the same location, but subsequently in the case of Magnum-PSI experiments.
Regarding exposures in PSI-2 it is important to consider possible errors induced by inhomogeneities in the plasma ion flux onto the target, which is used for the simultaneous exposure of the samples. Spectroscopy measurements of the line radiation emitted during the exposure of a pure W target, whose size exceeds the diameter of the hollow PSI-2 plasma profile, from [97] are shown in Figure 10.1. It can be seen that the radiation intensity emitted by sputtered W atoms is increased towards positive values of the plasma radius and not symmetric around the centre of the plasma column at a radius of 0 mm. In contrast, the Langmuir probe measurement assumes a symmetric plasma profile (see description in Section 4.1.1 and Figure 4.2). Hence possible asymmetries in the PSI-2 plasma profile are not taken into account. However, the plasma profile depends heavily on the plasma conditions such as the plasma composition and the incident ion energy as well as on the cathode used. The intensity distribution shown in Figure 10.1 was acquired during a pure neon plasma exposure and at incident ion energies of 280 eV, thus at conditions significantly different from the ones used in the reported PSI-2 experiments. For these, no intensity distribution was measured due to the too low sputtering fluxes. In [116] Thomson Scattering (TS) was used to measure the plasma temperature and density profile across the entire plasma diameter during D plasmas in PSI-2. The profiles were found to be approximately symmetric around the centre of the plasma column, as

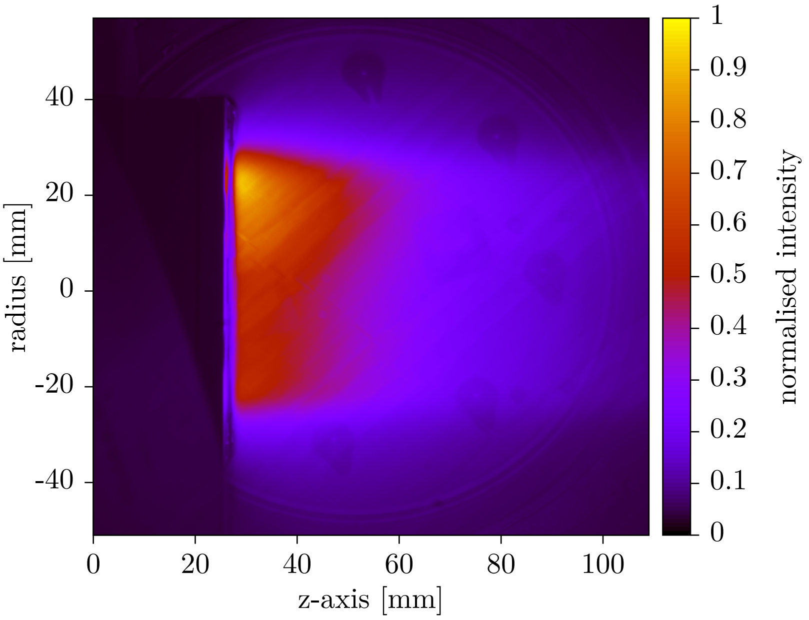

Figure 10.1.: Intensity distribution of WI line radiation (wavelength: 400.8 nm) measured during a pure neon plasma exposure at an incident ion energy of 280 eV, taken from [97]

assumed by Langmuir probe measurements. Further, it has to be noted that on average the PSI-2 cathode is exchanged every half a year, which implies that for every reported plasma exposure in PSI-2 another cathode was used. Hence, it is assumed that no systematic error is induced in the erosion measurements.

In Figure 10.2 the erosion results, mass loss Δm and surface recession d_e, of all samples exposed in the reported PSI-2 experiments are shown. The positions at which the samples were exposed (P1-8) are indicated on the W mask shown in Figure 10.3. To be able to compare the mass loss of W and WCrY, the obtained experimental values were divided by the respective material density, $\rho_W = 19.25\,\mathrm{g\,cm^{-3}}$ for W and $\rho_{WCrY} = 15.87\,\mathrm{g\,cm^{-3}}$ for WCrY. Further, all values are normalised to the maximum erosion value of the respective experiment. In some experiments there are a few locations filled with dummy samples, hence at these locations no erosion results are given. The graphs in Figure 10.2 further support the assumption that there is no systematic error induced by the plasma inhomogeneities since the position at which erosion was most intense varies between experiments. Erosion of pure W samples is not temperature-dependent so that possible differences in thermal isolation do not play a role. Thus these samples can be used to evaluate the geometry effect of the plasma source onto erosion. The relative standard deviation of the mass loss Δm of W samples exposed in D120P2, D220P, DAr120P and DHeAr120P was calculated to be 10 %, 5 %, 4 % and 15 %, respectively. Assuming the same eroded volume, the ratio of mass losses of W and WCrY amounts to $\Delta m_{WCrY}/\Delta m_W = 0.82$ (see Section 6.1). Put differently, Δm_{WCrY} should be reduced by 18 % in comparison to Δm_W. Consequently, it is concluded that the variation in erosion due to geometrical effects in PSI-2 does not significantly affect the comparison

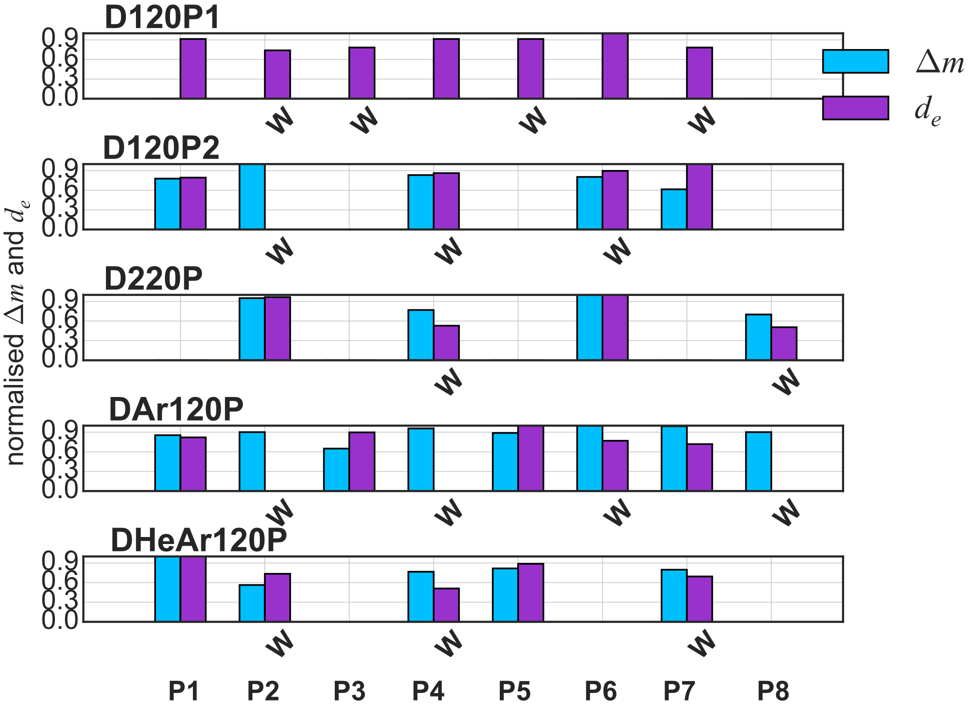

Figure 10.2.: Erosion results, mass loss Δm (normalised by division by the respective densities ρ_W and ρ_{WCrY}) and surface recession d_e, of all samples exposed in the reported PSI-2 experiments ordered according to their position on the used W mask. The position of the pure W samples is indicated, all sample positions can be found in the Appendix. The relative standard deviation of the mass loss Δm of W samples exposed in D120P2, D220P, DAr120P and DHeAr120P is 10 %, 5 %, 4 % and 15 %, respectively.

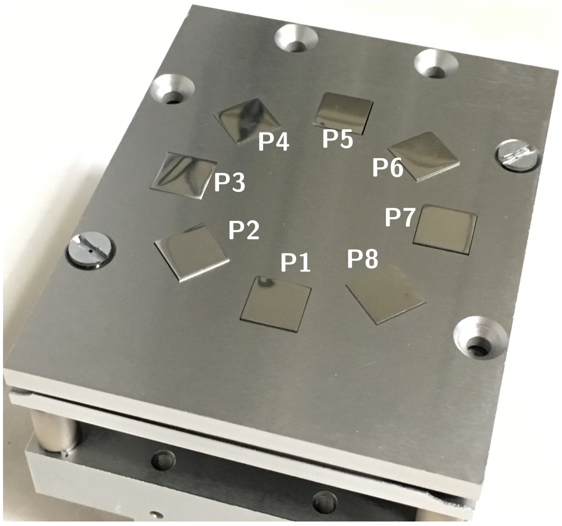

Figure 10.3.: Picture of W mask with samples installed for exposure in PSI-2. The sample positions are labelled P1-8.

of W and WCrY erosion. In experiments where diffusion had a notable impact on the erosion of WCrY samples, e.g. in D220P the WCrY samples were positioned at locations P2 and P6, erosion is increased at these locations. Similarly, increased erosion of WCrY samples is evident in DHeAr120P. Here the two WCrY samples were positioned at P1 and P5. All respective sample positions can be found in the Appendix (B).
Different to exposures in PSI-2, experiments in Magnum-PSI are conducted subsequently. This means that the samples are exposed each time at the same location. By means of the IR camera and the rotatable sample holder geometry it was possible to manually focus the centre of the plasma beam onto the sample under exposure. Due to biasing the beam width is increased leading to a flattened beam profile (see Figure 4.6 in Section 4.1.2). This flattened profile and the hence reduced peak flux density is measured by acquiring TS profiles of n_e and T_e. A flattened profile might deviate from the Gaussian distribution, which is assumed by the TS fitting procedure for calculating the plasma ion flux onto the target. This can lead to overestimating the ion flux onto the target as the peak amplitude of the actual profile is lower than that of the assumed Gaussian distribution. On the other hand, PSI processes at the target, such as the development of a Debye sheath, close to the position where the TS measurements are acquired, may lead to an underestimation of the plasma ion flux [117]. Whether the flux is under- or overestimated, since the plasma conditions are kept unchanged for all subsequent experiments, no significant difference in the relative fluences is assumed. Consequently, there is no error induced in the comparison of erosion results of W and WCrY samples exposed to the same fluence. Still, the absolute values of the obtained fluences may differ.

10.2. WCrY erosion - combined effects of ion irradiation and temperature-dependent surface composition

WCrY smart alloys are expected to show W-like erosion behaviour during plasma exposure due to preferential sputtering of the lighter alloying elements Cr and Y. That way the surface is depleted of these elements and the plasma faces a nearly pure W surface. To put this principle to test, plasma exposures carried out in the linear devices PSI-2 and Magnum-PSI targeted two different operational regimes: a *mild* regime with the ion energies of the main plasma species below the W sputter threshold, and a more *harsh* regime with ion energies at or above the W sputter threshold. The sample temperature was set to about 900 K in all experiments.

Plasma exposure at ion energies below the W sputter threshold

A plasma composed of solely D ions at an ion energy of 120 eV was chosen for the mild regime. The flux was in the order of 1×10^{21} ions/(m^{2}s) for PSI-2 exposures and in the order of 1×10^{23} ions/(m^{2}s) in Magnum-PSI experiments. Here fluences ranged from 1×10^{26} ions/m^2 to 2×10^{27} ions/m^2, whereas fluences were of the order of

1×10^{26} ions/m^2 in PSI-2 . In all experiments, WCrY showed W-like erosion behaviour, i.e. the samples experienced approximately the same surface recession d_e. At the same time, the mass loss Δm is reduced for WCrY. This is to be expected since the density of the WCrY alloy is lower than that of pure W.

Thanks to the OES system in Magnum-PSI, increased Cr sputtering could be detected at the start of the WCrY exposures. Then the signal caused by Cr sputtering decreased below the signal caused by W sputtering. This observation supports the depletion of Cr at the alloy surface due to preferential sputtering during the exposure: after a short time less Cr is sputtered since the surface consists mainly of pure W, which is sputtered much more slowly. The enriched shallow W layer acts as a protective layer for the remaining Cr, penetration depths of the low energetic D ions extend to only a few nm. After some time, enough W of the W-enriched layer has been sputtered so that Cr is accessed again. Cr is now consistently sputtered but at a much lower sputtering rate than at exposure start. A steady state balancing Cr sputtering, W sputtering and possible Cr transport from deeper layers develops. This state determines the erosion rate of the alloy. Erosion results in the case of mild plasma conditions at a sample temperature of 900 K suggest that the WCrY erosion rate is determined mainly by the W sputtering rate, making WCrY behave like pure W.

Surface analysis methods, such as SIMS, XPS and EDX, were employed to investigate plasma-induced changes in the alloy composition. For the PSI-2 exposures, a clear depletion of Y and Cr accompanied by W enrichment could be detected directly at the surface. In comparison, depletion of Cr and enrichment of W was less distinct in Magnum-PSI experiments. Although there is no clear fluence dependence inferable, the experiment conducted at the lowest fluence among the Magnum-PSI exposures showed the least distinct signatures of depletion and enrichment. EDX surface analysis for samples exposed in Magnum-PSI showed that on average in the first 100 nm below the surface, the Y content is increased, contrary to the Y signal evolution directly at the surface where Y is depleted. Cr depletion is detected directly at the surface, as well as in the first 100 nm below it. The same is true for the W enrichment. This behaviour is schematically illustrated in Figure 10.4.

Density Functional Theory calculations on the phase stability of WCrY smart alloys in the temperature range from 300 K to 1200 K presented in [118] suggest strong Y segregation in the WCrY system. Strong segregation of Y to the surface with a segregation energy of $\Delta H_Y = 0.3\,\text{eV}$ was also seen in the LEIS experiments in Section 8.1 starting at temperatures of 700 K. Segregation occurs predominantly at defects such as the grain boundaries or the surface. The manual grinding procedure used for sample preparation leads to an accumulation of defects up to about 1 µm below the surface. This is shown for example in Figure 7.3 in Chapter 7. Hence a possible explanation for the increased Y content seen by EDX could be Y segregation to this area with a high defect density once the WCrY sample is heated by plasma impact. Due to preferential sputtering, the Y is depleted close to the surface. Diffusive transport translates this plasma impact to deeper layers. Another factor impacting the subsurface Y content could be the high reactivity (higher than that of Cr and W) of Y with O. Y is the first element of the WCrY system to be oxidised, which could lead to an increased Y content in the subsurface layer if O is

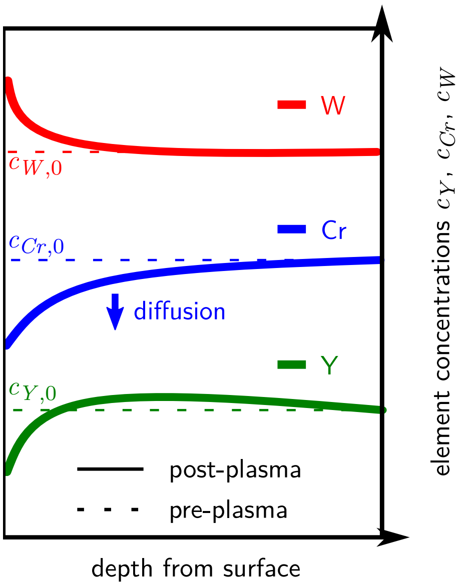

Figure 10.4.: Schematic drawing of concentration profiles of W, Cr and Y after plasma exposure.

present. Yet, the very low Y content complicates the analysis of plasma-induced changes in Y concentration and thus no XPS profiles were obtained. On the other hand by using O as the analysis beam in SIMS analysis, the sensitivity for Y detection is significantly above the noise level. Consequently, the depletion of Y directly at the surface was clearly detected using SIMS.

This depletion of Y and additionally the depletion of Cr are verified and even localised using EDX surface mapping for one of the PSI-2 experiments. The small black holes seen in SEM images on the surface after plasma exposure correspond to locations of preferentially sputtered Y. Moreover, Cr depletion detected on the EDX surface map corresponds to longer elongated craters or holes, which are localised around the grains. In the WCrY alloy, Y is present in the form of yttrium and oxide containing particles (called YO particles in this work) of the size of a few tenths of nm. The particles are predominantly located at the grain boundaries. Recent Atom Probe Tomography (APT) analysis at a depth of 3 µm below the surface of a WCrY samples oxidised at 1273 K confirms that the presence of O is bound to the presence of Y [43]. Further, the concentration of Cr is found to vary in between grains. At many grain boundaries the Cr concentration was found to be increased. The fact that Cr is often found along the grain boundaries as well as Y, in form of YO particles, explains the characteristic surface morphology after plasma exposure: selective sputtering of areas with high erosion yields results in a characteristic surface relief with etch pitches.

On SEM images of WCrY samples exposed in Magnum-PSI, the number and distinctiveness of the small black holes corresponding to Y depletion are decreased. In contrast to PSI-2 where re-deposition can be neglected, a plasma density increased by approximately two orders of magnitude in Magnum-PSI leads to significant re-deposition and possible self-sputtering. The probability for prompt re-deposition of W is around 1/3 .

These conditions lead to significant material mixing at the surface, which in turn can have an impact on the profiles of elemental composition obtained after plasma exposure. Since W has a higher mass than Cr and Y and re-deposition increases for heavier atoms, a larger fraction of the sputtered W is deposited after being sputtered in comparison to Cr and Y. The fact that depletion of Cr and Y are not easily distinguishable by SEM, and profiles are less shallow in comparison to PSI-2 experiments could be a result of this enhanced W re-deposition and material mixing at the surface. Significant re-deposition combined with high particle fluxes leads to strong re-organisation of the surface. [119] states that Magnum-PSI is designed to study PSI in the strongly-coupled regime. In this regime the mean-free path of sputtered particles is small in comparison to the plasma size so that the particles are trapped in the PSI region, which is the reason for the high prompt re-deposition probability. Additionally, the high particle flux drives the surface into states far from equilibrium, i.e. steady state sputter yields and surface composition. This in turn enhances surface diffusion and reactivity. Since (prompt) re-deposition and self-sputtering of W will play a crucial role in determining the material's erosion performance in future fusion devices [120], testing WCrY in the strongly-coupled regime is of crucial importance. Exposures in Magnum-PSI have shown similar erosion behaviour of W and WCrY in conditions where the energy of the main plasma ion species was set significantly below the W sputter threshold and at a sample temperature of 900 K. W sputtering is mainly caused by residual amounts of oxygen and other impurities which are not detectable via the OES system and whose concentrations are hence assumed to be considerably lower than 1 %. Based on the different plasma densities and therefore re-deposition conditions in the two linear devices it is difficult to investigate the flux dependence of enrichment and depletion. However, since plasma fluxes are increased by two orders of magnitude in Magnum-PSI, there is less time for the material surface to respond to the plasma irradiation. This could imply that thermally activated effects inside the material such as diffusion and segregation have less time to affect the subsurface elemental alloy composition.

SDTrimSP calculations simulating the plasma exposures in PSI-2 lead to matching experimental and model results without taking into account diffusion of alloying elements to the surface. No simulations were carried out for comparison with Magnum-PSI exposures since re-deposition is not reproducible using SDTrimSP. However, since for all experiments conducted in Magnum-PSI the volume loss of WCrY was reduced or similar compared to that of pure W, Cr diffusion leading to enhanced WCrY is assumed to be insignificant for the conditions of the experiments conducted in Magnum-PSI.

Plasma exposure at ion energies at or above the W sputter threshold

Experiments in the harsh plasma regime, with ion energies at or above the W sputter threshold, took place in PSI-2. The flux was in the order of 1×10^{21} ions/(m^2s), fluences ranged from 1×10^{25} ions/m^2 to 1×10^{26} ions/m^2 between experiments. Erosion of WCrY was only similar to W in experiment DAr120P, at a plasma composition of D+1 % Ar and an incident ion energy of 120 eV. At this ion energy, W is significantly sputtered by Ar (and residual impurity O), whereas D ion energies are clearly below the threshold for W sputtering. Hence it is assumed that for this experiment the erosion rate of WCrY is mainly determined by the W erosion rate, making WCrY behave similar to pure W. In comparison to pure D plasmas at 120 eV in PSI-2, the overall erosion of W and WCrY is increased by about a factor of 7 due to the addition of Ar to the plasma. However, the samples were only exposed to a fluence of 2×10^{25} ions/m^2, differences in the erosion of W and WCrY might become evident with extending fluence. On the other hand depletion of Y and Cr, in the form of small black holes and craters along the grain boundaries, is visible on the SEM images of the WCrY samples exposed in DAr120P and further confirmed in the XPS and SIMS analysis. Especially the preferential sputtering of the grain boundaries was clearly seen, even at lower magnification using LSCM.

In contrast to DAr120P, experimental results of the two other experiments in this regime, DHeAr120P at an incident ion energy of 120 eV and a plasma composition of D+5 % He+1 % and D220P at an incident ion energy of 220 eV in pure D plasma, show enhanced erosion of WCrY in comparison to W. An ion energy of 220 eV is just about the threshold for sputtering of W by D, similarly, the threshold for sputtering of W by He is just about 120 eV. Hence in the two cases where WCrY erosion was enhanced compared to W, the incident ion energy is just about the threshold value of the plasma component significantly sputtering W, namely D in D220P and He in DHeAr120P. In DHeAr120P there is additionally 1 % of Ar in the plasma, however, the He content is with 5 % dominant. In both of the cases where enhanced WCrY erosion was found, the SIMS and XPS profiles show depletion of Y and Cr accompanied by a W enrichment at the surface. In the profiles of all three experiments the depletion of Cr and enrichment of W is less pronounced than in the pure D sub-threshold exposures in PSI-2 (D120P1 and D120P2). Y depletion is equally visible for all experiments. Besides the surface roughness, diffusion and segregation processes complicate the interpretation of the elemental composition profiles. Such a profile is just a snapshot of the alloy composition after plasma exposures. Diffusion possibly smears out gradients induced by preferential sputtering and lowers the overall concentration below the surface as indicated by the blue arrow in Figure 10.4. In case of preferential sputtering of a multicomponent material, [121] and [122] observed that enrichment decreases with higher impact energies and with higher ion mass, respectively. Hence by adding any species heavier than D to the pure D plasma, or by increasing the ion energy from 120 eV, a more shallow enriched layer can be expected. Besides diffusion, surface segregation can lead to changes in the profiles even after plasma and during cool-down of the samples, keeping in mind that LEIS measurements revealed significant Cr surface segregation with a segregation energy of $\Delta H_{Cr} = 0.7\,\text{eV}$ already at a temperature above 700 K.

In addition to the effects of diffusion and segregation, the impact of the surface roughness of the ground and not polished samples was investigated. The most significant impact is expected for the SIMS analysis. Here the sputtering analysis is carried out under an angle of 45°, in contrast to EDX and XPS analysis where analysis beams at normal incidence are used. A mirror-like polished WCrY sample was measured using SIMS to see the impact on surface roughness on the analysis. One measurement was carried out with an O_2^- sputter beam, which is usually used for its increased sensitivity to metals, and an additional one with a Cs^+ sputter beam. Using a Cs^+ sputter beam enables detecting

O, on the downside the sensitivity for metals is decreased which is why the Y signal falls below the noise level. Additionally to W, Cr, Y and O, the carbon (C) signal is shown. The light impurity C is often encountered on sample surfaces. Both measurements are displayed in Figure 10.5. Comparing the top graph, the usual O_2^- measurement, with other pre-plasma measurements in Chapters 6 and 7, it becomes evident that for a polished surface the signal instabilities directly at the surface vanished. Besides this, the signals follow the same evolution as those of the ground and non-polished samples before plasma exposure. In the bottom graph it can be seen that an oxide layer of a few nm width exists at the surface. This is why in all the presented O_2^- measurements in this work, the W, Cr and Y signals are slightly decreased at the top surface. The increased Cr and W signals in this layer suggest that Cr and W are present in the form of oxides. This result agrees with the XPS results presented in 8.2, where W and Cr were always (partly) oxidised when being detected at the surface. Sputtering yields of oxidised metals differ from those of the pure metals, e.g. [107] states that the sputter threshold for oxidised W bombarded by D ions in the near-threshold energy range is significantly reduced. Thus an oxidised W topmost layer is expected to be sputtered faster. Additionally to the XPS results, the SIMS analysis of WCrY samples exposed in DHeAr120P (see Chapter 7) implies that the topmost surface of WCrY is already oxidised at room temperature in atmosphere. Further, other light impurities such as C are present on the surface. These additionally cause a low relative signal of W,Cr and Y directly at the surface. The noisiness of the C signal in Figure 10.5 is a result of the C content being close to the detection limit in the bulk material.
SDTrimSP simulations were carried out for the three experiments in this regime. It was found that in experiments D220P and DHeAr120P experimental results could only be matched by the simulation when diffusion of Cr was added to the model. In con-

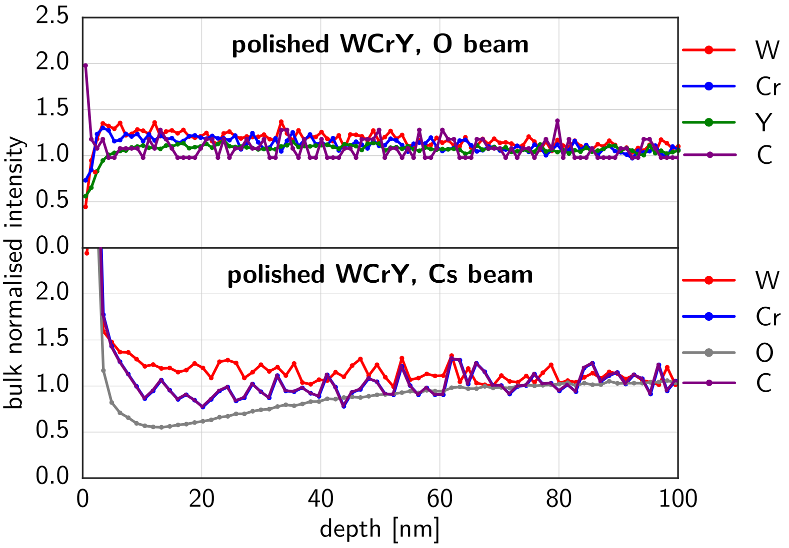

Figure 10.5.: SIMS analysis of a polished WCrY sample (not plasma-exposed) using an oxygen (O_2^-) sputter beam (top graph) and using a caesium (Cs^+) sputter beam (bottom graph).

trast, Cr diffusion could be neglected in DAr120P. Diffusion of Cr to the surface leads to enhanced sputtering of not only Cr but also W. In the vicinity of Cr, W atoms are sputtered more easily due to an intermediate Cr-W collision since for particles of similar mass the energy and momentum transfer is increased. This effect becomes crucial at incident ion energies close to the sputter threshold. For these energies it makes a significant difference in the erosion of WCrY if Cr is present at the surface. For fluxes in the order of 1×10^{21} ions/(m^{2}s) in PSI-2 exposures and temperatures of 900 K the diffusion rate of Cr is assumed to be fast enough to lead to enhanced WCrY erosion in the case of D220P and DHeAr120P. Cr is constantly resupplied to the surface where it is sputtered again and additionally leads to W sputtering, which inhibits the build-up of a significantly deep W-enriched layer. D220P served as an exemplary modelling case, here an extensive parameter scan was conducted to determine the diffusion coefficient of Cr in WCrY, $D_{Cr,WCrY}$. $D_{Cr,WCrY}$ was found to be around $1 \times 10^{-17}\,\mathrm{m^2\,s^{-1}}$. Samples used for D220P had an increased grain size compared to the samples used in all other experiments (see description of sample production in 3.3). Hence there may be a small difference in the Cr mobility by providing smaller grains and thus more grain boundaries in the material. Nevertheless, the value determined for $D_{Cr,WCrY}$ serves as a first estimate for the overall transport rate at which Cr is transported to the surface during D220P. For a more accurate determination of this and other material-specific parameters, such as the activation energy Q_a, extensive modelling outside the scope of the SDTrimSP simulations is necessary. Knowledge on the material-specific parameters would allow extrapolating the performance of WCrY to different experimental conditions, for instance a different sample temperature. LEIS measurements have shown that significant Cr surface segregation occurs already at a temperature of 700 K. At temperatures of 980 K the surface layer probed by LEIS was not enriched by W despite preferential sputtering of 250 eV D ions at a flux of 1×10^{18} ions/(m^{2}s). Yet, this finding is not easily comparable to the plasma exposures since here the plasma ion flux is at least 3 orders of magnitude higher.

SDTrimSP results gave further insight on the partial sputter yield evolution of W, Cr and Y within the WCrY alloy. Adding diffusion to the model leads to a delay in the partial yields approaching a steady state. Moreover, [123] and [124] have shown that the angle of incidence of the bombarding ions and the surface roughness have an impact on the sputter yield evolution. Whereas the angle of incidence can be defined in SDTrimSP and was set to the experimental value (normal incidence), surface roughness is neglected in the 1D simulations. Furthermore, it is not possible to reproduce the characteristic microstructure of the target: WCr grains with finely dispersed YO particles, which are predominantly located at the grain boundaries. 2D SDTrimSP were carried out to implement the microstructure into the model and qualitatively investigate the impact of diffusion occurring predominantly at the grain boundaries. It was found that with enhanced diffusion at the grain boundaries the characteristic surface morphology obtained after plasma exposure could be reproduced: W-enriched grains surrounded by valleys caused by preferential sputtering of Cr and Y at the grain boundaries.

Evaluation on the interdependency of erosion and diffusion rates

Generally, in case of sputtering of an alloy, the partial yields change with bombarding ion fluence and a steady state is only obtained for sufficiently high fluences [48]. The steady state sputter yields correspond to the stoichiometric composition of the bulk alloy (see Section 2.2). However, steady state is only obtained if the system is in equilibrium without sputtering, i.e. its composition is stable. After sintering of the mechanically alloyed W, Cr and Y powder, a solid solution of W and Cr is obtained for the WCrY bulk samples. According to the binary WCr phase diagram (see e.g. [125]) at a Cr content of 30 at%, W and Cr are not fully soluble at a temperature of 900 K. Hence both Cr and W rich phases will form when keeping the alloy at this temperature for long times. In [126] the microstructural stability of self-passivation WCrY alloys of the composition 89.5 wt% W - 10.0 wt% Cr - 0.5 wt% was tested by keeping the bulk alloy samples at different temperatures for long times. Keeping them at 923 K for 1000 h did not lead to notable changes in the microstructure. Hence diffusion driven processes are very slow, negligible compared to plasma-induced changes during the exposure of just several hours, at this temperature.

The surface concentrations in steady state are a function mainly of the mass and impact energy of the bombarding ions, the total sputtering yield is a result of these concentrations. Sputtered atoms originate from the topmost two or three atomic layers. Compositional changes, however, occur up to much larger depths, typically comparable to the range of the incident ions [48]. This layer of changed composition is called the altered layer. Its depth extends considerably beyond the interaction zone of incident and recoil particles if transport processes like thermal diffusion and thermal surface segregation become important. A schematic model of the alloy's subsurface layers is shown in Figure 10.6. Thermal diffusion can only counteract compositional changes and thus increase the thickness of the altered layer. In contrast, thermal segregation can produce compositional changes on its own such that it enforces or weakens compositional changes. Thus the thickness as well as the composition of the altered layer is temperature dependent. Both processes together lead to diffusive transport to the surface. Further, steady state is reached at a higher fluence in case of significant thermal transport processes. Whereas the altered layer thickness is independent of the fluence, the enrichment increases with fluence till steady state conditions are reached [127]. The thickness of the altered layer also extends with bombarding ion energy. [128] found that the removal of about one to two altered layer thicknesses was necessary to reach steady state conditions.

Besides being a function of fluence, temperature and sample composition, [51] states that steady state concentration profiles depend on the irradiation flux. The profiles are a result of the fluxes of particles being sputtered and the replenishment by the concentration gradient-driven diffusion flux. In this publication three different regimes are considered for different diffusive flux versus sputter flux ratios. In the diffusive flux dominated regime the surface composition remains constant under ion irradiation as the formation of a concentration gradient is suppressed by replenishing diffusion flux. Differently, in the erosion flux dominated regime replenishment by diffusion is negligible. In the third regime, the transition regime, the two contributions are of comparable magnitude result-

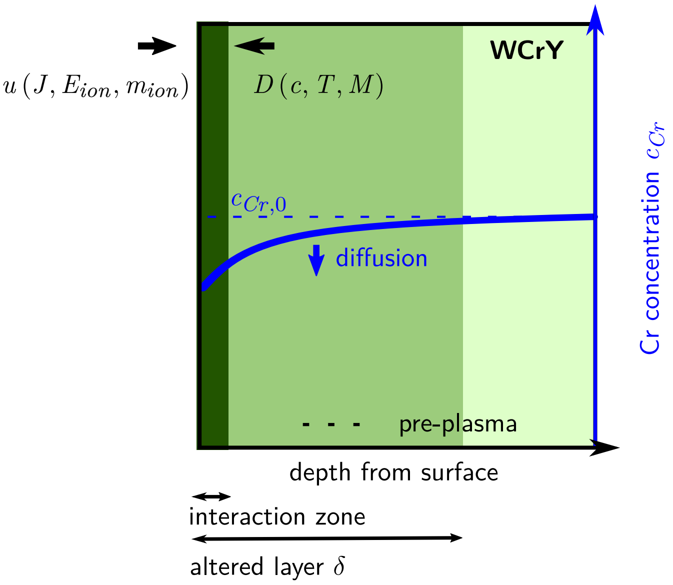

Figure 10.6.: Schematic model of subsurface layered structure with interaction zone and altered layer of thickness δ in WCrY alloy during plasma exposure. The erosion rate u depends mainly on the ion flux J, the incident ion energy E_{ion} and the mass of the incident ions m_{ion}, the diffusive flux D depends mainly on the sample temperature T and on the concentration c of the diffusing element. $c_{Cr,0}$ is the pre-plasma Cr concentration in the alloy.

ing in an intermediate profile. Since diffusive transport is temperature-dependent, at a fixed plasma ion composition and energy the regime is determined by the temperature of the exposed alloy material.
[129] calculated the thickness and concentration profile of the altered layer for steady state assuming that in this state the surface concentration of the high yield component (Cr in case of WCr) is zero. Using Fick's second law (see Equation (2.13)) the diffusion fluxes of material toward the surface being sputtered is incorporated. The relationship of the erosion rate u, the diffusion coefficient D and the thickness of the depleted zone δ is then given by Equation (10.1), which is ion flux (J) dependent since u is a function of J:

$$\delta = \frac{D}{u} \tag{10.1}$$

In experiment DHeAr120P (D+5 % He+1 % Ar plasma at an incident ion energy of 120 eV) diffusion was found to have a significant impact on the erosion of WCrY in comparison to that of W. XPS and EDX analysis confirmed that the layer of altered composition extends to depth of the order of about 100 nm below the surface. Further, the erosion rate can be approximated by dividing the surface recession d_e (of about 850 nm) by the quotient of average flux (5.5×10^{21} ions/(m^{2}s)) and total fluence (1.0×10^{26} ions/m^2). This yields a value of:

$$D = \delta \times u = 100\,\mathrm{nm} \times \frac{850\,\mathrm{nm}}{(1.0 \times 10^{26}\,\mathrm{ions/m^2})/(5.5 \times 10^{21}\,\mathrm{ions/(m^2s)})} \approx 1 \times 10^{-17}\,\mathrm{m^2\,s^{-1}}$$

This value agrees with the value determined with the aid of SDTrimSP modelling for the the diffusion coefficient of Cr in WCrY, $D_{Cr,WCrY}$ (see Section 7.3 for D220P, the PSI-2 experiment in pure D plasma at an incident ion energy of 220 eV). Other PSI-2 exposures at the same temperature of 900 K but with slightly varying plasma compositions, e.g. pure D in D120P or adding just 1 % of Ar in experiment DAr120P at the same ion energy of 120 eV, did show less significant diffusion. Consequently, it is assumed that for plasma fluxes of the order of 1×10^{21} ions/(m^2s) to 1×10^{22} ions/(m^2s), the transient flux regime is reached, where the contributions of erosion flux and diffusive flux to the steady state concentration profiles is of comparable magnitude. Hence small deviations in either the erosion rate u, which depends on the plasma composition, the incident ion energy and mass, or the diffusion flux D, which depends on the sample temperature and additionally on the concentration of the subsurface alloy concentration, lead to significant changes in the sputter yield compared to that of pure W. This assumption is confirmed by the finding that for the PSI-2 experiments described in the introduction to Chapter 8, varying the sample temperature at the same plasma parameters revealed a strong temperature dependence of the WCrY erosion.

In comparison to PSI-2 experiments, experiments in Magnum-PSI were conducted at ion fluxes in the order of 1×10^{23} ions/(m^2s). Here, just as for sub-threshold experiment D120P1 and D120P2 in PSI-2, diffusion was found to be negligible and WCrY erosion similar to that of W. It is assumed that at these high fluxes, the erosion flux dominates the surface composition. This is why especially at higher fluences when steady state sputtering has been reached for a long time, WCrY erosion becomes more and more similar to that of W. Still, here one has to keep in mind that re-deposition especially of W and also possible self-sputtering have an impact on the erosion rate.

Generally, the rates of the different processes impacting the alloy's surface composition and sputtering form a complex system of coupled equations since it contains many interdependencies. As shown in Figure 10.6, the erosion rate u depends mainly on the ion flux J, the incident ion energy E_{ion} and the mass of the incident ions m_{ion} and therefore the plasma composition. The diffusive flux D depends mainly on the sample temperature T and on the specific material microstructure M (e.g. grain size and distribution) and on the subsurface alloy concentration c which itself is dependent on the erosion and specific plasma composition. For instance, D or He ion energies close to the threshold show non-linear dependency on the surface alloy composition for binary WCr due to the effect of enhanced sputtering in case of an intermediate D-Cr/D-He collision (see Section 7.3). The depth-dependent composition of the surface layer from which sputtering occurs, $c_{ss}(x)$, is thus a function mainly of u and D: $c_{ss} = f(u(J, E_{ion}, m_{ion}), D(T, c, M))$

10.3. Plasma impact on the WCrY oxidation behaviour

The oxidation tests in Chapter 9 proved that the WCrY samples exposed in the different experiments conducted in PSI-2 successfully suppress W oxidation for up to 40 h in dry synthetic air at 1273 K containing 80 vol% Ar and 20 vol% O at 1 bar. Their oxidation performance is not deteriorated in comparison to reference WCrY samples of the same geometry. Yet, the PSI-2 sample geometry is not well suited for testing the impact of plasma exposure. Not all remnants from wire erosion can be removed by manual grinding for this geometry. Consequently, at the beginning of the oxidation there is an increased gradient of mass gain compared to the cubic WCrY samples usually used for oxidation testing. Yet, it could be shown that these surface effects do not play a role for the oxidation behaviour after 40 h.

The constant supply of Cr to the surface is crucial for the formation of a protective passivating Cr_2O_3 oxide scale. Bulk WCrY samples with the thickness of a few mm possess a sufficiently large Cr reservoir for successful passivation during several days to weeks in case of a reactor accident. The total Cr concentration does not drop below the critical value of 8 wt%, which [57] found to be the minimum concentration for effective passivation. Cr depletion was found to extend to at maximum the first 100 nm of the alloy after plasma exposure. After several days of oxidation the affected layer extends several 100 nm deep into the alloy. Thus, W oxidation of the Cr-depleted plasma-affected layer is negligible for an armour material of a few mm thickness, provided the total Cr reservoir of the alloy has not been depleted below the critical value of 8 wt%.

11. Summary and outlook

The aim of this thesis is to isolate the different parameters which determine the suitability of WCrY smart alloys, with a composition of 67.9 at% W - 31.1 at% Cr - 1.0 at% Y (corresponding to 88.0 wt% W - 11.4 wt% Cr - 0.6 wt% Y), as first wall material in future fusion devices such as DEMO and investigate their impact on the material's plasma performance. Dedicated experiments were carried out in the linear plasma devices PSI-2 and Magnum-PSI to investigate especially the alloy's erosion behaviour under different plasma conditions. In all plasma exposures the sample temperature was set to 900 K corresponding to DEMO first wall conditions. Two main test regimes for plasma exposures were determined. On the one hand a large fraction of the plasma particles in a fusion reactor will have impact energies which lie below the threshold for causing W erosion. On the other hand there will be particles with impact energies at or above the threshold and therefore causing significant W erosion. For experiments in PSI-2, binary collision-based modelling with the SDTrimSP code was used to simulate the impact of the ion irradiation onto the alloy composition and to investigate the effect of added thermal diffusion. Additional experiments, for which surface-sensitive analysis methods were employed, were executed focussing on the temperature dependence of the alloy's composition. To ascertain that the alloy is still able to suppress W oxidation after plasma exposure, the oxidation performance of plasma-exposed samples was tested.

It was found that the erosion of WCrY depends on various parameters. Most important are the partial sputtering rates of the alloy's components, which in turn depend on the plasma composition and the energy of the incident ions. Moreover, the sample temperature during exposure plays a significant role. Thermally activated processes such as diffusion and segregation result in the transport of Y and, due to its larger fraction in the alloy, more importantly Cr. IBA experiments revealed strong Cr segregation (with a segregation energy of $\Delta H_{Cr} = 0.7\,\mathrm{eV}$) and Y segregation ($\Delta H_Y = 0.3\,\mathrm{eV}$) starting from a temperature of 700 K. Further, thermal diffusion counteracts the build-up of Cr concentration gradients induced by preferential sputtering. Cr diffusion to the surface and the replenishment of the Cr-depleted subsurface layer has a significant impact on the erosion performance of WCrY in comparison to pure W. The presence of Cr in the vicinity of W leads to enhanced sputtering of WCrY in comparison to pure W. This effect becomes especially significant for ion energies close to the W sputter threshold.

Experimental results and SDTrimSP modelling suggest that for exposures in the mild plasma regime, at ion energies of 120 eV in pure D plasma in PSI-2 and Magnum-PSI, WCrY erosion is similar to that of pure W for fluxes up to $1 \times 10^{23}\,\mathrm{ions/(m^2s)}$ and fluences up to $2 \times 10^{27}\,\mathrm{ions/m^2}$. A W-enriched layer develops due to preferential sputtering of Cr and Y. The rates of Cr transport to the surface, due to diffusion and segregation, are negligible. The erosion rate of WCrY is determined by the W erosion rate, making

WCrY behave like pure W as a plasma-facing material.
In the harsh plasma regime, experiments were conducted in PSI-2 at fluxes in the order of 1×10^{21} ions/(m^{2}s) and fluences up to 1×10^{26} ions/m^2. Corresponding to this regime, two exposures were conducted with ion energies at the threshold for W: one experiment in pure D plasma at an ion energy of 220 eV and another one in mixed D+5 % He+1 % Ar plasma at an ion energy of 120 eV. WCrY erosion was found to be enhanced in comparison to pure W in both experiments. This enhanced erosion is caused by Cr diffusion to the surface leading to enhanced W sputtering. Via SDTrimSP modelling, the diffusion coefficient of Cr in WCrY was determined to be of the order of $1 \times 10^{-17}\,\mathrm{m^2\,s^{-1}}$. Consequently, in this experimental conditions the rate of Cr diffusion to the surface cannot be neglected, the erosion rate of WCrY is not determined mainly by that of W. In contrast, the third experiment conducted in the harsh regime, with a plasma composition of D+1 % Ar and at an incident ion energy of 120 eV, showed similar erosion for W and WCrY. In comparison to the pure D exposures at 120 eV erosion is severely increased due to the addition of Ar, which is clearly above the sputter threshold and thus significantly sputters W at these ion energies. Again, the WCrY erosion rate is determined mainly by that of pure W.
D retention after exposures in PSI-2 was measured to be close to the detection limit of 1×10^{-6} for all W and WCrY samples. In some cases the retention was increased for WCrY. The highest increase by a factor of 10 was measured for the mixed D+Ar+He exposure. [130] found that after D loading, the released D amount during thermal desorption measurements was about one order of magnitude higher for WCrY samples with a composition of 88.5 wt% W - 10.0 wt% Cr - 0.5 wt% Y in comparison to pure W. Generally, the solubility of D is low in W. At a temperature of 900 K during the exposures, D is easily released again and hence hardly detected during the NRA measurements. Still, if the D retention is about one order of magnitude increased for WCrY, the beneficial property of pure W as a first wall armour material with low hydrogen retention is depreciated. For more in-depth investigations on D retention experiments dedicated to measuring the D concentration during or directly after the plasma exposure are suggested.
The oxidation tests proved that the WCrY samples exposed in the different experiments conducted in PSI-2 successfully suppress W oxidation. Their oxidation performance is not deteriorated in comparison to reference WCrY samples of the same geometry; geometry effects in comparison to the cubic samples usually used for oxidation testing do not play a role after 40 h of oxidation. Plasma-exposure leads to a Cr depletion in, at maximum, the first 100 nm of the alloy. Losing this layer by W oxidation in case of a reactor accident is negligible for an armour material of a few mm thickness. Yet, it could be shown that thermal diffusion and thus Cr transport to the surface in combination with preferential sputtering lead to enhanced Cr loss for WCrY during plasma exposure. For the effective passivation of WCrY, the minimum total Cr content in the alloy has to amount to 8 wt%. For prolonged plasma exposure and thus Cr loss during several months or years of reactor operation, the size and and distribution of the remaining Cr reservoir have to be evaluated. This purpose requires assessing the rates of PWI and thermally activated processes, especially erosion and diffusion, in dependence of the

plasma parameters.

Taking all the above-mentioned results into account, the performance of WCrY smart alloys under fusion-relevant plasma conditions depends on the rates of the different plasma- and temperature-induced processes. Since prior to this work no investigations on the performance of WCrY had been carried out, it serves as an overview and narrows down the performance-relevant processes. In steady state, the sputtering yields of a multi-component material such as an alloy correspond to the stoichiometric alloy composition, which is 67.9 at% W - 31.1 at% Cr - 1.0 at% Y in case of WCrY smart alloys. Steady state is only obtained, after sufficiently long fluences, if the alloy's composition is stable without sputtering. Sputtering occurs from the topmost surface layer which extends over the two to three first atomic layers. The steady state composition profiles and hence the composition of this topmost layer depend on various parameters, most importantly the energy and mass of the incident ions. If thermal transport processes such as diffusion and segregation are significant at the present temperature, the layer in which compositional changes are induced during plasma impact extends beyond the interaction zone of projectile and recoil particles. Thermal diffusion counteracts the build-up of concentration gradients induced by plasma impact while thermal segregation weakens or enforces the gradients. Thus an increase in sample temperature has an impact on the composition and extension of the altered layer.

Since thermal processes transporting preferentially sputtered species to the surface and the erosion rate of these species compete, the concentration profiles and consequently the total alloy sputtering yield is flux-dependent. In case diffusive transport is the dominant process, preferentially sputtered species are resupplied constantly to the surface leading to an enhanced erosion of WCrY. This effect is especially strong for ion energies close to the sputter threshold of W due to lowering of the W sputter threshold in the vicinity of Cr. In the transient regime, rates of diffusive transport and erosion are of comparable magnitude such that small changes in the plasma composition or sample temperature result in WCrY showing either enhanced or equal erosion in comparison to W. The PSI-2 fluxes in the order of 1×10^{21} ions/(m^2s) are assumed to belong to this regime. DEMO first wall fluxes in steady state operation are assumed to be between 1×10^{20} ions/(m^2s) and 1×10^{21} ions/(m^2s) [28] at wall temperatures of 900 K. This range is comparable to that of the conducted experiments in PSI-2, thus the total alloy sputter yield is sensitive to small changes in the plasma composition such as the addition of heavier seeding ion species to the fuel hydrogen isotope ions. In this regime it is of paramount importance whether the energy of the main plasma species is significantly below or above or close to the W sputter threshold.

In contrast, Magnum-PSI fluxes of the order of 1×10^{23} ions/(m^2s) are firstly higher than the expected DEMO first wall fluxes and secondly are assumed to belong to the flux dominated regime. In this regime, at sample temperatures of 900 K, the WCrY total sputter yield is dominated by the erosion rate. However, in case of the Magnum-PSI experiments, the plasma density and strength of the magnetic field were significantly increased in comparison to PSI-2 experiments so that the effect of re-deposition of especially W cannot be neglected.

In addition to plasma edge seeding, transients leading to excessive heat and particle loads onto the PFCs could lead to both, enhanced erosion or diffusion rates. The possible extent and effects of these transient processes need further assessment.

In summary, since the rates of diffusion and erosion are strongly interdependent, the prediction of the steady state concentration profiles and thus the total sputter yield of WCrY in dependence of the plasma conditions represents a complex system of coupled equations. These depend sensitively on a variety of, for the most part, unknown material-specific constants such as activation energies or diffusion constants. Laboratory experiments such as the usage of linear devices, or methods dedicated to surface-sensitive analysis, allow to investigate the individual processes and their rates more closely.

In the future, a variety of different experiments could be carried out and methods applied with the aim of expanding the current knowledge of the WCrY response to plasma exposure and heating. On the one hand, further experiments with varying plasma conditions could be carried out in linear plasma devices. For instance, varying the Ar fraction of a D plasma at different ion energies could help investigating the impurity seeding level above which erosion rates for W and WCrY are critical for a first wall material. Increasing the fluence of the experiment conducted in mixed D+Ar plasma will help clarify if the reported result, similar erosion for W and WCrY, can be extrapolated to fusion-relevant operation times. Thin WCrY samples with a restricted Cr reservoir could be exposed to more exactly determine changes in the elemental composition profiles induced by diffusion. These profiles could then help defining material-specific parameters. Additionally, conducting exposures in the same linear device at different fluxes and temperatures could provide more insight into the rates of diffusive transport processes. Another approach for this purpose is extensive modelling using e.g. DFT calculations or molecular dynamic simulations. The alloy's microstructure is essential for its behaviour during operational or accidental conditions. Neutron irradiation in future fusion devices will lead to substantial microstructural changes. Here as well, modelling could help predicting these changes. Dedicated IBA experiments at different temperatures could be used for further insight of erosion and diffusion rates. One possibility is to measure the surface composition as a function of sputtering time.

Generally, the use of polished samples could simplify the interpretation of experimental results. This is especially important when using surface-sensitive analysis methods. Further, polished samples would help investigating plasma-induced changes in the surface morphology using SEM. Preferentially sputtered areas might be seen more clearly, the ripples formed during plasma ion irradiation might even be used to gain more insight into surface kinetics. Yet, one should keep in mind that WCrY samples are eventually designed for efficient passivation such that the improvement of the plasma performance of the samples should not deteriorate their oxidation performance.

Ultimately, in a fusion device the performance of a PFC material is a result of balancing the many PWI processes happening simultaneously. Additionally, there will be synergistic effects which cannot be investigated separately, such as the damage produced by neutron irradiation and coupled to this changes in the hydrogen isotope or He retention behaviour or the erosion resistance. For this reasons, in the framework of this thesis, WCrY and a W reference sample were installed in the tokamak ASDEX Upgrade for long-term exposure. This is described in Section 4.2. Figure 11.1 is a picture of the

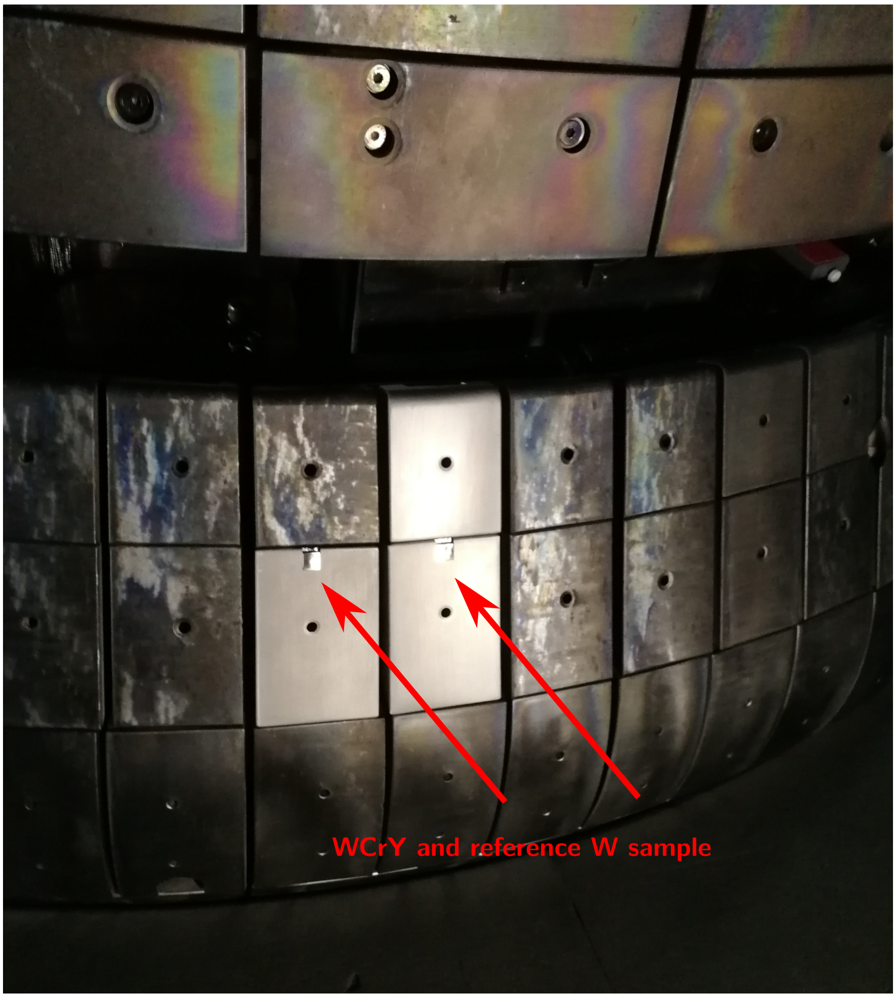

Figure 11.1.: Picture of a WCrY and W reference sample installed at the upper inner baffle of AUG prior to tokamak operation.

samples installed at the upper inner baffle of AUG. At the time of writing this thesis the samples were still installed so that no results can be reported. Depending on the conditions to which the samples were exposed during several months of tokamak operation, this experiment serves as a further test for the qualification of WCrY as first wall material of future fusion devices.

Bibliography

[1] **United Nations, Department of Economic and Social Affairs, Population Division**, “World Population Prospects: The 2017 Revision, Key Findings and Advance Tables”, no. ESA/P/WP/248, 2017.

[2] **International Energy Agency IEA**, “Key World Energy Statistics 2018: World Energy Atlas: Electrcity Consumption per Capita (MWh/capita) from 1973 to 2016”, 2018.

[3] **Umweltbundesamt**, “CO_2 Emission Factors for Fossil Fuels”, vol. CLIMATE CHANGE 28/2016, 2016.

[4] **N. Ghahramany, S. Gharaati, *et al.***, “New approach to nuclear binding energy in integrated nuclear model”, *Physics of Particles and Nuclei Letters*, vol. 8, no. 2, pp. 97–106, 2011, ISSN: 1547-4771. DOI: `10.1134/S1547477111020087`.

[5] **M. Kaufmann**, *Plasmaphysik und Fusionsforschung*, 2nd ed. Wiesbaden: Springer Fachmedien Wiesbaden, 2013, ISBN: 978-3-658-03238-8. DOI: `10.1007/978-3-658-03239-5`.

[6] **J. Wesson**, *Tokamaks*, 4th ed., ser. International series of monographs on physics. Oxford: Oxford Univ. Press, 2011, vol. 149, ISBN: 9780199592234.

[7] **IPP**, *Wendelstein 7-X Stellerator*, `https://www.ipp.mpg.de`. (visited on Jun. 12, 2019).

[8] **ITER Organisation**, *Schematic drawing of ITER reactor*, `https://www.iter.org`. (visited on Jun. 12, 2019).

[9] **E. Lassner and W. Schubert**, *Tungsten: Properties, Chemistry, Technology of the Element, Alloys, and Chemical Compounds.* Boston, MA: Springer US, 1999, ISBN: 978-1-4613-7225-7. DOI: `10.1007/978-1-4615-4907-9`.

[10] **R. Neu, J. Riesch, *et al.***, “Tungsten fibre-reinforced composites for advanced plasma facing components”, *Nuclear Materials and Energy*, vol. 12, pp. 1308–1313, Nov. 2016. DOI: `10.1016/j.nme.2016.10.018`.

[11] **A. Litnovsky, T. Wegener, *et al.***, “New oxidation-resistant tungsten alloys for use in the nuclear fusion reactors”, *Physica Scripta*, vol. T170, p. 014 012, 2017, ISSN: 0031-8949. DOI: `10.1088/1402-4896/aa81f5`.

[12] **P. Stangeby**, *The plasma boundary of magnetic fusion devices*, ser. Plasma physics series. Bristol: Institute of Physics Publ, 2000, ISBN: 9780750305594.

[13] **Schneider, R.**, *Plasma edge physics for tokamaks: IPP Report 12/1*, Max-Planck-Institut für Plasmaphysik, Ed., 2001.

[14] **D. C. McDonald, Y. Andrew, *et al.***, "Chapter 3: ELMy H-Mode Operation in JET", *Fusion Science and Technology*, vol. 53, no. 4, pp. 891–957, 2008, ISSN: 1536-1055. DOI: `10.13182/FST08-A1743`.

[15] *Fusion Physics*, ser. Non-serial Publications. Vienna: INTERNATIONAL ATOMIC ENERGY AGENCY, 2012, ISBN: 978-92-0-130410-0.

[16] **R. Fitzpatrick**, *Plasma Physics: An Introduction.* Hoboken: CRC Press, 2014, ISBN: 978-1-4665-9426-5.

[17] **A. Kirschner *et al.***, "Erosion and deposition mechanisms in fusion plasmas", *proceedings of the 11th Carolus Magnus Summer School on Plasma and Fusion Energy Physics*, vol. 11, 2013.

[18] **K. Schmid, K. Krieger, *et al.***, "DIVIMP modeling of tungsten impurity transport in ITER", *Journal of Nuclear Materials*, vol. 363-365, pp. 674–679, 2007, ISSN: 00223115. DOI: `10.1016/j.jnucmat.2007.01.045`.

[19] **S. Carpentier, R. A. Pitts, *et al.***, "Modelling of beryllium erosion–redeposition on ITER first wall panels", *Journal of Nuclear Materials*, vol. 415, no. 1, pp. 165–169, 2011, ISSN: 00223115. DOI: `10.1016/j.jnucmat.2010.10.081`.

[20] **R. Wenninger, R. Albanese, *et al.***, "The DEMO wall load challenge", *Nuclear Fusion*, vol. 57, no. 4, p. 046 002, 2017, ISSN: 0029-5515. DOI: `10.1088/1741-4326/aa4fb4`.

[21] **G. Federici, C. Bachmann, *et al.***, "DEMO design activity in Europe: Progress and updates", *Fusion Engineering and Design*, vol. 136, pp. 729–741, 2018, ISSN: 09203796. DOI: `10.1016/j.fusengdes.2018.04.001`.

[22] **R. Wenninger, R. Kembleton, *et al.***, "The physics and technology basis entering European system code studies for DEMO", *Nuclear Fusion*, vol. 57, no. 1, p. 016 011, 2017, ISSN: 0029-5515. DOI: `10.1088/0029-5515/57/1/016011`.

[23] **S. Cui, R. P. Doerner, *et al.***, "Thermal conductivity degradation and recovery in ion beam damaged tungsten at different temperatures", *Journal of Nuclear Materials*, vol. 511, pp. 141–147, 2018, ISSN: 00223115. DOI: `10.1016/j.jnucmat.2018.09.002`.

[24] **A. Calvo, K. Schlüter, *et al.***, "Self-passivating tungsten alloys of the system W-Cr-Y for high temperature applications", *International Journal of Refractory Metals and Hard Materials*, vol. 73, pp. 29–37, 2018, ISSN: 02634368. DOI: `10.1016/j.ijrmhm.2018.01.018`.

[25] **J. Roth, E. Tsitrone, *et al.***, "Recent analysis of key plasma wall interactions issues for ITER", *Journal of Nuclear Materials*, vol. 390-391, pp. 1–9, 2009, ISSN: 00223115. DOI: `10.1016/j.jnucmat.2009.01.037`.

[26] **M. Tokar**, "An assessment for the erosion rate of DEMO first wall", *Nuclear Fusion*, vol. 58, no. 1, p. 016 016, 2018, ISSN: 0029-5515. DOI: `10.1088/1741-4326/aa92dd`.

[27] **M. Beckers, W. Biel, *et al.***, "Investigations of the first-wall erosion of DEMO with the CELLSOR code", *Nuclear Materials and Energy*, vol. 12, pp. 1163–1170, 2017, ISSN: 23521791. DOI: `10.1016/j.nme.2017.01.006`.

[28] **Y. Igitkhanov, B. Bazylev, *et al.***, "The quantification of the key physics parameters for the DEMO fusion power reactor and analysis of the reactor relevant physics issues (KIT Scientific Reports ; 7661)", 2014. DOI: `10.5445/KSP/1000038935`.

[29] **W. Eckstein**, *Computer Simulation of Ion-Solid Interactions*, ser. Springer Series in Materials Science. Berlin and Heidelberg: Springer, 1991, vol. 10, ISBN: 978-3-642-73515-8. DOI: `10.1007/978-3-642-73513-4`.

[30] **R. J. Walker and M. R. Gilbert**, "Neutron activation of impurity seeding gases within a DEMO environment", *Fusion Engineering and Design*, vol. 124, pp. 892–895, 2017, ISSN: 09203796. DOI: `10.1016/j.fusengdes.2017.01.057`.

[31] W. Behrisch R.and Eckstein, Ed., *Sputtering by Particle Bombardment: Experiments and Computer Calculations from Threshold to MeV Energies*, ser. Topics in Applied Physics. Berlin Heidelberg: Springer-Verlag GmbH, 2007, vol. 110, ISBN: 978-3-540-44502-9. DOI: `10.1007/978-3-540-44502-9`.

[32] **M. Schmid**, *A Simple Sputter Yield Calculator*, `https://www.iap.tuwien.ac.at/www/surface/sputteryield`, 2006-2009. (visited on Apr. 29, 2019).

[33] **X. Yang and A. Hassanein**, "Atomic scale calculations of tungsten surface binding energy and beryllium-induced tungsten sputtering", *Applied Surface Science*, vol. 293, pp. 187–190, 2014, ISSN: 01694332. DOI: `10.1016/j.apsusc.2013.12.129`.

[34] **P. Sigmund**, "Theory of sputtering. i. sputtering yield of amorphous and polycrystalline targets", *Phys. Rev.*, vol. 184, pp. 383–416, 2 Aug. 1969. DOI: `10.1103/PhysRev.184.383`.

[35] **W. Eckstein and R. Preuss**, "New fit formulae for the sputtering yield", *Journal of Nuclear Materials*, vol. 320, no. 3, pp. 209–213, 2003, ISSN: 00223115. DOI: `10.1016/S0022-3115(03)00192-2`.

[36] **M. Küstner, W. Eckstein, *et al.***, "Angular dependence of the sputtering yield of rough beryllium surfaces", *Journal of Nuclear Materials*, vol. 265, no. 1-2, pp. 22–27, 1999, ISSN: 00223115. DOI: `10.1016/S0022-3115(98)00648-5`.

[37] **J. Roth, K. Sugiyama, *et al.***, "EUROFER as wall material: Reduced sputtering yields due to W surface enrichment", *Journal of Nuclear Materials*, vol. 454, no. 1-3, pp. 1–6, 2014, ISSN: 00223115. DOI: `10.1016/j.jnucmat.2014.07.042`.

[38] **J. W. Coenen, V. Philipps, *et al.***, "Analysis of tungsten melt-layer motion and splashing under tokamak conditions at TEXTOR", *Nuclear Fusion*, vol. 51, no. 8, p. 083 008, 2011, ISSN: 0029-5515. DOI: `10.1088/0029-5515/51/8/083008`.

[39] **V. Rohde and M. Balden**, "Arc erosion of full metal plasma facing components at the inner baffle region of ASDEX Upgrade", *Nuclear Materials and Energy*, vol. 9, pp. 36–39, 2016, ISSN: 23521791. DOI: `10.1016/j.nme.2016.09.006`.

[40] **G. De Temmerman, M. J. Baldwin, *et al.***, "Efficiency of thermal outgassing for tritium retention measurement and removal in ITER", *Nuclear Materials and Energy*, vol. 12, pp. 267–272, 2017, ISSN: 23521791. DOI: `10.1016/j.nme.2016.10.016`.

[41] **L. Buzi, G. de Temmerman, *et al.***, "Influence of tungsten microstructure and ion flux on deuterium plasma-induced surface modifications and deuterium retention", *Journal of Nuclear Materials*, vol. 463, pp. 320–324, 2015, ISSN: 00223115. DOI: `10.1016/j.jnucmat.2014.12.006`.

[42] **J. Roth and K. Schmid**, "Hydrogen in tungsten as plasma-facing material", *Physica Scripta*, vol. T145, p. 014 031, 2011, ISSN: 0031-8949. DOI: `10.1088/0031-8949/2011/T145/014031`.

[43] **F. Klein**, "Studies of oxidation resistant tungsten alloys at temperatures of 1100 k to 1475 k", PhD thesis, Ruhr-Universität-Bochum, Fakultät für Physik und Astronomie, 2019.

[44] **K. Schmid, V. Rieger, *et al.***, "Comparison of hydrogen retention in W and W/Ta alloys", *Journal of Nuclear Materials*, vol. 426, no. 1-3, pp. 247–253, 2012, ISSN: 00223115. DOI: `10.1016/j.jnucmat.2012.04.003`.

[45] **Y. Zayachuk, M. 't Hoen, *et al.***, "Deuterium retention in tungsten and tungsten–tantalum alloys exposed to high-flux deuterium plasmas", *Nuclear Fusion*, vol. 52, no. 10, p. 103 021, 2012, ISSN: 0029-5515. DOI: `10.1088/0029-5515/52/10/103021`.

[46] **M. 't Hoen, M. Balden, *et al.***, "Surface morphology and deuterium retention of tungsten after low- and high-flux deuterium plasma exposure", *Nuclear Fusion*, vol. 54, no. 8, p. 083 014, 2014, ISSN: 0029-5515. DOI: `10.1088/0029-5515/54/8/083014`.

[47] **S. Takamura, N. Ohno, *et al.***, "Formation of Nanostructured Tungsten with Arborescent Shape due to Helium Plasma Irradiation", *Plasma and Fusion Research*, vol. 1, p. 051, 2006, ISSN: 1880-6821. DOI: `10.1585/pfr.1.051`.

[48] **G. Betz and G. Wehner**, *Sputtering of multicomponent materials*, ser. Sputtering by Particle Bombardment II. Topics in Applied Physics. Springer, Berlin, Heidelberg, 1983, vol. 52, ISBN: 978-3-540-12593-8.

[49] **R. Sakamoto, E. Bernard, *et al.***, "Surface morphology in tungsten and RAFM steel exposed to helium plasma in PSI-2", *Physica Scripta*, vol. T170, p. 014 062, 2017, ISSN: 0031-8949. DOI: `10.1088/1402-4896/aa93a2`.

[50] H. Mehrer, Ed., *Diffusion in Solids: Fundamentals, Methods, Materials, Diffusion-Controlled Processes*, ser. Springer Series in Solid-State Sciences. Berlin Heidelberg: Springer-Verlag GmbH, 2007, vol. 155, ISBN: 978-3-540-71488-0. DOI: `10.1007/978-3-540-71488-0`.

[51] **U. von Toussaint, A. Mutzke, *et al.***, "Simulation of coupled sputter-diffusion effects", *Physica Scripta*, vol. T167, p. 014 023, 2016, ISSN: 0031-8949. DOI: `10.1088/0031-8949/T167/1/014023`.

[52] **G. Rowlands and D. P. Woodruff**, "The kinetics of surface and grain boundary segregation in binary and ternary systems", *Philosophical Magazine A*, vol. 40, no. 4, pp. 459–476, 1979, ISSN: 0141-8610. DOI: `10.1080/01418617908234852`.

[53] **P. Paufler**, "Physical metallurgy 3rd revised and enlarged edition", *Crystal Research and Technology*, vol. 20, no. 2, R. Cahn and P. Haasen, Eds., p. 270, 1985, ISSN: 0–444–86628–0. DOI: `10.1002/crat.2170200229`.

[54] **D. McLean**, *Grain boundaries in metals*, ser. Monographs on the physics and chemistry of materials. Clarendon Press, 1957.

[55] **A. V. Ruban, H. L. Skriver, *et al.***, "Surface segregation energies in transition-metal alloys", *Physical Review B*, vol. 59, no. 24, pp. 15 990–16 000, 1999, ISSN: 0163-1829. DOI: `10.1103/PhysRevB.59.15990`.

[56] **D. Maisonnier, I. Cook, *et al.***, "The European power plant conceptual study", *Fusion Engineering and Design*, vol. 75-79, pp. 1173–1179, 2005, ISSN: 09203796. DOI: `10.1016/j.fusengdes.2005.06.095`.

[57] **T. Wegener, F. Klein, *et al.***, "Development of yttrium-containing self-passivating tungsten alloys for future fusion power plants", *Nuclear Materials and Energy*, vol. 9, pp. 394–398, 2016, ISSN: 23521791. DOI: `10.1016/j.nme.2016.07.011`.

[58] **F. Koch and H. Bolt**, "Self passivating w-based alloys as plasma facing material for nuclear fusion", *Physica Scripta*, vol. T128, pp. 100–105, Mar. 2007. DOI: `10.1088/0031-8949/2007/t128/020`.

[59] **C. García-Rosales, P. López-Ruiz, *et al.***, "Oxidation behaviour of bulk W-Cr-Ti alloys prepared by mechanical alloying and HIPing", *Fusion Engineering and Design*, vol. 89, no. 7-8, pp. 1611–1616, 2014, ISSN: 09203796. DOI: `10.1016/j.fusengdes.2014.04.057`.

[60] **A. Litnovsky, T. Wegener, *et al.***, "New oxidation-resistant tungsten alloys for use in the nuclear fusion reactors", *Physica Scripta*, vol. T170, p. 014 012, 2017, ISSN: 0031-8949. DOI: `10.1088/1402-4896/aa81f5`.

[61] **D. J. Young**, *High temperature oxidation and corrosion of metals*, 2nd edition. Amsterdam and Boston and Heidelberg and London: Elsevier, 2016, ISBN: 978-0-08-100101-1.

[62] **F. Klein, T. Wegener, *et al.***, "On Oxidation Resistance Mechanisms at 1273 K of Tungsten-Based Alloys Containing Chromium and Yttria", *Metals*, vol. 8, no. 7, p. 488, 2018, ISSN: 2075-4701. DOI: `10.3390/met8070488`.

[63] **M. Gilbert, J.-C. Sublet, *et al.***, "Handbook of activation, transmutation, and radiation damage properties of the elements simulated using fispact-ii and tendl-2014; magnetic fusion plants", UK Atomic Energy Authority, Culham Science Centre, Abingdon, Oxfordshire,OX14 3DB, Tech. Rep. CCFER(16)36, 2015.

[64] **A. K. Lahiri**, *Applied Metallurgy and Corrosion Control.* Singapore: Springer Singapore, 2017, ISBN: 978-981-10-4683-4. DOI: `10.1007/978-981-10-4684-1`.

[65] **S. Telu, A. Patra, *et al.***, "Microstructure and cyclic oxidation behavior of W–Cr alloys prepared by sintering of mechanically alloyed nanocrystalline powders", *International Journal of Refractory Metals and Hard Materials*, vol. 36, pp. 191–203, 2013, ISSN: 02634368. DOI: `10.1016/j.ijrmhm.2012.08.015`.

[66] **F. Klein, T. Wegener, *et al.***, "Oxidation resistance of bulk plasma-facing tungsten alloys", *Nuclear Materials and Energy*, vol. 15, pp. 226–231, 2018, ISSN: 23521791. DOI: `10.1016/j.nme.2018.05.003`.

[67] **O. Guillon, J. Gonzalez-Julian, *et al.***, "Field-Assisted Sintering Technology/Spark Plasma Sintering: Mechanisms, Materials, and Technology Developments", *Advanced Engineering Materials*, vol. 16, no. 7, pp. 830–849, 2014, ISSN: 14381656. DOI: `10.1002/adem.201300409`.

[68] **ITER**, "Material Specification for the Supply of Tungsten Plates for the ITER Divertor IDM No.ITER D 2EDZJ4", *ITER Document*, 2010.

[69] **A. Kreter, C. Brandt, *et al.***, "Linear Plasma Device PSI-2 for Plasma-Material Interaction Studies", *Fusion Science and Technology*, vol. 68, no. 1, pp. 8–14, 2015, ISSN: 1536-1055. DOI: `10.13182/FST14-906`.

[70] **R. P. Doerner, A. Grossman, *et al.***, "Response of beryllium to deuterium plasma bombardment", *Journal of Nuclear Materials*, vol. 257, no. 1, pp. 51–58, 1998, ISSN: 00223115. DOI: `10.1016/S0022-3115(98)00435-8`.

[71] **H. van Eck, T. Abrams, *et al.***, "Operational characteristics of the high flux plasma generator Magnum-PSI", *Fusion Engineering and Design*, vol. 89, no. 9-10, pp. 2150–2154, 2014, ISSN: 09203796. DOI: `10.1016/j.fusengdes.2014.04.054`.

[72] **J. Scholten, P. A. van Zeijlmans Emmichoven, *et al.***, "Operational status of the Magnum-PSI linear plasma device", *Fusion Engineering and Design*, vol. 88, no. 9-10, pp. 1785–1788, 2013, ISSN: 09203796. DOI: `10.1016/j.fusengdes.2013.05.063`.

[73] **IPP**, *ASDEX Upgrade*, `https://www.ipp.mpg.de`. (visited on Jun. 30, 2019).

[74] **A. Kallenbach for the ASDEX Upgrade Team and the EUROfusion MST1 Team**, "Overview of ASDEX Upgrade results", *Nuclear Fusion*, vol. 57, no. 10, p. 102 015, 2017, ISSN: 0029-5515. DOI: `10.1088/1741-4326/aa64f6`.

[75] **A. Hakola, S. Koivuranta, *et al.***, "Erosion of tungsten and steel in the main chamber of ASDEX Upgrade", *Journal of Nuclear Materials*, vol. 463, pp. 162–165, 2014, ISSN: 00223115. DOI: `10.1016/j.jnucmat.2014.11.034`.

[76] **J. Goldstein, D. Newbury, *et al.***, *Scanning Electron Microscopy and X-Ray Microanalysis.* New York, NY: Springer New York, 2018, ISBN: 978-1-4939-6674-5. DOI: `10.1007/978-1-4939-6676-9`.

[77] **K. Kanaya and S. Okayama**, “Penetration and energy-loss theory of electrons in solid targets”, *Journal of Physics D: Applied Physics*, vol. 5, no. 1, pp. 43–58, 1972, ISSN: 00223727. DOI: `10.1088/0022-3727/5/1/308`.

[78] **J. H. Hubbell and S. M. Seltzer**, *X-Ray Mass Attenuation Coefficients, Radiation Physics Division, PML, NIST*, `https://www.nist.gov/pml/x-ray-mass-attenuation-coefficients`, 1989,1990,1996. (visited on May 27, 2019).

[79] **D. B. Hovis and A. H. Heuer**, “The use of laser scanning confocal microscopy (LSCM) in materials science”, *Journal of microscopy*, vol. 240, no. 3, pp. 173–180, 2010. DOI: `10.1111/j.1365-2818.2010.03399.x`.

[80] S. Paddock, Ed., *Confocal Microscopy: Methods and Protocols*, 2nd ed. 2014, ser. SpringerLink Bücher. New York, NY: Humana Press, 2014, vol. 1075, ISBN: 978-1-60761-847-8.

[81] **B. Schmidt and K. Wetzig**, *Ion Beams in Materials Processing and Analysis.* Vienna: Springer, 2013, ISBN: 978-3-211-99356-9. DOI: `10.1007/978-3-211-99356-9`.

[82] **W. Eckstein and R. Bastasz**, “A simple representation for the angular dependence of scattered and recoil particle energies”, *Nuclear Instruments and Methods in Physics Research Section B: Beam Interactions with Materials and Atoms*, vol. 29, no. 4, pp. 603–608, 1988. DOI: `10.1016/0168-583X(88)90467-3`.

[83] **H. R. Koslowski, S. R. Bhattacharyya, *et al.***, “Temperature-dependent in-situ LEIS measurement of W surface enrichment by 250 eV D sputtering of EUROFER”, *Nuclear Materials and Energy*, vol. 16, pp. 181–190, 2018, ISSN: 23521791. DOI: `10.1016/j.nme.2018.07.001`.

[84] **P. van der Heide**, *Secondary Ion Mass Spectrometry: An Introduction to Principles and Practices.* Hoboken: Wiley, 2014, ISBN: 978-1-118-48048-9. DOI: `10.1002/9781118916780`.

[85] **S. Fearn**, *An introduction to time-of-flight secondary ion mass spectrometry (ToF-SIMS) and its application to materials science*, ser. IOP concise physics. Bristol and San Rafael, Calif.: IOP Publ and Morgan & Claypool, 2015, ISBN: 978-1-6817-4088-1.

[86] **M. Tosa**, *Compendium of Surface and Interface Analysis*, The Surface Science Society of Japan, Ed. Singapore: Springer, 2018, ISBN: 978-981-10-6156-1.

[87] **Veeco Instruments, Inc.**, “Dektak 6M Manual: Software Version 8.34”, 2004.

[88] **G. van Rossum**, “Python tutorial”, Centrum voor Wiskunde en Informatica (CWI), Amsterdam, Tech. Rep. CS-R9526, May 1995.

[89] **The SciPy community**, *SciPy v1.3.0 Reference Guide*, `https://docs.scipy.org/doc/scipy/reference/generated/scipy.fftpack.fft.html`, 2008-2019. (visited on May 17, 2019).

[90] **P. van der Heide**, *X-ray photoelectron spectroscopy: An introduction to principles and practices.* Hoboken, NJ: Wiley, 2012, ISBN: 978-1-118-06253-1. DOI: `10.1002/9781118162897`.

[91] **N. Stojilovic**, "Why can't we see hydrogen in x-ray photoelectron spectroscopy?", *Journal of Chemical Education*, vol. 89, no. 10, pp. 1331–1332, Sep. 2012. DOI: `10.1021/ed300057j`.

[92] **J. Watts and J. Wolstenholme**, *An Introduction to Surface Analysis by XPS and AES.* Chichester, West Sussex, England ; New York: John Wiley & Sons Ltd, 2003, ISBN: 0-470 84712 3.

[93] **Y. Kamiura, K. Umezawa, *et al.***, "Characterization of Polycrystalline Tungsten Surfaces Irradiated with Nitrogen Ions by X-ray Photoelectron Spectroscopy", *MATERIALS TRANSACTIONS*, vol. 57, no. 9, pp. 1609–1614, 2016, ISSN: 1345-9678. DOI: `10.2320/matertrans.M2016107`.

[94] **A. Mutzke**, "SDTrimSP Version 5.00: IPP-Report", Max-Planck-Institut für Plasmaphysik, Garching, Germany, Tech. Rep. 12/8, 2011.

[95] **K. Sugiyama, M. Balden, *et al.***, "Erosion of EUROFER steel by mass-selected deuterium ion bombardment", *Nuclear Materials and Energy*, vol. 16, pp. 114–122, 2018, ISSN: 23521791. DOI: `10.1016/j.nme.2018.05.021`.

[96] **W. Eckstein**, "Sputtered Energy Coefficient and Sputtering Yield: IPP-Report", Max-Planck-Institut für Plasmaphysik, Garching, Germany, Tech. Rep. 17/29, 2011.

[97] **S. Ertmer**, "Spektroskopische Untersuchungen zur Zerstäubung von Wolfram an der linearen Plasmaanlage PSI-2", Master's thesis, Heinrich-Heine Universität Düsseldorf; Institut für Energie und Klimaforschung - Plasmaphysik am Forschungszentrum Jülich, 52428 Jülich, Germany, 2017.

[98] **A. Eksaeva, E. Marenkov, *et al.***, "ERO modelling of tungsten erosion in the linear plasma device PSI-2", *Nuclear Materials and Energy*, vol. 12, pp. 253–260, 2017, ISSN: 23521791. DOI: `10.1016/j.nme.2017.03.014`.

[99] **M. O'Mullane**, *Open-ADAS - Electron Impact Ionisation Coefficients*, `http://open.adas.ac.uk`, 2009. (visited on Jul. 10, 2019).

[100] **V. Alimov, J. Roth, *et al.***, "Deuterium retention in tungsten exposed to low-energy, high-flux clean and carbon-seeded deuterium plasmas", *Journal of Nuclear Materials*, vol. 375, no. 2, pp. 192–201, 2008, ISSN: 00223115. DOI: `10.1016/j.jnucmat.2008.01.008`.

[101] **T. Škereň, K. Temst, *et al.***, "Ion-induced roughening and ripple formation on polycrystalline metallic films", *New Journal of Physics*, vol. 15, no. 9, p. 093 047, Sep. 2013. DOI: `10.1088/1367-2630/15/9/093047`.

[102] **M. O'Mullane**, *Open-ADAS - Electron Impact Ionisation Coefficients*, `http://open.adas.ac.uk/detail/adf07/cadw/ca09_w.dat`, 2009. (visited on Jul. 10, 2019).

[103] **National Institute of Standards and Technology (NIST) - Physical Measurement Laboratory**, *NIST Atomic Spectra Database Lines Form*, `https://physics.nist.gov/PhysRefData/ASD/lines_form.html`. (visited on Jul. 7, 2019).

[104] **K. Sugiyama, K. Schmid, *et al.***, “Sputtering of iron, chromium and tungsten by energetic deuterium ion bombardment”, *Nuclear Materials and Energy*, vol. 8, pp. 1–7, 2016, ISSN: 23521791. DOI: `10.1016/j.nme.2016.05.016`.

[105] **Y. Hirooka, M. Bourham, *et al.***, “Evaluation of tungsten as a plasma-facing material for steady state magnetic fusion devices”, *Journal of Nuclear Materials*, vol. 196-198, pp. 149–158, 1992, ISSN: 00223115. DOI: `10.1016/S0022-3115(06)80022-X`.

[106] **T. Kenmotsu, T. Ono, *et al.***, “Effect of deuterium retention upon sputtering yield of tungsten by deuterons”, *Journal of Nuclear Materials*, vol. 415, no. 1, Supplement, S108–S111, 2011, Proceedings of the 19th International Conference on Plasma-Surface Interactions in Controlled Fusion, ISSN: 0022-3115. DOI: `https://doi.org/10.1016/j.jnucmat.2010.08.057`.

[107] **M. Guseva, A. Suvorov, *et al.***, “Sputtering of beryllium, tungsten, tungsten oxide and mixed W–C layers by deuterium ions in the near-threshold energy range”, *Journal of Nuclear Materials*, vol. 266-269, pp. 222–227, 1999, ISSN: 00223115. DOI: `10.1016/S0022-3115(98)00819-8`.

[108] **J. Roth, J. Bohdansky, *et al.***, “Data on low energy light ion sputtering: IPP-Report”, Max-Planck-Institut für Plasmaphysik, Garching, Germany, Tech. Rep. 9/26, 1979.

[109] **A. Mutzke**, “SDTrimSP-2D: Simulation of Particles Bombarding on a Two Dimensional Target- Version 2.0: IPP-Report”, Max-Planck-Institut für Plasmaphysik, Garching, Germany, Tech. Rep. 12/11, 2013.

[110] **K. De Lannoye**, “Temperature dependence of the erosion performance of WCrY Smart Alloys”, Master’s thesis, Deartment of Physics, Vrije Universiteit Brussel, 1000 Brussels, Belgium, 2019.

[111] **The SciPy community**, *SciPy v1.3.0 Reference Guide*, `https://docs.scipy.org/doc/scipy/reference/generated/scipy.optimize.curve_fit.html`, 2008-2019. (visited on Jun. 13, 2019).

[112] **G. C. Nelson**, “Summary Abstract: Semiempirical modeling of the background in low energy ion scattering spectra”, *Journal of Vacuum Science & Technology A: Vacuum, Surfaces, and Films*, vol. 4, no. 3, pp. 1567–1569, 1986, ISSN: 0734-2101. DOI: `10.1116/1.573508`.

[113] **R. Beikler and E. Taglauer**, “Surface segregation at the binary alloy CuAu (100) studied by low-energy ion scattering”, *Surface Science*, vol. 643, pp. 138–141, 2016, ISSN: 00396028. DOI: `10.1016/j.susc.2015.08.030`.

[114] **Thermo Fisher Scientific Inc.**, *XPS Simplified - Chromium, Transition Metal*, `https://xpssimplified.com/elements/chromium`, 2013-2019. (visited on Oct. 28, 2019).

[115] **T. Wegener**, “Tungsten-chromium-yttrium as self-passivating tungsten alloy”, PhD thesis, Rheinisch-Westfälische Technische Hochschule Aachen, 2020.

[116] **M. Hubeny**, “The dynamics of electrons in linear plasma devices and its impact on plasma surface interaction”, PhD thesis, Ruhr-Universität Bochum, Fakultät für Physik und Astronomie, 2018.

[117] **J. van den Berg**, personal communication, 2019.

[118] **D. Sobieraj**, *Phase stability of W-based high-entropy alloys and smart alloys*, Presentation during joint meeting on DEMO safety, high entropy and smart alloys, FZ Jülich, Germany, 2019.

[119] **G. De Temmerman, M. A. van den Berg, *et al.***, “High heat flux capabilities of the Magnum-PSI linear plasma device”, *Fusion Engineering and Design*, vol. 88, no. 6-8, pp. 483–487, 2013, ISSN: 09203796. DOI: `10.1016/j.fusengdes.2013.05.047`.

[120] **A. Kirschner, D. Tskhakaya, *et al.***, “Modelling of Impurity Transport and Plasma-Wall Interaction in Fusion Devices with the ERO Code: Basics of the Code and Examples of Application”, *Contributions to Plasma Physics*, vol. 56, no. 6-8, pp. 622–627, 2016, ISSN: 08631042. DOI: `10.1002/ctpp.201610014`.

[121] **P. Ray and V. Shutthanandan**, “Low-energy sputtering research”, Tuskegee University, Tuskegee, Alabama, Tech. Rep. NASA/CR-1999-209161, Jun. 1999.

[122] **R. R. Olson and G. K. Wehner**, “Composition variations as a function of ejection angle in sputtering of alloys”, *Journal of Vacuum Science and Technology*, vol. 14, no. 1, pp. 319–321, 1977. DOI: `10.1116/1.569198`.

[123] **R. Stadlmayr, P. S. Szabo, *et al.***, “Fluence dependent changes of surface morphology and sputtering yield of iron: Comparison of experiments with SDTrimSP-2D”, *Nuclear Instruments and Methods in Physics Research Section B: Beam Interactions with Materials and Atoms*, vol. 430, pp. 42–46, 2018. DOI: `10.1016/j.nimb.2018.06.004`.

[124] **R. Arredondo, M. Oberkofler, *et al.***, “Angle-dependent sputter yield measurements of keV D ions on W and Fe and comparison with SDTrimSP and SDTrimSP-3D”, *Nuclear Materials and Energy*, vol. 18, pp. 72–76, 2019, ISSN: 23521791. DOI: `10.1016/j.nme.2018.12.007`.

[125] **S. V. Nagender Naidu, A. M. Sriramamurthy, *et al.***, “The Cr-W (Chromium-Tungsten) system”, *Bulletin of Alloy Phase Diagrams*, vol. 5, no. 3, pp. 289–292, 1984, ISSN: 0197-0216. DOI: `10.1007/BF02868555`.

[126] **E. Sal, C. García-Rosales, *et al.***, “High temperature microstructural stability of self-passivating W-Cr-Y alloys for blanket first wall application”, *Fusion Engineering and Design*, 2019, ISSN: 09203796. DOI: `10.1016/j.fusengdes.2019.02.136`.

[127] **Z. L. Liau, J. W. Mayer, *et al.***, “Sputtering of PtSi”, *Journal of Applied Physics*, vol. 49, no. 10, pp. 5295–5305, 1978, ISSN: 0021-8979. DOI: `10.1063/1.324431`.

[128] **Z. L. Liau, W. L. Brown, *et al.***, “Surface-layer composition changes in sputtered alloys and compounds”, *Applied Physics Letters*, vol. 30, no. 12, pp. 626–628, 1977, ISSN: 0003-6951. DOI: `10.1063/1.89285`.

[129] **H. W. Pickering**, “Ion sputtering of alloys”, *Journal of Vacuum Science and Technology*, vol. 13, no. 2, pp. 618–621, 1976, ISSN: 0022-5355. DOI: `10.1116/1.569045`.

[130] **H. Maier, T. Schwarz-Selinger, *et al.***, “Deuterium retention in tungsten based materials for fusion applications”, *Nuclear Materials and Energy*, vol. 18, pp. 245–249, 2019, ISSN: 2352-1791. DOI: `https://doi.org/10.1016/j.nme.2018.12.032`.

A. Manual grinding procedure of samples prior to experiments

Manual grinding of W and WCrY samples follows the same procedure, as explained in Section 3.3. All grinding steps are performed for 90 s, after this time the grinding paper is changed. There is constant water supply onto the SiC paper during the grinding process. Depending on the number of samples, a force of 20 N to 40 N is applied. For example a force of 30 N is used for four samples, this value is reduced for a smaller and increased for a larger number of samples. The speed of rotation is 150 rotations/min. The order of the consecutive steps using increasingly fine SiC paper is:

- P400: grind at least three times until the visible dirt from wire erosion on the surface is removed
- P800: grind two times
- P1000:
  - 1. grind one time
  - 2. the ground surface is painted with a non water-soluble marker
  - 3. grind one time
  - 4. surface is checked for marker remnants:
    - ∗ if there are visible marker remnants: grind multiple times with P1000 or go back to P800 if marker remnants remain for several steps
    - ∗ if there are no visible marker remnants: go to next step
- P1200: grind two times

B. Sample measurements for the different plasma exposures

In the tables detailed results of sample characterisation before and after plasma exposure are given. The indicated sample position for samples exposed in PSI-2 corresponds to the position in the W mask (see Figure 10.3).

	weight loss [μg]	R_a [nm] before	R_a [nm] after	d_e [μm] measured	d_e [μm] calculated	sample position
D120P1-W1	na	532 ± 60	584 ± 36	0.17 ± 0.05	na	P2
D120P1-W2	na	26 ± 2	30 ± 2	0.18 ± 0.05	na	P7
D120P1-W3	na	32 ± 3	28 ± 3	0.21 ± 0.05	na	P5
D120P1-W4	na	28 ± 4	28 ± 2	0.18 ± 0.06	na	P3
D120P1-WCrY1	na	43 ± 7	61 ± 19	0.23 ± 0.05	na	P6
D120P1-WCrY2	na	32 ± 5	32 ± 5	0.21 ± 0.05	na	P1
D120P1-WCrY3	na	306 ± 33	319 ± 15	0.21 ± 0.05	na	P4

Table B.1.: Detailed results of samples exposed in D120P1.

	weight loss [μg]	R_a [nm] before	R_a [nm] after	d_e [μm] measured	d_e [μm] calculated	sample position
D120P2-W1	560 ± 170	28 ± 3	28 ± 4	0.26 ± 0.12	0.29 ± 0.14	P6
D120P2-W2	580 ± 420	39 ± 6	38 ± 4	0.25 ± 0.13	0.30 ± 0.25	P4
D120P2-W3	697 ± 49	28 ± 2	34 ± 3	na	0.36 ± 0.14	P2
D120P2-WCrY1	447 ± 235	22 ± 4	23 ± 3	0.23 ± 0.11	0.29 ± 0.18	P1
D120P2-WCrY2	353 ± 189	26 ± 4	24 ± 4	0.29 ± 0.10	0.23 ± 0.15	P7

Table B.2.: Detailed results of samples exposed in D120P2.

	weight loss [μg]	R_a [nm] before	R_a [nm] after	d_e [μm] measured	d_e [μm] calculated
D120M1-W	340 ± 10	20 ± 1	21 ± 1	0.17 ± 0.03	0.18 ± 0.01
D120M2-W	445 ± 10	19 ± 2	22 ± 4	0.21 ± 0.08	0.23 ± 0.01
D120M3-W	873 ± 10	25 ± 1	32 ± 0	0.38 ± 0.11	0.36 ± 0.45
D120M4-W	1160 ± 10	26 ± 7	44 ± 3	0.50 ± 0.06	0.36 ± 0.60
D120M1-WCrY	205 ± 10	23 ± 3	29 ± 3	0.25 ± 0.10	0.13 ± 0.01
D120M2-WCrY	395 ± 10	34 ± 2	32 ± 0	0.35 ± 0.05	0.25 ± 0.01
D120M3-WCrY	723 ± 10	28 ± 11	26 ± 0	0.37 ± 0.03	0.46 ± 0.01
D120M4-WCrY	955 ± 10	23 ± 1	28 ± 1	0.57 ± 0.06	0.60 ± 0.01

Table B.3.: Detailed results of samples exposed in D120M1-4.

	weight loss [μg]	R_a [nm] before	R_a [nm] after	d_e [μm] measured	d_e [μm] calculated	sample position
D220P-W1	1200 ± 10	41 ± 6	47 ± 6	0.46 ± 0.11	0.62 ± 0.10	P4
D220P-W2	1093 ± 10	28 ± 4	33 ± 5	0.44 ± 0.22	0.56 ± 0.10	P8
D220P-WCrY1	1223 ± 10	30 ± 4	34 ± 7	0.84 ± 0.17 (at corner: 0.90 ± 0.21)	0.77 ± 0.13	P2
D220P-WCrY2	1287 ± 10	24 ± 5	25 ± 4	0.87 ± 0.22	0.80 ± 0.13	P6

Table B.4.: Detailed results of samples exposed in D220P.

	weight loss [μg]	R_a [nm] before	R_a [nm] after	d_e [μm] measured	d_e [μm] calculated	sample position
DAr120P-W1	640 ± 10	53 ± 1	56 ± 7	na	0.32 ± 0.01	P8
DAr120P-W2	710 ± 10	31 ± 0	42 ± 3	0.30 ± 0.08	0.37 ± 0.01	P6
DAr120P-W3	680 ± 10	40 ± 1	45 ± 11	na	0.35 ± 0.01	P4
DAr120P-W4	640 ± 10	34 ± 1	39 ± 8	na	0.33 ± 0.01	P2
DAr120P-WCrY1	500 ± 10	34 ± 0	34 ± 3	0.32 ± 0.08	0.32 ± 0.01	P1
DAr120P-WCrY2	580 ± 10	37 ± 0	44 ± 9	0.28 ± 0.04	0.37 ± 0.01	P7
DAr120P-WCrY3	520 ± 10	25 ± 0	29 ± 0	0.39 ± 0.06	0.33 ± 0.01	P5
DAr120P-WCrY4	380 ± 10	34 ± 3	47 ± 0	0.35 ± 0.06	0.24 ± 0.01	P3

Table B.5.: Detailed results of samples exposed in DAr120P.

	weight loss [μg]	R_a [nm] before	R_a [nm] after	d_e [μm] measured	d_e [μm] calculated	sample position
DHeAr120P-W1	1547 ± 10	22 ± 5	38 ± 9	0.68 ± 0.04	0.80 ± 0.01	P7
DHeAr120P-W2	1093 ± 10	28 ± 3	37 ± 2	0.72 ± 0.07	0.57 ± 0.01	P2
DHeAr120P-W3	1487 ± 10	26 ± 0	35 ± 3	0.50 ± 0.06	0.77 ± 0.01	P4
DHeAr120P-WCrY1	1307 ± 10	27 ± 2	na	0.87 ± 0.10	0.82 ± 0.01	P5
DHeAr120P-WCrY2	1600 ± 10	46 ± 7	58 ± 12	0.98 ± 0.08	1.01 ± 0.01	P1

Table B.6.: Detailed results of samples exposed in DHeAr120P.

Acknowledgements

Throughout the writing of this dissertation I have received a great deal of support, assistance and guidance from a variety of people I would like to express my gratitude to:

I would first like to thank my doctoral supervisors, Prof. Dr. Christian Linsmeier from Ruhr-Universität Bochum and Prof. Dr. ir. Jean-Marie Noterdaeme as well as Prof. Dr. ir. Kristel Crombé from Universiteit Gent for giving me the opportunity to carry out this joint PhD project. Furthermore, I would like to express my deepest gratitude for the thorough proofreading of my thesis. I would further like to express my gratitude to Prof. Dr. Christian Linsmeier for his constant support and guidance and his insightful comments on my work. Special thanks go to Prof. Dr. Achim von Keudell for his commitment to be my second supervisor at the Ruhr-Universität Bochum.

Most of my research was carried out at the IEK-4 at Forschungszentrum Jülich. I gratefully acknowledge the guidance and support from my supervisor Dr. Andrey Litnovsky. In addition, I would like to thank him for proofreading.
Many other colleagues and friends in Jülich contributed to the successful completion of this PhD thesis and lightened up the sometimes tough periods of the PhD work. I greatly appreciate the help and advice in many scientific questions from Dr. Timo Dittmar. He, besides always having time to listen to my questions, inspired me to learn more about fusion already during my Bachelor thesis and finally to do a PhD in fusion.
Many thanks also go to Dr. Arkadi Kreter for his assistance with the PSI-2 experiments and often scheduling last minute experiments. I would further like to thank Dr. Marcin Rasinski for carrying out numerous FIB, SEM and EDX analyses on my samples, in case of unexpected rescheduling of the experiments under a certain time pressure, and discussing the results with me. Thanks to Dr. Uwe Breuer from ZEA-3 for carrying out a great number of SIMS analyses and explaining the SIMS operating principle as well as its limits related to the discussion of the obtained SIMS results. Dr. Nabi Aghdassi helped me greatly with the interpretation of the XPS results and acquainted himself thoroughly with the data acquired by Petra Hansen long before he started working in Jülich, which is why I would like to thank him. Thanks also to Petra for carrying out the experiments during her PhD thesis. My sincere thanks also go to Dr. Rudi Koslowski who showed great interest into the surface science-related questions of the WCrY system. He carried out experiments on the segregation of WCrY in his experimental setup ALI with great care and enthusiasm and was a great help in discussing the results and possible implications. Thanks also to Dr. Heinrich Hartmann from ZEA-3 for carrying out a number of Sputter-XPS analyses on the WCrY samples. I am very thankful for the possibility to do the metallurgical alloying and sintering of the WCrY samples at

IEK-1 provided by Dr. Jesus Julian-Gonzalez and Dr. Martin Bram.
I am also very grateful to all my fellow PhD students who helped me to take the obstacles of my PhD thesis with more ease and often enlightened the day with enjoyable lunch time or coffee break chats. Special thanks go to Dr. Felix Klein with whom I shared the office during my time in Jülich and who was always very supportive in all issues related to the oxidation of WCrY samples and carried out numerous oxidation experiments as well as FIB and SEM analyses for this work.

During my PhD, I spent a couple of months in Belgium, mostly at my home University in Gent and some days also at SCK.CEN in Mol as well as at the VUB in Brussels. I gratefully acknowledge the help and company of my fellow PhD students at the Department of Applied Physics, other Fusion DC students as well as my course mates during the classes I attended in Mol, Gent and Brussels. I would like to especially thank Karen De Lannoye, who was a great support during my time at the VUB. Furthermore, thanks to Karen for being a remarkably supportive and eager Master student and translating the abstract of this thesis into Dutch.

Experiments and further work did not only take place in Jülich, but also in other fusion research institutes where I was happy to encounter support and counsel during my PhD work.
My deep appreciation goes out to Dr. Andreas Mutzke from IPP Greifswald, who helped me significantly with carrying out simulations using the binary collision code SDTrimSP. Thanks for discussing the simulation results as well as model limits and the implications bound to them.
I would like to thank Dr. Albrecht Herrmann, Dr. Karl Krieger and Karsten Schlüter from IPP Garching for helping me with the preparations of the installation of WCrY and W in AUG. I am very thankful for the support from Karsten with using the LSCM at IPP Garching and additionally doing some measurements on my samples.
I gratefully acknowledge the help and fruitful discussions with Dr. Tom Morgan and the whole Magnum-PSI team at DIFFER in Eindhoven during my stay for the exposures carried out in Magnum-PSI as well as the discussion of the results afterwards.

My sincere thanks also go to Jan who has been a precious friend and supported me innumerable times during my PhD, discussed Physics-related questions and thoroughly proofread not only this PhD thesis.
A very special thank you to Stephan for your endless support, especially during the writing of this thesis. I could not have made it through the last months of my PhD without you.
Last but not least, I would like to thank my family and friends for always being there. Thank you for listening to my complaints during times where I was stuck and being understanding for the often limited time I had due to being busy with the PhD work.

My deepest thanks go to my parents who always gave me the opportunity and infinitive support to strive for my goals.

Curriculum Vitae

Personal data

Name:	Janina Schmitz
Date and place of birth:	19.08.1992 in Ahlen
Nationality:	German

Education

2003-2012	**Allgemeine Hochschulreife (A-levels)** Gymnasium Johanneum, Ostbevern, Germany bilingual (German, English), final grade: 1,3
2012-2015	**B.Sc. Physics** Heinrich-Heine-Universität, Düsseldorf, Germany Title of Bachelor thesis (at Institut für Energie- und Klimaforschung, Plasmaphysik (IEK-4), Forschungszentrum Jülich GmbH in Jülich, Germany): Charakterisierung und Optimierung der Ionenquellen des ARTOSS Experiments; Final grade: 1,3
2015-2016	**M.Sc. Fusion Energy** University of York, United Kingdom Title of Master thesis (at Culham Centre for Fusion Energy in Oxfordshire, United Kingdom): Analysis of filtered camera data from divertor region of the JET tokamak; Final grade: with distinction
2016-2019	**PhD student** Erasmus Mundus International Doctoral College in Fusion Science and Engineering, partner institutions: Forschungszentrum Jülich GmbH, Institut für Energie- und Klimaforschung, Plasmaphysik (IEK-4), Jülich, Germany; Max-Planck-Institut für Plasmaphysik, Garching, Germany; Ghent University, Belgium; Ruhr-Universität Bochum, Germany Topic: Development of tungsten alloy plasma-facing materials for the fusion power plant

Conferences and trainings

2015	**Summer University for Plasma Physics and Fusion Research**, Max-Planck Institut für Plasmaphysik Garching (Munich, Germany)
2016	**International Polytechnic Summer School**, Module: Introduction to Plasma Physics and Controlled Fusion (St. Petersburg, Russia)
2016-2019	**Doctoral Schools Ghent University** (Belgium), Courses: Leadership Foundation, Professional Networking, Advanced Academic English: Conference Skills, How to Get Published, High-resolution X-ray Tomography, General Relativity
2016-2019	**Helmholtz Interdisciplinary Doctoral Training in Energy and Climate Research** (Forschungszentrum Jülich GmbH, Germany), Courses: Project Management, Team Communication, Scientific Presentation, Getting Published
2017	**DPG-Frühjahrstagung der Sektion Materie und Kosmos** (Bremen, Germany), Talk *Plasma exposure of W-based smart alloys for the fusion power plant*
2017	**6th International Workshop on Plasma Material Interaction Facilities for Fusion Research** (Tsukuba, Japan), Talk *Plasma Exposure of WCrY Smart Alloys in the linear Plasma Device PSI-2*
2017	**International Conference on Fusion Reactor Materials** (Aomori, Japan), Poster *Smart alloys as advanced plasma-facing materials for fusion reactors*
2017	**International Energy Agency - Tungsten Workshop** (Aomori, Japan), Talk *Progress in R&D on Smart Tungsten Alloys*
2017	**DPG-Frühjahrstagung der Sektion Atome, Moleküle, Quantenoptik und Plasmen** (Erlangen, Germany), Talk *Impact of steady state deuterium plasmas on WCrY Smart Alloys*
2018	**23rd International Conference on Plasma Surface Interactions in Controlled Fusion Devices** (Princeton, United States) , Poster *Impact of Ar-seeded and pure D plasmas on WCrY Smart Alloys*
2018	**Eurofusion Task Meeting on Self-Passivating Tungsten-Based Alloys** (San Sebastian, Spain), Talk *Plasma exposure of WCrY smart alloys to pure D and mixed D, Ar plasmas in PSI-2*
2018	**Carolus Magnus Summer School on Plasma and Fusion Energy Physics** (Weert, Netherlands), Poster *Impact of Ar-seeded and pure D plasmas on WCrY Smart Alloys*
2018	**FuseNet PhD Event** (Aix-en-Provence, France), Poster *Plasma impact on self-passivating WCrY Smart Alloys*
2019	**DPG-Frühjahrstagung der Sektion Materie und Kosmos** (Munich, Germany), Talk *Impact of fusion-relevant plasmas on WCrY Smart Alloys*
2019	**17th International Conference on Plasma-Facing Materials and Components** (Eindhoven, Netherlands), Poster *On the plasma suitability of WCrY Smart Alloys -the effect of mixed D+Ar/He plasmas*

Publications

- A. R. Field, I. Balboa, P. Dremelow, J. Flanagan, C. Guillemaut, J. R. Harrison, A. Huber, V. Huber, B. Lipschultz, G. F. Matthews, A. Meigs, **J. Schmitz**, M. Stamp, N. R. Walkden and JET Contributors. Dynamics and stability of divertor detachment in H-mode plasmas on JET, *Plasma Physics and Controlled Fusion*, 59 095003, 2017.

- A. Litnovsky, T. Wegener, F. Klein, Ch. Linsmeier, M. Rasinski, A. Kreter, X. Y. Tan, **J. Schmitz**, J. W. Coenen, Y. Mao, J. Gonzalez-Julian, and M. Bram. New oxidation-resistant tungsten alloys for use in the nuclear fusion reactors, *Physica Scripta*, T170:014012, 2017.
- A. Litnovsky, T. Wegener, F. Klein, Ch. Linsmeier, M. Rasinski, A. Kreter, X. Y. Tan, **J. Schmitz**, Y. Mao, J. W. Coenen, M. Bram, and J. Gonzalez-Julian. Advanced smart tungsten alloys for a future fusion power plant, *Plasma Physics and Controlled Fusion*, 59(6):064003, 2017.
- A. Wynn, B. Lipschultz, I. Cziegler, J. Harrison, A. Jearvinen, G. F. Matthews, **J. Schmitz**, B. Tal, M. Brix, C. Guillemaut, D. Frigione, A. Huber, E. Joffrin, U. Kruzei, F. Millitello, A. Nielsen, N. R. Walkden, S. Wiesen and JET Contributors. Investigation into the formation of the scrape-off layer density shoulder in JET ITER-like wall L-mode and H-mode plasmas, *Nuclear Fusion*, 58 056001, 2018.
- F. Klein, T. Wegener, A. Litnovsky , M. Rasinski , X. Y. Tan, **J. Schmitz**, Ch. Linsmeier , J. W. Coenen, H. Du, J. Mayer, and U. Breuer. On Oxidation Resistance Mechanisms at 1273 K of Tungsten-Based Alloys Containing Chromium and Yttria, *Metals*, 8(7):488, 2018.
- **J. Schmitz**, A. Litnovsky, F. Klein, T. Wegener, X. Y. Tan, M. Rasinski, A. Mutzke, P. Hansen, A. Kreter, A. Pospieszczyk, S. Möller, J. W. Coenen, Ch. Linsmeier, U. Breuer, J. Gonzalez-Julian, and M. Bram. WCrY smart alloys as advanced plasma-facing materials – exposure to steady-state pure deuterium plasmas in PSI-2, *Nuclear Materials and Energy*, 15:220-225, 2018.
- F. Klein, T. Wegener, A. Litnovsky, M. Rasinski, X. Y. Tan, J. Gonzalez-Julian, **J. Schmitz**, M. Bram, J. W. Coenen, and Ch. Linsmeier. Oxidation resistance of bulk plasma-facing tungsten alloys, *Nuclear Materials and Energy*, 15:226-231, 2018.
- A. Litnovsky, F. Klein, **J. Schmitz**, T. Wegener, Ch. Linsmeier, M. R. Gilbert, M. Rasinski, A. Kreter, X. Y. Tan, Y. Mao, J. W. Coenen, M. Bram, and J. Gonzalez-Julian. Smart first wall materials for intrinsic safety of a fusion power plant, *Fusion Engineering and Design*, 136(B):878-882, 2018.
- X. Y. Tan, F. Klein, A. Litnovsky, T. Wegener, **J. Schmitz**, Ch. Linsmeier, J. W. Coenen, U. Breuer, M. Rasinski, P. Li, L. M. Luo, and Y. C. Wu. Evaluation of the high temperature oxidation of W-Cr-Zr self-passivating alloys, *Corrosion Science*, 147:201-211, 2019.
- F. Klein, A. Litnovsky, T. Wegener, X. Y. Tan, J. Gonzalez-Julian, M. Rasinski, **J. Schmitz**, Ch. Linsmeier, M. Bram, and J. W. Coenen. Sublimation of advanced tungsten alloys under DEMO relevant accidental conditions. *Fusion Engineering and Design*, 146(A):1198-1202, 2019.

- **J. Schmitz**, A. Litnovsky, F. Klein, X. Y. Tan, U. Breuer, M. Rasinski, S. Ertmer, A. Kreter, J. Gonzalez-Julian, M. Bram, J. W. Coenen, and Ch. Linsmeier. Argon-seeded plasma exposure and oxidation performance of tungsten-chromium-yttrium smart alloys. *Tungsten*, 2661-8036:1–10, 2019.
- **J. Schmitz**, A. Mutzke, A. Litnovsky, F. Klein, X. Y. Tan, T. Wegener, P. Hansen, N. Aghdassi, A. Eksaeva, M. Rasinski, S. Ertmer, A. Kreter, J. Gonzalez-Julian, J. W. Coenen, Ch. Linsmeier and M. Bram. Preferential Sputtering induced Cr-Diffusion during Plasma Exposure of WCrY Smart Alloys. *Journal of Nuclear Materials*, 526: 151767, 2019.
- **J. Schmitz**, A. Litnovsky, F. Klein, K. De Lannoye, A. Kreter, M. Rasinski, U. Breuer, J. Gonzalez-Julian, M. Bram, J. W. Coenen and Ch. Linsmeier. On the plasma suitability of WCrY Smart Alloys - the effect of mixed D+Ar/He plasmas. *Physica Scripta*, in press, 2019.
- H. R. Koslowski, **J. Schmitz** and Ch. Linsmeier. Segregation and Preferential Sputtering of Cr in WCrY Smart Alloy. *Nuclear Materials and Energy*, in press, 2019.